WCAP-16996-NP
Revision 1

April 2015

Realistic LOCA Evaluation Methodology Applied to the Full Spectrum of Break Sizes (FULL SPECTRUM LOCA Methodology)

Volume I
WCOBRA/TRAC-TF2 Models and Correlations

WCAP-16996-NP
Revision 1

Realistic LOCA Evaluation Methodology Applied to the Full Spectrum of Break Sizes (FULL SPECTRUM LOCA Methodology)

Author's Name	Author's Department
Jeffrey R. Kobelak*	LOCA Integrated Services
Dr. Katsuhiro Ohkawa*	LOCA Integrated Services
Dr. Liping Cao*	LOCA Integrated Services
Aaron M. Everhard*	LOCA Integrated Services
Dr. Jun Liao*	LOCA Integrated Services
Nikolay P. Petkov*	LOCA Integrated Services
Michael A. Shockling*	LOCA Integrated Services

April 2015

Reviewer: Mitchell E. Nissley*
Safety Analysis and Licensing

Approved: Amy J. Colussy*, Manager
LOCA Integrated Services

*Electronically approved records are authenticated in the electronic document management system.

Westinghouse Electric Company LLC
1000 Westinghouse Drive
Cranberry Township, PA 16066, USA

TABLE OF CONTENTS

TABLE OF CONTENTS (cont.)

TABLE OF CONTENTS (cont.)

TABLE OF CONTENTS (cont.)

TABLE OF CONTENTS (cont.)

TABLE OF CONTENTS (cont.)

TABLE OF CONTENTS (cont.)

TABLE OF CONTENTS (cont.)

LIST OF TABLES

VOLUME 1

LIST OF TABLES (cont.)

LIST OF TABLES (cont.)

LIST OF FIGURES

VOLUME 1

LIST OF FIGURES (cont.)

LIST OF FIGURES (cont.)

LIST OF FIGURES (cont.)

LIST OF FIGURES (cont.)

LIST OF FIGURES (cont.)

LIST OF FIGURES (cont.)

LIST OF FIGURES (cont.)

LIST OF FIGURES (cont.)

LIST OF FIGURES (cont.)

EXECUTIVE SUMMARY

Westinghouse's previously approved best-estimate Large Break loss-of-coolant accident (LBLOCA) methodology (or Evaluation Model (EM)) is described in WCAP-16009-P-A (Nissley et al., 2005). The methodology is referred to as the Automated Statistical Treatment of Uncertainty Method (ASTRUM) and is applicable to Westinghouse designed 3- and 4-loop plants with emergency core cooling system (ECCS) injection into the cold legs, Westinghouse designed 2-loop plants with upper plenum injection (UPI) and Combustion Engineering designs. The ASTRUM EM is based on the use of WCOBRA/TRAC as the system code. The ASTRUM EM was also submitted as part of the AP1000® Design Control Document (APP-GW-GL-700, Rev. 19).

The ASTRUM EM addressed Large Break LOCA scenarios with a minimum size of 1.0 ft^2. In this report the applicability of the Westinghouse best-estimate LOCA EM was extended to consider smaller break size, therefore including what traditionally are defined as Small and Intermediate Break LOCA scenarios. The new realistic LOCA EM is called FULL SPECTRUM™ LOCA (FSLOCA™) methodology. The term 'Full Spectrum' specifies that the new EM is intended to resolve the full spectrum of LOCA scenarios which result from a postulated break in the cold leg of a pressurized water reactor, PWR (While this EM is also applicable for analysis of breaks at other loop locations, such as the hot leg, these breaks are not limiting compared with the cold leg break). The break sizes considered in the Westinghouse FULL SPECTRUM LOCA include any break size in which break flow is beyond the capacity of the normal charging pumps, up to and including a double ended guillotine (DEG) rupture with a break flow area equal to two times the pipe area.

As in previous EMs, the FULL SPECTRUM LOCA methodology was patterned after the Code Scaling, Applicability, and Uncertainty (CSAU) methodology developed under the guidance of the U.S. Nuclear Regulatory Commission (NRC) (Boyack et al., 1989). The development roadmap is consistent with Regulatory Guide 1.203.

For the FULL SPECTRUM LOCA methodology WCOBRA/TRAC was modified by replacing the 1D Module (based on TRAC-PD2) with the TRAC-PF1/MOD2 code and adding a few improvements to the 3D module (based on Westinghouse modified COBRA-TF). One of the major changes is the addition of an explicit non-condensable gas transport equation within the 3D module. The replacement of TRAC-PD2 with TRAC-PF1/MOD2 allows the extension of a two-fluid, six-equation formulation of the two-phase flow to the 1D loop components. This new code has been named WCOBRA/TRAC-TF2 where "TF2" is an identifier that reflects the use of a three-field (TF) formulation of the 3D module derived by COBRA-TF and a two-fluid (TF) formulation of the 1D module based on TRAC-PF1/MOD2.

With the exception of the additional tracking of a non-condensable gas field, and few minor upgrades needed to address Small Break LOCA scenarios, the Vessel model is equivalent to the Vessel model of the approved version of WCOBRA/TRAC. Requests for additional information (RAIs) identified during the early review of the code that led to the approval of the original CQD (Bajorek et al., 1998) and

subsequent ASTRUM EM (Nissley et al., 2005), and associated responses should still be applicable. In a few instances, as in the downcomer region, a more refined noding scheme has been adopted to improve accuracy or provide more consistency across the various test facilities. Such noding choices have been justified by assessing the model against large and full scale experiments.

The FULL SPECTRUM LOCA EM explicitly considers the effects of fuel pellet thermal conductivity degradation (TCD), and other burnup-related effects. Accordingly, the fuel rod performance data input into the FSLOCA EM is PAD5, which explicitly models TCD.

The FULL SPECTRUM LOCA EM is intended to be applicable to all PWR fuel designs with Zirconium alloy cladding. Most of the data considered in the methodology is based on Zircaloy-4 and ZIRLO® cladding. [

]^{a,c}

The uncertainty methodology is based on a direct Monte Carlo sampling of the uncertainty attributes. The overall uncertainty is bounded using a non-parametric statistical method similar to the ASTRUM EM. However, sample size is increased to reduce the variability of the estimator. The break size spectrum is divided in two regions. Region-I provides coverage of what typically are defined as Small Break LOCA scenarios and stretch into Intermediate Break LOCA. Region-II starts from Intermediate Break size and include what typically are defined Large Break LOCA scenarios. A 95/95 joint-probability statement is developed for the key parameters that are needed to demonstrate compliance with 10 CFR 50.46 acceptance criteria.

The code models, their assessment, and conclusions on model biases and uncertainties are aimed to be generic and applicable to the same class of plants covered by the ASTRUM EM. When modeling aspects are specific to a particular PWR design, the choice was made to focus attention on the Westinghouse 3-loop PWR with cold leg ECCS injection. Therefore, the demonstration plant analysis is limited to such a design.

1 ROADMAP OF FULL SPECTRUM LOCA (FSLOCA) METHODOLOGY

1.1 BACKGROUND

Westinghouse's previously approved best-estimate Large Break Loss-of-Coolant Accident (LBLOCA) methodology (or Evaluation Model (EM)) is described in WCAP-16009-P-A (Nissley et al., 2005). The methodology is referred to as the Automated Statistical Treatment of Uncertainty Method (ASTRUM) and is applicable to Westinghouse designed 3- and 4-loop plants with emergency core cooling system (ECCS) injection into the cold legs, Westinghouse designed 2-loop plants with upper plenum injection (UPI) and Combustion Engineering designs. The ASTRUM EM is based on the use of WCOBRA/TRAC as the system code. The ASTRUM EM was also approved for the AP1000 pressurized water reactor (PWR) as part of the AP1000 Design Control Document (APP-GW-GL-700, Rev. 19).

The methodology was patterned after the Code Scaling, Applicability, and Uncertainty (CSAU) methodology developed under the guidance of the U.S. Nuclear Regulatory Commission (NRC) (Boyack et al., 1989). The only significant difference from the CSAU methodology is in the application of the uncertainty analysis to the PWR (Element 3 of the CSAU methodology). In ASTRUM the uncertainties are combined using non-parametric order statistics.

The purpose of the new FULL SPECTRUM LOCA (FSLOCA) EM is to build on the ASTRUM EM, by extending the applicability of the WCOBRA/TRAC code to include the treatment of Small and Intermediate Break Loss-of-Coolant (SBLOCA and IBLOCA) scenarios. The term 'Full Spectrum' specifies that the new EM is intended to resolve the full spectrum of LOCA scenarios which result from a postulated break in the cold leg of a PWR. The break sizes considered in the Westinghouse FSLOCA™ methodology include any break size in which break flow is beyond the capacity of the normal charging pumps, up to and including a double ended guillotine (DEG) rupture with a break flow area equal to two times the pipe area.

For the FSLOCA methodology, WCOBRA/TRAC was modified by replacing the 1D Module (based on TRAC-PD2) with the TRAC-P[1] [ ]^{a,c} code and adding a few improvements to the 3D module (based on Westinghouse modified COBRA-TF). One of the major changes is [ ]^{a,c}. The replacement of TRAC-PD2 with TRAC-P [ ]^{a,c} allows the extension of a two-fluid, six-equation formulation of the two-phase flow to the 1D loop components. This new code has been named WCOBRA/TRAC-TF2 where "TF2" is an identifier that reflects the use of a three-field (TF) formulation of the 3D module derived by COBRA-TF and a two-fluid (TF) formulation of the 1D module based on TRAC-P [ ]^{a,c}.

The purpose of this report is to describe the FSLOCA methodology. The documentation is divided into three volumes for a total of 32 sections. The three volumes, in sequence, are the building blocks of the methodology:

1. Due to the use of different code version identifiers among various institutions, later discussions herein refer to TRAC-P as TRAC-P [ ]^{a,c}.

- Volume I: WCOBRA/TRAC-TF2 Models and Correlations
- Volume II: WCOBRA/TRAC-TF2 Assessment
- Volume III: Full Spectrum LOCA Uncertainty Methodology and Demonstration Plant Analysis

The previous methodologies (i.e., the Code Qualification Document (CQD), WCAP-12945-P-A and ASTRUM, WCAP-16009-P-A) were developed following Regulatory Guide (RG) 1.157 (USNRC, 1989). Around the time development of the FSLOCA EM began, the NRC released RG 1.203 (USNRC, 2005) which expands on the principles of RG 1.157, while providing a more systematic approach to the development and assessment process of an Evaluation Model. Therefore, the development and documentation of the FSLOCA methodology follows the Evaluation Model Development and Assessment Process (EMDAP) which is documented in RG 1.203. The EMDAP high level flow chart is provided in Figure 1-1. While RG 1.203 expands upon RG 1.157, there are certain aspects in RG 1.157 which are more detailed than RG 1.203 which is why both RGs were used during the development and documentation of the FSLOCA EM.

The development of the FSLOCA EM is described in Volume 1 (Sections 1 through 11). This section (Section 1) provides a roadmap of the FSLOCA methodology. Section 2 presents Elements 1 and 2 of the EMDAP process which are pertinent to the development of the FSLOCA Phenomena Identification and Ranking Table (PIRT). This is a key step in the definition of the functional requirements of the EM and the development of the assessment base. Section 2 assesses what phenomena are adequately modeled in the existing (large break) code version and what phenomena require new, improved models, in particular for small and intermediate break LOCAs. Sections 3 through 11 describe the details of the WCOBRA/TRAC-TF2 code starting from the derivation of the conservation equations to the physical models and correlations necessary to close the equation set. Each model description starts from its physical basis, proceeds on to how the model is actually coded and concludes with statements regarding its scaling and applicability for the purpose of a LOCA analysis in a PWR.

The first step in the EMDAP requires the specification of the EM analysis purpose, transient class, and power plant class. The PIRT developed in Section 2 is intended to be comprehensive and therefore cover the same power plant classes as the previous methodology (ASTRUM). In other words, key elements of the PIRT, the code assessment, and conclusions on model biases and uncertainties are aimed to be generic and applicable to the same class of plants covered by the ASTRUM EM. When modeling aspects are specific to a particular PWR design, the choice was made to focus attention on the Westinghouse 3-loop PWR with cold leg ECCS injection. Therefore, the demonstration plant analysis is limited to such a design.

1.2 MAPPING OF FSLOCA EM DEVELOPMENT TO REGULATORY GUIDANCE, REGULATORY GUIDE 1.203 (EMDAP)

To the extent possible the EMDAP process (RG 1.203) was followed as a roadmap in the development and documentation of the FSLOCA EM. Consistent with the previous RG 1.157 the EMDAP is based on the CSAU roadmap. The new Standard Review Plan (SRP) (NUREG-0800, USNRC, 2007) and RG 1.203 (USNRC, 2005) both endorse CSAU as an acceptable structured process. RG 1.203 describes a structured EMDAP which follows the same principles of the CSAU roadmap, while adding more emphasis and structure to the EM development process, starting from the definition of the objectives, the functional requirements, and the assessment and leads to the evaluation model adequacy decision.

The six basic principles of the EMDAP have been followed in the development of the FSLOCA EM. For example:

1. ***Determine requirements for the evaluation model.*** The PIRT is developed for the purpose of identifying the functional requirements of the methodology. A code is selected and evaluated to assess its capability in modeling the important phenomena. Limitations and areas of improvement are identified in this process and lead to the definition of functional requirements of the EM. This process is discussed further in Section 2.

2. ***Develop an assessment base consistent with the determined requirements.*** Once the EM functional requirements are identified, a review of the available data for assessment of such functionalities is performed. This leads to the development of a comprehensive assessment matrix which comprises Separate Effect Tests (SETs) and Integral Effects Tests (IETs), as well as analytical or numerical benchmarks that provide additional support. The goal here is first to ensure that the EM is performing the intended function adequately, and second to allow for the development of statements with regard to the biases and uncertainties which will ultimately lead to a decision of the adequacy of the EM. This principle is a basis for discussion in Section 2 as well.

3. ***Develop the evaluation model.*** The evaluation model is based on the system code (WCOBRA/TRAC-TF2) and its associated modeling options and initial and boundary conditions that are needed to analyze the LOCA events in accordance with the requirements determined in the first principle. The models and features of WCOBRA/TRAC-TF2 are discussed in the remainder of Volume 1 (Sections 3 through 11).

4. ***Assess the adequacy of the evaluation model.*** Focusing on all the important phenomena identified following the first principle, the code (WCOBRA/TRAC-TF2) is assessed against the database developed based on the second principle to establish the inherent capability of the EM to achieve the desired results relative to the figures of merit derived from the General Design Criteria (GDC). The assessment is an iterative process and integral in the development of the code. Initial assessments were made during the early phase of code development to minimize the need for later corrective actions. The cycle of EM-development and EM-assessment is repeated until the EM is able to predict all the experiments in the database to a satisfactory degree. Note that 'EM' is used here instead of 'code' to emphasize that EM comprises code and input options, such as noding strategy. The final results of the assessments are presented in Volume 2.

5. ***Follow an appropriate quality assurance protocol during the EMDAP.*** Quality assurance standards, as required in Appendix B to 10 CFR Part 50, are followed during the development and assessment of the code and associated documentation. Due to the complexity of the EM, several engineering design reviews, which included a panel of independent experts, were held at different stages of the development process.

6. ***Provide comprehensive, accurate, up-to-date documentation***. This is the objective of the documentation contained in Volumes 1 through 3. Portions of the documentation were derived from previously NRC-approved Topical Reports (ASTRUM (Nissley et al., 2005) and the CQD (Bajorek et al., 1998) methodologies). However, the material herein has been re-edited in its entirety to reflect the EM changes and to define stand-alone comprehensive documentation to facilitate NRC review. Where applicable, some of the material associated with the 1D components was obtained from the TRAC-M Theory Manual (Spore et al., 2000). This is the most complete documentation available to describe TRAC-P [ ]^{a,c}. This version of TRAC-P was used to replace the 1D Module of WCOBRA/TRAC MOD7A in creating WCOBRA/TRAC-TF2 as discussed in Section 2.5. The FSLOCA methodology also builds upon and addresses a large volume of Requests for Additional Information (RAIs) which resulted from the review of the CQD (Bajorek et al., 1998) and ASTRUM (Nissley et al., 2005) EMs.

Principles 1 through 5 focus on the EM development and assessment. However, the EM model is not completed until a workable uncertainty methodology is developed. This is the focus of Volume 3, which provides the description of the methodology and a sample application of the FSLOCA EM to a selected PWR.

In the following, the development and documentation of the FSLOCA methodology is mapped to each individual step of the EMDAP providing further details on compliance with the RG 1.203.

1.2.1 EMDAP Element 1 (Step 1): Analysis Purpose, Transient Class and Power Plant Class

The scenario being addressed by the FSLOCA methodology is a postulated loss-of-coolant accident that is initiated by an instantaneous rupture of a reactor coolant system (RCS) pipe. The break type considered is either a double-ended guillotine, defined as a complete severance of the pipe resulting in unimpeded flow from either end, or a split break, defined as a partial tear. The break size considered for a split break ranges from the break size at which the break flow is beyond the capacity of the normal charging pumps up to a size equal to the area of a double ended guillotine rupture.

The PIRT developed in Section 2 is intended to be comprehensive and therefore to cover the same power plant classes included in the previous methodology (ASTRUM). This includes Westinghouse designed 3- and 4-loop plants with ECCS injection into the cold legs, Westinghouse designed 2-loop plants with upper plenum injection (UPI) and Combustion Engineering (CE) designs. The validation discussed in Volume II and uncertainty method discussed in Volume III are intended to cover Westinghouse-designed 3- and 4-loop plants with ECCS injection into the cold legs, and CE designs (excluding CE PWRs with low (< 400 psia) safety injection tank setpoints). The application of the methodology is demonstrated in Section 31 for a Westinghouse-designed 3-loop plant.

While the LOCA is considered a single scenario, the evolution of the transient is strongly influenced by the break sizes. Therefore, three different sub-scenarios are identified in the Westinghouse FSLOCA methodology: Small Break LOCAs, Intermediate Break LOCAs and Large Break LOCAs, and for each one a different division in periods is provided. Section 2 will describe the scenario in more detail.

The purpose of the analysis is to evaluate the three LOCA figures of merit (Peak Clad Temperature (PCT), Maximum Local Oxidation (MLO) and Core-Wide Oxidation (CWO)) and show compliance with the GDC for ECCS performance.

1.2.2 EMDAP Element 1 (Step 2): Specification of Figures of Merit

For the purpose of a LOCA analysis, the figures of merit are the first three criteria of 10 CFR 50.46. In particular the PCT and MLO are selected during the development of the PIRT discussed in Step 3 and presented in Section 2. However, during the assessment, other related performance measures are identified in conjunction with the main figures of merit above to satisfy the fourth guiding principle objective. For example, since compensating errors in the code can unintentionally lead to correct answers for the wrong reasons, additional performance measures serve as physical tracking points and additional proof of accuracy. These types of considerations can be found in Volume 2.

1.2.3 EMDAP Element 1 (Steps 3 and 4): Phenomena Identification and Ranking Table

The development of the PIRT is a key element in any methodology derived from the CSAU. The PIRT is presented in Section 2. In adherence with the new RG 1.203, emphasis is given in using the PIRT as a tool to achieve the definition of the EM functional requirements.

This completes Element 1 of the EMDAP.

1.2.4 EMDAP Element 2 (Step 5): Specify Objectives for Assessment Base

This is the first step of Element 2 and is intended to satisfy the second basic principle of the EMDAP. The principal need for a database is to assess the EM and, when needed, develop correlations. The selection of the database is a direct result of the requirements established in Element 1. As such, the database includes:

1. Separate Effects Tests (SETs) used to develop and assess groups of empirical correlations and other closure models associated to the important phenomena.

2. Integral Effect Tests (IETs) used to assess system interactions and global code capability.

3. Plant transient data, when needed and if available.

4. Simple test problems used to illustrate fundamental calculational device capability.

A systematic process has been used to identify an adequate assessment data base. The rationale for each test and relationship to the PIRT and EM functional requirements is discussed in Volume 2.

1.2.5 EMDAP Element 2 (Steps 6, 7 and 8): Definition of the Assessment Base and Applicability

A comprehensive assessment base is developed and presented in Section 2. Full scale or prototypical data is used when possible, while scaling considerations are provided otherwise for each test. Attention is also given to the range of applicability of the dataset with regard to the expected conditions in the PWR.

A distinction is given to the dataset used for the development (in Volume 1) and an independent dataset utilized for the assessment described in Volume 2.

1.2.6 EMDAP Element 2 (Step 9): Determine Experimental Uncertainties as Appropriate

Step 9 of the EMDAP specifically asks to specify the uncertainties in the database. This information is not always available. These uncertainties are sometimes related to the uncertainty in the test measurements; other times there is uncertainty associated with the data reduction process. When possible, experimental uncertainties will be properly characterized and appropriate consideration will be given in the uncertainty analysis.

1.2.7 EMDAP Element 3 (Steps 10, 11 and 12): Develop Evaluation Model

The engine of the FSLOCA EM is a new version of the WCOBRA/TRAC MOD7A code (Nissley et al., 2005 and Bajorek et al., 1998) renamed WCOBRA/TRAC-TF2.

WCOBRA/TRAC MOD7A Revision 1 was validated and approved as part of the Westinghouse best-estimate LBLOCA EM (Bajorek et al., 1998 and Dederer et al., 1999). WCOBRA/TRAC MOD7A Revision 6 was approved by the NRC as part of ASTRUM EM (Nissley et al., 2005). Subsequently, Revision 7 was released to reflect error corrections and minor improvements which included some additional features for special applications. These changes were reported under the 10 CFR 50.46 reporting requirements process.

The WCOBRA/TRAC MOD7A code uses a two-fluid, three-field representation of flow in the vessel component. The three fields are a vapor field, a continuous liquid field, and an entrained liquid droplet field. Each field uses a separate set of continuity, momentum, and energy equations with one exception. A common energy equation is used by the continuous liquid and the entrained liquid droplet fields.

The one-dimensional (1D) components consist of all the major components in the primary system, such as pipes, pumps, valves, steam generators, accumulators, and the pressurizer. The 1D components were represented in WCOBRA/TRAC by a two-phase, five-equation, drift flux model which originated from the TRAC-PD2 code. This formulation consisted of two equations for the conservation of mass, two equations for the conservation of energy, and a single equation for the conservation of momentum.

The development of WCOBRA/TRAC-TF2 started from WCOBRA/TRAC MOD7A Revision 7. One of the major modifications included in the new code was the replacement of the 1D Module, which was based on TRAC-PD2, with the TRAC-P [ ]^{a,c} code. This extends the use of a two-fluid six-equation formulation of the two-phase flow to the 1D loop components. The other major change was [ ]^{a,c}. Other changes were added to extend applicability of the code to small and intermediate break LOCA scenarios and are discussed in detail in this Topical Report.

The new code has been renamed to WCOBRA/TRAC-TF2, where "TF2" is an identifier that reflects the use of three-field (TF) formulation of the 3D module derived by COBRA-TF and a two-fluid (TF) formulation of the 1D module based on TRAC-P [ ]^{a,c}.

Following the requirements established in Element 1 of the EMDAP, a code development plan was devised, and followed software development standards and procedures, which are an integral part of Westinghouse Software Development Quality Assurance (QA) procedures and best practices. Such procedures satisfy RG 1.203 guidelines, such as design specifications, documentation requirements, programming standards and procedures, transportability requirements, quality assurance procedures and configuration control procedures.

Sections 3 through 11 of Volume 1 describe in detail the code structure, starting from the development of the basic conservation equations and their numerical integration in Section 3, and following with the description of all the closure relationships required to close the equation set. Each model is described starting from the physical basis, to scaling and applicability, to the scenario of interest (a LOCA in a PWR), and details on the model as coded.

1.2.8 EMDAP Element 4 (Steps 13, 14 and 15): Bottom-Up Evaluation of Models

EM adequacy is assessed in two parts. The first part is described by EMDAP Steps 13 through15, which ask for an examination of all important closure models and correlations by considering their pedigree, applicability, fidelity to appropriate fundamental or SET data, and scalability. This is the objective of Sections 3 through 11 of Volume 1.

Most of the models or closure relationships were developed or available from existing database literature. In a few instances, specialized models have been developed using specific SET data which was then removed from the Validation and Verification (V&V) database to maintain transparency in the assessment. Models have also been evaluated, and sometimes modified or improved, to better simulate the full spectrum of conditions expected in a LOCA transient. The goal was to ensure that the same fundamental correlations apply over the wide range of conditions which cover the full spectrum of break sizes. Models are not tailored to a specific scenario or break size. Models at their fundamental level are based on the local thermal-hydraulic conditions and are therefore independent of the global system behavior or time evolution.

As such, models range of applicability and scalability concerns have been addressed. A discussion for each model can be found in Sections 3 through 11.

1.2.9 EMDAP Element 4 (Steps 16, 17, 18 and 19): Top-Down Evaluation of Models

The second part of the assessment (EMDAP Steps 16-19) pertains to the top-down evaluations of code-governing equations, numerics, the integrated performance of each code, and the integrated performance of the overall EM. This is what sometimes is referred to as code V&V and is the topic of Volume 2 of this topical report.

WCOBRA/TRAC-TF2 models are developed for SETs, IETs, and additional numerical or analytical benchmark problems to validate the performance of specific models once integrated into the code. A consistent noding philosophy was developed for the code validation against experimental data, and for nuclear power plant (NPP) calculations. One objective has also been to minimize deviations from nodalization schemes that were developed for the previously approved methodology (WCAP-16009-P-

A). This goal has been achieved and noding changes have been minimized both in the vessel component as well as in the loops.

Also, user guidance for the code options (e.g., maximum time step sizes, convergence criteria, models options, etc.) has been developed to ensure consistency during the assessment.

As far as SETs, significant emphasis has been given to full-scale or prototypical data. When this was not possible, effort has been dedicated to satisfy any scalability concerns. To the extent possible, noding strategy and modeling options are set such that bias is minimized, or if not possible, to bias results in the conservative direction. At the same time, compensating error analyses are performed to ensure that good results are not achieved as a result of biases off-setting each other.

For each SET analysis, the controlling parameters or processes are identified. Results of the assessment also provide the ranging of such key parameters, which has to be considered in the uncertainty analysis. The assessments results are provided in various sections of Volume 2, with the objective of supporting the adequacy decision on the EM applicability by the end of Volume 2. The ranging and uncertainty methodology is discussed in Volume 3.

The assessment with SETs is augmented with numerical benchmarks against thought or first-principle problems. This additional assessment is discussed in Section 23.

IETs are used to study the overall behavior of the EM and interaction among sub-models. Experiments conducted in the Rig-of-Safety Assessment (ROSA) test facility were selected to cover the SBLOCA scenarios while the Loss-of-Fluid-Test (LOFT) and the large scale Cylindrical Core Test Facility (CCTF) are intended to cover the LBLOCA scenarios. LOFT also provides some overlap between the small break and large break scenarios. Results from the assessments against ROSA and LOFT tests are provided in Section 21 and Section 22, respectively. Assessment against CCTF is presented in Section 19.

The last section of Volume 2 (Section 24) provides the summary and conclusions on the assessment which will support the EM adequacy decision (EMDAP Step 20).

WCOBRA/TRAC-TF2 was shown to be applicable for the specified accident scenario (any LOCA with a break size beyond the capability of the charging pumps) and the specified power plant class.

1.2.10 EMDAP Element 4 (Step 20): Determine Evaluation Model Biases and Uncertainties

The ranging and uncertainty methodology is the topic of Volume 3. The code assessment leads to the determination and quantification of model biases and uncertainties. The development of the uncertainty methodology is discussed in Section 29. Consistent with the CSAU roadmap, the uncertainty has to be ultimately propagated or convoluted statistically during the plant analysis. The statistical procedure used to propagate the uncertainties is the subject of Section 30. [

]^{a,c} The procedure is designed to generate a sample of the LOCA 'population,' and then statistical inference procedures are used to develop probabilistic statements that show compliance with the 10 CFR 50.46 criteria.

For some models a detailed uncertainty analysis could not be performed. For those models, the assessment showed that sufficient conservative bias was retained in the EM to justify their applicability. However, note that conservative biases resulting from phenomena that are conservatively predicted by WCOBRA/TRAC-TF2 are ignored in the uncertainty analysis.

1.3 ORGANIZATION OF THE REPORT

The documentation is divided in three volumes for a total of 32 sections.

Volume 1: FULL SPECTRUM LOCA Evaluation Model Development

Section 1, herein, presents the FSLOCA EM Topical roadmap. A background subsection discussed the previous methodologies (CQD (Bajorek et al., 1998) and ASTRUM (Nissley et al., 2005)). The following subsection discusses the mapping of the FSLOCA EM to the RG. In particular, the relationship of the FSLOCA EM to RG 1.203 (EMDAP) and CSAU (RG.1.157) is discussed. The compliance with each of the EMDAP steps is discussed and mapped to the appropriate sections in the topical report.

Section 2 provides the functional requirements for the methodology. The cornerstone is the development of the FULL SPECTRUM LOCA PIRT. The process used to evaluate the code, and the identification of the code changes required, are discussed. This also includes the development of the EM assessment base.

Sections 3 through 11 describe the models and correlations used in WCOBRA/TRAC-TF2. These sections are very similar to Sections 2 through 10 of WCAP-16009-P-A (Nissley, et al., 2005), with the exception of the code changes associated with the 1D module (now based on TRAC-PF1), and the inclusion of the non-condensable gas in the 3D module (VESSEL component).

Section 3 describes the conservation equations and numerical methods used in WCOBRA/TRAC-TF2. Flow regimes are described in Section 4, and the interfacial area for each regime is discussed. Section 5 provides information on momentum transfer, including the models and correlations used to determine interfacial shear, form loss and pressure drop, droplet breakup on structures, and entrainment/de-entrainment phenomena. The methods used to evaluate interfacial heat and mass transfer are described in Section 6. The wall-to-fluid heat transfer models and correlations are discussed in Section 7, while the thermal-mechanical behavior of the structures used to model nuclear fuel rods and experimental fuel rod simulators is contained in Section 8.

Sections 3 through 8 use a common nomenclature to the extent practical. Since WCOBRA/TRAC-TF2 is the result of merging two codes, i.e., COBRA-TF for the 3D Module and TRAC-P [ ]^{a,c} for the 1D Module, nomenclature could differ between the two modules, but is consistent within each module.

Section 9 describes the kinetics model and decay heat models, and uses a separate nomenclature. Special component models, used to model equipment such as pumps, steam generators, and safety injection, are described in Section 10. Section 11 provides information on the calculation of the thermodynamic and transport properties of water, and common fuel rod and RCS structural materials.

Sections 3 through 11 include four elements that appear as subheadings. **"Model Basis"** identifies the model or correlation and gives reference to its origin and technical basis. **"Model as Coded"** provides specific information on how the models and correlations are programmed in the code. Numerical ramps, limits, and approximations of the true correlation are identified where applicable. **"Scaling Considerations"** addresses scaling and applicability concerns of the models from a bottom-up view of the code. The **"Conclusions"** section describes the applicability of the models for best-estimate LOCA calculations. Simulations that are used to validate the models and correlations are sometimes identified.

Volume 2: WCOBRA/TRAC-TF2 Assessment Report

This volume describes the code assessment against SETs, IETs, and additional numerical or analytical benchmarks which further support the validation of the code. Regarding the SET assessment, the tests are grouped into sections based on the phenomena that have been addressed by the experiments and each section focuses on a particular process. Each section contains the following elements:

1. Test objectives and physical processes investigated.

2. Relationship to the PIRT and description of relevant physical phenomenon.

3. Test facility description, test procedures, scaling discussion, test conditions and comparison to the range of conditions in PWR.

4. For each experimental campaign, tests selected for the assessment and basis of the selection.

5. WCOBRA/TRAC-TF2 model description, simulation and analysis of results.

The assessment of the results is based on selected figures of merit which are used to judge the quality of the predictions. The code predictions are compared to the data. The data reduction or interpretation process is discussed. When possible, the uncertainty on the data is evaluated such that it can be properly characterized in the comparison with the code predictions. Finally, a general summary and conclusion on the assessment of the specific phenomena is provided.

Section 12 describes the assessment of the break (critical) flow model. This also includes the assessment of the offtake model, which defines the boundary conditions (quality) at the break location to properly reflect the vapor pull-through or liquid entrainment for bottom or top breaks.

Section 13 focuses on the assessment of the two-phase mixture level swell phenomenon which is an important process, in particular during the boiloff phase of a small break scenario.

Sections 14 and 15 make up the complete assessment of the core heat transfer model. This includes tests which were designed to address the LBLOCA phases (blowdown, refill and reflood), as well as tests designed for conditions which are more typical of boiloff in a SBLOCA scenario. Section 14 provides a description of the test facilities (prototypical rod bundles experiments) along with scaling and applicability of the tests. Section 15 presents the associated code simulations and discussion of results. Special considerations are given to the reflood heat transfer regime because of the inter-relationship with the quench front progression, entrainment and spacer grid effects.

Section 16 discusses the assessment of the horizontal stratified flow regime. Special effort has been given in the development of a pseudo-mechanistic horizontal stratified and wavy dispersed flow regime. This section provides the results of the assessment of the code against relevant data.

The direct condensation between the cold liquid injected by the SI and the vapor in a stratified cold leg is a complex, but important phenomenon which required the development of a specialized condensation model. The assessment of this model against an independent database is presented in Section 17.

Section 18 discusses the assessment of the loop seal clearance phenomenon, which is an important process during a postulated SBLOCA transient.

Section 19 provides the validation of specific hydrodynamic models such as Counter Current Flow Limitation (CCFL), entrainment and de-entrainment and liquid carryover. Also, condensation in the 3D components is assessed here, to complete the assessment initiated in Section 17. This section includes the assessment of several large scale test facilities (LSTF), such as Upper Plenum Test Facility (UPTF) and CCTF.

Section 20 is dedicated to the assessment of specific additional components used in PWR models and analysis. The accumulator model is assessed against experimental blowdown data from Indian Point 2 and Callaway. The effect of nitrogen discharge at the end of accumulator blowdown is assessed by comparing code predictions with experimental data from International Standard Problem 25 (Achilles). The pump and cold leg nozzle models are also assessed in this section.

Sections 21 and 22 describe the assessment against the IETs. ROSA SBLOCA experiments, as well as natural circulation tests, are presented together with the WCOBRA/TRAC-TF2 simulations in Section 21. Section 22 discusses the simulation of selected LOFT experiments for large, small, and intermediate breaks.

Section 23 discusses additional validation, analytical or numerical benchmarks with first principle thought problems. Section 24 provides a compensating error analysis, a general assessment summary, and conclusions.

Volume 3: FSLOCA Uncertainty Methodology and Demonstration Plant Analyses

Volume 3 represents the body of work, beyond the code assessment discussed in Volume 2, which is required for the development of the final uncertainty methodology.

Section 25 is a compilation of the plant sources of uncertainty. Some are based on the plant physical configuration and initial operating conditions; others are postulated reactor accident boundary conditions such as the break location/orientation, reactor trip assumptions, offsite power availability, steam generator tube plugging, etc. Considerations on the effect of operator actions are also discussed in this section.

Section 26 provides a detailed description of the WCOBRA/TRAC-TF2 model for selected PWRs. The nodalization follows (to the extent practical) the noding guidelines developed during the code assessment presented in Volume 2. Section 27 describes the simulation of selected reference transients for the PWRs. The transients considered here range from small to large break LOCA events.

Section 28 documents scoping and sensitivity studies performed on the representative PWRs to study effects such as the break location and orientation and other important parameters to provide further support to methodology decisions.

Section 29 is the overall compilation of all the uncertainty elements or contributors to the total uncertainty. This includes the summary code assessment with the generation of uncertainty distributions or probability density functions (PDFs); the review of the scoping studies and the selection of the uncertainty elements associated with the plant analysis; the initial and boundary conditions uncertainty treatment and the fuel rod model and heat transfer uncertainties.

Section 30 provides the technical basis for the selected uncertainty methodology [ ]^{a,c}. This includes a description of the method, theoretical support and justification of assumptions.

Section 31 is the description of the FULL SPECTRUM LOCA analysis process. The section includes the process roadmap of a typical analysis using the FULL SPECTRUM LOCA EM and a demonstration analysis for a select PWR.

Section 32 provides the methodology summary and its compliance with 10 CFR 50.46, Regulatory Guide 1.203 and selected aspects of Regulatory Guide 1.157. The review against the Regulatory Guides also provides a methodology summary and supports the EM adequacy decision for its intended purpose.

1.4 REFERENCES

1. Bajorek, S. M., et al., 1998, "Code Qualification Document for Best Estimate LOCA Analysis," WCAP-12945-P-A, Volume 1, Revision 2, and Volumes 2 through 5, Revision 1, and WCAP-14747 (Non-Proprietary).

2. Boyack, B., et al., 1989, "Quantifying Reactor Safety Margins: Application of Code Scaling, Applicability, and Uncertainty (CSAU) Evaluation Methodology to a Large-Break, Loss-of-Coolant Accident," NUREG/CR-5249.

3. Dederer, S. I., et al., 1999, "Application of Best Estimate Large Break LOCA Methodology to Westinghouse PWRs with Upper Plenum Injection," WCAP-14449-P-A, Revision 1, and WCAP-14450-NP-A, Revision 1 (Non-Proprietary).

4. Nissley, M.E., et al., 2005, "Realistic Large Break LOCA Evaluation Methodology Using Automated Statistical Treatment of Uncertainty Method (ASTRUM)," WCAP-16009-P-A, Revision 0, and WCAP-16009-NP-A, Revision 0 (Non-Proprietary).

5. Spore, J.W., et al., 2000, "TRAC-M/FORTRAN 90 (Version 3.0) Theory Manual", LA-UR-00-910.

6. USNRC, 1989, "Best-Estimate Calculations of Emergency Core Cooling System Performance," Regulatory Guide 1.157.

7. USNRC, 2005, "Transient and Accident Analysis Methods," Regulatory Guide 1.203.

8. USNRC, 2007, "Standard Review Plan for the Review of Safety Analysis Reports for Nuclear Power Plants," NUREG-0800.

9. Westinghouse Electric Company, 2011, "AP1000 Design Control Document," Revision 19, APP-GW-GL-700.

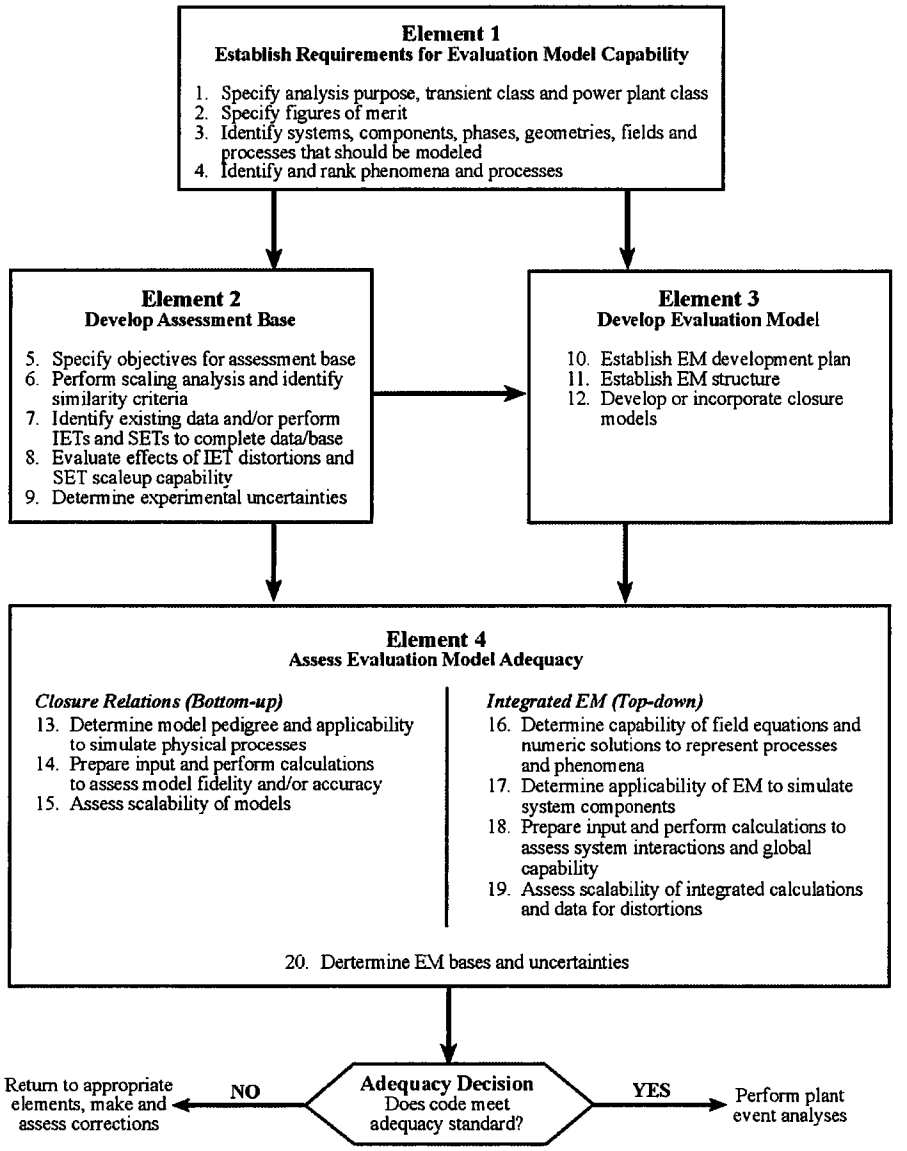

Figure 1. Elements of Evaluation Model Development and Assessment Process (EMDAP)

Figure 1-1 Evaluation Model Development and Assessment Process (EMDAP) – High Level Flow Chart (RG 1.203)

2 EVALUATION MODEL FUNCTIONAL REQUIREMENTS

2.1 INTRODUCTION

As discussed in Section 1, Element 1 of the Evaluation Model Development and Assessment Process (EMDAP) (Regulatory Guide 1.203, USNRC, 2005) focuses on how to establish the requirements for the Evaluation Model (EM). Figure 2-1 illustrates the process.

The process starts with the specification of the analysis purpose, the transient class and power plant class covered by the EM. This was addressed in Section 1.2.1. The next steps are the definition of the figures of merit and the Phenomena Identification and Ranking Table (PIRT) (Steps 2 through 4 of Figure 2-1) which are discussed in detail in this section. The process leads to the development of the evaluation model functional requirements which are two-fold:

1. Identification of model changes which are required for WCOBRA/TRAC-TF2 to satisfy the PIRT
2. Development and identification of the assessment base of the code

Point 2 above defines the list of Separate Effect Tests (SETs) and Integral Effect Tests (IETs) which will be used to assess the code and develop conclusions with regard to the bias and uncertainties of the code and EM.

2.2 FIGURES OF MERIT (EMDAP STEP 2)

The figures of merit considered in the FULL SPECTRUM LOCA (FSLOCA) PIRT are consistent with the 10 CFR 50.46 acceptance criteria.

2.3 PHENOMENA IDENTIFICATION AND RANKING TABLE (EMDAP STEPS 3 AND 4)

One of the most important efforts in developing a best-estimate methodology is the identification of those processes and phenomena that have the most dominant influence on the selected transient. A phenomena identification and ranking process is used to list processes of importance and indicate at what times in the transient each process occurs. A single PIRT is provided for the FSLOCA methodology. Phenomena are identified by major system component and a ranking is assigned for each period of the three sub-scenarios described in Section 2.3.1.

Westinghouse has previously developed both Large Break Loss-of-Coolant Accident (LBLOCA) and Small Break LOCA (SBLOCA) PIRTs, and these PIRTs were the subject of NRC review (for the Large Break LOCA PIRT) and independent peer review (for the Small Break LOCA PIRT). It should be noted that the SBLOCA and LBLOCA PIRTs have been developed by Westinghouse at different times, prior to the initiation of the FSLOCA program, and involved different independent reviewers. Therefore, some differences exist in the approaches followed to develop these PIRTs. For example, ranking for the original LBLOCA PIRT ranged from 1 to 9, while for the SBLOCA PIRT a qualitative scale (Low, Medium, and High) had been preferred. Also, several phenomena in the LBLOCA PIRT were left unranked, while the SBLOCA PIRT provided a ranking for all plausible phenomena included in the PIRT.

The FSLOCA PIRT was developed following the approach outlined in (Boyack, 1989). First, a list of plausible phenomena was prepared, using the existing LBLOCA and SBLOCA PIRTs as the starting point. Next, phenomena were ranked for importance through the various periods identified for the transient. Relative rankings in the FSLOCA PIRT were assigned using the following criteria:

H = The process is considered to have high importance. Accurate modeling of the process during the particular period is considered to be crucial to the correct prediction of the transient.

M = The process is considered to have medium importance. The process must be modeled with sufficient detail to obtain accuracy in the simulation; however, the process is expected to have less impact on the overall results than those ranked high.

L = The process is not considered to be very important during the transient. The phenomena needs to be modeled in the code (or accounted for in the methodology), but inaccuracies in modeling these processes are not considered likely to have a significant impact on the overall transient results.

N/A = The process is considered insignificant, or does not occur at all. This process need not be modeled or be taken into consideration, as it has an insignificant impact on results.

Table 2-1 summarizes the FSLOCA phenomena and the relative rankings. This section provides a discussion on each of the major categories in the PIRT, describes the rationale for the rankings and defines the phenomena considered under the heading "Process" in Table 2-1.

2.3.1 LOCA Scenario Specification

The scenario being addressed by the Westinghouse FSLOCA methodology is a postulated loss-of-coolant accident that is initiated by an instantaneous rupture of a reactor coolant system (RCS) pipe. The break type considered is either a double-ended guillotine, defined as a complete severance of the pipe resulting in unimpeded flow from either end, or a split break, defined as a partial tear. The break size considered in the Westinghouse FSLOCA methodology includes any break size such that break flow is beyond the capacity of the normal charging pumps up to and including a double ended guillotine rupture with a break flow area two times the pipe area.

The scenario considered is assumed to be a LOCA with the most limiting single failure to the Emergency Core Cooling System (ECCS).

Sensitivity studies based on Appendix K methods have identified a cold leg break to be the most limiting in terms of location. [

]^{a,c}

The Westinghouse uncertainty analysis considers only the limiting cold leg split break for Region I, and considers the limiting cold leg split break and double ended cold leg guillotine break to be equally probable for Region II. This treatment bounds other breaks for the following reasons:

[

]^{a,c}

Based on these considerations, it is concluded that the Westinghouse uncertainty analysis for the limiting cold leg break bounds all other breaks.

There are other considerations such as the availability of offsite power which has an impact on events such as the pump trip, the Safety Injection (SI) delay due to diesel generator start-up time, and others. This will be treated within the methodology and will be discussed in Volume 3.

The FSLOCA EM analysis purpose was discussed in Section 1.2.1. As far as the power plant class is concerned, the PIRT presented herein is intended to be comprehensive and therefore to cover the same power plant classes included in the previous methodology (ASTRUM), which includes Westinghouse-designed 3- and 4-loop plants with ECCS injection into the cold legs, Westinghouse-designed 2-loop plants with upper plenum injection (UPI), and Combustion Engineering designs.

While any LOCA is considered as the scenario, the evolution of the transient is strongly influenced by the break size. Therefore, three different sub-scenarios are identified in the Westinghouse FSLOCA PIRT: Small Break LOCAs, Intermediate Break LOCAs (IBLOCA) and Large Break LOCAs, and for each one a different division in periods is provided.

2.3.1.1 Small Break LOCA Periods Specification

During a Small Break LOCA, the RCS depressurizes to the pressurizer low-pressure setpoint, actuating a reactor trip signal. The ECCS is aligned for delivery following the generation of an "S" signal when the pressurizer low/low-pressure setpoint is reached. The ECCS includes redundant trains of SI pumps which inject into the cold legs. The pressurized accumulators provide additional borated water to the RCS in the event of a LOCA. Once sufficient RCS depressurization occurs as a result of a LOCA, accumulator injection commences.

During a Small Break LOCA transient, the reactor system depressurizes and mass is lost out the break as the RCS drains to the break elevation, while mass is added from the SI pumps and eventually the accumulators. Water injected by the SI pumps and accumulators must be sufficient so that acceptable core cooling is provided for the spectrum of Small Break LOCA transients.

It is useful to divide the small break transient into several periods in order to identify and rank the various phenomena. Some phenomena are important for certain periods of time but are insignificant at other times. However, prediction of that phenomenon during its time of importance may be crucial to the accurate prediction of the overall transient. The small break transient is characterized by five periods;

Blowdown, natural circulation, loop seal clearance, boiloff, and core recovery. The duration of each period is break size dependent, and each is characterized as follows:

Blowdown (BLD)

On initiation of the break, there is a rapid depressurization of the primary side of the RCS. Reactor trip is initiated on a low pressurizer pressure setpoint (approximately 1860 psia). Loss of condenser steam dump effectively isolates the steam generator (SG) secondary side, causing it to pressurize to the safety valve setpoint (approximately 1100 psia) and release steam through the safety valves. An SI signal occurs when the primary pressure decreases below the pressurizer low-low pressure setpoint (approximately 1760 psia), and SI begins after some delay time. The RCS remains nearly liquid solid for most of the Blowdown period, with phase separation starting to occur in the upper head, upper plenum, and hot legs near the end of this period. During the Blowdown period, the break flow is single-phase liquid. Eventually, the entire RCS saturates, the rapid depressurization ends, and the RCS reaches a pressure just above the SG secondary side pressure.

Natural Circulation (NC)

At the end of the Blowdown period, the RCS pressure reaches a quasi-equilibrium condition that can last for several hundred seconds, during which the SG secondary side acts as a heat sink. During this period, the system drains from the top down with voids beginning to form at the top of the SG tubes and continuing to form in the upper head and top of the upper plenum regions. There is still adequate liquid to allow significant natural circulation two-phase flow around the loops; decay heat is removed through condensation in the SGs during this time. Significant coolant mass depletion continues from the RCS, and vapor generated in the core is trapped within the upper regions by liquid plugs in the loop seals, while a low quality flow still exits the break. This period is referred to as the natural circulation period.

Loop Seal Clearance (LSC)

The third period is the loop seal clearance period. When the liquid level in the downhill side of the pump suction piping is depressed to the bottom of the loop seal, steam previously trapped in the RCS can be vented to the cold leg break. The break flow, previously a low quality mixture, transitions to primarily steam. Prior to loop seal venting, the static head balances within the RCS can cause the vessel collapsed mixture level to depress into the core. Following the venting, the vessel level recovers to about the cold leg elevation, as the imbalances throughout the RCS are relieved.

Boiloff (BO)

Following loop seal venting, the vessel mixture level continues to decrease due to the boiloff of the remaining liquid inventory since the RCS pressure is generally still too high to allow sufficient ECCS injection by the high pressure SI pumps. The mixture level will reach a minimum, in some cases resulting in core uncovery, before the RCS has depressurized to the point where the break flow is less than the rate at which ECCS water is delivered.

Core Recovery (REC)

The vessel mass inventory is replenished from its minimum with ECCS water and the core recovers. The transient is terminated once the entire core is quenched and the pumped SI flow exceeds the break flow; operator action may facilitate this process.

2.3.1.2 Large Break LOCA Periods Specification

A LBLOCA transient can be characterized by three distinct periods: Blowdown, refill and reflood. The Blowdown period extends from the initiation of the break until the primary side depressurizes sufficiently that emergency core cooling (ECC) water can start to penetrate the downcomer. The flow out of the break is high, but limited by critical flow phenomena. Boiling and flashing occur in the core as the flow reverses, shutting down the fission process. The hot fuel rods quickly exceed the critical heat flux, as the core flow reverses, resulting in a sharp reduction in heat transfer to the coolant. The cladding temperature rises rapidly as the initial stored energy in the fuel pellets is transferred to the cladding. Within the next several seconds, coolant in all regions of the vessel and loops begins to flash. The break flow becomes saturated, and is substantially reduced. This reduces the depressurization rate, and may also lead to a short period of positive core flow as the intact loop pumps continue to supply coolant to the vessel. Cladding temperatures may be reduced, and some portions of the core may rewet.

Two-phase conditions in the pumps reduce their effectiveness, and the core flow again reverses. Significant core cooling occurs as the fission process is shutting down, and the main heat source becomes decay heat generated in the fuel rods.

At approximately 10 to 15 seconds after the break, the RCS pressure decreases to the point where accumulators begin injecting cold water into the cold legs. As this water flows into the downcomer, it is initially swept out of the vessel and into the broken cold leg by the continuing high flow of steam from the core.

Approximately 20 to 30 seconds after the break, the RCS has depressurized to a level approaching that of the containment, and refill begins. The ECCS water from the accumulators and the pumped safety injection penetrates the steam upflow in the downcomer, refilling the lower plenum within a few seconds. As the coolant enters the core, the reflooding process begins.

The flow into the core is oscillatory, as cold water rewets the hot fuel rods, generating steam. This steam, and the water it entrains, must pass through the vessel upper plenum, the broken loop hot leg, the steam generator, and the pump before it can be vented out the break. Entrained water that enters the steam generators is also vaporized, increasing the flow path resistance. Because of the relatively low flow during this time period, cladding temperatures continue to slowly increase until the water level in the core reaches several feet. After about two to four minutes, the cladding temperatures in the higher regions of the core begin to decrease due to heat transfer to the dispersed droplet flow. Eventually, the entire core rewets and the long-term cooling phase begins.

The scenario for a 2-loop plant with UPI is the same through Blowdown and refill. The low-head safety injection flow into the upper plenum begins during the refill period. Reflood is initiated by the intact loop accumulator, and then continues as the UPI water drains down the low-power peripheral regions of the

core. The steam flow up the hotter internal regions of the core prevents downflow from the upper plenum, and cooling of the hot assemblies is by bottom-up reflood, as in 3- and 4-loop plants.

2.3.1.3 Intermediate Break LOCA Periods Specification

The Intermediate Break LOCA Scenario presents characteristics that are intermediate between the Small Break LOCA and the Large Break LOCA. IBLOCAs have not been the subject of as much attention as either the small break or Large Break LOCA, as they have historically been considered less limiting than large break events. However, they are a necessary part of the Westinghouse FULL SPECTRUM LOCA methodology as they represent a transition between the two, Small and Large Break LOCA scenarios discussed above. An intermediate break is defined as follows:

[

]^{a,c}

In Intermediate Break LOCAs, core recovery occurs due to accumulator injection. Because of the rapid depressurization, the accumulators inject early in the transient, relative to a Small Break LOCA. However, because only limited steam flows back up the downcomer, only minimal bypass of accumulator water will occur. Rather, the injected water can fall freely into the downcomer. There is a time lag between the start of accumulator injection and the peak cladding temperature (PCT) turn-around time, because of the relatively long period of time it may take to fill the downcomer, which can be almost empty at the start of injection. It can be observed that the intermediate break is not associated to a specific size, but rather to a physical behavior that is intermediate between small break and large break, and lacks some defining features of either the Small and Large Break LOCA scenarios (for example the natural circulation and loop seal clearance phases for the small breaks, the ECC bypass during the refill phase of a Large Break LOCA). The break sizes associated with intermediate breaks will therefore be somewhat plant dependent, but in general intermediate breaks will present break sizes ranging from 10-inch equivalent diameter to 1.0 square foot in area.

An IBLOCA transient can be characterized by three distinct periods: Blowdown/depressurization, accumulator injection and SI injection. The Blowdown/depressurization period extends from the initiation of the break until the primary side depressurizes sufficiently that Accumulator Injection is initiated. During an Intermediate Break LOCA, the RCS depressurizes to the pressurizer low-pressure setpoint, actuating a reactor trip signal, and the control rods insert.

The ECCS is aligned for delivery following the generation of an "S" signal when the pressurizer low/low-pressure setpoint is reached. The ECCS includes redundant trains of SI pumps which inject into the cold legs and/or reactor vessel. During the Blowdown phase, system pressure continues to decrease, as RCS inventory is lost at the break. During Blowdown, the cold leg will reach saturation conditions, and two-phase flow at the break will lead to a reduction in the break flow rate. The break flow remains in a

critical flow condition throughout this phase. As core inventory is lost, the core may heat up during this phase due to decay heat generation.

Once sufficient RCS depressurization occurs as a result of a LOCA, accumulator injection commences. The accumulator injection phase is characterized by a rapid refill of the downcomer and of the core that will terminate any heatup initiated during the Blowdown phase. During this phase, SI and accumulator flow will maintain the core quenched.

As the accumulator empties, nitrogen will surge from the accumulator to the reactor coolant system. During this last phase, only pumped SI flow will be available to maintain core cooling. A second heatup may occur if SI flow is not sufficient to match decay heat and the mass inventory decreases. Nitrogen in the system may affect the system response. This phase and the transient are considered complete when SI flow consistently exceeds break flow and the core is quenched.

2.3.2 Identification of System, Components, Processes and Ranking

2.3.2.1 Fuel Rod

Stored Energy

The stored energy is the total energy content of the fuel rods, and its spatial distribution, at the initiation of the transient. The stored energy is primarily a function of axial and radial power distributions throughout the core, pellet-clad gap conductance, and fuel thermal conductivity. The time in the fuel cycle at which the transient occurs affects the stored energy primarily through the fuel thermal conductivity and the gap conductance. [

]^{a,c}

Clad Oxidation

At high temperatures the zirconium base metal in the clad undergoes an exothermic reaction with the steam. [

]^{a,c}

Decay Heat

Fission product decay heat is calculated using the American National Standards Institute/American Nuclear Society (ANSI/ANS) 5.1-1979 model. Implementation of the model includes consideration of the spatial distribution, and uncertainty of the decay heat itself. The power history during the transient is also considered in the Westinghouse analysis methodology. This affects the local power of all fuel rods included at the PCT location.

[

]^{a,c}

[

]^{a,c}

Clad Deformation (Burst Strain, Relocation)

As the system depressurizes below the rod internal pressure, clad swelling and burst can occur. Fuel pellet fragments can relocate into the ballooned section of the clad at the burst location, thereby increasing the local heat generation rate. The clad burst temperature depends on the differential pressure across the clad. Burst strain depends on the metallurgical phase of the clad at the time of burst. [

]^{a,c}

2.3.2.2 Core

Critical Heat Flux

CHF is the process of boiling crisis in the hot assembly. Depending on the break size, this may occur at different times during the transient (early on for larger breaks).

[

]^{a,c}

[

]^{a,c}

Post-Critical Heat Flux Heat Transfer/Steam Cooling

Post-CHF (or steam cooling) describes the heat transfer from uncovered portions of the fuel rod. The regimes for post-CHF heat transfer include the inverted annular, dispersed droplet film boiling, transition boiling, and single-phase convection regimes. The criteria that define the boundaries of those regimes are T_{min} and the void fraction. Grid effects are included in this phenomenon.

[

]^{a,c}

Rewet/T_{min}

Following uncovery, T_{min} affects the quenching/rewetting of a cladding segment. T_{min} is the rewet temperature when the cladding is in the inverted annular flow regime, and is the minimum film boiling temperature when the cladding is in the dispersed flow film boiling regime.

[

]^{a,c}

Heat Transfer to a Covered Core

The heat transfer regimes of saturated and subcooled nucleate boiling, in addition to single-phase convection to liquid, encompass heat transfer to a covered core. [

]^{a,c}

Radiation Heat Transfer

Radiation heat transfer is the surface-to-surface thermal radiation heat transfer in the core. [

]^{a,c}

3D Flow/Core Natural Circulation

The importance of distinguishing between several channels of different geometries is recognized in the Westinghouse methodology. The hardware in the reactor upper plenum can affect the amount of flow the fuel assemblies receive during the Blowdown downflow period for the large breaks when the flow is from the upper plenum and upper head into the core. The guide tube assemblies have a direct flow communication path to the upper head. In some plants, there are free-standing mixers on the upper core plate that are solid cylinders approximately 11.5 – 13 inches high so that for the assembly to receive direct flow of any pooled water, the water must pool to a higher elevation. There may also be orifices on the upper core plate that reduce the flow area between the upper plenum and the core. These hardware and geometry effects have to be modeled to accurately predict the flow split for the different assemblies, because there will be different flows entering the top of the core channels. The presence of a low-power zone on the edge of the core provides an easier flow path from the upper plenum to the lower plenum. The low-power zone may be at powers that are sufficiently low for this channel to quench early such that, after quench, the steam generation will be low. As a result, the liquid in the upper plenum can more easily bypass the center regions of the core and drain down the low-power region. This effect must be modeled, or otherwise the flow through the center region of the core may be over estimated. The effect of channel geometry differences in the core is less pronounced during periods characterized by more stable conditions since the liquid level moves up the core uniformly. However, radial power shapes in the core can lead to a thermal chimney effect with higher induced flows in the hot assembly as a result of internal natural convection circulations. Three-loop, four-loop, and UPI plants have similar hardware and utilize low-leakage fuel management loading patterns.

[

]^{a,c}

[

]^{a,c}

Void Generation/Void Distribution

The void generation and distribution refers to the generation and distribution of steam and their effect on the mixture level. The interfacial drag and form losses in the core contribute to the two-phase level. Flashing also contributes to the void fraction distribution, and is considered a contributor to the two-phase level.

[

]^{a,c}

[

]^{a,c}

Entrainment/De-entrainment

Entrainment/de-entrainment describes the axial entrainment of liquid at a quench front and de-entrainment at higher elevations in the bundle. The ranking provided herein is mostly based on the description of the different reflood process for small and large breaks that has been discussed above.

[

]^{a,c}

Flow Reversal/Stagnation

This phenomenon is specific to the larger break scenarios, and in particular for the Blowdown phase of the transient since it determines how much flow will pass through the core versus how much of the flow will go to the broken loop. This parameter depends on the break size being analyzed, the flow path resistances, and the performance of the reactor coolant pumps. [

]^{a,c}

Flow Resistance

The hydraulic restrictions to flow in the core can have an effect on the transient. [

]^{a,c}

Water Storage in Barrel/Baffle Region

The former plate region is included since it contains a potentially significant source of available volume (about 25 percent of that residing in the core for some plants) and has small drain holes distributed axial (and radially). [

]^{a,c}

2.3.2.3 Upper Head

Draining/Flashing/Mixture Level

The liquid inventory in the upper head initially drains through the guide tubes, until the depressurization causes flashing in this region. A two-phase mixture will then continue the draining process, until the mixture level drops below the top of the guide tubes. This process affects the initial flow split through the broken and intact loop hot legs, and the core.

[

]^{a,c}

Venting

Later in a LOCA transient, steam generated in the core will either be vented through the hot legs, the hot leg nozzle gaps, or the upper head. The ability to vent steam through the upper head is strongly dependent on the flow area of the spray nozzles, the flow path connecting the upper head and the downcomer. For plants designed to keep the upper head at the cold leg temperature, this area is relatively large and upper head venting capability is increased relative to plants designed with a low bypass flow to the upper head during normal operation.

[

]^{a,c}

[

]^{a,c}

Metal Heat Release

The upper support plate and the reactor vessel head are thick structures that are initially at elevated temperatures (about 550°F to 620°F). These and other structures in the upper head become a heat source as the system depressurizes.

[

]^{a,c}

Initial Fluid Temperature

The initial fluid temperature in the upper head region will be either equal to the cold leg temperature, or close to the hot leg temperature, depending on the spray nozzle flow area. This will affect the timing at which flashing occurs in the upper head, causing the flow through the guide tubes to switch from single phase liquid to a two-phase mixture.

[

]^{a,c}

2.3.2.4 Upper Plenum

Hot Assembly Location

The specific geometries of the hardware that exists in the reactor upper plenum will result in different flows into the assemblies from the upper plenum and upper head during Blowdown. Depending on whether the hot assembly is located under a guide tube, a support column, a free-standing mixer, or an orifice plate will affect the flow rate into or out of the hot assembly at the upper core plate.

[

]^{a,c}

[

]a,c

Entrainment/De-entrainment

Depending on the steam velocities in the core, droplets can be entrained into the upper plenum, and potentially out through the hot legs to the steam generators. De-entrainment on the upper plenum structures will result in the build-up of a pool; steam flow from the core can also re-entrain water from the pool and out the hot legs.

[

]a,c

Draining/Fallback/CCFL

Water draining from the upper plenum region, or falling back after entrainment from the core, can contribute to core cooling. The amount of water that can drain may be limited by counter-current flow limitation phenomena, wherein the steam upflow is sufficient to limit or prevent draining.

[

]a,c

[

]^{a,c}

Mixture Level/Phase Separation

This phenomenon is related to the upper plenum liquid inventory throughout the transient, as it affects draining and fallback to the core, and entrainment out the hot legs to the steam generators.

[

]^{a,c}

Metal Heat Release

The upper core plate, internals structures, and core barrel are initially at elevated temperatures (about 550°F to 620°F). These structures become a heat source as the system depressurizes.

[

]^{a,c}

Hot Leg-Downcomer Gap Flow

Small gaps exist at the interface of the core barrel and the hot leg nozzles. These are the leakage paths that exist between the hot leg nozzles and upper downcomer region during all operating modes. Physically, these represent the small residual radial gaps between the core barrel hot leg nozzle tips and the reactor vessel hot leg nozzle inner surfaces. Their presence, by design, allows the upper plenum shroud/core barrel to be installed and removed. These gaps exist even after differential thermal expansion of the core barrel, relative to the reactor pressure vessel, has occurred at rated operating conditions. These gaps can account for as much as 1 percent leakage flow directly from the upper downcomer to the hot legs during normal operation. These gaps open up as the reactor is shut down and brought to cold conditions. The radial gap is on the order of 0.1 inches for cold conditions, and on the order of 0.01 to 0.02 inches for hot operating conditions. The hot leg circumference is about 94 inches for each leg in the Westinghouse NSSS.

Later in the transient, steam generated in the core will either be vented through the hot legs, the hot leg-downcomer gaps, or the upper head. [

]^{a,c}

[

]^{a,c}

Condensation

Condensation of steam can occur when it mixes with water that is sufficiently subcooled. Condensation could occur in the upper plenum, provided there is a mechanism for the introduction of subcooled water and steam.

There is no mechanism for the introduction of subcooled water into the upper plenum, except for UPI plants for those phases that include low head safety injection. In those phases, condensation will affect the entrainment process, and the CCFL/draining process. [

]^{a,c}

2.3.2.5 Hot Leg

Entrainment/De-entrainment

[

]^{a,c}

Horizontal Stratification/Flow Regime

For cold leg breaks, the flow regime in the hot leg [

]^{a,c}

Flow Reversal (Bulk)

Flow reversal in the Hot Leg [

]^{a,c}

Metal Heat Release

Metal heat release ranking for the hot leg is [ ]^{a,c}

2.3.2.6 Pressurizer/Surge Line

Level Swell/Flashing

Reactor trip can be initiated on pressurizer level or pressurizer pressure, [

]^{a,c}

Metal Heat Release/Heaters

For small breaks, the stored energy in the pressurizer vessel wall (and possibly the heater rods as well) may affect the draining of the pressurizer and the depressurization rate; [

]^{a,c}

[

]a,c

Interface Heat Transfer

For small breaks, interface heat transfer is ranked [

]a,c

Surge Line Flow/Flooding

[

]a,c

Phase Separation at Branch Tee

This is the flow split and flow interaction between vapor and liquid phases at a tee junction. In a conventional PWR, this process applies only to the pressurizer surge line connection. For a break in the cold leg, the flow exclusively exits from the pressurizer into the hot leg, from where it can flow into the upper plenum. Flow back into the pressurizer does not occur. [

]a,c

2.3.2.7 Steam Generator

Primary Side Heat Transfer/Condensation in U-tubes

This refers to the heat transfer processes on the primary side of the SG tubes. If condensation occurs, it affects the amount of vapor present and the resistance to flow through the generator.

[

]^{a,c}

Non-Condensable Gas Effects

This refers to the limitation of condensation heat transfer by the presence of a non-condensable gas such as nitrogen.

[

]^{a,c}

Secondary Side Heat Transfer

[

]^{a,c}

[

]^{a,c}

Secondary Side Level

This is the two-phase level on the secondary side of the SG. As long as the tubes remain covered, the heat transfer coefficient on the secondary side is high when the secondary serves as a heat sink (as it is in a saturated or subcooled nucleate boiling regime). If the secondary side level drops so that tubes are uncovered, the generator ceases to be an effective sink for heat transfer.

[

]^{a,c}

Secondary Side Stratification & Recirculation

This describes the hydraulic behavior of the SG secondary side during the transient. As the main feedwater trips, flow through the tube bundle is reduced and the secondary side may stratify. Recirculation affects the heat transfer from/to the tubes.

[

]^{a,c}

Atmospheric Dump Valve (ADV)/Safety Relief Valve (SRV) Mass Flow & Energy Release

The SG secondary side pressure and liquid level governs the mass and energy flow out of the secondary side safety relief valves. This process controls secondary pressure and helps to cool the secondary side.

[

]^{a,c}

Flow Regime/CCFL

This refers to the flow regime in the primary side of the steam generator, and in particular the hydraulic processes on the primary side in the SG tubes that lead to liquid holdup on the uphill side and voiding at the top of the U-tube.

[

]^{a,c}

Steam Binding

This process is only relatively important when high liquid entrainment from the upper plenum is carried into the steam generator U-tubes, while the SG is acting as a heat source. The vaporization of the liquid leads to pressure increase and a reduction of the core inlet flow rate.

[

]^{a,c}

Multi-tube Behavior

This refers to differences in flow behavior that may occur due to variation in path length. In a U-tube SG, tubes along the bundle periphery are significantly longer than those near the center. The potential for multi-tube effects is greatest when condensation is occurring and the flow is two-phase.

[

]^{a,c}

Primary Flow Resistance (Two-Phase DP)

This is the two-phase pressure drop through the SG. [

]^{a,c}

Metal Heat Release

This is included for the SG for completeness but is ranked [

]^{a,c}

2.3.2.8 Pump Suction Piping/Loop Seal

Horizontal Stratification

This refers to the presence of the horizontal stratified flow regime in the loop seal piping allowing vapor from the SG to slip through the loop seal to the pump.

[

]^{a,c}

CCFL

This refers to countercurrent flow limit in the vertical uphill section of piping leading to the pump.

[

]^{a,c}

Entrainment/Flow Regime/Interfacial Drag

This refers to the entrainment of liquid from the stratified layer at the bottom of the horizontal section of loop seal piping, and the carryout of this liquid from the region.

[

]^{a,c}

Flow Resistance

This refers to the single- and two-phase pressure drop through the loop seal region.

[

]^{a,c}

Metal Heat Release

This is included with the crossover leg piping for completeness but is ranked [

]^{a,c}

2.3.2.9 Pump

One- and Two-Phase Performance

This refers to the pumping efficiency of, and the turbulence imparted by, the RCP while the inlet conditions are one- and two-phase. [

]^{a,c}

Coastdown Performance

This involves the effect the pump has on the flow between the time the pump is tripped, and the time when the impeller completes its coastdown. Note that the effects of pump friction/windage losses are included in this process.

[

]^{a,c}

[

]^{a,c}

Flow Resistance

This refers to hydraulic resistance to flow passing through the pump.

[

]^{a,c}

Pump CCFL

This refers to the limitation of liquid flow back through the pump to the loop seal region by steam flowing towards the break. In most PWRs the design includes a weir to prevent backflow through the pump, which limits this process to periods when the level in the cold leg is higher than the weir height.

[

]^{a,c}

[

]^{a,c}

Metal Heat Release

[

]^{a,c}

2.3.2.10 Cold Leg/Safety Injection

In the Westinghouse FSLOCA EM, the break is assumed to occur in the cold leg, as this represents the most limiting location for both small and large breaks. In general, the cold leg is connected, via single or multiple tees, to the accumulator and the pumped safety injection. Phenomena relative to the flow delivered by accumulator safety injection on the cold leg are discussed here, as well as phenomena relative to the pumped safety injection. The accumulator tank is discussed separately in Section 2.3.2.11.

Interfacial Heat Transfer (Condensation)

This is condensation of steam in the cold leg. Two different condensation phenomena are identified. The more important of the two is condensation that occurs on and about the stream of subcooled water injected into the cold leg from the pumped SI system and/or the accumulator. This jet is subcooled, and breakup of the jet can generate a large interfacial area for condensation. Second, condensation may occur over the whole cold leg at the interface between flowing liquid and steam, being heavily influenced by the flow regime (mainly stratified versus annular flow) existing in the cold leg.

[

]^{a,c}

[

]a,c

Non-Condensable Effects

In the cold leg, this refers to the effect that nitrogen has on condensation in the cold leg. The rankings for this effect generally follow those assigned for condensation.

[

]a,c

[ ]^{a,c}

Flow Regime

This refers to the prediction of the flow regime existing in the cold leg and its influence on condensation in the cold leg. In particular, the prediction of the horizontal stratified flow regime in the cold leg is included, as in this flow regime lower interfacial heat transfer is expected.

[

]^{a,c}

Metal Heat Release

This is included with the cold leg for completeness but is ranked [
]^{a,c}

Spilling Flow Treatment (Pumped SI)

The treatment of the pumped SI flow in terms of flow spilled at the break versus flow delivered is considered. Spilled flow depends on the break dimension and location on the cold leg.

[

]^{a,c}

2.3.2.11 Accumulator

Injection Flow Rate/Line Resistance

This refers to the rate at which liquid is discharged from the accumulator, which depends upon the cover gas expansion coefficient and the hydraulic resistances to accumulator flow in the check valve and in the line connecting the accumulator to the cold leg.

[

]^{a,c}

Check Valve Hysteresis

The behavior of the check valves in the accumulator delivery line is considered.

[

]^{a,c}

[

]^{a,c}

Nitrogen Discharge

The accumulator nitrogen provides the main source of non-condensable gas in the system during the LOCA transient. While the potential effects of non-condensables are discussed elsewhere as applicable, it is recognized that the accumulator cover gas provides the main source of non-condensable gas in the system, and thus the relative discharge process is discussed.

[

]^{a,c}

Interfacial Heat Transfer

Although the accumulators are subject to essentially adiabatic expansion in Large Break LOCAs, where the transient time is short, Small Break LOCAs occur over considerably longer duration. The heat transfer is more important between the nitrogen and accumulator tank wall in Small Break LOCAs, and the gas expansion coefficient may be affected. Heat transfer between the non-condensable gas and subcooled water may also occur within the accumulator.

[

]^{a,c}

Metal Heat Release

This is included for the accumulator for completeness but is ranked [

]^{a,c}

Broken Loop Accumulator Treatment

Similar to the *Spilling Flow Treatment (Pumped SI)* process discussed in Section 2.3.2.10, this refers to the treatment of the accumulator flow on the broken cold leg in terms of flow spilled at the break versus

flow delivered. Spilled flow depends on the break dimension and location on the cold leg. Ranking is based on analogous considerations to those provided for the *Spilling Flow Treatment (Pumped SI)*.

[

]^{a,c}

2.3.2.12 Downcomer

The downcomer is attached to both broken and intact cold legs. Following a rupture, coolant from the downcomer exits through the broken cold leg as the system depressurizes. When the system pressure decreases below a set point, accumulators inject borated water into the intact cold legs where two-phase fluid and the subcooled liquid from the accumulators mix and the steam is condensed. Depending on the degree of subcooling and amount of steam flow, liquid may remain subcooled as it flows into the downcomer where more condensation takes place. If the break size is large enough, the steam from the core also exits from the broken cold leg through downcomer and may delay the accumulator liquid from penetrating down into the lower plenum. This is called ECCS bypass phenomenon. This phenomenon is only present in Large Break LOCAs where the steam from the core passes through the downcomer on its way out of the broken cold leg.

Condensation

The condensation occurs in the downcomer because of SI and accumulator water reaching the downcomer in subcooled conditions.

[

]^{a,c}

[

]

]^{a,c}

Non-condensable Effects

This is the effect that nitrogen has on condensation in the downcomer. The main source of nitrogen is accumulators. The dissolved nitrogen and hydrogen in the coolant are negligible compared to the accumulator nitrogen. The rankings for this effect follow those assigned for the non-condensable effect in the cold legs.

[

]^{a,c}

Flow Resistance

This is the effect that the flow resistance in the downcomer has on the coolant flow and distribution throughout the transient. The broken cold leg nozzle is excluded from this item.

[

]^{a,c}

[

]^{a,c}

Reactor Pressure Vessel Internals/Vessel Wall Stored Energy

This is the effect of the heat release to the fluid from the downcomer metal structures.

[

]^{a,c}

3D Effects

This refers to multidimensional flow that may occur in the downcomer and its impact on the transient.

[

]^{a,c}

[

]^{a,c}

Mixture Level/Flashing/Void Fraction

This refers to the two-phase level in the downcomer. Flashing may contribute to voiding in the downcomer during Blowdown, and is considered part of the mixture level process. Later in the transient, the heat release from the vessel wall may cause boiling which would affect the mixture level significantly.

[

]^{a,c}

Counter-current, Slug, and Non-equilibrium Flows

This refers to the counter-current, slug, and non-equilibrium flows that are characteristic of the ECC bypass phenomena.

[

]^{a,c}

Entrainment/De-entrainment

This refers to the entrainment of water from the top of the downcomer level by steam flowing around the downcomer to the break.

[

]^{a,c}

Liquid Level Oscillations

Liquid level oscillations are a gravity-driven reflood phenomenon which is a result of the heat released in the core and the corresponding pressure drop in the loops.

[

]^{a,c}

2.3.2.13 Lower Plenum

Lower Plenum Sweep-Out/Multidimensional Flow

During Blowdown, if the depressurization rate is high enough to allow steam generated in the core exit to the broken cold leg via the lower plenum and downcomer, there would be multidimensional flows in the lower plenum which then results in sweep-out of liquid from the vessel lower plenum. It is understood

that the sweep-out of liquid and amount of liquid remaining at the end of Blowdown is a consequence of multidimensional flows.

[

]^{a,c}

Hot-wall Effect (Void Generation or Boiling)

This is the effect of the heat release to the fluid from the lower plenum metal structures.

[

]^{a,c}

2.3.2.14 Break

Critical Flow

The critical flow phenomenon is the fact that the break flow rate is limited by the local sonic velocity at the throat and not by the reservoir pressure. Since the break flow rate determines the depressurization and inventory and mass distribution in the vessel, it is easy to see a high ranking of this phenomenon.

[

]^{a,c}

[

]a,c

Containment Pressure

The break flow rate is influenced by the containment pressure only when the break flow is subcritical. This is the case after the Blowdown phase is ended for larger break size transients.

[

]a,c

Upstream Flow Regime

This refers to the effect that the assumed orientation has on the break flow. The break can occur at the top, bottom, or side of a pipe, and depending on the stratification in the pipe the upstream conditions influence the break quality. For example, for a break on the bottom of the pipe, vapor can be pulled through the liquid layer to the break face yielding a quality greater than zero. A break at the top of the pipe may entrain water from the level lower in the pipe to the break face yielding a quality less than 1.0. Break locations may be assumed anywhere in the coolant loops or their attached auxiliary piping.

[

]a,c

Upstream Fluid Mixing

This refers to the effect that the degree of fluid mixing upstream of the break has on the break flow. In a split break, the break sees fluid with different flow quality/enthalpy approaching. This effect recognizes

that the currently available data may not cover a condition that may exist at the break which has some distribution in either void fraction, quality, and/or enthalpy.

[

]^{a,c}

Non-condensable Effects

This refers to the effect that nitrogen may have on critical break flow. The presence of nitrogen in the two-phase mixture can have a significant impact on the choke flow rate especially in the subcooled liquid. Because the accumulator is the major source of nitrogen, SI spill assumption, accumulator/SI line configuration, and worst failure assumption may have an impact on the ranking.

[

]^{a,c}

Cold Leg Nozzle Flow Resistance

The broken cold leg nozzle resistance could have a significant effect on the break flow since the throat pressure is impacted by the nozzle pressure loss throughout the transient, which also influences the flow split between the vessel side flow path and the pump discharge side flow path, which then impacts the core flow during the Blowdown.

[

]^{a,c}

[

]a,c

2.3.3 PIRT: Summary and Conclusions

The list of dominant phenomena identified by the PIRT process for the LBLOCA scenario were already developed and documented in the original Code Qualification Document (CQD, Bajorek et al., 1998). The list of phenomena is repeated here for convenience:
[

]a,c

Many of these models are also important at smaller breaks while some are not significant or applicable (e.g., ECCS bypass). However, the development of the integrated FSLOCA PIRT identified additional phenomena which become more relevant as the break size gets smaller. These are:
[

]a,c

The importance of some phenomena expands over the full spectrum of break sizes. In those cases the associated models need to be applicable and validated over the full range of conditions expected over the full spectrum of break sizes. There are phenomena that appear to become relevant only for smaller break sizes. These phenomena were either classified as non important or not applicable during LBLOCA scenario.

The phenomena or processes listed in the PIRT are sometimes a broad combination of various sub-processes. For example:
[

]a,c

[

]^{a,c}

2.4 REQUIREMENT ANALYSIS/ASSESSMENT FOR WCOBRA/TRAC-TF2 MODELS

This section documents the process and the results of the functional requirement analysis. The current NRC-licensed code (WCOBRA/TRAC (Nissley et al., 2005)) was assessed against the FSLOCA PIRT to evaluate the current model capabilities and determine what was needed to extend its applicability to

Intermediate and Small Break LOCA. The current code is documented in the ASTRUM topical report (Nissley et al., 2005), the CQD (Bajorek et al., 1998), and the UPI best-estimate topical report (Dederer et al., 1999).

The 1D Module of WCOBRA/TRAC (based on TRAC-PD2 drift flux formulation) was considered in the assessment. The use of a five-equation model (mixture velocity + drift flux model) does not allow an adequate horizontal stratification modeling. The donoring is determined by the mixture velocity direction but the quantities associated with the relative velocity are convected using the relative velocity in TRAC-PD2 (or 1D components of WCOBRA/TRAC), which often generates a mass error in very slow draining transients since the donor selection is often wrong. This led to the decision to replace the 1D Module based on TRAC-PD2 code with a 1D Module based on TRAC-P [ ]^{a,c} and, as such, extend the two-fluid formulation to the loop. As a result, review of the 1D Loop components presented herein refers directly to TRAC-P [ ]^{a,c}.

The six-equation two fluid model extended to the loop provides an adequate formulation of both the stratified flow simulation required for SBLOCA and also limits the mass error during slow draining transients. Non-condensable transport is also already implemented in TRAC-P [ ]^{a,c}.

The TRAC-M Theory Manual (Spore et al., 2000) and TRAC-M Assessment Manual (Boyack et al., 2001) were surveyed for expected capabilities of TRAC-P [ ]^{a,c} relative to the requirements listed in Section 2.3. The assessment manual contains a few comparisons to analytical solutions as well as a small set but wide variety of test simulation results which are useful for a preliminary assessment. The analytical assessment problems included two steady-state heat-conduction problems, a fill-and-drain hydrodynamic problem, and a U-tube manometer problem.

The separate-effects tests included tests that evaluated counter-current flow limitation (CCFL), condensation, critical flow, loop-oscillatory behavior, core reflood, and downcomer ECC flow penetration. The separate-effects core reflood assessments included a Lehigh rod-bundle test, two Full-Length Emergency Core Heat Transfer (FLECHT) Separate-Effects and System-Effects Tests (SEASET) reflood tests, a Cylindrical Core Test Facility (CCTF) test, and two Upper-Plenum Test Facility (UPTF) tests. The integral-effects test assessments included the LOFT L2-6 loss-of-coolant transient and the LOFT L6-1 loss-of-steam load transient, the CCTF Run 54 reflood test, and the Slab Core Test Facility (SCTF) Run 719 reflood test. Documented improvements implemented in TRAC-P [ ]^{a,c} that are relevant to Small and Intermediate LOCA applications are:

1. Horizontal Stratified flow: Simulation with modified TRAC-P [ ]^{a,c} shows adequate performance at high pressure.

2. Non-condensable gas field: Accumulator nitrogen is modeled explicitly.

3. Functional trip logic.

For the FSLOCA Methodology, WCOBRA/TRAC was thus modified by replacing the 1D Module (based on TRAC-PD2) with the TRAC-P [ ]^{a,c} code and adding a few improvements to the 3D module (based on the Westinghouse modified COBRA-TF). This extends the use of a two-fluid six-equation formulation of the two-phase flow to the 1D loop components. The new code has been renamed

to WCOBRA/TRAC-TF2 where "TF2" is an identifier that reflects the use of three-field (TF) formulation of the 3D module derived by COBRA-TF and a two-fluid (TF) of the 1D module based on TRAC-P [ ]^{a,c}.

The initial assessment of the WCOBRA/TRAC and TRAC-P [ ]^{a,c} is provided in Table 2-2, which identifies major areas requiring further development effort. The review of both the 3D module and 1D module of the code led to development of the functional requirements which are discussed herein. Section 2.4.1 describes the process utilized to define the functional requirements and the results are discussed in Section 2.4.2.

2.4.1 Assessment Process

For each medium and high ranked phenomena of the FSLOCA PIRT, the following questions were asked to help identify and prioritize the important models for implementation consideration:

1. Is there a physical model (or set of models) capable of describing a particular phenomenon in the code? Identify relevant sections in previous documentation where the model is described and the validation/assessment was made.

2. If yes, is the model validated to work in a range expected in SB, IB LOCA as well as LBLOCA conditions and geometries?

3. Are there validation test data available (SETs and/or IETs) for validation of the model(s) in the expanded range of SB and IB LOCAs?

Using the FSLOCA PIRT medium and high rank list shown in Table 2-1, the modeling capability of the WCOBRA/TRAC code was assessed relative to phenomena expected to play important roles in smaller break size LOCAs. For each high ranked phenomenon, basic physical models required to predict the event/process were identified and compared against the models in the base code (WCOBRA/TRAC). A similar process has been followed in the examination of the TRAC-P [ ]^{a,c} module for each phenomenon related in the 1D loop components. The deficiencies and/or a lack of physical models were identified.

2.4.2 Review of WCOBRA/TRAC and TRAC-P [ ]^{a,c} Capabilities and Assessment Results

The results of the code assessment are summarized in Table 2-2. Table 2-2 shows processes/phenomena considered, ranking for the three sub-scenarios, existence/non-existence of the corresponding physical models in the base code, WCOBRA/TRAC, the reference to model description and the validation effort, and a preliminary evaluation relative to SB and IB as well as LB LOCA conditions. Phenomena which are considered of low importance or N/A for all phases are included in Table 2-2, but generally not discussed in detail.

In Table 2-2, Column 2, phenomena with ranking of high (H) or medium (M) in one or more phases are highlighted. The ranking is represented in three lines with the top one representing the five phases of the small break (Blowdown (BLD), Natural Circulation (NC), Loop Seal Clearance (LSC), Boiloff (BO),

Recovery (REC)), the middle line showing three phases of the intermediate break (Blowdown (BLD), Accumulator Injection (ACC), Safety Injection (SI)), and the bottom line representing the Large Break LOCAs (Blowdown (BLD), Refill, Reflood). The notation follows in order the phases of each sub-scenario. For instance:

- Small Break → BLD/NC/LSC/BO/REC
- Intermediate Break → BLD/ACC/SI
- Large Break → BLD/Refill/Reflood

For example for the first element, e.g., fuel rod stored energy we have: [

]^{a,c}

Table 2-2 is intended to guide the functional requirements for the FSLOCA EM. However, for the current implementation, the FSLOCA EM focus is limited to cold leg injection PWRs. UPI plant requirements are excluded from Table 2-2.

The third column shows whether the code contains a physical model or a collection of models which describe the process/phenomenon of interest. The fourth column shows applicable section(s) from the CQD (Bajorek et al., 1998) where a particular model is described, and where assessments/uncertainty analyses are performed. The last column gives comments relative to the need for improvement for SB/IB LOCA analysis. Comments highlighted in red indicate that some improvements are necessary.

2.4.2.1 Summary of Phenomena Requiring Improved Physical Models

The models discussed in this section were determined to be deficient and/or lacking for prediction of Small and/or Intermediate Break LOCA phenomena and/or processes.

Fuel Rod

[

]^{a,c}

Core

[

]^{a,c}

[

]a,c

Hot Leg

[

]a,c

Steam Generator

[

]a,c

[

]a,c

Pump Suction Piping/Loop Seal Clearance

[

]a,c

Pump

[

]a,c

Cold Leg/Safety Injection

[

]a,c

[

]^{a,c}

Break

[

]^{a,c}

Accumulator Nitrogen

[

]^{a,c}

2.5 WCOBRA/TRAC-TF2 DEVELOPMENT STRATEGY

The initial point is to redefine the general architecture of the code by replacing the 1D Module with the TRAC-P [ ]^{a,c}. In practice this was achieved by inserting the WCOBRA/TRAC 3D Module (based on COBRA-TF formulation) into the TRAC-P [ ]^{a,c} code while

deactivating the TRAC-P [ ]^{a,c} 3D component. The process required a re-design of the coupling logic between the two codes (modules) to suit a two-fluid (six-equation) formulation versus the previous drift-flux (5-equation) formulation at the 1D/3D junction.

Once the platform was developed, the new code was renamed as WCOBRA/TRAC-TF2 where "TF2" is an identifier that reflects the use of three-field (TF) formulation of the 3D module derived by COBRA-TF and a two-fluid (TF) of the 1D module based on TRAC-P [ ]^{a,c}.

In summary the updates can be divided in three stages. The first affects the general architecture or 'numerical engine' of the code, the second is the changes to the 3D (VESSEL) module and the third is the functional changes to the 1D (Loop) module.

The code upgrades were then considered to meet the functional requirements discussed in Section 2.4. The updates are divided among the three groups described above. The changes to the numerical engine are discussed in Section 2.5.1; the code changes that apply to the 3D module are in Section 2.5.2 and the code changes pertinent to the 1D module are in Section 2.5.3.

2.5.1 General Structure Functional Requirements for WCOBRA/TRAC-TF2

These are changes that have an impact on the solution scheme and general architecture of the code. In particular these are:

[

]^{a,c}

2.5.2 Functional Requirements for 3D Vessel Module

Following is the list of model developments and/or improvements that were identified for the 3D module (VESSEL component) of WCOBRA/TRAC-TF2:

[

]^{a,c}

2.5.3 Functional Requirements for 1D (Loops) Module

Following is the list of model developments and/or improvements that were identified for the 1D module (Loop components) of WCOBRA/TRAC-TF2:

[

]^{a,c}

2.5.4 Software Development Plan for WCOBRA/TRAC-TF2

A Software Development Plan was developed for WCOBRA/TRAC-TF2. The plan is designed to suit an incremental development process. The necessary code revisions that were identified in Sections 2.5.1 and 2.5.2 require both major and minor development tasks. Major updates are ones that have impact on the structure of the conservation equations or the numerical scheme. [

]^{a,c}

The updates/upgrades to closure relationships, models and correlations which are documented in Sections 2.5.1 and 2.5.2, tend to be contained within a single routine or group of routines.

The development of the fundamental portion of the code requires careful step-by-step modifications but does not require iterations with the simulation results, therefore a staged delivery model would be suitable. On the other hand, the development of physical models would most likely require several iterations with test simulations, which would be better dealt with by an evolutionary delivery approach, which anticipates many cycles of iterations. Figure 2-2 shows schematically the development lifecycle of WCOBRA/TRAC-TF2.

Volume 2 of this topical report provides the result of the final V&V performed with the frozen version of the WCOBRA/TRAC-TF2 code. The final version of the code for this topical report was frozen as Version 1.3, and put under configuration control before proceeding with the calculations.

2.6 DEVELOPMENT OF THE ASSESSMENT DATABASE

2.6.1 Objective for the Assessment Base

Consistently with EMDAP Step 5, the assessment database was constructed to include the following elements:

1. SETs used to develop and assess groups of empirical correlations and other closure models associated to the important phenomena.

2. IETs used to assess system interactions and global code capability.

3. Plant transient data, when needed and if available.

4. Simple test problems used to illustrate fundamental calculational device capability.

A systematic process has been used to identify an adequate assessment data base. The rationale for each test and relationship to the PIRT and EM functional requirements is discussed in Volume 2.

2.6.2 Definition of the Assessment Base (SETs and IETs)

Models are developed and presented in Sections 3 through 11 (Volume 1). Most of these models are available from the open literature and were developed and assessed independently by the original authors of such models and correlations. This is what we call 'developmental' assessment, which supports the scaling and applicability of specific models. The 'developmental' assessment is not discussed in this section, but rather the scaling and applicability of each model is discussed in the corresponding sections of Volume 1. The focus here is the development of the assessment base for the models or group of models as coded in WCOBRA/TRAC-TF2. This is what we refer to as code Validation and Verification (V&V). The V&V database identified for the various models and processes is discussed as follows.

A large V&V database was considered for the previously approved best-estimate LBLOCA Methodology (Bajorek et al., 1998). Most of the database was also used to confirm LBLOCA applicability of the new WCOBRA/TRAC-TF2 code. The validation basis was then extended to also cover small and intermediate breaks, and the overall assessment basis is presented in Tables 2-3 to 2-6.

Post CHF Heat Transfer in Rod Bundles

Conditions of interest are a full range of pressure from high to low pressure and wide range of vapor velocity. Rod bundle data used in the assessment is compiled in Tables 2-3 and 2-4. Semiscale S-7-10D (Shimeck, 1980) assessed as a Separate Effect Test mode was also included to cover situations with a deep core uncovery during the boiloff period of a postulated severe Small Break LOCA.

Core Mixture Level

Conditions of interest are high to medium pressure during boiloff condition. Available validation tests are:

1. G-1 Core Uncovery Tests, WCAP-9764 (Anderson, 1980)
2. Westinghouse G-2 Core Uncovery Tests, EPRI NP-1692 (Andreychek, 1981)
3. The JAERI-TPTF Critical Heat Flux Bundle Tests by Guo (Guo, et al., 1993)
4. ORNL-THTF Uncovered Bundle Tests by Anklam (Anklam, et al., 1982)

Non-condensable Gas Transport Capability and Effect on Condensation

Available validation tests are LOFT and ACHILLES. Additionally the gas transport capability was assessed against thought problems presented in Section 23.

Steam Generator Primary Side Heat Transfer (Condensation)

This is relevant during a Small Break LOCA to characterize the reflux condensation. Selected validation tests are the ROSA-IV NC tests.

Steam Generator Primary Side Flow Regime/CCFL

Similarly to the SG heat transfer, this is relevant during a Small Break LOCA to characterize the reflux condensation. Selected validation tests are the ROSA-IV NC tests.

Pump Suction Piping/Loop Seal Clearance

The time at which the loop seal clears, the liquid remaining in the loop seal, and the pressure drop across the loop seal depend on several physical processes: the rate at which steam is generated in the core; the condensation rate in the steam generator; the volume flow rate out the break; interfacial drag between the liquid and vapor in the loop seal; wall drag; and bubble rise velocity in the pump suction leg. The first three items in the list combine to determine the pressure difference across the loop seal prior to venting and the net vapor velocity through the loop seal once venting occurs. Interfacial and wall drag play a role in the final liquid inventory and loop seal pressure drop. Bubble rise is not expected to be a major process in determining final inventory and pressure drop.

There are three distinct phases in the loop seal clearance process. The first phase described above is the hydrostatic clearance phase, the second phase is the slugging phase, and the third phase is the entrainment phase. The slugging phase follows the initial vapor blow-through and is dominated by gravity versus pressure driven sloshing within the loop seal and an oscillatory pressure differential across the loop seal. Once sufficient liquid is removed from the loop seal slugging ceases and liquid is now removed by velocity driven steam entrainment of liquid from unstable waves. The final liquid level in the loop seal is determined by the steam velocity, which also establishes whether slugging or entrainment dominates the process.

The tests that best describe these phenomena are the UPTF, Full Scale PWR Loop Seal Tests at 3 and 15 bars. Despite the pressure being rather low, this is the only full-scale steam/water test available. The pressure scaling will be addressed in the validation documentation (Section 18).

Horizontal Stratified Flow Regime

Conditions of interest are in the high-to-medium pressure range and flow in a horizontal primary piping. The available validation test is the JAERI ROSA IV-TPTF horizontal flow test (Asaka, 1991).

Cold Leg/Safety Injection Direct Condensation

The condensation heat transfer rate at the horizontal stratified surface is low. When SI is injected, the SI jet promotes the condensation in the vicinity of the jet. The condensation efficiency observed in the experiments was as high as 80 to 90%, much higher than the condensation rate expected at the stratified surface. A special model was added in WCOBRA/TRAC-TF2 to model the direct steam condensation induced by the SI jet impinging into the liquid layer of a stratified cold leg. The correlation was developed from a subset of the COSI experiments and the model was validated with additional tests as discussed in Section 17.

Critical Flow in Complex Geometries

The conditions of interest include the full pressure range, subcooling and from low to high quality. Detailed reviews of available critical flow data were performed by various researchers, namely by Abdollahian et al. (1982), Ilic et al. (1986), and by Holmes and Allen (1998). The dataset given in Ilic et al. (1986) was investigated here (Section 12) and screened, since as-reported upstream conditions were suspect.

Critical Flow and Upstream Flow Regime Effect

A special model is added to account for the orientation of the break (top, side or bottom). This is relevant when the flow in the pipe (cold leg) is stratified. When the primary fluid is stratified, vapor pull-through and liquid entrainment may become important in determining the quality upstream of break. Judging from the break orientation tests conducted at ROSA (Kukita, 1991 and Asaka, 1990), a proper modeling of the entrainment at the break is required to show that the break orientation does not have a strong effect on the 2.5% and 0.5% cold leg break. The 0.5% hot leg did have a strong influence due to the break orientation (Kukita, 1991).

TPFL data are available at 500, 650 and 900 psia for side and bottom break configurations. TPFL did not examine the branchline at the top of the main pipe. Therefore, a correlation by Ardron and Bryce (1990) and normalized data points from other experiments can be used to compare the code prediction.

Non-Condensable Effect on Critical Flow

Non-condensable effects on the critical flow are considered. The critical flow model contains multiple models. Each model is typically responsible for specific upstream conditions. All of these sub-models need to be consistent with the presence of non-condensable gas in the vapor phase.

Accumulator Nitrogen and Non-Condensable Effects on Condensation

Particularly during an IBLOCA, the nitrogen discharge may be high enough to partially suppress the condensation, but not high enough to completely shut it off, therefore an appropriate model that captures the nitrogen effects is needed. The model selected is Young and Bajorek (1997). The effect of the non-condensable injection in the downcomer and its impact on the initial reflood is demonstrated by examining the ACHILLES tests and LOFT tests.

Coupled Containment Calculation

While the containment pressure is only ranked high in Large Break LOCAs, the code should be able to provide the consistent containment pressure for intermediate and Large Break LOCAs so that the use of overly conservative containment pressures could be avoided. This is only relevant during the portion of the transient when the flow is unchoked (subcritical). The validation will be simply based on benchmarking the solution obtained with the containment-coupled code with the un-coupled calculation.

Table 2-5 summarizes the assessment matrix developed to cover the small break sub-scenario processes. The rationale by which tests were selected for a given test facility or test campaign is discussed individually for each test in the corresponding sections of Volume 2. The criteria were based mainly on the reliability of the data and, to a lesser extent, the availability of the data itself.

Integral Effect Tests

The LOFT test facility was originally simulated to address the LBLOCA scenario with the approved version of the code (CQD, Bajorek et al., 1998). LOFT was also considered here. In addition, tests with smaller break sizes than those simulated with LOFT are modeled with WCOBRA/TRAC-TF2 to provide coverage of intermediate breaks and overlap with the small breaks.

ROSA (LSTF) Small Break series and ROSA natural circulation tests (Section 21) were considered for the integral assessment of the small break scenario. ROSA SB tests include a 10% cold leg break (side break), a 5% cold leg break (side break), three 2.5% cold leg breaks (a side break, a top break and a bottom break), and a 0.5% break.

ROSA (LSTF) tests were selected instead of corresponding Semiscale tests mainly because of better scaling characteristics of ROSA (1/48 vs. 1/1700). There are also many other reasons which favor the ROSA test facility versus Semiscale. Semiscale was affected by significant scaling distortion, mainly because of the excessive heat losses. Because of the bigger volume-to-wall area ratio in ROSA, heat losses are negligible in that test facility. Steam Generators (SGs) in ROSA consider 141 U-tubes while SGs in Semiscale have only 6 tubes.

[

]^{a,c}

[

]^{a,c}

2.6.3 Evaluation of the Assessment Base (SETs and IETs)

The EMDAP Steps 6, 7, 8 and 9 (Figure 2-4) require a qualification of the assessment base which includes scaling analyses, identification of IETs distortions and SETs scale-up capability. Moreover, experimental uncertainties should be identified as appropriate. These considerations are provided for each test considered in the discussion of the assessment in Volume 2.

2.6.4 Additional Assessment

Section 2.6.2 described the validation basis of WCOBRA/TRAC-TF2 against the critical phenomena identified in the PIRT and covering the whole spectrum of postulated break sizes. This final assessment requires some additional validation, and in particular some numerical thought problems, and has two key objectives:

1. Complete the validation basis with the evaluation of critical issues that have not been completely addressed with the base assessment. In essence, some specific limitations of the previous validation are analyzed and completed through this assessment.

2. Use a series of numerical problems, for which an analytical solution can be developed, to verify not only that WCOBRA/TRAC-TF2 correctly predicts the complex physical phenomena analyzed in the previous section, but is also capable of providing a physically sound solution to some standard problems, thus verifying the overall code robustness and quality. Consistent with RG 1.203, these numerical problems are performed "to illustrate fundamental calculational device capability."

To achieve these objectives the following additional tests were considered:

1. GE Blowdown (Findlay and Sozzi, 1981) – The level swell analysis documented in Section 13 relies mostly on steady state tests. The objective of the GE Blowdown analysis is to assess the WCOBRA/TRAC-TF2 code in a Blowdown, dynamic-type transient. This section will also demonstrate that the WCOBRA/TRAC-TF2 level swell prediction remains adequate in these conditions.

2. Semiscale – The Level Swell and Boiloff analyses documented in Section 13 are all characterized by relatively low clad temperature. Selected Semiscale tests are analyzed herein to verify the WCOBRA/TRAC-TF2 performance when clad temperatures are higher.

Finally, the following numerical thought problems, or analytical benchmarks were added to the assessment base:

1. 1D PIPE Manometer – This is the classical manometer problem and was exercised with the 1D (Loop) components of WCOBRA/TRAC-TF2 (Hewitt, 1992).

2. 3D VESSEL Manometer Problem – Same problem as above, but was modeled with the 3D module.

3. 1D PIPE Steam Expulsion Test – A vertical pipe initially containing superheated steam is gradually filled with subcooled liquid. This problem was simulated using 1D PIPE component of the code (Hewitt, 1992).

4. 3D VESSEL Steam Expulsion Test – Same problem as above, modeled with the 3D module.

5. 1D PIPE Fill and Drain Test – This problem examines the behavior of a two-phase mixture level crossing cell boundaries (Frepoli, 2003 and Aktas, 2003).

6. 3D VESSEL Fill and Drain Test – Same problem as above, modeled with the 3D module

7. Non-condensable gas transport test and condensation test – These are thought problems to study how the code simulates the transport of non-condensable gas and condensation effects.

2.7 REFERENCES

1. Abdollahian, D., et al., 1982, "Critical Flow Data Review and Analysis," EPRI NP-2192.

2. Aktas, B., 2003, "Level Tracking in Thermal-Hydraulic Simulations of Nuclear Reactors," A Thesis in Nuclear Engineering, PSU.

3. Anderson, T. M., 1980, "Documentation of the Westinghouse Core Uncovery Tests and the Small Break Evaluation Model Core Mixture Level Model," WCAP-9764 (Proprietary).

4. Andreychek, T. S., 1981, "Heat Transfer Above the Two-Phase Mixture Level Under Core Uncovery Conditions in a 336-Rod Bundle," Volumes 1 and 2, EPRI NP-1692.

5. Anklam, T. M., et al., 1982, "Experimental Investigations of Uncovered-Bundle Heat Transfer and Two-Phase Mixture-Level Swell Under High-Pressure Low Heat-Flux Conditions," NUREG/CR-2456.

6. Ardron, K. H. and Bryce, W. M., 1990, "Assessment of horizontal stratification entrainment model in RELAP5/MOD2 by comparison with separate effects experiments," *Nuclear Engineering and Design* 122, pp. 263-271.

7. Asaka, H., et al., 1990, "Results of 0.5% Cold-Leg Small-Break LOCA Experiments at ROSA-IV/LSTF: Effect of Break Orientation," *Journal of Experimental Thermal and Fluid Science*, 3, pp. 588-596.

8. Asaka, H., Kukita, Y., Anoda, Y., et al., 1991, "Improvement of TRAC-PF1 Interfacial Drag Model for Analysis of High-Pressure Horizontally-Stratified Two-Phase Flow," *Journal of Nuclear Science and Technology*, Vol. 28, No. 1, pp. 33-44.

9. Bajorek, S. M., et al., 1998, "Code Qualification Document for Best Estimate LOCA Analysis," WCAP-12945-P-A, Volume 1, Revision 2, and Volumes 2 through 5, Revision 1, and WCAP-14747 (Non-Proprietary).

10. Boyack, B., et al., 1989, "Quantifying Reactor Safety Margins: Application of Code Scaling, Applicability, and Uncertainty (CSAU) Evaluation Methodology to a Large-Break, Loss-of-Coolant Accident," NUREG/CR-5249.

11. Boyack, B. E., et al., 2001, "TRAC-M/F77, Version 5.5 Developmental Assessment Manual," LA-UR-01-2105.

12. Dederer, S. I., et al., 1999, "Application of Best Estimate Large Break LOCA Methodology to Westinghouse PWRs with Upper Plenum Injection," WCAP-14449-P-A, Revision 1, and WCAP-14450-NP-A, Revision 1 (Non-Proprietary).

13. Findlay, J. A. and Sozzi, G. L., 1981, "BWR Refill-Reflood Program Task 4.8 – Model Qualification Task Plan," NUREG/CR-1899.

14. Frepoli, C., et al., 2003, "Notes on the implementation of a fully-implicit numerical scheme for a two-phase three-field flow model," *Nuclear Engineering and Design*, 225, pp. 191-217.

15. Guo, Z., et al., 1993, "Critical Heat Flux for Rod Bundle Under High-Pressure Boil-off Conditions," JAERI-M 93-238.

16. Hewitt, G. F., Delhaye, J. M. and Zuber, N., 1992, Multiphase Science and Technology, Vol. 6, Hemisphere Publishing Corporation.

17. Holmes, B. J. and Allen, E. J., 1998, "A Review of Critical Flow Data for Pressurised Water Reactor Safety Studies," *Multiphase Science and Technology*, Volume 10, pp. 141-302.

18. Ilic, V., Banerjee, S. and Behling, S., 1986, "A Qualified Database for the Critical Flow of Water," EPRI-NP-4556.

19. Kukita, Y., et al., 1991, "Summary of ROSA-IV LSTF first-phase test program – Integral simulation of PWR small-break LOCAs and transients," *Nuclear Engineering and Design*, 131, pp. 101-111.

20. Nissley, M. E., et al., 2005, "Realistic Large Break LOCA Evaluation Methodology Using Automated Statistical Treatment of Uncertainty Method (ASTRUM)," WCAP-16009-P-A, Revision 0, and WCAP-16009-NP-A, Revision 0 (Non-Proprietary).

21. Shimeck, D. J., 1980, "Analysis of Semiscale MOD-3 Small Break Test S-07-10 and S-07-10D," prepared for the U.S. Nuclear Regulatory Commission under Department of Energy Contract No. DE-AC07-761DO1570.

22. Spore, J. W., et al., 2000, "TRAC-M/Fortran 90 (Version 3.0) Theory Manual," LA-UR-00-910.

23. USNRC, 2005, "Transient and Accident Analysis Methods," Regulatory Guide 1.203.

24. Yonomoto, T., et al., 1987, "Onset Criterion for Liquid Entrainment in Reflooding Phase of a LOCA," *J. Nuclear Science and Technology*, 24 [10], pp. 798-810.

25. Young, M.Y. and Bajorek, S.M., 1997, "The Effect of Noncondensables on Condensation in Reactor LOCA Transients," *AICHE SYMPOSIUM SERIES*, Vol. 314, pp 6-13.

Table 2-1 PIRT for Full Spectrum LOCA for Westinghouse and Combustion Engineering Plants

Process											

a,c

Table 2-1 (cont.) PIRT for Full Spectrum LOCA for Westinghouse and Combustion Engineering Plants

a,c

Process											

Table 2-1 (cont.) PIRT for Full Spectrum LOCA for Westinghouse and Combustion Engineering Plants

Process											

a,c

Table 2-1 (cont.) PIRT for Full Spectrum LOCA for Westinghouse and Combustion Engineering Plants

a,c

Process											

Table 2-2 Requirement Assessment Against FSLOCA PIRT: Model Availability and Need

a,c

Table 2-2 (cont.) Requirement Assessment Against FSLOCA PIRT: Model Availability and Need

a,c

Table 2-2 (cont.) Requirement Assessment Against FSLOCA PIRT: Model Availability and Need

a,c

Table 2-2 (cont.) Requirement Assessment Against FSLOCA PIRT: Model Availability and Need

a,c

Table 2-2 (cont.) Requirement Assessment Against FSLOCA PIRT: Model Availability and Need

a,c

Table 2-2 (cont.) Requirement Assessment Against FSLOCA PIRT: Model Availability and Need

a,c

Table 2-2 (cont.) Requirement Assessment Against FSLOCA PIRT: Model Availability and Need

a,c

Table 2-2 (cont.) Requirement Assessment Against FSLOCA PIRT: Model Availability and Need

a,c

Table 2-2 (cont.) Requirement Assessment Against FSLOCA PIRT: Model Availability and Need

a,c

Table 2-2 (cont.) Requirement Assessment Against FSLOCA PIRT: Model Availability and Need

a,c

Table 2-2 (cont.) Requirement Assessment Against FSLOCA PIRT: Model Availability and Need

a,c

Table 2-2 (cont.) Requirement Assessment Against FSLOCA PIRT: Model Availability and Need

a,c

Table 2-2 (cont.) Requirement Assessment Against FSLOCA PIRT: Model Availability and Need

a,c

Table 2-3 V&V Matrix for Large Break LOCA Sub-Scenario, Phases: Blowdown and Refill								
Facility			**Phenomena**					
SET/IET	**Test Feature**	**No. of Tests**	**Critical Flow**	**Break Res.**	**Fuel Rod**	**Heat Transfer**	**ECC Bypass**	**Condensation**
ORNL	Upflow Blowdown cooling, 17x17	3				X		
G-1	Downflow Blowdown cooling, 15x15	6				X		
G-2	Downflow Blowdown cooling, 17x17	4				X		
G-2 Refill	Refill, 17x17	7				X		
Marviken	Full Scale Critical Flow	27	X					
UPTF8	Full Scale, Steam-Water Mixing	7						X
UPTF6	Full Scale, ECCS Bypass, Downcomer Cond.	5		X			X	X
LOFT	Sub Scale Critical Flow Nuclear Rods	4	X	X	X	X	X	X

Table 2-4 V&V Matrix for Large Break LOCA Sub-Scenario, Phases: Reflood and Refill

Facility			Phenomena					
SET/IET	Test Feature	No. of Tests	Heat Transfer	Cond.	N2 Inject.	Fuel Rod	Entrainment De-Entrainment	UP Drain Dist
G2 Reflood	Forced reflood, cosine, 17x17, MVG	3	X				X	
FLECHT LFR	Full Length Emergency Cooling Heat Transfer Tests, Forced reflood, cosine, 15x15	3	X				X	
FLECHT SEASET (Reflood)	FLECHT-Separate Effects and System Effects Tests, Forced reflood, cosine, 17x17	5	X				X	
FLECHT SEASET (Steam Cooling)	FLECHT-Separate Effects and System Effects Tests, Single Phase Vapor, cosine, 17x17	8	X					
FLECHT Skewed	Forced reflood, skewed power, 15x15	5	X				X	
ACHILLES	Gravity Reflood with N2	1	X		X		X	
UPTF29B	Full Scale UP Entrainment	6					X	
UPTF25A	Full Scale DC Entrainment (superheated wall/saturated wall)	4		X			X	
CCTF	Gravity Reflood, Core & UP Entrainment (1/21 scale)	1	X				X	
LOFT	Nuclear Core Scaled (1/48) PWR	4	X	X	X	X	X	

Table 2-5 V&V Matrix for Small Break LOCA Processes, Separate Effect Tests

Small Break Process	Test	Comments
Break Flow	EPRI-NP-4556 +additional Marviken Dataset represents approximately 3200 points from 53 geometries, and 10 facilities, containing data from 13 to 2500 psia. The geometrical range: $0 < L < 2300$ mm, $0.464 < DH < 500$ mm.	Available data appears to span PWR ranges of conditions for break area, upstream subcooling, flow quality. (V. Ilic, S. Banerjee and S. Behling, "A Qualified Database for the Critical Flow of Water," EPRI-NP-4556, May, 1986.)
Mixture Level	ORNL, W G-1& G-2 Boiloff, TPTF, GE Blowdown, Semiscale S-7-10D (SET Mode)	Data covers PWR expected range of pressure and bundle power.
Horizontal Flow Regimes	JAERI-TPTF Tests	Horizontal stratified regime transitions predicted according to Taitel-Dukler map.
Loop Seal Clearance	UPTF Loop Seal Tests	Data covers full scale geometry, provides information for range of Jg that covers PWRs.
Fuel Rod Models: Nuclear Rod Models Heat Transfer	Various sets of test data from LBLOCA, ORNL-THTF (Uncovered Bundle Tests)	Fuel rod models were assessed and quantified for large break. Data representative of SBLOCA conditions.
Pump Performance	Pump Specific Data from LBLOCA	Empirical pump data; assessed for Large Break LOCA.
SI Condensation	COSI Tests, SB-CL-05 (SET Mode)	High pressure SI condensation.
Break Flow, entrainment at Break	TPFL	Single and two-phase critical break flow measurements available. Orientation effect.

Table 2-6 V&V Matrix for Small Break LOCA Processes, Integral Effect Tests		
Small Break Process	**Test**	**Comments**
Break Flow, entrainment at Break	LOFT L3-1, ROSA: 10% CL (side), 5% CL (side), 2.5% CL (side), 2.5% CL (top), 2.5% CL (bottom), 0.5% CL (side)	Single and two-phase critical break flow measurements available. Orientation effect.
Mixture Level	ROSA: 10% CL, 5% CL, 2.5% CL, and 0.5% CL	Range of break sizes. Vessel inventories and system wide mass distributions.
Steam Generator Hydraulics	ROSA NC and SB-CL series.	Provides information on system wide phase separation, primary-secondary heat transfer.
Loop Seal Clearance	ROSA: 10% CL, 5% CL, 2.5% CL, 0.5% CL	Provides information on LSC phenomena.
Fuel Rod Models: Nuclear Rod Models: Heat Transfer:	ROSA SB-CLs	Nuclear rods: No additional tests beyond LB LOCA were examined. Clad heatup & PCTs.
IBLOCAs	ROSA 10%, LOFT L5-1	10% Cold Leg, and a 14 in ACC line Break.

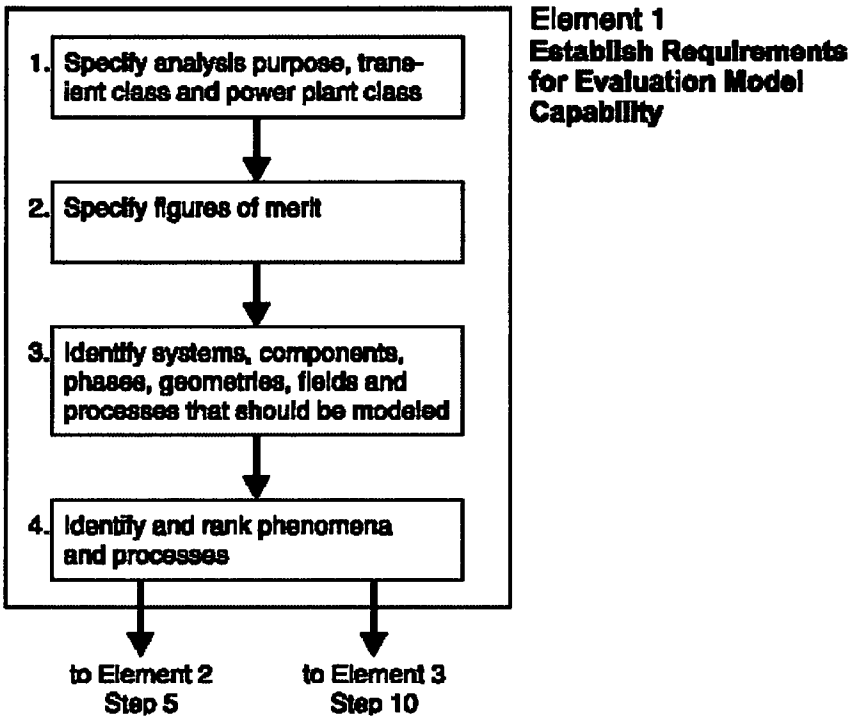

Figure 2-1 EMDAP Element 1 Process

[a,c

]

Figure 2-2 WCOBRA/TRAC-TF2 Code Development Process

[a,c

]

Figure 2-3 [

]a,c

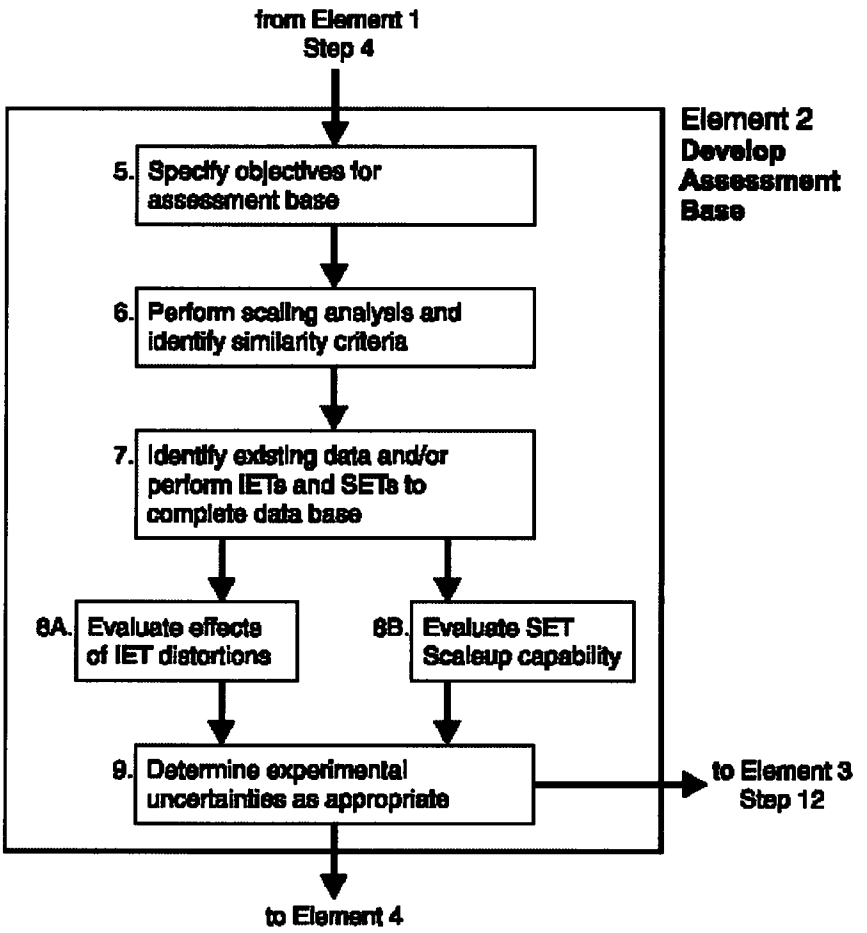

Figure 2-4 EMDAP Element 2

3 WCOBRA/TRAC-TF2 CONSERVATION EQUATIONS

3.1 INTRODUCTION

This section describes the WCOBRA/TRAC-TF2 conservation equations and numerical solution methods for the vessel and one-dimensional components. The governing equations for the vessel and the one-dimensional components use different representations of two-phase flow and are discussed separately. Sections 3.2 and 3.3 describe the conservation equations and the three-dimensional computational cell structure used in the vessel component, while Sections 3.4 and 3.5 discuss the one-dimensional components. The numerical solution methods for the vessel component and the one-dimensional components, the timestep size selection, and convergence criteria are described in Section 3.6.

WCOBRA/TRAC-TF2 uses a two-fluid, three-field representation of flow in the vessel component. The three fields are a combined-gas field (steam and non-condensables), a continuous liquid field and an entrained liquid drop field. Each field in the vessel uses a set of three dimensional continuity, momentum, and energy equations with one exception. A common energy equation is used by both the continuous liquid and the entrained liquid drop fields. An additional continuity equation of the non-condensable gas field completes the equation set.

The one-dimensional components consist of all the major components in the primary system, such as pipes, pumps, valves, steam generators, accumulators, and the pressurizer. The one-dimensional components are represented by a two-phase, two-fluid model. This formulation consists of two equations for the conservation of mass, two equations for the conservation of energy, two equations for the conservation of momentum, and two equations for the conservation of non-condensable gas mass and liquid solute concentration. Closure for the field equations requires specification of the interfacial friction, interfacial heat and mass transfer, and other thermodynamic and constitutive relationships.

3.2 VESSEL COMPONENT CONSERVATION EQUATIONS (MODEL BASIS)

The two-fluid formulation used in the vessel component employs a separate set of conservation equations and constitutive relations for each phase. The effects of one phase on another are accounted for by the interaction terms appearing in the governing equations. The conservation equations have the same form for each phase; only the constitutive relations and physical properties differ. Note that although usually derived for a two-phase flow, the two-fluid formulation can be readily extended to multi-phase flow.

This section describes the development of the two-fluid, three-field conservation equations solved in the vessel component of WCOBRA/TRAC-TF2. The two-fluid phasic conservation equations are presented in Section 3.2.1 along with the physical assumptions necessary to obtain them. Expressions representing the three-field conservation equations are presented in Section 3.2.2.

3.2.1 Three-Field Equation Formulation

The three-field formulation used in the vessel component of WCOBRA/TRAC-TF2 is a straightforward extension of the two-fluid model. The fields included are combined-gas, continuous liquid, and entrained liquid. Dividing the liquid phase into two fields is the most convenient and physically reasonable way of

handling flows where the liquid can appear in both film and droplet form. In such flows, the motion of the droplets can be quite different from the motion of the film, so a single set of average liquid phase equations cannot adequately describe the liquid flow or the interaction between liquid and combined-gas.

The average conservation equations used in the vessel module of WCOBRA/TRAC-TF2 are derived following the methods of Ishii (1977). The average used is a simple Eulerian time average over a time, assumed to be long enough to smooth out the random fluctuations present in a multiphase flow, but short enough to preserve any global unsteadiness in the flow. The resulting average equations can be cast in either the mixture form or the two-fluid form. Because of its greater physical appeal and broader range of application, the two-fluid approach is used as the foundation for WCOBRA/TRAC-TF2.

The phasic conservation equations in their most general form describe the time-averaged behavior of phase k, which can be any phase in a multiphase flow. The averaging process used to obtain these equations is based on the work of Ishii (1977). A detailed description of this averaging process for the COBRA/TRAC code is presented in Appendix A of Thurgood et al. (1983), and is not repeated here. The generalized phasic conservation equations are as follows:

Conservation of Mass

$$\frac{\partial}{\partial t}(\alpha_k \rho_k) + \nabla \cdot (\alpha_k \rho_k \underline{u}_k) = \Gamma_k''' \tag{3-1}$$

Conservation of Momentum

$$\frac{\partial}{\partial t}(\alpha_k \rho_k \underline{u}_k) + \nabla \cdot (\alpha_k \rho_k \underline{u}_k \underline{u}_k) = -\alpha_k \nabla P + \alpha_k \rho_k \underline{g} + \nabla \cdot \left[\alpha_k \left(\underline{\underline{\sigma}}_k + \underline{\underline{T}}_k^T\right)\right] + \underline{M}_k^d + \underline{M}_k^\Gamma \tag{3-2}$$

Conservation of Energy

$$\frac{\partial}{\partial t}(\alpha_k \rho_k H_k) + \nabla \cdot (\alpha_k \rho_k H_k \underline{u}_k) = -\nabla \cdot \left[\alpha_k \left(\underline{q}_k + \underline{q}_k^T\right)\right] + \Gamma_k''' H_k^i + q_{i,k}''' + \alpha_k \frac{\partial P}{\partial t} \tag{3-3}$$

where the terms are defined as:

α_k	=	average k-phase void fraction
ρ_k	=	average k-phase density
$\underline{u}_k$	=	average k-phase velocity vector
Γ_k'''	=	average rate of mass transfer to phase k from the other phases
$\underline{g}$	=	acceleration of gravity vector
P	=	average pressure
$\underline{\underline{\sigma}}_k$	=	average k-phase viscous stress tensor (stress deviator)
$\underline{\underline{T}}_k^T$	=	k-phase turbulent (Reynolds) stress tensor
$\underline{M}_k^\Gamma$	=	average supply of momentum to phase k due to mass transfer to phase k

$\underline{M}_k^d$ = average drag force on phase k by the other phases

H_k = average k-phase enthalpy

H_k^i = enthalpy of phase k associated with interfacial mass transfer

$\underline{q}_k$ = average k-phase conduction vector

$\underline{q}_k^T$ = k-phase turbulent heat flux vector

$q_{i,k}'''$ = heat flow to k-phase

The generalized phasic conservation equations considered for the vessel component assume that:

1. Gravity is the only body force.
2. There is no volumetric heat generation in the fluid.
3. The total pressure is the same in all phases.
4. Internal dissipation can be neglected in the energy equation.
5. $\alpha_k \frac{DP}{Dt}$ may be approximated by $\alpha_k \frac{\partial P}{\partial t}$ in the energy equation. ($\alpha_k u_k \nabla P$ is negligible in the vessel region.)

While the third assumption simplifies the conservation equations considerably, it does limit their applicability. The fifth simplification was made for the Vessel component where the pressure gradient term can be neglected[1]. For situations typical of those expected in large and small break loss-of-coolant accidents, these assumptions are justified.

3.2.2 Vessel Component Three-Field Conservation Equations

The WCOBRA/TRAC-TF2 vessel component uses a three-field representation of a two-fluid flow. The three-field conservation equation formulation uses four continuity equations, including the non-condensable gas field, three momentum equations, and two energy equations. (The continuous liquid and the entrained liquid fields are assumed to be in thermal equilibrium, which eliminates one of the energy equations.) The equations for each field are obtained directly from Equations 3-1 through 3-3 by introducing the three-field notation and several simplifying assumptions.

The subscripts gas, ℓ, and e refer to the combined-gas which includes steam and non-condensable gas, continuous liquid, and entrained liquid fields, respectively. The three fields are coupled by the combined-gas generation and entrainment rate terms. The term Γ''' represents the average rate of vapor generation per unit volume. Since both liquid fields contribute to the vapor generation rate, Γ''' can be expressed as,

$$\Gamma''' = \Gamma_\ell''' + \Gamma_e''' \tag{3-4}$$

1. Justification for this simplification can be found in SQ.6, pages 34-40 of RAIS, Appendix-C, Part 4 of WCAP-12945-P-A (Bajorek, 1998).

If η^2 denotes the fraction of total vapor generation coming from the entrained liquid field, then $\Gamma_e''' = \eta\Gamma'''$ and $\Gamma_\ell''' = (1-\eta)\Gamma'''$.

In addition to phase change, the two liquid fields also exchange mass by entrainment. Let S_{ent}''' represent the average net rate of entrainment per unit volume. With the definitions for S_{ent}''' and η, the mass transfer terms can be written as:

$$\Gamma_{gas}''' = \Gamma''' \tag{3-5}$$

$$\Gamma_\ell = -\Gamma_\ell''' - S_{ent}''' = -(1-\eta)\,\Gamma''' - S_{ent}''' \tag{3-6}$$

$$\Gamma_e = -\Gamma_e''' + S_{ent}''' = -\eta\,\Gamma''' + S_{ent}''' \tag{3-7}$$

The terms $\underline{M}_{gas}^d$, $\underline{M}_\ell^d$, and $\underline{M}_e^d$ represent the momentum exchange at the interface. These interfacial momentum terms can be expressed as:

$$\underline{M}_{gas}^d = -\underline{\tau}_{i,g\ell}''' - \underline{\tau}_{i,ge}''' \tag{3-8}$$

$$\underline{M}_\ell^d = \underline{\tau}_{i,g\ell}''' \tag{3-9}$$

$$\underline{M}_e^d = \underline{\tau}_{i,ge}''' \tag{3-10}$$

where:

$\underline{\tau}_{i,g\ell}'''$ is the average drag force per unit volume by the combined-gas on the continuous liquid,

and

$\underline{\tau}_{i,ge}'''$ is the average drag force per unit volume by the combined-gas on the entrained liquid.

The momentum exchange due to mass transfer between the three fields can be written as,

$$\underline{M}_{gas}^\Gamma = (\Gamma_e'''\,\underline{U}_\Gamma) + (\Gamma_\ell'''\,\underline{U}_\Gamma) = \Gamma'''\,\underline{U}_\Gamma \tag{3-11}$$

$$\underline{M}_\ell^\Gamma = -(\Gamma_\ell'''\,\underline{U}_\Gamma) - (S_{ent}'''\,\underline{U}_{Se}) = -(1-\eta)\Gamma'''\,\underline{U}_\Gamma - S_{ent}'''\,\underline{U}_{Se} \tag{3-12}$$

$$\underline{M}_e^\Gamma = -(\Gamma_e'''\,\underline{U}_\Gamma) + (S_{ent}'''\,\underline{U}_{Se}) = -\eta\Gamma'''\,\underline{U}_\Gamma + S_{ent}'''\,\underline{U}_{Se} \tag{3-13}$$

2. RAI1-13 (Bajorek, 1998)

Note also that the velocities associated with the mass transfer rate are the phase velocities of the source. If, for example, $\Gamma'''_\ell > 0$ (evaporation), $U_\Gamma = U_\ell$. Otherwise (condensation), $U_\Gamma = U_{gas}$. U_{Se} is the velocity associated with the entrainment source. Similarly, if $S'''_{ent} > 0$ (entrainment), $U_{Se} = U_\ell$. Otherwise (de-entrainment), $U_{Se} = U_e$. The underscore implies that these velocities are vectors. In the following momentum equations, this convention will be used.

Note that $\underline{M}^\Gamma_{gas}$ is due only to mass transfer from vapor generation, but $\underline{M}^\Gamma_\ell$ and $\underline{M}^\Gamma_e$ are due to both vapor generation and entrainment.

Three-Field Model Assumptions

The following assumptions are used to obtain the WCOBRA/TRAC-TF2 vessel component three-field conservation Equations 3-1 through 3-3:

1. The turbulent stresses and the turbulent heat flux of the entrained phase are neglected. Thus,

$$\underline{\underline{T}}^T_e = 0$$
$$\underline{q}^T_e = 0 \qquad (3\text{-}14)$$

2. Viscous stresses can be partitioned into wall shear and fluid-fluid shear, and fluid-fluid shear can be neglected in the entrained liquid phase. With this assumption,

$$\nabla \bullet (\alpha_e \underline{\underline{\tau}}_e) = \underline{\tau}'''_{w,e}$$
$$\nabla \bullet (\alpha_{gas} \underline{\underline{\tau}}_{gas}) = \underline{\tau}'''_{w,gas} + \nabla \bullet (\alpha_{gas} \underline{\underline{\sigma}}_{gas}) \qquad (3\text{-}15)$$
$$\nabla \bullet (\alpha_\ell \underline{\underline{\tau}}_\ell) = \underline{\tau}'''_{w,\ell} + \nabla \bullet (\alpha_\ell \underline{\underline{\sigma}}_\ell)$$

The force tensors exerted on the entrained liquid, combined gas, and continuous liquid are $\underline{\underline{\tau}}_e$, $\underline{\underline{\tau}}_{gas}$, and $\underline{\underline{\tau}}_\ell$, respectively.

Forces exerted by the wall on the combined-gas, entrained liquid, and continuous liquid are $\underline{\tau}'''_{w,gas}$, $\underline{\tau}'''_{w,e}$, and $\underline{\tau}'''_{w,\ell}$, respectively.

The fluid-fluid viscous stress tensors are $\underline{\underline{\sigma}}_{gas}$ and $\underline{\underline{\sigma}}_\ell$.

3. The conduction heat flux can be partitioned into a wall term and a fluid-fluid conduction term. The latter is assumed to be negligible in the entrained liquid. Thus,

$$-\nabla \bullet \left(\alpha_{gas} \underline{Q}_{gas}\right) = -\nabla \bullet \left(\alpha_{gas} \underline{q}_{gas}\right) + Q'''_{wgas}$$

$$-\nabla \bullet (\alpha_e \underline{Q}_e + \alpha_\ell \underline{Q}_\ell) = -\nabla \bullet (\alpha_\ell \underline{q}_\ell) + Q'''_{w\ell} \quad (3\text{-}16)$$

Where Q'''_{wgas} and $Q'''_{w\ell}$ are the wall heat transfer rates per unit volume to the vapor and liquid, respectively; $\underline{q}_\ell$ is the fluid-fluid conduction vector for the continuous liquid; and $\underline{q}_{gas}$ is the fluid-fluid conduction vector for the vapor. Additionally, $\underline{Q}_{gas}$, $\underline{Q}_e$, and $\underline{Q}_\ell$ are the heat transfer vectors for vapor, entrained liquid, and continuous liquid, respectively.

4. All mass moving to the phase interface is at its bulk phasic enthalpy while mass leaving the phase interface is at its saturation (H_g or H_f). Therefore,

$$H^i_{gas} = \begin{cases} H_g(P_{steam}) & \text{or} \\ H_v \end{cases}$$

$$H^i_\ell = \begin{cases} H_f(P) & \text{or} \\ H_\ell \end{cases} \quad (3\text{-}17)$$

5. Non-condensable gas is in thermal and mechanical equilibrium with steam.

The three-field conservation equations used in the WCOBRA/TRAC-TF2 vessel component are arrived at by substituting the definitions (3-5) through (3-13) and assumptions (3-14) through (3-17) into Equations 3-1, 3-2, and 3-3. The resulting expressions for conservation of mass, momentum, and energy are listed in Sections 3.2.2.1, 3.2.2.2, and 3.2.2.3.

3.2.2.1 Conservation of Mass

Combined-Gas Field

$$\frac{\partial}{\partial t}\left(\alpha_{gas}\rho_{gas}\right) + \nabla \cdot \left(\alpha_{gas}\rho_{gas}\underline{U}_{gas}\right) = \Gamma''' \quad (3\text{-}18)$$

Continuous Liquid Field

$$\frac{\partial}{\partial t}(\alpha_\ell \rho_\ell) + \nabla \cdot (\alpha_\ell \rho_\ell \underline{U}_\ell) = -\Gamma'''_\ell - S'''_{ent} = -(1-\eta)\Gamma''' - S'''_{ent} \quad (3\text{-}19)$$

Entrained Liquid Field

$$\frac{\partial}{\partial t}(\alpha_e \rho_\ell) + \nabla \cdot (\alpha_e \rho_\ell \underline{U}_e) = -\Gamma'''_e + S'''_{ent} = -\eta\Gamma''' + S'''_{ent} \tag{3-20}$$

Non-Condensable Gas Field

$$\frac{\partial}{\partial t}(\alpha_{gas} \rho_{NC}) + \nabla \cdot (\alpha_{gas} \rho_{NC} \underline{U}_{gas}) = 0. \tag{3-21}$$

3.2.2.2 Conservation of Momentum

Combined-Gas Field

$$\begin{aligned}\frac{\partial}{\partial t}(\alpha_{gas} \rho_{gas} \underline{U}_{gas}) + \nabla \cdot (\alpha_{gas} \rho_{gas} \underline{U}_{gas} \underline{U}_{gas}) = -\alpha_{gas} \nabla P + \alpha_{gas} \rho_{gas} \underline{g} + \nabla \cdot \left[\alpha_{gas} (\underline{\underline{\sigma}}_{gas})\right] \\ - \underline{\tau}'''_{w,gas} - \underline{\tau}'''_{i,g\ell} - \underline{\tau}'''_{i,ge} + \Gamma''' \underline{U}_\Gamma\end{aligned} \tag{3-22}$$

Where $\underline{\tau}'''_{w,gas}$, $\underline{\tau}'''_{i,g\ell}$, and $\underline{\tau}'''_{i,ge}$ are the force exerted by the wall on combined gas, the interfacial force between the gas and continuous liquid, and the interfacial force between gas and entrained droplet, respectively.

Continuous Liquid Field

$$\begin{aligned}\frac{\partial}{\partial t}(\alpha_\ell \rho_\ell \underline{U}_\ell) + \nabla \cdot (\alpha_\ell \rho_\ell \underline{U}_\ell \underline{U}_\ell) = -\alpha_\ell \nabla P + \alpha_\ell \rho_\ell \underline{g} \\ + \nabla \cdot [\alpha_\ell (\underline{\underline{\sigma}}_\ell)] - \underline{\tau}'''_{w,\ell} + \underline{\tau}'''_{i,g\ell} - (1-\eta)\Gamma''' \underline{U}_\Gamma - (S'''_{ent} \underline{U}_{Se})\end{aligned} \tag{3-23}$$

Entrained Liquid Field

$$\begin{aligned}\frac{\partial}{\partial t}(\alpha_e \rho_\ell \underline{U}_e) + \nabla \cdot (\alpha_e \rho_\ell \underline{U}_e \underline{U}_e) = -\alpha_e \nabla P + \alpha_e \rho_\ell \underline{g} - \underline{\tau}'''_{w,e} \\ + \underline{\tau}'''_{i,ge} - \eta\Gamma''' \underline{U}_\Gamma + (S'''_{ent} \underline{U}_{Se})\end{aligned} \tag{3-24}$$

3.2.2.3 Conservation of Energy

Combined-Gas Field

$$\begin{aligned}\frac{\partial}{\partial t}(\alpha_{gas} \rho_{gas} H_{gas}) + \nabla \cdot (\alpha_{gas} \rho_{gas} H_{gas} \underline{U}_{gas}) = -\nabla \cdot \left[\alpha_{gas} (\underline{q}_{gas})\right] + \Gamma''' H^i_{gas} \\ + q'''_{i,gas} + q'''_{\ell,NC} + Q'''_{w,gas} + \alpha_{gas} \frac{\partial P}{\partial t}\end{aligned} \tag{3-25}$$

Liquid Fields

$$\frac{\partial}{\partial t}\left[(\alpha_\ell+\alpha_e)\rho_\ell H_\ell\right]+\nabla\cdot\left(\alpha_\ell\rho_\ell H_\ell \underline{U}_\ell\right)+\nabla\cdot\left(\alpha_e\rho_\ell H_\ell \underline{U}_e\right)$$
$$=-\nabla\cdot\left[\alpha_\ell\left(\underline{q}_\ell+\underline{q}_\ell^{T}\right)\right]-\Gamma'''H_\ell^i+q_{i,\ell}'''-q_{\ell,NC}'''+Q_{w,\ell}'''+(\alpha_\ell+\alpha_e)\frac{\partial P}{\partial t} \quad (3\text{-}26)$$

$q_{\ell,NC}'''$ is the heat transfer between liquid and the non-condensable gas.

The use of a single energy equation for the combined continuous liquid and liquid droplet fields means that both fields are assumed to be at the same temperature. In regions where both liquid droplets and liquid films are present, this can be justified in view of the large rate of mass transfer between the two fields, which will tend to draw both to the same temperature.

3.2.3 Subchannel Coordinate Formulation

The vessel component in WCOBRA/TRAC-TF2 is represented with a subchannel coordinate system. Because of its greater adaptability, the subchannel formulation is often selected over the Cartesian formulation when modeling complex or irregular geometries. The subchannel approach is typically used for rod bundle thermal-hydraulic analysis. Fixed transverse coordinates are not used in the subchannel formulation. Instead, all transverse or lateral flows are assumed to occur through "gaps." Thus, one transverse momentum equation applies to all gaps regardless of the gap orientation. This reduces the number of component momentum equations to only two; vertical and transverse.

The capability to include the fluid-to-fluid conduction vectors, $\nabla\cdot\left[\alpha_k\left(\underline{q}_k\right)\right]$, and viscous stress terms, $\nabla\cdot[\alpha_k(\underline{\underline{\sigma}}_k)]$ is programmed into WCOBRA/TRAC-TF2. [

]^{a,c} In the subchannel coordinate system, x is the axial coordinate and u is the velocity in that direction. The transverse (or lateral) direction is denoted by z, and w is the velocity of the lateral flow.

Combined-Gas Conservation of Mass

$$\frac{\partial}{\partial t}\left(\alpha_{gas}\rho_{gas}A_x\right)+\frac{\partial}{\partial x}\left(\alpha_{gas}\rho_{gas}u_{gas}A_x\right)-\sum_k\left(\alpha_{gas}\rho_{gas}w_{gas}L_g\right)_k=\Gamma'''A_x \quad (3\text{-}27)$$

Continuous Liquid Conservation of Mass

$$\frac{\partial}{\partial t}\left(\alpha_\ell \rho_\ell A_x\right)+\frac{\partial}{\partial x}\left(\alpha_\ell \rho_\ell u_\ell A_x\right)-\sum_k\left(\alpha_\ell \rho_\ell w_\ell L_g\right)_k=-(1-\eta)\Gamma'''A_x-S'''_{ent}A_x \tag{3-28}$$

Entrained Liquid Conservation of Mass

$$\frac{\partial}{\partial t}\left(\alpha_e \rho_\ell A_x\right)+\frac{\partial}{\partial x}\left(\alpha_e \rho_\ell u_e A_x\right)-\sum_k\left(\alpha_e \rho_\ell w_e L_g\right)_k=-\eta\Gamma'''A_x+S'''_{ent}A_x \tag{3-29}$$

Non-Condensable Gas Conservation of Mass

$$\frac{\partial}{\partial t}\left(\alpha_{gas} \rho_{NC} A_x\right)+\frac{\partial}{\partial x}\left(\alpha_{gas} \rho_{NC} u_{gas} A_x\right)-\sum_k\left(\alpha_{gas} \rho_{NC} w_{gas} L_g\right)_k=0. \tag{3-30}$$

Note that the combined-gas velocity components in Equation 3-30 are equal to the steam vapor velocity components, because the steam vapor and the non-condensable gas are assumed to be in mechanical equilibrium:

$$\begin{aligned} u_{gas} &= u_v \\ w_{gas} &= w_v \end{aligned} \tag{3-31}$$

Additionally, the axial and transverse velocities associated with the mass transfer process will be defined as,

$$\underline{U}_\Gamma=\begin{Bmatrix} u_\Gamma \\ w_\Gamma \end{Bmatrix} \text{ and, } \underline{U}_{Se}=\begin{Bmatrix} u_{Se} \\ w_{Se} \end{Bmatrix}$$

Combined-Gas Conservation of Momentum

Vertical Momentum

$$\begin{aligned} &\frac{\partial}{\partial t}\left(\alpha_{gas} \rho_{gas} u_{gas} A_x\right)+\frac{\partial}{\partial x}\left(\alpha_{gas} \rho_{gas} u_{gas} u_{gas} A_x\right)-\sum_k\left(\alpha_{gas} \rho_{gas} u_{gas} w_{gas} \frac{L_g}{2}\right)_k \\ &=-\alpha_{gas}\frac{\partial P}{\partial x}A_x-\alpha_{gas}\rho_{gas} g A_x-\tau'''_{x,w,gas}A_x-\tau'''_{x,i,g\ell}A_x-\tau'''_{x,i,ge}A_x+\Gamma''' u_\Gamma A_x \end{aligned} \tag{3-32}$$

Transverse Momentum

$$\frac{\partial}{\partial t}\left(\alpha_{gas}\rho_{gas}w_{gas}A_z\right)+\frac{\partial}{\partial z}\left(\alpha_{gas}\rho_{gas}w_{gas}w_{gas}A_z\right)+\frac{\partial}{\partial x}\left(\alpha_{gas}\rho_{gas}w_{gas}u_{gas}A_z\right)$$
$$-\frac{\Delta x}{\Delta z}\sum_{k^\circ}\left(\alpha_{gas}\rho_{gas}w_{gas}w^{o}_{gas}\frac{L^{o}_{g}}{2}\right)_{k^\circ} \qquad (3\text{-}33)$$
$$=-\alpha_{gas}\frac{\partial P}{\partial z}A_z-\tau'''_{z,w,gas}A_z-\tau'''_{z,i,g\ell}A_z-\tau'''_{z,i,ge}A_z+\Gamma'''w_\Gamma A_z$$

Continuous Liquid Conservation of Momentum

Vertical Momentum

$$\frac{\partial}{\partial t}\left(\alpha_\ell\rho_\ell u_\ell A_x\right)+\frac{\partial}{\partial x}\left(\alpha_\ell\rho_\ell u_\ell u_\ell A_x\right)-\sum_k\left(\alpha_\ell\rho_\ell u_\ell w_\ell\frac{L_g}{2}\right)_k=-\alpha_\ell A_x\frac{\partial P}{\partial x}-\alpha_\ell\rho_\ell A_x g \qquad (3\text{-}34)$$
$$-\tau'''_{x,w\ell}A_x+\tau'''_{x,v\ell}A_x-(1-\eta)\Gamma'''u_\Gamma A_x-S'''_{ent}u_{Se}A_x$$

Transverse Momentum

$$\frac{\partial}{\partial t}\left(\alpha_\ell\rho_\ell w_\ell A_z\right)+\frac{\partial}{\partial z}\left(\alpha_\ell\rho_\ell w_\ell w_\ell A_z\right)+\frac{\partial}{\partial x}\left(\alpha_\ell\rho_\ell w_\ell u_\ell A_z\right)-\frac{\Delta x}{\Delta z}\sum_{k^\circ}\left(\alpha_\ell\rho_\ell w_\ell w^{o}_{\ell}\frac{L^{o}_{g}}{2}\right)_{k^\circ}= \qquad (3\text{-}35)$$
$$-\alpha_\ell A_z\frac{\partial P}{\partial z}-\tau'''_{z,w\ell}A_z+\tau'''_{z,g\ell}A_z-(1-\eta)\Gamma'''w_\Gamma A_Z-S'''_{ent}w_{Se}A_Z$$

Entrained Liquid Conservation of Momentum

Vertical Momentum

$$\frac{\partial}{\partial t}\left(\alpha_e\rho_\ell u_e A_x\right)+\frac{\partial}{\partial x}\left(\alpha_e\rho_\ell u_e u_e A_x\right)-\sum_k\left(\alpha_e\rho_\ell u_e w_e\frac{L_g}{2}\right)_k=-\alpha_e\rho_\ell A_x g$$
$$-\alpha_e A_x\frac{\partial P}{\partial x}-\tau'''_{x,we}A_x+\tau'''_{x,ve}A_x-\eta\Gamma'''u_\Gamma A_x+S'''_{ent}u_{Se}A_x \qquad (3\text{-}36)$$

Transverse Momentum

$$\frac{\partial}{\partial t}\left(\alpha_e\rho_\ell w_e A_z\right)+\frac{\partial}{\partial z}\left(\alpha_e\rho_\ell w_e w_e A_z\right)+\frac{\partial}{\partial x}\left(\alpha_e\rho_\ell w_e u_e A_z\right)-\frac{\Delta x}{\Delta z}\sum_{k^\circ}\left(\alpha_e\rho_\ell w_e w^{o}_{e}\frac{L^{o}_{g}}{2}\right)_{k^\circ}= \qquad (3\text{-}37)$$
$$-\alpha_e A_z\frac{\partial P}{\partial z}-\tau'''_{z,we}A_z+\tau'''_{z,ve}A_z-\eta\Gamma'''w_\Gamma A_Z+S'''_{ent}w_{Se}A_Z$$

Combined-Gas Conservation of Energy

$$\frac{\partial}{\partial t}\left(\alpha_{gas}\rho_{gas}H_{gas}A_x\right)+\frac{\partial}{\partial x}\left(\alpha_{gas}\rho_{gas}H_{gas}u_{gas}A_x\right)-\sum_k\left(\alpha_{gas}\rho_{gas}H_{gas}w_{gas}L_g\right)_k$$
$$=\Gamma'''H^i_{gas}A_x+q'''_{i,gas}A_x+q'''_{\ell,NC}A_x+Q'''_{w,gas}A_x+\alpha_{gas}\frac{\partial P}{\partial t}A_x \quad (3\text{-}38)$$

Liquid Conservation of Energy

$$\frac{\partial}{\partial t}\left[(\alpha_\ell+\alpha_e)\rho_\ell H_\ell A_x\right]+\frac{\partial}{\partial x}\left(\alpha_\ell\rho_\ell H_\ell u_\ell A_x\right)+\frac{\partial}{\partial x}\left(\alpha_e\rho_\ell H_\ell u_e A_x\right)$$
$$-\sum_k\left(\alpha_\ell\rho_\ell H_\ell w_\ell L_g\right)_k-\sum_k\left(\alpha_e\rho_\ell H_\ell w_e L_g\right)_k \quad (3\text{-}39)$$
$$=-\Gamma'''H^i_\ell A_x+q'''_{i,\ell}A_x-q'''_{\ell,NC}A_x+Q'''_{w,\ell}A_x+(\alpha_\ell+\alpha_e)\frac{\partial P}{\partial t}A_x$$

The following notation has been used in the subchannel equations:

u	=	vertical velocity
w	=	transverse velocity
u_Γ	=	vertical velocity associated with evaporation and condensation
w_Γ	=	transverse velocity associated with evaporation and condensation
u_{Se}	=	vertical velocity associated with entrainment and de-entrainment
w_{Se}	=	transverse velocity associated with entrainment and de-entrainment
w^o	=	orthogonal gap velocity
A_x	=	axial flow area of subchannel
A_z	=	transverse flow area of gap ($= L_g\Delta X$)
L_g	=	gap width
L^o_g	=	orthogonal gap width
x	=	axial coordinate
z	=	transverse coordinate

Subscript k refers to gap k
Subscript k^o refers to orthogonal gap k^o

3.3 VESSEL COMPONENT COMPUTATIONAL CELL STRUCTURE (MODEL AS CODED)

3.3.1 Introduction

The three-field conservation equations for multidimensional flow in the vessel component are presented in Section 3.2. Sections 4 through 11 of this document provide a description of the physical models required for their closure. The finite-difference form of these equations is presented here, and the term by term correspondence between the conservation equations and the finite-difference equations is identified.

The finite-difference equations are written in a semi-implicit form using donor cell differencing for the convected quantities. Since a semi-implicit form is used, the timestep, Δt, is limited by the material Courant limit.

$$\Delta t < \left| \frac{\Delta X}{U} \right| \tag{3-40}$$

where ΔX is the mesh spacing and U is the fluid velocity.

Section 3.6.5.3 provides a description of the WCOBRA/TRAC-TF2 timestep size control and convergence criteria.

The finite-difference equations are written such that they may be solved on Cartesian coordinates or using the subchannel formulation in which some of the convective terms in the transverse momentum equations are neglected and idealistic assumptions are made concerning the shape of the transverse momentum control volumes.

The computational mesh and finite-difference equations are described using the generalized subchannel notations. These equations are equivalent to the three-dimensional Cartesian equations when the limiting assumptions of the subchannel formulation are not used and the mesh is arranged on a rectangular grid (Figure 3-1).

3.3.2 Vessel Component Computational Mesh

The equations are solved using a staggered-difference scheme where the velocities are obtained at the mesh cell faces and the state variables, such as pressure, density, enthalpy, and void fraction, are obtained at the cell center. The mesh cell is characterized by its axial cross-sectional area, A_X, its height, ΔX, and the width of its connection with adjacent mesh cells, L_g. The basic mesh cell is shown in Figure 3-2. The basic mesh cell may be used to model any one, two, or three-dimensional region. The dimensionality of the flow is dependent upon the number of faces on the cell that connect with adjacent mesh cells.

The size of a mesh cell used to model the flow field inside of a reactor vessel is generally quite large because the volume of the reactor vessel is very large and the cost of using a fine mesh in solving the two-fluid equations for the whole vessel would be prohibitive. However, many important flow paths and flow phenomena may be overlooked when a large mesh size is used in some areas of the vessel. This can be minimized by allowing a variable mesh size within the vessel. A finer mesh can be used in areas where

a more detailed calculation of the flow field is required. The vessel component has been set up to allow such a variable mesh size. The variable mesh is formed by connecting two or more cells to any or all of the faces of a mesh cell, as illustrated in Figure 3-3. A single mesh cell with area A_1 is shown connected to four mesh cells above it with areas A_2, A_3, etc. These four mesh cells may connect through transverse connections L_2, L_3, etc., to allow transverse flow in that region, or they may not connect to each other forming one or more one-dimensional flow paths that connect to mesh cell 1.

The mesh cells shown in Figure 3-2 and Figure 3-3 represent the mesh for the scalar continuity and energy equations. The momentum equations are solved on a staggered mesh where the momentum cell is centered on the scalar mesh cell boundary. The mesh cells for vertical and transverse velocities are shown in Figure 3-4 and Figure 3-5, respectively.

The vertical velocities are subscripted with I and j, where I (channel index) identifies the location of the mesh cell within the horizontal plane and j (level index) identifies its vertical location. The mesh cells for the scalar equations carry the same subscripts, but their mesh cell centers lie a distance $(\Delta X_J)/2$ below the mesh cell center for the correspondingly subscripted velocity and are denoted by the capital letter J in the discussion below. Thus the height of momentum cell-j, $\Delta X_j=(\Delta X_{J+1}+\Delta X_J)/2$.

Transverse velocities are subscripted with k and J where k (gap index) identifies the location of the mesh cell in the horizontal plane and J identifies its vertical location. The node centers for the scalar equations and transverse momentum equations lie in the same horizontal plane.

The finite-difference equations are written using this subscripting convention based on the mesh as defined above.

3.3.3 Vessel Component Finite-Difference Equations

The finite-difference equations follow. Quantities that are evaluated at the old time carry the superscript n. Donor cell quantities that have the superscript $\tilde{n}$ are evaluated at the old time, and form the explicit portions of the equations. The new-time values have the superscript n+1. Velocities with tilde, "~", indicate that they are tentative velocities obtained by solving the momentum equations and are discussed in Section 3.6.2.1. Note that mass and energy equations are written in the form of residual errors. The corresponding term in the conservation equation for each term in the finite-difference equation is provided in the brackets below each equation, along with a verbal description of the term. The subscripts I (channel index) and k (gap index) are assumed to be obvious and are not shown.

3.3.3.1 Conservation of Mass Equations

The channel index "I" is implied in the following continuity equations.

Combined-Gas Mass Equation

$$E_{c,gas,J}^{n+1} = \frac{\Delta x_J A_{c,J}}{\Delta t}\left[\left(\alpha_{gas}\rho_{gas}\right)_J^{n+1} - \left(\alpha_{gas}\rho_{gas}\right)_J^{n}\right] + \sum_{KA=1}^{NA}\left[\left(\alpha_{gas}\rho_{gas}\right)_{KA}^{\tilde{n}} \tilde{u}_{gas,KA}^{n+1} A_{m,KA}\right] - \sum_{KB=1}^{NB}\left[\left(\alpha_{gas}\rho_{gas}\right)_{KB}^{\tilde{n}} \tilde{u}_{gas,KB}^{n+1} A_{m,KB}\right] - \Delta x_J \sum_{KL=1}^{NKK}\left[L_{KL}\left(\alpha_g\rho_g\right)_{J,KL}^{\tilde{n}} \tilde{w}_{gas,KL}^{n+1}\right] - \Gamma_J^{n+1} - S_{c,gas,J}^{n+1} \quad (3\text{-}41)$$

Liquid Mass Equation

$$E_{c,\ell,J}^{n+1} = \frac{\Delta x_J A_{c,J}}{\Delta t}\left[\left(\alpha_\ell\rho_\ell\right)_J^{n+1} - \left(\alpha_\ell\rho_\ell\right)_J^{n}\right] + \sum_{KA=1}^{NA}\left[\left(\alpha_\ell\rho_\ell\right)_{KA}^{\tilde{n}} \tilde{u}_{\ell,KA}^{n+1} A_{m,KA}\right] - \sum_{KB=1}^{NB}\left[\left(\alpha_\ell\rho_\ell\right)_{KB}^{\tilde{n}} \tilde{u}_{\ell,KB}^{n+1} A_{m,KB}\right] - \Delta x_J \sum_{KL=1}^{NKK}\left[L_{KL}\left(\alpha_\ell\rho_\ell\right)_{J,KL}^{\tilde{n}} \tilde{w}_{\ell,KL}^{n+1}\right] + (1-\eta)\Gamma_J^{n+1} + S_{ent,J}^{n} - S_{c,\ell,J}^{n+1} \quad (3\text{-}42)$$

Entrained Liquid Mass Equation

$$E_{c,e,J}^{n+1} = \frac{\Delta x_J A_{c,J}}{\Delta t}\left[\left(\alpha_e\rho_\ell\right)_J^{n+1} - \left(\alpha_e\rho_\ell\right)_J^{n}\right] + \sum_{KA=1}^{NA}\left[\left(\alpha_e\rho_\ell\right)_{KA}^{\tilde{n}} \tilde{u}_{e,KA}^{n+1} A_{m,KA}\right] - \sum_{KB=1}^{NB}\left[\left(\alpha_e\rho_\ell\right)_{KB}^{\tilde{n}} \tilde{u}_{e,KB}^{n+1} A_{m,KB}\right] - \Delta x_J \sum_{KL=1}^{NKK}\left[L_{KL}\left(\alpha_e\rho_\ell\right)_{J,KL}^{\tilde{n}} \tilde{w}_{e,KL}^{n+1}\right] + \eta\Gamma_J^{n+1} - S_{ent,J}^{n} - S_{c,\ell,J}^{n+1} \quad (3\text{-}43)$$

Non-Condensable Mass Equation

$$E_{c,NC,J}^{n+1} = \frac{\Delta x_J A_{c,J}}{\Delta t}\left[\left(\alpha_{gas}\rho_{NC}\right)_J^{n+1} - \left(\alpha_{gas}\rho_{NC}\right)_J^{n}\right] + \sum_{KA=1}^{NA}\left[\left(\alpha_{gas}\rho_{NC}\right)_{KA}^{\tilde{n}} \tilde{u}_{gas,KA}^{n+1} A_{m,KA}\right] - \sum_{KB=1}^{NB}\left[\left(\alpha_{gas}\rho_{NC}\right)_{KB}^{\tilde{n}} \tilde{u}_{gas,KB}^{n+1} A_{m,KB}\right] - \Delta x_J \sum_{KL=1}^{NKK}\left[L_{KL}\left(\alpha_{gas}\rho_{NC}\right)_{J,KL}^{\tilde{n}} \tilde{w}_{gas,KL}^{n+1}\right] - S_{c,NC,J}^{n+1} \quad (3\text{-}44)$$

$$\begin{bmatrix}\text{Residual Continuity}\\ \text{Equation Error}\\ E_c\end{bmatrix} = \begin{bmatrix}\text{Rate of Change of Mass}\\ A\frac{\partial}{\partial t}(\alpha_k\rho_k)\end{bmatrix} + \begin{bmatrix}\text{Rate of Mass Efflux in the Vertical Direction}\\ \frac{\partial \alpha_k\rho_k U_k}{\partial X}A\end{bmatrix} - \begin{bmatrix}\text{Rate of Mass Efflux in the Transverse Direction}\\ \sum_{KL}(\alpha_k\rho_k W_k)_{KL} L_{KL}\end{bmatrix} - \begin{bmatrix}\text{Rate of Creation of Vapor Mass Due to Phase Change}\\ \Gamma_k\end{bmatrix} - \begin{bmatrix}\text{Mass Efflux Due to Entrainment}\\ S_{ent}\end{bmatrix} - \begin{bmatrix}\text{Phase Source Term}\\ S_c\end{bmatrix}$$

$A_{c,J}$ is the scalar (or continuity) cell area. ΔX_J is the scalar cell height. Thus, $A_{c,J}\Delta X_J$ is the volume of Cell-J. $A_{m,j}$ is the momentum area of momentum cell j.

The rate of mass efflux in the transverse direction is given as the sum of the mass entering the cell through all transverse connections to all of the faces. The total number of transverse connections to the cell is NKK. The rate of mass efflux in the vertical direction is given as the sum of the mass entering (or leaving) the cell through all vertical connections to the top and bottom of the cell. The total number of connections to the top of the cell is NA and the number of connections to the bottom of the cell is NB.

The velocity in each of the convection terms is taken to be the new-time value, while the convected quantity, in this case, $(\alpha_k \rho_k)^{\tilde{n}}$, is taken at the old time. The mass creation term is evaluated at the new-time. However, it consists of an implicit and explicit part. For example, in the case of subcooled liquid and saturated or superheated steam without non-condensables, the rate of mass generation due to phase change as predicted by Equation (6-110) in Section 6, Γ_J^{n+1}, is given by:

$$\Gamma_J^{n+1} = -\frac{(h_i A_i)_\ell^n (H_f - H_\ell)^{n+1}}{[C_{p\ell}(H_v - H_f)]^n} - \frac{(h_i A_i)_v^n (H_g - H_v)^{n+1}}{[C_{pv}(H_g - H_\ell)]^n} \tag{3-45}$$

Here, H_v is the enthalpy of steam, and H_g is the enthalpy of saturated steam in the combined-gas phase, H_ℓ is the enthalpy of liquid, and H_f is the enthalpy of saturated liquid in the liquid phase. The product of the interfacial area and the heat transfer coefficient, the specific heats, and the heat of vaporization are all evaluated at the old time value and form the explicit portion of the mass creation term, while the enthalpies are evaluated at the new-time value, forming the implicit portion. This term is also multiplied by the ratio $(1-\alpha_{gas}^{n+1})/(1-\alpha_{gas}^{n})$ for vaporization or $\alpha_{gas}^{n+1}/\alpha_{gas}^{n}$ for condensation. This is done to provide an implicit ramp that will cause the interfacial area to go to zero as all of the donor phase is depleted. An explicit ramp is also applied to the product $(h_i A_i)^n$ to cause it to go to zero as the volume fraction of the donor phase approaches zero. The entrainment rate is explicit and is also multiplied by implicit and explicit ramps that force it to zero as the donor liquid phase is depleted.

The last term in the equations is the phase mass source term and is evaluated at the new-time. This term accounts for sources of vapor mass that are exterior to the vessel mesh. These sources include one-dimensional component connections, mass injection boundary conditions, and pressure boundary conditions. These source terms will be defined in Section 3.3.4.1.

3.3.3.2 Conservation of Momentum Equations

Vertical Direction

The channel index "I" is implied in the following momentum equations. The net entrainment rate, S_{ent} is further expanded as $S_{ent} = S_E - S_D$, where S_E, is the entrainment rate and S_D, is the de-entrainment rate. The net vapor generation, Γ, is expanded to Γ_E, the evaporation rate, or Γ_C, the condensation rate. If $\Gamma > 0$, $\Gamma_E = \Gamma$, and $\Gamma_C = 0$, and if $\Gamma < 0$, $\Gamma_E = 0$, and $\Gamma_C = \Gamma$.

Momentum equations in the vertical direction are presented in the form of mass flow rate yields for each vessel momentum cell j.

Combined-Gas Phase

$$
\begin{aligned}
F_{gas,j}^{n+1} = F_{gas,j}^{n} &+ \frac{\Delta t}{\Delta x_j}\left\{\sum_{KB=1}^{NB}\left[\left(\alpha_{gas}\rho_{gas}u_{gas}\right)_{KB}^{n\square}u_{gas,KB}^{n}A_{m,KB}\right]-\sum_{KA=1}^{NA}\left[\left(\alpha_{gas}\rho_{gas}u_{gas}\right)_{KA}^{n\square}u_{gas,KA}^{n}A_{m,KA}\right]\right\} \\
&+\Delta t\left\{\sum_{LB=1}^{NKB}\left[\left(\alpha_{gas}\rho_{gas}u_{gas}\right)_{LB}^{n\square}w_{gas,LB}^{n}\frac{L_{LB}}{2}\right]-\sum_{LA=1}^{NKA}\left[\left(\alpha_{gas}\rho_{gas}u_{gas}\right)_{LA}^{n\square}w_{gas,LA}^{n}\frac{L_{LA}}{2}\right]\right\} \\
&-\Delta t\left(\alpha_{gas}\rho_{gas}\right)_j^n gA_{m,j}-\Delta t\frac{\left(P_{J+1}^{n+1}-P_J^{n+1}\right)}{\Delta x_j}\alpha_{gas,j}^{n}A_{m,j} \\
&-\Delta tK_{x,w,gas,j}^{n}\left(2u_{gas,j}^{n+1}-u_{gas,j}^{n}\right)A_{m,j} \\
&-\Delta tK_{x,i,gas,\ell,j}^{n}\left[2\left(u_{gas}-u_\ell\right)_j^{n+1}-\left(u_{gas}-u_\ell\right)_j^{n}\right]A_{m,j} \\
&-\Delta tK_{x,i,gas,e,j}^{n}\left[2\left(u_{gas}-u_e\right)_j^{n+1}-\left(u_{gas}-u_e\right)_j^{n}\right]A_{m,j} \\
&-\frac{\Delta t}{\Delta x_j}\left[\Gamma_C u_{gas}-(1-\eta)\Gamma_E u_\ell-\eta\Gamma_E u_e\right]_j^n+\frac{\Delta tS_{x,m,gas,j}^{n}}{\Delta x_j}
\end{aligned}
\tag{3-46}
$$

Continuous Liquid Phase

$$
\begin{aligned}
F_{\ell,j}^{n+1} = F_{\ell,j}^{n} &+ \frac{\Delta t}{\Delta x_j}\left\{\sum_{KB=1}^{NB}\left[\left(\alpha_\ell\rho_\ell u_\ell\right)_{KB}^{\tilde{n}}u_{\ell,KB}^{n}A_{m,KB}\right]-\sum_{KA=1}^{NA}\left[\left(\alpha_\ell\rho_\ell u_\ell\right)_{KA}^{\tilde{n}}u_{\ell,KA}^{n}A_{m,KA}\right]\right\} \\
&+\Delta t\left\{\sum_{LB=1}^{NKB}\left[\left(\alpha_\ell\rho_\ell u_\ell\right)_{LB}^{\tilde{n}}w_{\ell,LB}^{n}\frac{L_{LB}}{2}\right]-\sum_{LA=1}^{NKA}\left[\left(\alpha_\ell\rho_\ell u_\ell\right)_{LA}^{\tilde{n}}w_{\ell,LA}^{n}\frac{L_{LA}}{2}\right]\right\} \\
&-\Delta t\left(\alpha_\ell\rho_\ell\right)_j^n gA_{m,j}-\Delta t\frac{\left(P_{J+1}^{n+1}-P_J^{n+1}\right)}{\Delta x_j}\alpha_{\ell,j}^{n}A_{m,j} \\
&-\Delta tK_{x,w,\ell,j}^{n}\left(2u_{\ell,j}^{n+1}-u_{\ell,j}^{n}\right)A_{m,j} \\
&+\Delta tK_{x,i,gas,\ell,j}^{n}\left[2\left(u_{gas}-u_\ell\right)_j^{n+1}-\left(u_{gas}-u_\ell\right)_j^{n}\right]A_{m,j} \\
&+\frac{\Delta t}{\Delta x_j}(1-\eta)\left(\Gamma_C u_{gas}-\Gamma_E u_\ell\right)_j^n+\frac{\Delta t}{\Delta x_j}\left(S_D u_e-S_E u_\ell\right)_j^n \\
&+\frac{\Delta tS_{x,m,\ell,j}^{n}}{\Delta x_j}
\end{aligned}
\tag{3-47}
$$

Entrained Liquid Phase

$$
\begin{aligned}
F_{e,j}^{n+1} = F_{e,j}^{n} &+ \frac{\Delta t}{\Delta x_{j+1/2}}\left\{\sum_{KB=1}^{NB}\left[\left(\alpha_e\rho_\ell u_e\right)_{KB}^{\tilde{n}} u_{e,KB}^{n} A_{m,KB}\right] - \sum_{KA=1}^{NA}\left[\left(\alpha_e\rho_\ell u_e\right)_{KA}^{\tilde{n}} u_{e,KA}^{n} A_{m,KA}\right]\right\} \\
&+ \Delta t\left\{\sum_{LB=1}^{NKB}\left[\left(\alpha_e\rho_\ell u_e\right)_{LB}^{\tilde{n}} w_{e,LB}^{n}\frac{L_{LB}}{2}\right] - \sum_{LA=1}^{NKA}\left[\left(\alpha_e\rho_\ell u_e\right)_{LA}^{\tilde{n}} w_{e,LA}^{n}\frac{L_{LA}}{2}\right]\right\} \\
&- \Delta t\left(\alpha_e\rho_\ell\right)_j^{n} g A_{m,j} - \Delta t\frac{\left(P_{J+1}^{n+1} - P_j^{n+1}\right)}{\Delta x_j}\alpha_{e,j}^{n} A_{m,j} \\
&- \Delta t K_{x,w,e,j}^{n}\left(2u_{e,j}^{n+1} - u_{e,j}^{n}\right)A_{m,j} \\
&+ \Delta t K_{x,i,gas,e,j}^{n}\left[2\left(u_{gas} - u_e\right)_j^{n+1} - \left(u_{gas} - u_e\right)_j^{n}\right]A_{m,j} \\
&+ \frac{\Delta t}{\Delta x_j}\eta\left(\Gamma_C u_{gas} - \Gamma_E u_e\right)_j^{n} - \frac{\Delta t}{\Delta x_j}\left(S_D u_e - S_E u_\ell\right)_j^{n} + \frac{\Delta t S_{x,m,e,j}^{n}}{\Delta x_j}
\end{aligned}
\tag{3-48}
$$

The definition for the vertical mass flow rates for the different phases denoted by variables $F_{k,j}^{n+1}$ and $F_{k,j}^{n}$ at the new and old time levels in the prior equations is presented in Equation 3-53.

$$
\begin{bmatrix} \text{New} \\ \text{Time} \\ \text{Flowrate} \\ \\ \left(\alpha_k\rho_k u_k A_m\right)^{n+1} \end{bmatrix} = \begin{bmatrix} \text{Old} \\ \text{Time} \\ \text{Flowrate} \\ \\ \left(\alpha_k\rho_k u_k A_m\right)^{n} \end{bmatrix} - \begin{bmatrix} \text{Efflux of Momentum at Bottom of Cell.} \\ \text{- Efflux of Momentum at Top of Cell.} \\ \\ \\ A\Delta t\dfrac{\partial}{\partial x}\left(\alpha_k\rho_k u_k u_k\right) \end{bmatrix}
$$

$$
+ \begin{bmatrix} \text{Rate of Efflux of Momentum in} \\ \text{the Transverse Direction} \\ \\ \sum_{KL}\left(\alpha_k\rho_k u_k w_k\right)_{KL} L_{KL}\Delta t \end{bmatrix} - \begin{bmatrix} \text{Gravitational} \\ \text{Term} \\ \\ \alpha_k\rho_k g\,\Delta t \end{bmatrix}
$$

$$
- \begin{bmatrix} \text{Pressure Gradient} \\ \text{Force} \\ \\ \Delta t\alpha_k\dfrac{\partial P}{\partial x} \end{bmatrix} - \begin{bmatrix} \text{Wall Shear} \\ \\ \\ \Delta t\tau_w \end{bmatrix} + \begin{bmatrix} \text{Interfacial Shear} \\ \\ \\ \left(\tau_{i,v\ell} + \tau_{i,ve}\right)\Delta t \end{bmatrix}
$$

$$+\left[\begin{array}{c}\text{Momentum Exchange Due}\\ \text{to Mass Transfer}\\ \text{Between Fields}\\ \\ (\Gamma u_k + S_{ent} u_k)\Delta t\end{array}\right] + \left[\begin{array}{c}\text{Momentum Source Term}\\ \\ \\ \\ \Delta t S_m\end{array}\right]$$

The momentum efflux in the vertical direction is given as the sum of the momentum entering (or leaving) the cell through all vertical connections. The total number of momentum mesh cells facing the top of the cell is NA and the total facing the bottom of the cell is NB. The momentum efflux in the transverse direction is given as the sum of the momentum entering (or leaving) the cell through all transverse connections. The total number of transverse connections to the top half of the momentum cell is NKA. The total number of connections to the bottom half of the cell is NKB. To achieve stability with this semi-implicit formulation of the momentum equation, donor cell momentum, $(\alpha_k \rho_k u_k)^{\tilde{n}}$, is convected by the velocities at the momentum cell face through the minimum area of the connections at the momentum cell face. That is, the flow area $A_{m,KB}$ is selected as the minimum of the flow area in momentum cell j and in the cell below, j – 1. Similarly, the flow area $A_{m,KA}$ is selected as the minimum of the flow area in cell j and the cell above it, j + 1.

A simple linear average between adjacent momentum cell velocities is taken to obtain the velocity at momentum cell faces since velocities are not computed at this location:

$$u_{KB} = \frac{u_j + u_{j-1}}{2} \text{ and } u_{KA} = \frac{u_{j+1} + u_j}{2} \tag{3-49}$$

Likewise, linear averages are used to obtain other variables at a location where they are not defined. The void fraction of the momentum cell is given as,

$$\alpha_j = \frac{\alpha_J + \alpha_{J+1}}{2} \tag{3-50}$$

and the density is given as,

$$\rho_j = \frac{\rho_J + \rho_{J+1}}{2} \tag{3-51}$$

Velocities are obtained from the flow computed by the mass flow rate, $(\alpha_k \rho_k u_k A_m)$, by dividing it by the momentum cell macroscopic density and momentum cell area.

$$u_{k,j} = \frac{(\alpha_k \rho_k u_k A_m)_j}{(\alpha_k \rho_k A_m)_j} \tag{3-52}$$

The pressures in the pressure force term are taken at the new-time, as are the velocities in the wall shear and interfacial shear terms. The shear terms have been weighted toward the new-time velocity by differencing $(u^{n+1})^2$ term as,

$$(u^{n+1})^2 = (u^n + u^{n+1} - u^n)^2 = (u^n)^2 + 2u^n(u^{n+1} - u^n) + (u^{n+1} - u^n)^2 \approx (u^n)^2 + 2u^n(u^{n+1} - u^n) = u^n(2u^{n+1} - u^n)$$

and expressing the stress term as,

$$C_D \frac{\rho}{2}(u^{n+1})^2 = C_D \frac{\rho}{2} u^n(2u^{n+1} - u^n) = K(2u^{n+1} - u^n)$$

Where C_D is the drag coefficient, and K is the shear stress coefficient. All other terms and variables are computed using old time values. The donor phase momentum is convected during mass exchange between fields. The explicit viscous and turbulent shear stresses will be expanded in the next section.

The vertical mass flow rates at the new and old time levels, respectively, Equations 3-46, 3-47, and 3-48 are given by the following:

$$\begin{aligned} F_{k,j}^{n+1} &= (\alpha_k \rho_k u_k)_j^{n+1} A_{m,j} \\ F_{k,j}^{n} &= (\alpha_k \rho_k u_k)_j^{n} A_{m,j} \end{aligned} \tag{3-53}$$

where k = gas, ℓ, or e.

Transverse Direction

The gap index "k" is implied in the following momentum equations.

Momentum equations in the transverse direction are presented in the form of mass flow rate yields for each vessel momentum gap k at J-level (omitting index-k):

Combined-Gas Phase

$$
\begin{aligned}
W_{gas,J}^{n+1} = W_{gas,J}^{n} &+ \frac{\Delta t \Delta x_J}{\Delta z_J}\left\{\sum_{LII=1}^{NKII}\left[\left(\alpha_{gas}\rho_{gas}w_{gas}\right)_{LII}^{\tilde{n}} w_{gas,LII}^{n} L_{LII}\right] - \sum_{LJJ=1}^{NKJJ}\left[\left(\alpha_{gas}\rho_{gas}w_{gas}\right)_{LJJ}^{\tilde{n}} w_{gas,LJJ}^{n} L_{LJJ}\right]\right\} \\
&+ \frac{\Delta t \Delta x_J}{\Delta z_J}\left\{\sum_{KO=1}^{NG}\left[\left(\alpha_{gas}\rho_{gas}w_{gas}\right)_{KO}^{\tilde{n}} w_{gas,KO}^{o,n}\frac{L_{KO}}{2}\right]\right\} \\
&+ \frac{\Delta t}{\Delta z_J}\left\{\sum_{IB=1}^{NCB}\left[\left(\alpha_{gas}\rho_{gas}w_{gas}\right)_{IB}^{\tilde{n}} u_{gas,IB}^{n} A_{z,IB}\right] - \sum_{IA=1}^{NCA}\left[\left(\alpha_{gas}\rho_{gas}w_{gas}\right)_{IA}^{\tilde{n}} u_{gas,IA}^{n} A_{z,IA}\right]\right\} \\
&- \Delta t\frac{\left(P_{JJ}^{n+1} - P_{II}^{n+1}\right)}{\Delta z_J}\alpha_{gas,J}^{n} L_J \Delta x_J \\
&- \Delta t K_{z,w,gas,J}^{n}\left(2w_{gas,J}^{n+1} - w_{gas,J}^{n}\right)L_J \Delta x_J \\
&- \Delta t K_{z,i,gas,\ell,J}^{n}\left[2\left(w_{gas} - w_{\ell}\right)_J^{n+1} - \left(w_{gas} - w_{\ell}\right)_J^{n}\right]L_J \Delta x_J \\
&- \Delta t K_{z,i,gas,e,J}^{n}\left[2\left(w_{gas} - w_{e}\right)_J^{n+1} - \left(w_{gas} - w_{e}\right)_J^{n}\right]L_J \Delta x_J \\
&- \frac{\Delta t}{\Delta x_J}\left[\Gamma_C w_{gas} - (1-\eta)\Gamma_E w_{\ell} - \eta\Gamma_E w_e\right]_J^{n} + \frac{\Delta t S_{z,m,gas,J}^{n}}{\Delta x_J}
\end{aligned}
\tag{3-54}
$$

where:

$$A_{z,IB} = \left(\frac{L\Delta Z}{2}\right)_{IB} \text{ and } A_{z,IA} = \left(\frac{L\Delta Z}{2}\right)_{IA}$$

$A_{z,IB}$ is a half of connecting area to gap momentum cell below, and $A_{z,IA}$ is a half of connecting area to gap momentum cell above.

Continuous Liquid Phase

$$
\begin{aligned}
W_{\ell,J}^{n+1} = W_{\ell,J}^{n} &+ \frac{\Delta t \Delta x_J}{\Delta z_J}\left\{\sum_{LII=1}^{NKII}\left[\left(\alpha_\ell \rho_\ell w_\ell\right)_{LII}^{\tilde{n}} w_{\ell,LII}^{n} L_{LII}\right] - \sum_{LJJ=1}^{NKJJ}\left[\left(\alpha_\ell \rho_\ell w_\ell\right)_{LJJ}^{\tilde{n}} w_{\ell,LJJ}^{n} L_{LJJ}\right]\right\} \\
&+ \frac{\Delta t \Delta x_J}{\Delta z_J}\left\{\sum_{KO=1}^{NG}\left[\left(\alpha_\ell \rho_\ell w_\ell\right)_{KO}^{\tilde{n}} w_{\ell,KO}^{o,n} \frac{L_{KO}}{2}\right]\right\} \\
&+ \frac{\Delta t}{\Delta z_J}\left\{\sum_{IB=1}^{NCB}\left[\left(\alpha_\ell \rho_\ell w_\ell\right)_{IB}^{\tilde{n}} u_{\ell,IB}^{n} A_{z,IB}\right] - \sum_{IA=1}^{NCA}\left[\left(\alpha_\ell \rho_\ell w_\ell\right)_{IA}^{\tilde{n}} u_{\ell,IA}^{n} A_{z,IA}\right]\right\} \\
&- \Delta t \frac{\left(P_{JJ}^{n+1} - P_{II}^{n+1}\right)}{\Delta z_J} \alpha_{\ell,J}^{n} L_J \Delta x_J \\
&- \Delta t K_{z,w,\ell,J}^{n}\left(2 w_{\ell,J}^{n+1} - w_{\ell,J}^{n}\right) L_J \Delta x_J \\
&+ \Delta t K_{z,i,gas,\ell,J}^{n}\left[2\left(w_{gas} - w_\ell\right)_J^{n+1} - \left(w_{gas} - w_\ell\right)_J^{n}\right] L_J \Delta x_J \\
&+ \frac{\Delta t}{\Delta x_J}(1-\eta)\left(\Gamma_C w_{gas} - \Gamma_E w_\ell\right)_J^{n} + \frac{\Delta t}{\Delta x_J}\left(S_D w_e - S_E w_\ell\right)_J^{n} + \frac{\Delta t S_{z,m,\ell,J}^{n}}{\Delta x_J}
\end{aligned}
\tag{3-55}
$$

Entrained Liquid Phase

$$
\begin{aligned}
W_{e,J}^{n+1} = W_{e,J}^{n} &+ \frac{\Delta t \Delta x_J}{\Delta z_J}\left\{\sum_{LII=1}^{NKII}\left[\left(\alpha_e \rho_\ell w_e\right)_{LII}^{\tilde{n}} w_{e,LII}^{n} L_{LII}\right] - \sum_{LJJ=1}^{NKJJ}\left[\left(\alpha_e \rho_\ell w_e\right)_{LJJ}^{\tilde{n}} w_{e,LJJ}^{n} L_{LJJ}\right]\right\} \\
&+ \frac{\Delta t \Delta x_J}{\Delta z_J}\left\{\sum_{KO=1}^{NG}\left[\left(\alpha_e \rho_\ell w_e\right)_{KO}^{\tilde{n}} w_{e,KO}^{o,n} \frac{L_{KO}}{2}\right]\right\} \\
&+ \frac{\Delta t}{\Delta z_J}\left\{\sum_{IB=1}^{NCB}\left[\left(\alpha_e \rho_\ell w_e\right)_{IB}^{\tilde{n}} u_{e,IB}^{n} A_{z,IB}\right] - \sum_{IA=1}^{NCA}\left[\left(\alpha_e \rho_\ell w_e\right)_{IA}^{\tilde{n}} u_{e,IA}^{n} A_{z,IA}\right]\right\} \\
&- \Delta t \frac{\left(P_{JJ}^{n+1} - P_{II}^{n+1}\right)}{\Delta z_J} \alpha_{e,J}^{n} L_J \Delta x_J \\
&- \Delta t K_{z,w,e,J}^{n}\left(2 w_{e,J}^{n+1} - w_{e,J}^{n}\right) L_J \Delta x_J \\
&+ \Delta t K_{z,i,gas,e,J}^{n}\left[2\left(w_{gas} - w_e\right)_J^{n+1} - \left(w_{gas} - w_e\right)_J^{n}\right] L_J \Delta x_J \\
&+ \frac{\Delta t}{\Delta x_J}\eta\left(\Gamma_C w_{gas} - \Gamma_E w_e\right)_k^{n} - \frac{\Delta t}{\Delta x_J}\left(S_D w_e - S_E w_\ell\right)_J^{n} + \frac{\Delta t S_{z,m,e,J}^{n}}{\Delta x_J}
\end{aligned}
\tag{3-56}
$$

The definition for the transverse mass flow rates for the different phases denoted by variables $W_{k,j}^{n+1}$ and $W_{k,j}^{n}$ at the new and old time levels in the prior equations is presented in Equation 3-59.

$$\begin{bmatrix}\text{New}\\ \text{Time Gap}\\ \text{Flowrate}\\ \\ (\alpha_k \rho_k w_k A_Z)^{n+1}\end{bmatrix} = \begin{bmatrix}\text{Old}\\ \text{Time}\\ \text{Flowrate}\\ \\ (\alpha_k \rho_k w_k A_Z)^{n}\end{bmatrix} - \begin{bmatrix}\text{Transverse}\\ \text{Momentrum Efflux}\\ \text{by Transverse Convection}\\ \\ \Delta t \frac{\partial(\alpha_k \rho_k w_k w_k A_Z)}{\partial Z}\end{bmatrix} + \begin{bmatrix}\text{Transverse}\\ \text{Momentum Efflux}\\ \text{by Orthogonal}\\ \text{Transverse Convection}\\ \\ \sum_{NK}(\alpha_k \rho_k w_k w_k^{\circ} L_g)\Delta t\end{bmatrix}$$

$$+ \begin{bmatrix}\text{Transverse}\\ \text{Momentum}\\ \text{by Vertical Convection}\\ \\ \Delta t \frac{\partial}{\partial X}\alpha_k \rho_k w_k u_k A_Z\end{bmatrix} - \begin{bmatrix}\text{Pressure Gradient}\\ \text{Force}\\ \\ \\ \alpha_k A_Z \frac{\partial P}{\partial Z}\Delta t\end{bmatrix} - \begin{bmatrix}\text{Transverse}\\ \text{Wall Shear}\\ \\ \\ \tau_{wZ}''' A_Z \Delta t\end{bmatrix}$$

$$+ \begin{bmatrix}\text{Interfacial Drag Between}\\ \text{Vapor and Continuous Liquid}\\ \\ \tau_{iZ,v\ell}''' A_Z \Delta t\end{bmatrix} + \begin{bmatrix}\text{Interfacial Drag Between}\\ \text{Vapor and Drops}\\ \\ \tau_{iZ,ve}''' A_Z \Delta t\end{bmatrix}$$

$$+ \begin{bmatrix}\text{Transverse Momentum}\\ \text{Exchange Due to Mass}\\ \text{Transfer Between Fields}\\ \\ (\Gamma w_k + S w_k)\Delta t\end{bmatrix} + \begin{bmatrix}\text{Transverse Momentum}\\ \text{Source Term}\\ \\ \\ S_m \Delta t\end{bmatrix}$$

As in the vertical momentum equations, the pressures in the pressure force term and the velocities in the wall and interfacial drag term are the new-time values, while all other terms and variables are computed using old time values. The momentum efflux by transverse convection is given as the sum of the momentum entering (or leaving) the cell through all transverse connections. Momentum convected by transverse velocities (that are in the direction of the transverse velocity being solved for) is the sum of the momentum entering (or leaving) through mesh cell faces connected to the face of the mesh cell for which the momentum equation is being solved. NKII is the number of mesh cells facing the upstream face of the mesh cell and NKJJ is the number facing the downstream face of the mesh cell. Momentum convected out the sides of the mesh cell by velocities that are orthogonal to the velocity to be solved for, but lying in the same horizontal plane, is given by the sum of the momentum convected into (or out of) cells connected to the sides of the transverse momentum mesh cell. The number of cells connected to the mesh cell under

consideration, whose velocities are orthogonal to its velocity, is given by NG. The momentum convected by vertical velocities through the top and bottom of the mesh cell is the sum of the momentum convected into (or out of) cells connected to the top and bottom of the mesh cell. This momentum depends on the number of cells connected to the top (NCA) and bottom (NCB) of the mesh cell.

A simple linear average is used to obtain velocities at mesh cell faces, LII (upstream) and LJJ (downstream):

$$w_{LII} = \frac{w_{J,II} + w_J}{2} \text{ and } w_{LJJ} = \frac{w_J + w_{J,JJ}}{2} \tag{3-57}$$

$w_{J,II}$ indicates the velocity at J-level of the upstream gap connected to the gap-k, and $w_{J,JJ}$ indicates the velocity at J-level of the downstream gap connected to the gap-k. Linear averages also are used to obtain other variables at a location where they are not defined. Velocities are obtained from the flows computed by transverse momentum equations. To obtain the phasic velocities, the flows are divided by the momentum cell macroscopic density and transverse momentum flow area:

$$w_{k,J} = \frac{(\alpha_k \rho_k w_k L \Delta X)_J}{(\alpha_k \rho_k L \Delta X)_J} \tag{3-58}$$

Donor cell differencing is used for all convective terms and the donor phase momentum is convected in the mass transfer terms. The viscous and turbulent shear stresses are omitted as discussed in Section 3.2.3.

The transverse mass flow rates at the new and old time level, respectively, in Equations 3-54, 3-55, and 3-56 are given by the following:

$$\begin{aligned} W_{k,J}^{n+1} &= (\alpha_k \rho_k w_k)_J^{n+1} L_J \Delta x_J \\ W_{k,J}^{n} &= (\alpha_k \rho_k w_k)_J^{n} L_J \Delta x_J \end{aligned} \tag{3-59}$$

where k=gas, ℓ, or e.

3.3.3.3 Conservation of Energy Equations

Energy equations are presented in the form of residual error yields for each vessel cell J.

Combined-Gas Energy Equation

$$\begin{aligned} E_{e,gas,J}^{n+1} = {} & \frac{\Delta x_J A_{c,J}}{\Delta t}\left[(\alpha_{gas}\rho_{gas}H_{gas})_J^{n+1} - (\alpha_{gas}\rho_{gas}H_{gas})_J^{n}\right] + \sum_{KA=1}^{NA}\left[(\alpha_{gas}\rho_{gas}H_{gas})_{KA}^{\tilde{n}}\,\tilde{u}_{gas,KA}^{n+1}A_{m,KA}\right] \\ & - \sum_{KB=1}^{NB}\left[(\alpha_{gas}\rho_{gas}H_{gas})_{KB}^{\tilde{n}}\,\tilde{u}_{gas,KB}^{n+1}A_{m,KB}\right] - \Delta x_J \sum_{KL=1}^{NKK}\left[L_{KL}(\alpha_{gas}\rho_{gas}H_{gas})_{KL}^{\tilde{n}}\,\tilde{w}_{gas,KL}^{n+1}\right] \\ & - (\Gamma H_{gas}^{i})_J^{n+1} - S_{e,gas,J}^{n+1} - q_{i,v,J}^{n+1} - q_{\ell,NC,J}^{n+1} - Q_{w,g,J}^{n} - \frac{\Delta x_J A_{c,J}}{\Delta t}\alpha_{gas,J}^{n}\left(P_J^{n+1} - P_J^{n}\right) \end{aligned} \tag{3-60}$$

Liquid Energy Equation

$$
\begin{aligned}
E_{e,\ell,J}^{n+1} = {} & \frac{\Delta x_J A_{c,J}}{\Delta t}\left\{\left[(\alpha_\ell+\alpha_e)\rho_\ell H_\ell\right]_J^{n+1}-\left[(\alpha_\ell+\alpha_e)\rho_\ell H_\ell\right]_J^{n}\right\} \\
& + \sum_{KA=1}^{NA}\left[(\alpha_\ell\rho_\ell H_\ell)_{KA}^{\tilde{n}}\,\tilde{u}_{\ell,KA}^{n+1}A_{m,KA}+(\alpha_e\rho_\ell H_\ell)_{KA}^{\tilde{n}}\,\tilde{u}_{e,KA}^{n+1}A_{m,KA}\right] \\
& - \sum_{KB=1}^{NB}\left[(\alpha_\ell\rho_\ell H_\ell)_{KB}^{\tilde{n}}\,\tilde{u}_{\ell,KB}^{n+1}A_{m,KB}+(\alpha_e\rho_\ell H_\ell)_{KB}^{\tilde{n}}\,\tilde{u}_{e,KB}^{n+1}A_{m,KB}\right] \\
& - \Delta x_J \sum_{KL=1}^{NKK} L_{KL}\left[(\alpha_\ell\rho_\ell H_\ell)_{KL}^{\tilde{n}}\,\tilde{w}_{\ell,KL}^{n+1}+(\alpha_e\rho_\ell H_\ell)_{KL}^{\tilde{n}}\,\tilde{w}_{e,KL}^{n+1}\right] \\
& + \left(\Gamma H_\ell^i\right)_J^{n+1}-S_{e,\ell,J}^{n+1}-q_{i,\ell,J}^{n+1}+q_{\ell,NC,J}^{n+1}-Q_{w,\ell,J}^{n}-\frac{\Delta x_J A_{c,J}}{\Delta t}(\alpha_\ell+\alpha_e)_J^n\left(P_J^{n+1}-P_J^n\right)
\end{aligned}
\tag{3-61}
$$

$$
\begin{bmatrix}\text{Residual Energy Error}\\ E_e\end{bmatrix} = \begin{bmatrix}\text{Rate of Change of Enthalpy}\\ A\frac{\partial}{\partial t}(\alpha_k\rho_k H_k)\end{bmatrix} + \begin{bmatrix}\text{Rate of Efflux of Enthalpy in the Vertical Direction}\\ \frac{\partial}{\partial X}(A\,\alpha_k\rho_k H_k u_k)\end{bmatrix}
$$

$$
- \begin{bmatrix}\text{Rate of Efflux of Enthalpy in the Transverse Direction}\\ \sum_{KL}(\alpha_k\rho_k H_k w_k)_{KL}L_{KL}\end{bmatrix} - \begin{bmatrix}\text{Energy Efflux Due To Mass Transfer Between Fields}\\ \Gamma_k' H_k^i\end{bmatrix}
$$

$$
- \begin{bmatrix}\text{Interfacial Heat Transfer}\\ q_i'\end{bmatrix} - \begin{bmatrix}\text{Heat Addition from Solid}\\ Q_w\end{bmatrix} - \begin{bmatrix}\text{Pressure Derivative}\\ A\,\alpha_k\frac{\partial P}{\partial t}\end{bmatrix} - \begin{bmatrix}\text{Energy Source Term}\\ S_e\end{bmatrix}
$$

Again, the rate of energy efflux in the transverse direction is the sum of all transverse connections on all faces of the cell; the rate of energy efflux in the vertical direction is the sum of all connections to the top and bottom of the cell. New-time velocities convect the donor cell, $(\alpha_k\rho_k H_k)^{\tilde{n}}$, which is evaluated using old time values. New-time enthalpies are convected in the phase change term. The interfacial heat transfer term, like the vapor generation term, has an implicit temperature difference and an explicit heat transfer coefficient and interfacial area. The wall heat transfer is explicit. The energy source terms corresponding to the mass source terms will be defined in the next section. The fluid conduction and turbulent heat flux are omitted in these equations as discussed in Section 3.2.3.

3.3.4 Source, Viscous, and Turbulence Terms

Terms not fully expanded in the presentation of the finite-difference equations in Section 3.3.3 are presented in this section. These include the mass, energy, and momentum source terms. The viscous shear stress tensors, the turbulent shear stress tensors, the fluid conduction vector, and the turbulent heat flux vector are omitted in the difference equations since they are not used for LOCA applications as discussed in Section 3.2.3.

3.3.4.1 Mass, Energy, and Momentum Source Terms

Two types of source terms are required for the mass, energy, and momentum finite-difference equations. The first type is associated with one-dimensional component connections to the vessel mesh, and the second type is associated with arbitrary boundary conditions that may be specified anywhere in the vessel mesh.

3.3.4.1.1 Vessel Connection Source Terms

The vessel connection energy and mass source terms have an implicit and an explicit term. The phasic velocities in the source terms are taken at the new-time and represent the implicit portion of the source term. Subscript p (for pipe) refers to the 1D component that is connected to vessel cell J. The donor cell quantities (denoted by the $\tilde{n}$ superscript) are computed using currently known values and therefore explicit. The donor cell is determined by the sign of the velocities; if the flow is entering the vessel, the properties of the 1D component p are used; if the flow is leaving the vessel, the properties of the vessel cell J are used.

The finite-difference form of the mass and energy source terms are the following:

Combined-Gas Mass Source Term

[ ] a,c (3-62)

Liquid Mass Source Term

[ ] a,c (3-63)

Entrained Liquid Mass Source Term

[ ] a,c (3-64)

Non-Condensable Mass Source Term

[ ] a,c (3-65)

Combined-Gas Energy Source Term

[ ]a,c (3-66)

Liquid Energy Source Term

[ ]a,c (3-67)

Where (-s) is an integer (1 or -1) flag which switches the numerical sign of the velocity based on the junction orientation. Positive sign means connection is from the 3D to 1D. Note that the sign convention is that a source (of mass or energy) is positive if it is directed from the 1D to the 3D (Vessel inflow). Because of the 1D and 3D conventions difference, (-s) operator is required in the expressions above.

[

]a,c

3.3.4.1.2 Vessel (1D/3D) Connection Momentum Source Terms

The 1D/3D momentum source terms are fully explicit. Both horizontal and vertical pipes may be connected to the vessel mesh. However, only one pipe connection is allowed per vessel mesh cell. In all cases it has been assumed that the pipe is normal to the face of the vessel mesh cell. The momentum source in both the lateral and vertical directions can be expressed by the following equations.

Vertical Phasic Momentum Source to channel-I, momentum cell-j is expressed as,

$$S^n_{m,k,j} = \left[(\alpha_k \rho_k u_k)^{\tilde{n}}_{1D/3D} u^n_{k,B} A_{1D/3D}\right] \tag{3-68}$$

and, if the connecting gap is specified, the transverse Phasic Momentum Source to gap k, cell-J3D is,

$$S^n_{m,k,J} = \left[(\alpha_k \rho_k w_k)^{\tilde{n}}_{1D/3D} w^n_{k,B} A_{1D/3D}\right] \tag{3-69}$$

where, the velocities used for the donoring are defined using the user supplied 1D3D connection information as,

$$u^n_{k,B} = \frac{1}{2}\left(u^n_{k,J3D} + u^n_{k,p}\right)$$

and, if the connecting gap is specified,

$$w^n_{k,B} = \frac{1}{2}\left(w^n_{k,J3D} + u^n_{k,p}\right)$$

The donored quantities are evaluated as,

$$(\alpha_k \rho_k u_k)^{\tilde{n}}_{1D/3D} = \begin{cases} (\alpha_k \rho_k u_k)^{\tilde{n}}_{p} & \text{if the flow is from 1D to 3D} \\ (\alpha_k \rho_k u_k)^{\tilde{n}}_{J3D} & \text{if the flow is from 3D to 1D} \end{cases}$$

$$(\alpha_k \rho_k w_k)^{\tilde{n}}_{1D/3D} = \begin{cases} (\alpha_k \rho_k u_k)^{\tilde{n}}_{p} & \text{if the flow is from 1D to 3D} \\ (\alpha_k \rho_k w_k)^{\tilde{n}}_{J3D} & \text{if the flow is from 3D to 1D} \end{cases}$$

where, J3D is the user specified level in the 1D/3D connection channel, I_{1D3D}, and k = gas, ℓ, or e.

3.3.4.1.3 Boundary Condition Source Terms

There are five basic types of boundary conditions that may be specified within the vessel mesh. The first type allows the user to specify the pressure and the mixture enthalpy in any cell. The normal momentum equations are then solved on the cell faces to obtain flows into or out of the cell. If the flow is out of the cell, properties specified within the cell are convected to surrounding cells. If the flow is into the cell, properties of surrounding cells are convected into the specified cell. However, since the properties of the cell are specified, the pressure, temperature, and void fractions do not change accordingly, so the pressure boundary condition can act as a mass, energy, and momentum sink, if flow is into the cell, or source, if flow is out of the cell.

The second type of boundary condition allows the user to specify the mixture enthalpy and the continuity mass flow rate at the top of the cell. It is assumed that all three phases have the same velocity at the cell face. No momentum solution is performed at the top of the cell for this case since the flow is specified. Otherwise, the boundary condition behaves in the same way as the first type of boundary condition, acting as a source (or sink) of mass, momentum, and energy, depending on the direction of flow.

The third type of boundary condition specifies a zero flow on any mesh cell face, and therefore does not produce any mass, momentum, or energy sources.

The fourth type of boundary condition allows the user to specify a mass and energy source in any computational cell without changing the computed fluid properties within the cell. Again, all three phases are assumed to travel at the mixture velocity, and the amount of flow is determined by the volume fraction of each phase specified in the boundary condition. Momentum of this source is added only if the flow is in the transverse direction and into the vessel mesh, or if flow is out of the mesh.

The fifth type of boundary condition is not used in any of the WCOBRA/TRAC-TF2 test simulations or in a PWR analysis, but is described here for completeness. This final type of boundary condition allows the user to specify a pressure sink to be connected to any cell. A simple momentum equation is solved between the sink pressure and the cell pressure, and the resulting flow produces a mass, momentum, and energy sink if flow is out of the vessel and a mass and energy source if the flow is into the vessel. The sink vapor momentum equation is as follows:

$$\left(\alpha_g \rho_g w_g A\right)_{SINK}^{n+1} = \left(\alpha_g \rho_g w_g A\right)_{SINK}^{n} + \frac{\Delta t}{\Delta X} A_{SINK} \left(P_{SINK} - P_J\right)^n$$

(3-70)

$$- K_{w,SINK} U_{g_{SINK}}^n - K_{i,g\ell} \left(u_g - u_\ell\right)_{SINK} - K_{i,ge} \left(u_g - u_e\right)_{SINK}$$

Transverse and vertical momentum is convected out of the vessel mesh by the sink velocity computed from the above equation in the same way that vessel/pipe connections convect momentum from the mesh. The same equations may be used to represent the sink momentum sources if the pipe velocity is replaced with the sink velocity in the source equations.

3.4 CONSERVATION EQUATIONS FOR ONE-DIMENSIONAL COMPONENTS (MODEL BASIS)

3.4.1 Introduction

WCOBRA/TRAC-TF2 uses a two-phase, two-fluid model in the one-dimensional components (Spore et al., 2000). The hydrodynamic formulation consists of three equations for the conservation of mass, including the non-condensable gas, two equations for the conservation of energy, and two equations for the conservation of momentum. Closure of the field equations requires specification of thermodynamic functions, interphase heat and mass transfer, and other constitutive relationships.

Each of the field equations is described below in the context of a quasi-one-dimensional flow in a pipe of non-uniform cross-sectional area. The principal assumptions that permit the field equations to be easily integrated over the cross-sectional area are: no slip at the wall and small transverse pressure gradients. The latter assumption allows the individual phase density cross-sectional profiles to be assumed flat; thus, these densities represent their own averages.

When values of cell-centered variables are needed at cell edges, an average of some form is required. The methods discussed here use values only from the volumes immediately adjacent to the given edge, so the averages are always in the following form:

$$\langle Y \rangle_{j+1/2} = w_{j+1/2} Y_j + \left(1 - w_{j+1/2}\right) Y_{j+1} \tag{3-71}$$

For simple 1D flow, terms expressing mass and energy flow for the j-th- finite volume then have the following form:

$$\frac{\partial}{\partial x_j}(Yu) = \frac{\left[w_{j+1/2} Y_j + \left(1 - w_{j+1/2}\right) Y_{j+1}\right] u_{j+1/2} - \left[w_{j-1/2} u_{j-1} + \left(1 - w_{j-1/2}\right) Y_j\right] u_{j-1/2}}{\Delta x} \tag{3-72}$$

$$\frac{\partial}{\partial x_j}(Yu) = \frac{\langle Y \rangle_{j+1/2} u_{j+1/2} - \langle Y \rangle_{j-1/2} u_{j-1/2}}{\Delta x} \tag{3-72a}$$

The form is more complex for 1D flow with a spatially varying cross-sectional flow area. In this case the mass flux term is abbreviated as:

$$\nabla_j \cdot (Yu) =$$

$$\frac{[w_{j+1/2} Y_j + (1 - w_{j+1/2}) Y_{j+1}] (A_{j+1/2} u_{j+1/2}) - [w_{j-1/2} Y_{j-1} + (1 - w_{j-1/2}) Y_j] (A_{j-1/2} u_{j-1/2})}{vol_j} \tag{3-73}$$

where $A_{j+1/2}$ is the flow area between cells j and j+1 and vol_j is the volume of the j-th cell.

The related derivative used in the finite-difference momentum flux involves the use of a more complicated averaging method. This is driven by a need to model Bernoulli flows when appropriate and to conserve momentum properly when a side-junction flow is present. To aid in understanding the basic numerical methods, it is worth noting that with no area changes or side junctions, the numerical form of the velocity gradient is:

$$\left.\frac{\partial u}{\partial x}\right|_{j+1/2} = \frac{(1 - w_{j+1/2}) u_{j+3/2} + (2w_{j+1/2} - 1) u_{j+1/2} - w_{j+1/2} u_{j-1/2}}{\Delta x} \tag{3-74}$$

For flows in 1D channels with variable cross-sectional area, the momentum-transfer term is abbreviated as $u_{j+1/2} \nabla_{j+1/2} u$.

3.4.2 Conservation of Mass

The conservation of mass equations are the following:

Combined-Gas Mass Equation

$$\frac{\partial (\alpha_g \rho_g)}{\partial t} + \nabla \left((\alpha_g \rho_g) \cdot \underline{u}_g \right) = \Gamma \tag{3-75}$$

Liquid Mass Equation

$$\frac{\partial (\alpha_\ell \rho_\ell)}{\partial t} + \nabla \left((\alpha_\ell \rho_\ell) \cdot \underline{u}_\ell \right) = -\Gamma \tag{3-76}$$

An alternative to solving one of the phasic mass equations is to solve the mixture mass equation, which is obtained by summing 3-75 and 3-76. This yields the following result:

Mixture Mass Equation

$$\frac{\partial(\alpha_g\rho_g+\alpha_\ell\rho_\ell)}{\partial t}+\nabla\left((\alpha_g\rho_g)\cdot\underline{u}_g+(\alpha_\ell\rho_\ell)\cdot\underline{u}_\ell\right)=0 \tag{3-77}$$

Solving either Equation 3-75 or Equation 3-76 together with 3-77 is equivalent to solving both Equations 3-75 and 3-77.

Non-Condensable Gas Mass Equation

The non-condensable gas field is assumed to be in thermal equilibrium with any steam that is present and to move with the same velocity as the steam (mechanical equilibrium). Hence, only a single mass-continuity equation is needed to track the non-condensable gas.

$$\frac{\partial(\alpha_g\rho_a)}{\partial t}+\nabla\left((\alpha_g\rho_a)\cdot\underline{u}_g\right)=0 \tag{3-78}$$

With this field present, the total gas density and energy are sums of the vapor and the non-condensable components,

$$\rho_g=\rho_v+\rho_a \tag{3-79}$$

and

$$\rho_g e_g=\rho_v e_v+\rho_a e_a \tag{3-80}$$

We assume Dalton's law applies; therefore,

$$P=P_v+P_a \tag{3-81}$$

The subscripts v and a indicate, respectively, the steam and air properties; the code normally applies the thermodynamic properties for air to the non-condensable gas. The code user may, however, select hydrogen or helium as an alternative.

Liquid-Solute Concentration Equation

WCOBRA/TRAC-TF2 includes a mass-continuity equation for a solute moving with the liquid field.

$$\frac{\partial(\alpha_\ell m\rho_\ell)}{\partial t}+\nabla\left((\alpha_\ell m\rho_\ell)\cdot\underline{u}_\ell\right)=S_m \tag{3-82}$$

where m is the solute concentration (mass of solute/unit mass of liquid water) in the liquid phase.

The solute does not affect the hydrodynamics directly. If we assume that the solute represents orthoboric acid, the amount of the dissolved and the plated-out orthoboric acid in the core may affect the hydrodynamics indirectly through neutronic-reactivity feedback corresponding to user-specified input values obtained from a boron-mass reactivity-coefficient table. If the solute concentration exceeds the orthoboric-acid solubility at the liquid temperature in a specific hydrodynamic cell, we assume that the excess solute in that cell plates out. Plating on structures can occur if the cell fluid flashes or boils and thus increases the concentration beyond the solubility limit. We also assume that any plated-out solute instantaneously redissolves to the maximum allowable concentration if more liquid enters the cell. Because the solute does not affect the hydrodynamics directly, the solute variable may be used as a tag to track the movement of fluid from a specific source through the system.

3.4.3 Conservation of Momentum

The conservation of momentum equations are the following:

Combined-Gas Momentum Equation

$$\frac{\partial \underline{u}_g}{\partial t} + \underline{u}_g \cdot \nabla \underline{u}_g = -\frac{1}{\rho_g} \cdot \nabla P - \frac{C_i}{\alpha_g \rho_g} \cdot \left|\underline{u}_g - \underline{u}_\ell\right| \cdot \left(\underline{u}_g - \underline{u}_\ell\right) - \frac{\Gamma^+}{\alpha_g \rho_g} \cdot \left(\underline{u}_g - \underline{u}_\ell\right) - \frac{C_{wg}}{\alpha_g \rho_g} \cdot \left|\underline{u}_g\right| \cdot \underline{u}_g - \underline{g} \cdot \cos\theta \quad (3\text{-}83)$$

Continuous Liquid Momentum Equation

$$\frac{\partial \underline{u}_\ell}{\partial t} + \underline{u}_\ell \cdot \nabla \underline{u}_\ell = -\frac{1}{\rho_\ell} \cdot \nabla P - \frac{C_i}{\alpha_\ell \rho_\ell} \cdot \left|\underline{u}_\ell - \underline{u}_g\right| \cdot \left(\underline{u}_\ell - \underline{u}_g\right) + \frac{\Gamma^-}{\alpha_\ell \rho_\ell} \cdot \left(\underline{u}_\ell - \underline{u}_g\right) - \frac{C_{w\ell}}{\alpha_\ell \rho_\ell} \cdot \left|\underline{u}_\ell\right| \cdot \underline{u}_\ell - \underline{g} \cdot \cos\theta \quad (3\text{-}84)$$

3.4.4 Conservation of Energy

The conservation of energy equations are the following:

Combined-Gas Energy Equation

$$\frac{\partial(\alpha_g \rho_g e_g)}{\partial t} + \nabla\left((\alpha_g \rho_g e_g) \cdot \underline{u}_g\right) = -P \cdot \left[\frac{\partial \alpha_g}{\partial t} + \nabla\left(\alpha_g \cdot \underline{u}_g\right)\right] + q_{wg} + q_{dg} - \left(q_{ig} + q_{g\ell}\right) + \Gamma \cdot h_v^* \quad (3\text{-}85)$$

Mixture Energy Equation

$$\frac{\partial(\alpha_g\rho_g e_g + \alpha_\ell\rho_\ell e_\ell)}{\partial t} + \nabla\left((\alpha_g\rho_g e_g)\cdot \underline{u}_g + (\alpha_\ell\rho_\ell e_\ell)\cdot \underline{u}_\ell\right) = -P\cdot\left[\nabla\left(\alpha_g\cdot \underline{u}_g + \alpha_\ell\cdot \underline{u}_\ell\right)\right] + q_{wg} + q_{w\ell} + q_{dg} + q_{d\ell} \quad (3\text{-}86)$$

3.4.5 Closure of the Conservation Equations

Closure is obtained for these equations using normal thermodynamic relations and specifications for the interfacial drag coefficients (C_i), the interfacial heat transfer (q_{ig} and $q_{i\ell}$), the phase-change rate (Γ), the wall-shear coefficients (C_{wg} and $C_{w\ell}$), and the wall heat flows (q_{wg} and $q_{w\ell}$).

The phase-change rate required by the equation set is evaluated from a simple thermal energy-jump relation:

$$\Gamma = \frac{q_{ig} + q_{i\ell}}{h_v^* - h_\ell^*} \quad (3\text{-}87)$$

where:

$$q_{ig} = \frac{P_v}{P}\cdot h_{ig}A_i\cdot\frac{T_g - T_S(P_v)}{V_c} \quad (3\text{-}88)$$

and

$$q_{i\ell} = h_{i\ell}A_i\cdot\frac{T_\ell - T_S(P_v)}{V_c} \quad (3\text{-}89)$$

Here A_i is the interfacial area, h_{ig} and $h_{i\ell}$ are HTCs, and $T_S(P_v)$ is the saturation temperature corresponding to the partial steam pressure. The term Γ^+ is equal to Γ for positive Γ and zero for negative Γ; Γ^- is equal to Γ for negative Γ and zero for positive Γ. The quantities h_v^* and h_ℓ^* are the appropriate enthalpies of the vapor and liquid, respectively. These enthalpies are the bulk fluid enthalpy for the phase moving to the interface and the saturation enthalpy for the product of the phase change.

Using Newton's law of cooling extended to a thermal non-equilibrium situation, the wall heat-transfer terms assume the form:

$$q_{wg} = h_{wg}A_w\cdot\frac{T_w - T_g}{V_c} \quad (3\text{-}90)$$

and

$$q_{w\ell} = h_{w\ell} A_w \cdot \frac{T_w - T_\ell}{V_c} \tag{3-91}$$

where A_w is the actual heated surface area. The h_{wg} and $h_{w\ell}$ of the cell include the information regarding the portion of the wall having gas and liquid contact.

The mass equations are written in fully conservative form to permit the construction of a numerical scheme that rigorously conserves some measure of the system fluid mass. The energy equations are written in a partially conservative form to make numerical solution simpler than would be possible if the fully conservative form (bulk kinetic-energy terms included) were used. The non-conservative form of the momentum equations also permits simpler numerical solution strategies and can generally be justified because the presence of wall friction makes the fully conservative form of the momentum equation far less useful.

3.5 ONE-DIMENSIONAL COMPONENT COMPUTATIONAL CELL STRUCTURE (MODEL AS CODED)

3.5.1 Introduction

A one-dimensional component is divided into a number of one-dimensional computational cells as shown in Figure 3-6. The five partial differential equations are solved using a staggered difference scheme in which the gas/liquid velocities are obtained at the cell interfaces, and the void fraction, pressure and liquid, and vapor temperatures are obtained at the cell centers. The subscript j denotes a cell centered quantity and subscripts j-1/2 and j+1/2 denote the cell interfaces.

3.5.2 One-Dimensional Component Computational Mesh

The geometry of the mass and energy control volumes is characterized by five independent variables: axial length ΔX_j, volume V_j, cross-sectional areas at the cell faces $A_{j-1/2}$, $A_{j+1/2}$, and the hydraulic diameter D_h. All of these are specified by the user. Associated with each fluid cell is a one-dimensional heat slab. This has a surface area in contact with the fluid which is consistent with the volume and length of the energy control volume. The geometry of the heat slab is characterized by a radius and a thickness.

The momentum control volume is centered at the cell interface j+1/2 and has faces at the cell centers on either side i.e., at j and j+1. The geometry of the momentum control volume is characterized by the length,

$$\overline{\Delta X}_{j+1/2} = \frac{1}{2}\left(\Delta X_j + \Delta X_{j+1}\right) \tag{3-92}$$

volume,

$$\overline{V}_{j+1/2} = \frac{1}{2}\left(V_j + V_{j+1}\right) \tag{3-93}$$

flow areas,

$$A_j = \frac{V_j}{\Delta X_j} \tag{3-94}$$

$$A_{j+1} = \frac{V_{j+1}}{\Delta X_{j+1}} \tag{3-95}$$

and the hydraulic diameter D_h. The geometry of the momentum control volume is principally determined by the geometry of the corresponding mass and energy control volumes.

3.5.3 One-Dimensional Component Finite Difference Formulation

When fluid flow is modeled with an explicit method, timestep sizes are restricted by the Courant limit as:

$$\Delta t \le k \cdot \frac{\Delta x}{|u| + c} \tag{3-96}$$

where Δx is a characteristic mesh length, u is the flow velocity, c is the speed of sound, and parameter k varies in value depending on the details of the method, but here can be taken to be 1.0. This simple class of methods is appropriate when it is important to track the details of pressure wave propagation (e.g., shock waves). However, in most reactor transients, this level of detail is not important. At most, continuity waves (moving liquid levels or froth fronts) must be followed. Frequently the transient is simply an evolution between quasi-steady states.

Both the Implicit Continuous Eulerian (ICE) and semi-implicit methods relax the explicit restrictions on timestep size by evaluating terms involved in pressure wave propagation at the new (n+1) time level. For a simple form of the momentum equation, this requires new time values in the pressure gradient term as given by:

$$\frac{\left(u_{j+1/2}^{n+1} - u_{j+1/2}^{n}\right)}{\Delta t} + u_{j+1/2}^{n} \left.\frac{\partial u^n}{\partial x}\right|_{j+1/2} + \frac{1}{\langle \rho \rangle_{j+1/2}^{n}} \frac{\left(P_{j+1}^{n+1} - P_j^{n+1}\right)}{\Delta x} + K_{j+1/2}^{n} u_{j+1/2}^{n+1} \left|u_{j+1/2}^{n}\right| = 0 \tag{3-97}$$

Similarly, relaxation of the restrictions on timestep size also requires that velocities involved in flux of mass and energy be evaluated at the new time level. The equations then become:

$$\frac{\left(\rho_j^{n+1} - \rho_j^{n}\right)}{\Delta t} + \frac{\partial}{\partial x_j}\left(\rho^n u^{n+1}\right) = 0 \tag{3-98}$$

$$\frac{\left(\rho_j^{n+1} e_j^{n+1} - \rho_j^{n} e_j^{n}\right)}{\Delta t} + \frac{\partial}{\partial x_j}\left(\rho^n e^n u^{n+1}\right) + P_j^{n+1} \frac{\left(u_{j+1/2}^{n+1} - u_{j-1/2}^{n+1}\right)}{\Delta x} \tag{3-99}$$

where, heat sources or sinks = 0.

By using the above equation structure, information on a pressure disturbance in any cell is available to any other cell during the same timestep. This eliminates the sound speed from the Courant stability limit, leaving what is commonly referred to as the "material Courant" stability limit $\left(\Delta t < (\Delta x)/|u|\right)$. The absolute value of flow velocity remains in the denominator of the expression because information relevant to continuity waves is still propagated only one cell per timestep by the semi-implicit method.

Completion of the problem definition requires a choice of two independent variables from the four thermodynamic variables: pressure, temperature, density, and specific internal energy. Density is not a good choice because of the need to model liquid solid regions. Given the low compressibility of liquid, a small error in a solution for density can translate to a significant error in pressure. When pressure is designated as an independent variable, a small error in the solution for pressure results in an even smaller fractional error in density. The choice of the second independent variable is driven by considerations beyond the simple equations presented above. Multiphase and multicomponent systems tend toward an equilibrium in which the phases and/or components are all at the same temperature. This behavior is reflected in constitutive relations for interphase (or wall-to-fluid) heat transfer that depend on differences of temperatures and that must be evaluated implicitly with respect to these temperature differences in the numerical equations. When the gas phase contains a mixture of species, all species are assumed to be at the same temperature. Selecting temperature as an independent variable in these situations can significantly simplify final solution of the equations.

Equations of state provide density and internal energy as functions of pressure and temperature. The relationships are generally nonlinear; therefore, the combination of discretized flow equations and state equations yields a coupled set of nonlinear equations. A key feature of this program is that an iterative method is used to obtain a solution to the nonlinear equations. The nonlinear equations are not simply replaced by a linearized approximation.

A stability analysis of these semi-implicit equations introduces limitations on weighting factors used for cell-edge averages. The equations are unconditionally unstable unless:

$$w_{j+1/2} \geq (1/2)\left(1+\frac{\Delta t|u_{j+1/2}|}{\Delta x_{j+1/2}}\right) \text{ for } u_{j+1/2} \geq 0 \tag{3-100}$$

$$w_{j+1/2} \leq (1/2)\left(1-\frac{\Delta t|u_{j+1/2}|}{\Delta x_{j+1/2}}\right) \text{ for } u_{j+1/2} < 0 \tag{3-101}$$

When the inequalities are replaced with equalities in the above expression, a difference scheme with the minimal permitted numerical diffusion results. However, experience with a range of two-phase flow problems has resulted in the final adoption of the following more robust choice of weighting factors:

$$w_{j+1/2} = 1 \text{ for } u_{j+1/2} \geq 0$$
$$w_{j+1/2} = 0 \text{ for } u_{j+1/2} < 0 \tag{3-102}$$

This is the standard donor cell difference method.

3.5.3.1 Semi-Implicit Formulation

The existing solution procedure relies on the finite-difference momentum equations containing no more than the first power of the new-time velocity. This permits a direct solution for u^{n+1} as a linear function of adjacent new-time pressures. First, assume that the new-time velocity is not very different from the old-time velocity, or:

$$u^{n+1}_{j+1/2} = u^{n}_{j+1/2} + \delta u_{j+1/2} \tag{3-103}$$

Now, substitute this expression into the fully implicit wall friction term as follows:

$$\begin{aligned} K^{n}_{j+1/2} u^{n+1}_{j+1/2} \left| u^{n+1}_{j+1/2} \right| &= K^{n}_{j+1/2} \left(u^{n}_{j+1/2} + \delta u_{j+1/2} \right) \left| u^{n}_{j+1/2} + \delta u_{j+1/2} \right| \\ &= 2K^{n}_{j+1/2} \left| u^{n}_{j+1/2} \right| \delta u_{j+1/2} + K^{n}_{j+1/2} u^{n}_{j+1/2} \left| u^{n}_{j+1/2} \right| + 0\left(\delta u^2\right) \end{aligned} \tag{3-104}$$

Finally, drop terms containing δu^2 and replace δu with the difference between the new- and old-time velocity to give:

$$K^{n}_{j+1/2} u^{n+1}_{j+1/2} \left| u^{n+1}_{j+1/2} \right| \approx 2K^{n}_{j+1/2} u^{n+1}_{j+1/2} \left| u^{n}_{j+1/2} \right| - K^{n}_{j+1/2} u^{n}_{j+1/2} \left| u^{n}_{j+1/2} \right| \tag{3-105}$$

In the two-phase flow equations, the same linearized implicit approximation is applied to the interfacial drag term.

When using the semi-implicit equations as part of the Stability-Enhancing Two Step (SETS) method, it was found that a linearization of the implicit momentum-flux term can improve the stability of the momentum equation. The direct impact on the semi-implicit equations is reflected in the following equation:

$$u_{j+1/2} \left. \frac{\partial u}{\partial x} \right|_{j+1/2} = \left[\beta u^{n+1}_{j+1/2} + (1-\beta) u^{n}_{j+1/2} \right] \left. \frac{\partial u^{n}}{\partial x} \right|_{j+1/2} \tag{3-106}$$

where:

$$\beta = \begin{bmatrix} 1 \text{ for } \left.\frac{\partial u^n}{\partial x}\right|_{j+1/2} \geq 0 \\ 0 \text{ for } \left.\frac{\partial u^n}{\partial x}\right|_{j+1/2} < 0 \end{bmatrix}$$

With the special modifications to momentum-flux and friction terms, the finite-difference form of the momentum equation becomes:

$$\frac{\left(u_{j+1/2}^{n+1} - u_{j+1/2}^{n}\right)}{\Delta t} + \left[\beta u_{j+1/2}^{n+1} + (1-\beta) u_{j+1/2}^{n}\right]\left(\frac{\partial u^n}{\partial x}\right)\Bigg|_{j+1/2} + \frac{1}{\langle \rho \rangle_{j+1/2}^{n}} \frac{\left(P_{j+1}^{n+1} - P_{j}^{n+1}\right)}{\Delta x} \qquad (3\text{-}107)$$
$$+ 2K_{j+1/2}^{n} u_{j+1/2}^{n+1} \left|u_{j+1/2}^{n}\right| - K_{j+1/2}^{n} u_{j+1/2}^{n} \left|u_{j+1/2}^{n}\right| = 0$$

3.5.3.1.1 Semi-Implicit Method Adapted to Two-Phase Flow

Extension of the numerical method to the two-phase, two-fluid model is relatively straightforward. Special modifications to the method are necessary to treat changes from two-phase to single-phase flow and are described below. Source terms are present to model phase change and heat transfer. These are generally implicit with respect to driving temperature difference and explicit with respect to any coefficient. The importance of gravitationally driven liquid flow requires an accurate model of gravitational force along the direction of motion. This uses an input angle (θ) between a vector from the center of cell j to the center of cell j+1 and a vector directed against gravity. In the application of the code, θ is more generally the inverse cosine ($\cos^{-1}$) of the change in elevation between cell centers divided by the flow length between cell centers.

To shorten notation in the following difference equations, some subscripts associated with location have been eliminated. For velocities not contained in spatial differences, the subscript denoting spatial location is assumed to be j+1/2. For cell-centered variables, the assumed subscript is j. The phrase "combined gas" refers to the mixture of non-condensable gas and steam, which is assumed to move with no interspecies diffusion.

Semi-Implicit Momentum Equations

Combined Gas

$$\begin{aligned}&\frac{\left(u_g^{n+1}-u_g^n\right)}{\Delta t}+\left[\beta_g u_g^{n+1}+\left(1-\beta_g\right)u_g^n\right]\nabla_{j+1/2}u_g^n\\&+\frac{C_i^n\left|u_g^n-u_\ell^n\right|}{\left\langle\alpha_g\rho_g\right\rangle_{j+1/2}^n}\left[2\left(u_g^{n+1}-u_\ell^{n+1}\right)-\left(u_g^n-u_\ell^n\right)\right]\\&+\frac{1}{\left\langle\rho_g\right\rangle_{j+1/2}^n}\frac{\left(P_{j+1}^{n+1}-P_j^{n+1}\right)}{\Delta x_{j+1/2}}+\frac{\Gamma_{j+1/2}^{+n}}{\left\langle\alpha_g\rho_g\right\rangle_{j+1/2}^n}\left(u_g^{n+1}-u_\ell^{n+1}\right)\\&+\frac{C_{wg}}{\left\langle\alpha_g\rho_g\right\rangle_{j+1/2}^n}\left(2u_g^{n+1}-u_g^n\right)\left|u_g^n\right|+g\cos\theta=0\end{aligned}\tag{3-108}$$

Liquid

$$\begin{aligned}&\frac{\left(u_\ell^{n+1}-u_\ell^n\right)}{\Delta t}+\left[\beta_\ell u_\ell^{n+1}+\left(1-\beta_\ell\right)u_\ell^n\right]\nabla_{j+1/2}u_\ell^n\\&+\frac{C_i^n\left|u_\ell^n-u_g^n\right|}{\left\langle\alpha_\ell\,\rho_\ell\right\rangle_{j+1/2}^n}\left[2\left(u_\ell^{n+1}-u_g^{n+1}\right)-\left(u_\ell^n-u_g^n\right)\right]\\&+\frac{1}{\left\langle\rho_\ell\right\rangle_{j+1/2}^n}\frac{\left(P_{j+1}^{n+1}-P_j^{n+1}\right)}{\Delta x_{j+1/2}}+\frac{\Gamma_{j+1/2}^{-n}}{\left\langle\alpha_\ell\,\rho_\ell\right\rangle_{j+1/2}^n}\left(u_\ell^{n+1}-u_g^{n+1}\right)\\&+\frac{C_{w\ell}}{\left\langle\alpha_\ell\,\rho_\ell\right\rangle_{j+1/2}^n}\left(2u_\ell^{n+1}-u_\ell^n\right)\left|u_\ell^n\right|+g\cos\theta=0\end{aligned}\tag{3-109}$$

Semi-Implicit Mass Equations

Combined Gas

$$\frac{\alpha_j^{n+1}\rho_{gj}^{n+1}-\alpha_j^n\rho_{gj}^n}{\Delta t}+\nabla_j\cdot\left[\alpha^n\rho_g^n u_g^{n+1}\right]=\Gamma^{n+1}\tag{3-110}$$

Non-Condensable Gas

$$\frac{\left[\alpha_{g,j}^{n+1}\rho_{aj}^{n+1}-\alpha_{g,j}^n\rho_{aj}^n\right]}{\Delta t}+\nabla_j\cdot\left[\alpha_g{}^n\rho_a^n u_g^{n+1}\right]=0\tag{3-111}$$

Liquid

$$\frac{[\alpha_{\ell,j}^{n+1}\rho_{\ell j}^{n+1}-(1-\alpha_j^n)\rho_{\ell j}^n]}{\Delta t}+\nabla_j\cdot[\alpha_\ell^n\rho_\ell^n u_\ell^{n+1}]=-\Gamma^{n+1} \tag{3-112}$$

Liquid Solute

$$\frac{[\alpha_\ell^{n+1}\tilde{m}^{n+1}\rho_\ell^{n+1}-\alpha_\ell^n m^n\rho_\ell^n]}{\Delta t}+\nabla_j\cdot[\alpha_\ell^n m^n\rho_\ell^n u_\ell^{n+1}]=0 \tag{3-113}$$

$$m^{n+1}=\min\left[\tilde{m}^{n+1}+\frac{S_c^n}{\alpha_\ell^{n+1}\rho_\ell^{n+1}},m_{max}\right] \tag{3-114}$$

and

$$S_c^{n+1}=(\tilde{m}^{n+1}-m^{n+1})\alpha_\ell^{n+1}\rho_\ell^{n+1}+S_c^n \tag{3-115}$$

Semi-Implicit Energy Equations

Combined Gas

$$\frac{[\alpha_{g,j}^{n+1}\rho_{gj}^{n+1}e_{gj}^{n+1}-\alpha_{g,j}^n\rho_{gj}^n e_{gj}^n]}{\Delta t}+\nabla_j\cdot[\alpha_g^n\rho_g^n e_g^n u_g^{n+1}]+P^{n+1}\left[\frac{(\alpha_g^{n+1}-\alpha_g^n)}{\Delta t}+\nabla_j\cdot(\alpha_g^n u_g^{n+1})\right] \tag{3-116}$$
$$=q_{wg}^{n+1}+q_{dg}^n+q_{ig}^{n+1}+\Gamma^{n+1}h_{sg}^{n+1}$$

Total Fluid (Gas and Liquid)

$$\frac{[\alpha_{g,j}^{n+1}\rho_{gj}^{n+1}e_{gj}^{n+1}+\alpha_{\ell,j}^{n+1}\rho_{\ell j}^{n+1}e_{\ell j}^{n+1}]-\alpha_{g,j}^n\rho_{gj}^n e_{gj}^n+\alpha_{\ell,j}^n(\rho_{\ell j}^n e_{\ell j}^n)}{\Delta t}$$
$$+\nabla_j\cdot[\alpha_g^n\rho_g^n e_g^n u_g^{n+1}+\alpha_\ell^n\rho_\ell^n e_\ell^n u_\ell^{n+1}]+P^{n+1}\nabla_j\cdot[\alpha_\ell^n u_\ell^{n+1}+\alpha_{g,j}^n u_g^{n+1}] \tag{3-117}$$
$$=q_{wg}^{n+1}+q_{w\ell}^{n+1}+q_{d\ell}^n+q_{dg}^n$$

The wall heat transfer to the gas and liquid, q_{wg} and $q_{w\ell}$, and the interfacial mass-transfer rate, Γ, also require further definition. Note the mixture of old- and new-time values in these terms. The choice of old-time heat transfer coefficients was driven by the desire to simplify the implementation of the method, but can result in bounded instabilities during calculations. These terms are given by:

$$q_{w\ell}^{n+1}=h_{w\ell}^n A_w(T_w^n-T_\ell^{n+1})/vol \tag{3-118}$$

$$q_{wg}^{n+1}=h_{wg}^n A_w(T_w^n-T_g^{n+1})/vol \tag{3-119}$$

and

$$\Gamma^{n+1} = \frac{-\left(q_{ig}^{n+1} + q_{i\ell}^{n+1}\right)}{\left(h_v'\right)^{n+1} - \left(h_\ell'\right)^{n+1}} \tag{3-120}$$

where:

$$q_{ig}^{n+1} = \left(\frac{P_v}{P}\right)^n h_{ig}^n A_i^n \frac{\left(T_{sat}^{n+1} - T_g^{n+1}\right)}{vol} \tag{3-121}$$

and

$$q_{i\ell}^{n+1} = h_{i\ell}^n A_i^n \frac{\left(T_{sat}^{n+1} - T_\ell^{n+1}\right)}{vol} \tag{3-122}$$

Further definition is also needed for a special set of density averages used in the momentum equations. Cell-edge densities used in the denominator of Equations 3-108 and 3-109 are defined to produce a good prediction of hydrostatic pressure heads. For example, the edge-average gas macroscopic density is defined as:

$$\left\langle \alpha_g \rho \right\rangle_{j+1/2}^n = \frac{\Delta x_j \left(\alpha_g \rho\right)_j^n + \Delta x_{j+1} \left(\alpha_g \rho\right)_{j+1}^n}{\Delta x_j + \Delta x_{j+1}} \tag{3-123}$$

A similar definition holds for the cell-edge liquid macroscopic density. The edge-average microscopic densities are somewhat more complex. For example,

$$\left\langle \rho_g \right\rangle_{j+1/2}^n = \left\langle \alpha_g \rho_g \right\rangle_{j+1/2}^n \left[\frac{\Delta x_j \alpha_{g,j}^n + \Delta x_{j+1} \alpha_{g,j+1}^n}{\Delta x_j + \Delta x_{j+1}} \right]^{-1} \tag{3-124}$$

This particular average is necessary for consistency within the SETS equations, where macroscopic densities have a more fundamental importance within the solution.

The above finite volume-flow equations hold only when a two-phase mixture is present at both the old-and new-time levels. Modifications are necessary when the old- or new-time level fluid state is single phase, which is described in the next section.

The momentum equations are evaluated in subroutine TF1DS1 for 1D flow. This evaluation takes the solution form illustrated by Equations 3-108 and 3-109 for velocities as linear functions of the new-time pressure gradient. Terms in the mass and energy equations are evaluated in subroutine TF1DS (TFPLN for a plenum). This includes terms for the Jacobian matrix needed to solve this nonlinear system with a Newton iteration. The iteration is driven by subroutine HOUT.

3.5.3.1.2 Basics of the SETS Method

The goal of the SETS method was to eliminate the material Courant stability limit with minimal alterations to the existing semi-implicit method. Given the success of the semi-implicit method in propagating information about sound waves, a correction step was devised to perform a similar propagation of information on continuity waves. As a very simple example, consider the single-phase mass equation. For each timestep, the semi-implicit method is used to establish the new-time velocity field. Next, the following correction (or "stabilizer") step is used to obtain a final value of the new-time density:

$$\frac{\left(\rho_j^{n+1}-\rho_j^n\right)}{\Delta t}+\frac{\partial}{\partial x_j}\left(\rho^{n+1}u^{n+1}\right)=0 \tag{3-125}$$

On the surface, this appears to be a fully implicit finite-difference equation. It is not, however, because the new-time velocities (u^{n+1}) are all known numbers obtained from the semi-implicit step. New-time densities are the only unknowns in this system of equations. Information about a density change in any given computational cell is propagated to all other cells within the same timestep.

The pattern of evaluation of semi-implicit and stabilizer equations is not the same for the momentum equations as it is for the mass and energy equations. All mass and energy equations follow the above pattern of a semi-implicit step followed by a stabilizer step. However, the analogous momentum-stabilizer equation is evaluated before the evaluation of the semi-implicit equations. A solution is better behaved when the velocity used for transport of mass and energy is a direct result of a pressure-balanced solution.

For the special example of 1D single-phase flow, the SETS difference equations are:

Stabilizer Momentum Equation

$$\begin{aligned}&\frac{\left(\tilde{u}_{j+1/2}^{n+1}-u_{j+1/2}^n\right)}{\Delta t}+u_{j+1/2}^n\left.\frac{\partial\tilde{u}^{n+1}}{\partial x}\right|_{j+1/2}\\&+\frac{1}{\langle\rho\rangle_{j+1/2}^n}\frac{P_{j+1}^n-P_j^n}{\Delta x}+K_{j+1/2}^n\left(2\tilde{u}_{j+1/2}^{n+1}-u_{j+1/2}^n\right)\left|u_{j+1/2}^n\right|=0\end{aligned} \tag{3-126}$$

Semi-Implicit Equation Step

$$\begin{aligned}&\frac{\left(u_{j+1/2}^{n+1}-u_{j+1/2}^n\right)}{\Delta t}+u_{j+1/2}^n\left.\frac{\partial\tilde{u}^{n+1}}{\partial x}\right|_{j+1/2}\\&+\frac{1}{\langle\rho\rangle_{j+1/2}^n}\frac{\tilde{P}_{j+1}^{n+1}-\tilde{P}_j^{n+1}}{\Delta x}+K_{j+1/2}^n u_{j+1/2}^{n+1}\left|u_{j+1/2}^n\right|=0\end{aligned} \tag{3-127}$$

$$\frac{\left(\tilde{\rho}_j^{n+1}-\rho_j^n\right)}{\Delta t}+\frac{\partial}{\partial x_j}\rho^n u^{n+1}=0 \tag{3-128}$$

and

$$\frac{\left(\tilde{\rho}_j^{n+1}\tilde{e}_j^{n+1}-(\rho e)_j^n\right)}{\Delta t}+\frac{\partial}{\partial x_j}\rho^n e^n u^{n+1}+\tilde{P}_j^{n+1}\frac{u_{j+1/2}^{n+1}-u_{j-1/2}^{n+1}}{\Delta x}=0 \tag{3-129}$$

Stabilizer Mass and Energy Equations

$$\frac{\left(\rho_j^{n+1}-\rho_j^n\right)}{\Delta t}+\frac{\partial}{\partial x_j}\rho^n u^{n+1}=0 \tag{3-130}$$

and

$$\frac{(\rho e)_j^{n+1}-(\rho e)_j^n}{\Delta t}+\frac{\partial}{\partial x_j}(\rho e)^{n+1}u^{n+1}+\tilde{P}_j^{n+1}\frac{u_{j+1/2}^{n+1}-u_{j-1/2}^{n+1}}{\Delta x}=0 \tag{3-131}$$

A tilde above a variable indicates that it is a first estimate of the new-time value. Actual new-time variables have a superscript "n+1" and no tilde. Note that the only result of the above semi-implicit step appears to be just a new-time velocity field. In practice the situation is more complex. To save computational time, temperatures and pressures that are fully consistent with the densities and energies obtained from solving the stabilizer mass and energy equations are never calculated. If the correlation used to obtain an old-time wall friction coefficient requires temperature or pressure, the values used would be those obtained during the solution of the semi-implicit equation step. Note that each of the above equations is solved once per timestep.

3.5.3.1.3 Enhancements to the SETS Method

As with the semi-implicit method, linearized implicit terms are introduced in the momentum equation to improve the behavior of friction and momentum transfer. The improved friction terms are identical to those derived in Section 3.5.3.1. The momentum-transfer terms are somewhat more complex. First, the new-time velocity and velocity gradient are linearized in the following forms:

$$\tilde{u}_{j+1/2}^{n+1}=u_{j+1/2}^n+\delta u_{j+1/2} \tag{3-132}$$

$$\nabla\tilde{u}_{j+1/2}^{n+1}=\nabla\tilde{u}_{j+1/2}^n+\delta\left(\nabla\tilde{u}_{j+1/2}\right) \tag{3-133}$$

Substitution of these relationships into the implicit form of the momentum-transfer term gives:

$$\begin{aligned} u_{j+1/2}^{n+1}\nabla\tilde{u}_{j+1/2}^{n+1} &= \left(u_{j+1/2}^{n}+\delta u_{j+1/2}\right)\left(\nabla\tilde{u}_{j+1/2}^{n}+\delta\left(\nabla u_{j+1/2}\right)\right) \\ &= u_{j+1/2}^{n}\nabla\tilde{u}_{j+1/2}^{n}+\delta u_{j+1/2}^{n}\nabla\tilde{u}_{j+1/2}^{n}+u_{j+1/2}^{n}\delta\left(\nabla u_{j+1/2}\right)+\delta u_{j+1/2}^{n}\delta\left(\nabla u_{j+1/2}\right) \end{aligned} \tag{3-134}$$

Keeping only terms with no more than the first power of a variation and back-substituting the variations in terms of differences between old- and new-time variables gives:

$$\tilde{u}_{j+1/2}^{n+1}\nabla\tilde{u}_{j+1/2}^{n+1} \approx u_{j+1/2}^{n}\nabla\tilde{u}_{j+1/2}^{n+1}+\left(\tilde{u}_{j+1/2}^{n}-u_{j+1/2}^{n}\right)\nabla\tilde{u}_{j+1/2}^{n} \tag{3-135}$$

When using the semi-implicit equations as part of the SETS method, it was found that a linearization of the implicit momentum-flux term can improve the stability of the motion equation. Details of this linearization are presented in the next subsection. The direct impact on the semi-implicit equations is reflected in the following equation:

$$u_{j+1/2}\nabla u_{j+1/2}^{n+1} = \left[\beta u_{j+1/2}^{n+1}+(1-\beta)u_{j+1/2}^{n}\right]\nabla u_{j+1/2}^{n+1} \tag{3-136a}$$

Therefore:

$$\tilde{u}_{j+1/2}^{n+1}\nabla\tilde{u}_{j+1/2}^{n+1} \approx u_{j+1/2}^{n}\nabla_{j+1/2}\tilde{u}_{j+1/2}^{n+1}+\beta\left(\tilde{u}_{j+1/2}^{n+1}-u_{j+1/2}^{n}\right)\nabla_{j+1/2}\tilde{u}_{j+1/2}^{n} \tag{3-136}$$

where:

$$\beta = \begin{bmatrix} 1 \text{ for } \left.\dfrac{\partial u^{n}}{\partial x}\right|_{j+1/2} \geq 0 \text{ and } u_{j+1/2}^{n}\tilde{u}_{j+1/2}^{n} > 0 \\ 0 \text{ for } \left.\dfrac{\partial u^{n}}{\partial x}\right|_{j+1/2} < 0 \text{ and } u_{j+1/2}^{n}\tilde{u}_{j+1/2}^{n} \leq 0 \end{bmatrix}$$

With these modifications, the final form of the stabilizer momentum equation is:

$$\begin{aligned} &\frac{\left(\tilde{u}_{j+1/2}^{n+1}-u_{j+1/2}^{n}\right)}{\Delta t}+u_{j+1/2}^{n}\nabla_{j+1/2}\tilde{u}_{j+1/2}^{n+1}+\beta\left(\tilde{u}_{j+1/2}^{n+1}-u_{j+1/2}^{n}\right)\nabla_{j+1/2}\tilde{u}_{j+1/2}^{n} \\ &+\frac{1}{\langle\rho\rangle_{j+1/2}^{n}}\frac{\left(P_{j+1}^{n}-P_{j}^{n}\right)}{\Delta x}+K_{j+1/2}^{n}\left(2\tilde{u}_{j+1/2}^{n+1}-u_{j+1/2}^{n}\right)\left|u_{j+1/2}^{n}\right| = 0 \end{aligned} \tag{3-137}$$

The following revised form of the motion equation in the semi-implicit step has a minor change in the flux term to increase the robustness of the method further:

$$\frac{\left(u_{j+1/2}^{n+1}-u_{j+1/2}^{n}\right)}{\Delta t}+u_{j+1/2}^{n}\nabla_{j+1/2}\tilde{u}_{j+1/2}^{n+1}+\beta\left(u_{j+1/2}^{n+1}-u_{j+1/2}^{n}\right)\nabla_{j+1/2}\tilde{u}_{j+1/2}^{n} + \frac{1}{\langle\rho\rangle_{j+1/2}^{n}}\frac{\left(P_{j+1}^{n+1}-P_{j}^{n+1}\right)}{\Delta x}+K_{j+1/2}^{n}\left(2u_{j+1/2}^{n+1}-u_{j+1/2}^{n}\right)\left|u_{j+1/2}^{n}\right|=0 \tag{3-138}$$

One significant modification is introduced in the stabilizer mass and energy equations. To save computational effort and overhead associated with the communication of more variables, the stabilizer equations listed in the previous section are not directly solved. Instead, the actual equations solved are the result of subtracting the semi-implicit equations from the corresponding stabilizer equations.

Stabilizer Mass and Energy Equations as Solved

$$\frac{\left(\rho_{j}^{n+1}-\tilde{\rho}_{j}^{n+1}\right)}{\Delta t}+\frac{\partial}{\partial x_{j}}\left(\rho^{n+1}u^{n+1}\right)=\frac{\partial}{\partial x_{j}}\left(\rho^{n}u^{n+1}\right) \tag{3-139}$$

and

$$\frac{(\rho e)_{j}^{n+1}-\tilde{\rho}_{j}^{n+1}\tilde{e}_{j}^{n+1}}{\Delta t}+\frac{\partial}{\partial x_{j}}\left((\rho e)^{n+1}u^{n+1}\right)=\frac{\partial}{\partial x_{j}}\left((\rho e)^{n}u^{n+1}\right) \tag{3-140}$$

The advantage of this approach is more apparent in the application of the method to the full two-phase flow equations. In that case, all source terms (mass and energy transfer) are canceled out of the equations to be solved. The disadvantage of this approach is that the rigorous mass conservation of Equation 3-131 is lost. Mass conservation associated with Equation 3-139 depends on the level of convergence of the iterative solution for the semi-implicit equations.

3.5.3.1.4 The SETS Method Adapted to Two-Phase Flow

The two-phase forms of the SETS equations contain some significant modifications. The first, which improves code robustness, is an initial evaluation of the momentum equations that is used solely to provide an improved prediction of the interfacial force terms needed in the standard stabilizer momentum equations.

Equations for Prediction of Interfacial Drag Force

Combined Gas

$$\begin{aligned}
&\frac{\left(\tilde{u}_g^{n+1}-u_g^n\right)}{\Delta t}+u_g^n\nabla_{j+1/2}\tilde{u}_g^n+\beta\left(\tilde{u}_g^{n+1}-u_g^n\right)\nabla_{j+1/2}\tilde{V}_g^n \\
&+\frac{C_i^n\left|u_g^n-u_\ell^n\right|}{\left\langle\alpha_g\rho_g\right\rangle_{j+1/2}^n}\left[2\left(\tilde{u}_g^{n+1}-\tilde{u}_\ell^{n+1}\right)-\left(u_g^n-u_\ell^n\right)\right] \\
&+\frac{1}{\left\langle\rho_g\right\rangle_{j+1/2}^n}\frac{\left(P_{j+1}^n-P_j^n\right)}{\Delta x_{j+1/2}}+\frac{\Gamma_{j+1/2}^{+n}}{\left\langle\alpha_g\rho_g\right\rangle_{j+1/2}^n}\left(\tilde{u}_g^{n+1}-\tilde{u}_\ell^{n+1}\right) \\
&+\frac{C_{wg}}{\left\langle\alpha_g\rho_g\right\rangle_{j+1/2}^n}\left(2\tilde{u}_g^{n+1}-u_g^n\right)\left|u_g^n\right|+g\cos\theta=0
\end{aligned} \tag{3-141}$$

where "j+1/2" subscript on the velocity in the equation above was omitted for simplicity, and:

$$\begin{aligned}
\beta&=0,\ \text{if}\ \nabla_{j+1/2}u^n<0\quad\text{or}\quad u^n\tilde{u}^n<0 \\
&=1,\ \text{if}\ \nabla_{j+1/2}u^n\geq 0\quad\text{and}\quad u^n\tilde{u}^n\geq 0
\end{aligned};$$

Liquid

$$\begin{aligned}
&\frac{\left(\hat{u}_\ell^{n+1}-u_\ell^n\right)}{\Delta t}+u_\ell^n\nabla_{j+1/2}\tilde{u}_\ell^n+\beta\left(\hat{u}_\ell^{n+1}-u_\ell^n\right)\nabla_{j+1/2}\tilde{u}_\ell^n \\
&+\frac{C_i^n\left|u_g^n-u_\ell^n\right|}{\left\langle\alpha_\ell\rho_\ell\right\rangle_{j+1/2}^n}\left[2\left(\hat{u}_\ell^{n+1}-\hat{u}_g^{n+1}\right)-\left(u_\ell^n-u_g^n\right)\right] \\
&+\frac{1}{\left\langle\rho_\ell\right\rangle_{j+1/2}^n}\frac{\left(P_{j+1}^n-P_j^n\right)}{\Delta x_{j+1/2}}-\frac{\Gamma_{j+1/2}^{-n}}{\left\langle\alpha_\ell\rho_\ell\right\rangle_{j+1/2}^n}\left(\hat{u}_\ell^{n+1}-\hat{u}_g^{n+1}\right) \\
&+\frac{C_{w\ell}}{\left\langle\alpha_\ell\rho_\ell\right\rangle_{j+1/2}^n}\left(2\hat{u}_\ell^{n+1}-u_\ell^n\right)\left|u_\ell^n\right|+g\cos\theta=0
\end{aligned} \tag{3-142}$$

Edge-average densities follow the definitions provided in the discussion of the semi-implicit method [Equations 3-123 and 3-124].

The velocities obtained from the above equations are used to decouple the vapor and liquid stabilizer motion equations. The prediction of the interfacial force term is good enough such that the interfacial force term in the following stabilizer equations does not need to depend on the new-time stabilizer

velocities. As a result, the liquid stabilizer momentum equation contains only liquid stabilizer (tilde) velocities as unknowns. The liquid and gas equations are two completely independent systems of equations, which are solved separately.

Stabilizer Momentum Equations

Combined Gas

$$\frac{\left(\tilde{u}_g^{n+1}-u_g^n\right)}{\Delta t}+u_g^n\nabla_{j+1/2}\tilde{u}_g^{n+1}+\beta\left(\tilde{u}_g^{n+1}-u_g^n\right)\nabla_{j+1/2}\tilde{u}_g^n$$
$$+\frac{C_i^n\left|u_g^n-u_\ell^n\right|}{\left\langle\alpha_g\rho_g\right\rangle_{j+1/2}^n}\left[2\left(\hat{u}_g^{n+1}-\hat{u}_\ell^{n+1}\right)-\left(u_g^n-u_\ell^n\right)\right]$$
$$+\frac{1}{\left\langle\rho_g\right\rangle_{j+1/2}^n}\frac{\left(P_{j+1}^n-P_j^n\right)}{\Delta x_{j+1/2}}+\frac{\Gamma_{j+1/2}^{+n}}{\left\langle\alpha_g\rho_g\right\rangle_{j+1/2}^n}\left(\hat{u}_g^{n+1}-\hat{u}_\ell^{n+1}\right) \quad (3\text{-}143)$$
$$+\frac{C_{wg}}{\left\langle\alpha_g\rho_g\right\rangle_{j+1/2}^n}\left(2\hat{u}_g^{n+1}-u_g^n\right)\left|u_g^n\right|+g\cos\theta=0$$

Liquid

$$\frac{\left(\tilde{u}_\ell^{n+1}-u_\ell^n\right)}{\Delta t}+u_\ell^n\nabla_{j+1/2}\tilde{u}_\ell^{n+1}+\beta\left(\tilde{u}_\ell^{n+1}-u_\ell^n\right)\nabla_{j+1/2}\tilde{u}_\ell^n$$
$$+\frac{C_i^n\left|u_g^n-u_\ell^n\right|}{\left\langle\alpha_\ell\rho_\ell\right\rangle_{j+1/2}^n}\left[2\left(\hat{u}_\ell^{n+1}-\hat{u}_g^{n+1}\right)-\left(u_\ell^n-u_g^n\right)\right]$$
$$+\frac{1}{\left\langle\rho_\ell\right\rangle_{j+1/2}^n}\frac{\left(P_{j+1}^n-P_j^n\right)}{\Delta x_{j+1/2}}-\frac{\Gamma_{j+1/2}^{-n}}{\left\langle\alpha_\ell\rho_\ell\right\rangle_{j+1/2}^n}\left(\hat{u}_\ell^{n+1}-\hat{u}_g^{n+1}\right) \quad (3\text{-}144)$$
$$+\frac{C_{w\ell}}{\left\langle\alpha_\ell\rho_\ell\right\rangle_{j+1/2}^n}\left(2\tilde{u}_\ell^{n+1}-u_\ell^n\right)\left|u_\ell^n\right|+g\cos\theta=0$$

Momentum Equations for the SETS Semi-Implicit Step

The equations solved during the semi-implicit step are almost identical to those presented in Section 3.5.3.1.1 but are reproduced here in the Newton iteration scheme to avoid ambiguity in details of the implementation. The primary difference between the momentum equation in a pure semi-implicit method and its corresponding form in the semi-implicit step of SETS is the use of stabilizer velocities for momentum transport.

Combined-Gas Momentum Equation

$$(u_g)_{j+1/2}^{v+1}\cdot(1+A)+B\cdot\left((u_g)_{j+1/2}^{v+1}-(u_\ell)_{j+1/2}^{v+1}\right)+\frac{(\Delta t)^n}{(\rho_g)^n}\cdot\nabla\left((\delta P)^{v+1}\right)_{j+1/2}=(RHS_g)_{j+1/2}^{v} \quad (3\text{-}145)$$

Continuous Liquid Momentum Equation

$$(u_\ell)_{j+1/2}^{v+1}\cdot(1+C)+D\cdot\left((u_\ell)_{j+1/2}^{v+1}-(u_g)_{j+1/2}^{v+1}\right)+\frac{(\Delta t)^n}{(\rho_\ell)^n}\cdot\nabla\left((\delta P)^{v+1}\right)_{j+1/2}=(RHS_\ell)_{j+1/2}^{v} \quad (3\text{-}146)$$

where:

$$(RHS_g)^v=(u_g)^n-(\Delta t)^n\times\left[(u_g)^n\cdot\nabla(\tilde{u}_g)^{n+1}-\beta_g\cdot(u_g)^n\cdot\nabla(\tilde{u}_g)^n+\frac{1}{(\rho_g)^n}\cdot\nabla P^v\right.$$
$$\left.-\frac{(C_i)^n}{(\alpha_g\rho_g)^n}\cdot\left|(u_g)^n-(u_\ell)^n\right|\cdot\left((u_g)^n-(u_\ell)^n\right)-\frac{(C_{wg})^n}{(\alpha_g\rho_g)^n}\cdot\left|(u_g)^n\right|\cdot(u_g)^n+g\cdot\cos\theta\right] \quad (3\text{-}147)$$

$$(RHS_\ell)^v=(u_\ell)^n-(\Delta t)^n\times\left[(u_\ell)^n\cdot\nabla(\tilde{u}_\ell)^{n+1}-\beta_\ell\cdot(u_\ell)^n\cdot\nabla(\tilde{u}_\ell)^n+\frac{1}{(\rho_\ell)^n}\cdot\nabla P^v\right.$$
$$\left.-\frac{(C_i)^n}{(\alpha_\ell\rho_\ell)^n}\cdot\left|(u_\ell)^n-(u_g)^n\right|\cdot\left((u_\ell)^n-(u_g)^n\right)-\frac{(C_{w\ell})^n}{(\alpha_\ell\rho_\ell)^n}\cdot\left|(u_\ell)^n\right|\cdot(u_\ell)^n+g\cdot\cos\theta\right] \quad (3\text{-}148)$$

$$A=(\Delta t)^n\times\left\{\beta_g\cdot\nabla(\tilde{u}_g)^n+\frac{(C_{wg})^n}{(\alpha_g\rho_g)^n}\cdot\left|(u_g)^n\right|\cdot 2\right\} \quad (3\text{-}149)$$

$$B=(\Delta t)^n\times\left\{\frac{(C_i)^n}{(\alpha_g\rho_g)^n}\cdot\left|(u_g)^n-(u_\ell)^n\right|\cdot 2+\frac{(\Gamma^+)^n}{(\alpha_g\rho_g)^n}\right\} \quad (3\text{-}150)$$

$$C=(\Delta t)^n\times\left\{\beta_\ell\cdot\nabla(\tilde{u}_\ell)^n+\frac{(C_{w\ell})^n}{(\alpha_\ell\rho_\ell)^n}\cdot\left|(u_\ell)^n\right|\cdot 2\right\} \quad (3\text{-}151)$$

$$D=(\Delta t)^n\times\left\{\frac{(C_i)^n}{(\alpha_\ell\rho_\ell)^n}\cdot\left|(u_\ell)^n-(u_g)^n\right|\cdot 2-\frac{(\Gamma^-)^n}{(\alpha_\ell\rho_\ell)^n}\right\} \quad (3\text{-}152)$$

$$\beta_g=\begin{cases}1 & \text{if } \nabla(\tilde{u}_g)^n\geq 0 \text{ and } (u_g)^n\cdot(\tilde{u}_g)^n\geq 0\\ 0 & \text{if } \nabla(\tilde{u}_g)^n<0 \text{ or } (u_g)^n\cdot(\tilde{u}_g)^n<0\end{cases} \quad (3\text{-}153)$$

$$\beta_\ell = \begin{cases} 1 & \text{if } \nabla(\tilde{u}_\ell)^n \geq 0 \text{ and } (u_\ell^n)\cdot(\tilde{u}_\ell^n) \geq 0 \\ 0 & \text{if } \nabla(\tilde{u}_\ell)^n < 0 \text{ or } (u_\ell^n)\cdot(\tilde{u}_\ell^n) < 0 \end{cases} \quad (3\text{-}154)$$

where:

$\tilde{u}_g$, $\tilde{u}_\ell$ = Stabilizer velocity
n = timestep number
ν = Newton iteration count

Basic Semi-Implicit Mass Equations

These equations differ from those in a pure semi-implicit method; the resulting void fraction and new-time thermodynamic variables are intermediate results. Final new-time values for these variables are formally set by the stabilizer mass and energy equations. Individual thermodynamic variables also are carefully distinguished from products that comprise macroscopic densities and energies. These macroscopic quantities [e.g., $(\alpha\rho_g)$] are a direct result of the solution of the stabilizer mass and energy equations at the end of the previous timestep. Another key difference is found in the modified form of the divergence operator, which can involve an unusual mixture of new- and old-time values [see Equation 3-160].

Combined Gas

$$\frac{[\tilde{\alpha}_{g,j}^{n+1}\tilde{\rho}_{gj}^{n+1} - (\alpha_g\rho_g)_j^n]}{\Delta t} + \nabla_j \cdot \left[(\alpha_g\rho_g)^n u_g^{n+1}\right] = \tilde{\Gamma}^{n+1} \quad (3\text{-}155)$$

Non-Condensable Gas

$$\frac{[\tilde{\alpha}_{g,j}^{n+1}\tilde{\rho}_{aj}^{n+1} - (\alpha_g\rho_a)_j^n]}{\Delta t} + \nabla_j \cdot \left[(\alpha_g\rho_a)^n u_g^{n+1}\right] = 0 \quad (3\text{-}156)$$

Liquid

$$\frac{\left|\tilde{\alpha}_{\ell,j}^{n+1}\ \tilde{\rho}_{\ell j}^{n+1} - [\alpha_\ell\ \rho_\ell]_j^n\right|}{\Delta t} + \nabla_j \cdot \left[\alpha_\ell\ \rho_\ell\right]^n u_\ell^{n+1} = -\tilde{\Gamma}^{n+1} \quad (3\text{-}157)$$

Basic Energy Equations

Combined Gas

$$\begin{aligned}&\frac{[\tilde{\alpha}_{g,j}^{n+1}\tilde{\rho}_{gj}^{n+1}\tilde{e}_{gj}^{n+1}-(\alpha_g\rho_g e_g)_j^n]}{\Delta t}+\nabla_j\cdot\left[(\alpha_g\rho_g e_g)^n u_g^{n+1}\right]\\&+\tilde{P}^{n+1}\left[\frac{(\tilde{\alpha}_g^{n+1}-\alpha_g^n)}{\Delta t}+\nabla_j\cdot(\alpha_g^n u_g^{n+1})\right]\\&=\tilde{q}_{wg}^{n+1}+q_{dg}^n+\tilde{q}_{ig}^{n+1}+\tilde{\Gamma}^{n+1}\tilde{h}_{sg}^{n+1}\end{aligned}\tag{3-158}$$

Total Fluid (Gas and Liquid)

$$\begin{aligned}&\frac{\left\{\tilde{\alpha}_{gj}^{n+1}\tilde{\rho}_{gj}^{n+1}\tilde{e}_{gj}^{n+1}+(1-\tilde{\alpha}_{gj}^{n+1})\tilde{\rho}_{gj}^{n+1}\tilde{e}_{gj}^{n+1}-\left[(\alpha_g\rho_g e_g)_j^n+\alpha_\ell\rho_\ell e_\ell\right]_j^n\right\}}{\Delta t}\\&+\nabla_j\cdot\left\{(\alpha_g\rho_g e_g)^n u_g^{n+1}+\left[\alpha_\ell\rho_\ell e_\ell\right]^n u_\ell^{n+1}\right\}\\&+\tilde{P}^{n+1}\nabla_j\cdot[\alpha_\ell^n u_\ell^{n+1}+\alpha_g^n u_g^{n+1}]\\&=\tilde{q}_{wg}^{n+1}+\tilde{q}_{w\ell}^{n+1}+q_{d\ell}^n+q_{dg}^n\end{aligned}\tag{3-159}$$

The divergence operator is revised during the semi-implicit step to improve modeling accuracy of situations in which flux can be predominately attributed to phase change in the cell for which the continuity equation is being evaluated. The idea is to use new-time information for that portion of the flux associated with the same cell as the equation (cell j). This makes the local solution more sensitive to variation in phase-change rates. In terms of the notation used for the basic definition of the divergence operator, the revised form is:

$$\begin{aligned}&\tilde{\nabla}_j\cdot(Y^n u_g^{n+1})=\\&\frac{\left[w_{j+1/2}Y_j'+(1-w_{j+1/2})Y_{j+1}^n\right]A_{j+1/2}u_{j+1/2}-\left(w_{j-1/2}Y_{j-1}^n+(1-w_{j-1/2})Y_j'\right)A_{j-1/2}u_{j-1/2}}{vol_j}\end{aligned}\tag{3-160}$$

The special feature of this operator is that all occurrences of Y_i^n in the normal finite-volume divergence operator are replaced by a mixed time average defined as:

$$Y_j'=\gamma\,Y_j^{n+1}+(1-\gamma)Y_j^n\tag{3-161}$$

The weighting factor γ is determined by several considerations. For flow that is single phase over the entire timestep, γ is set to zero. When the net predicted flow out of a cell of either phase exceeds the current mass in that cell, the weight is set to one (new-time cell-centered quantities are fluxed). For less dramatic situations, three ratios are computed. The first ratio has as a numerator the sum of the change in cell vapor mass for the timestep due to all mass fluxes plus twice the change due to boiling. The ratio's

denominator is the cell's mass decrease due only to outwardly directed vapor mass flows (positive number). The second ratio is the analog of the first as applied to the liquid phase. For the third ratio, the numerator adds half the old-time cell liquid mass to the predicted change in cell liquid mass for the timestep. The denominator is half of the mass change due to outwardly directed flows at the cell's edges (negative number). When other considerations are not in control, the maximum of the three ratios is limited to the range of zero through one and is used for γ.

The first two ratios force the use of a cell-centered implicit value when outflow of a phase is almost exclusively the result of phase-change terms. The factor will also force this implicit evaluation when phase change is not significant and inflow significantly exceeds the outflow. The third ratio becomes important when some liquid outflow is present and a prediction is made that over half of the existing liquid mass will flow or boil away during the timestep.

The mixture of old- and new-time values of the quantity being fluxed results in a difference scheme for this step that is not rigorously conservative. However, the standard finite-volume divergence operator is applied in the stabilizer mass and energy equations, restoring conservation to the final fluxes of mass and energy.

In the stabilizer mass and energy equations, the new-time velocity values are fixed by the semi-implicit step, as are all new-time terms marked with a tilde. In the stabilizer combined-gas mass equation, the only unknown new-time variables are the macroscopic gas densities $(\alpha_g\rho_g)^{n+1}$. For the non-condensable mass equation, the only unknowns are the terms $(\alpha_g\rho_a)^{n+1}$, and for the liquid mass equation, the only unknowns are the terms $(\alpha_\ell\rho_\ell)^{n+1}$. In the stabilizer combined-gas energy equation, the only unknown new-time variables are the macroscopic gas energy densities $(\alpha_g\rho_g e_g)^{n+1}$. For the liquid energy equation, the only unknowns are the terms $(\alpha_\ell\rho_\ell e_\ell)^{n+1}$.

Stabilizer Mass Equations

Combined Gas

$$\frac{\left[\left(\alpha_g\rho_g\right)_j^{n+1}-\left(\alpha_g\rho_g\right)_j^{n}\right]}{\Delta t}+\nabla_j\cdot\left[\left(\alpha_g\rho_g\right)^{n+1}u_g^{n+1}\right]=\tilde{\Gamma}_j^{n+1} \tag{3-162}$$

Non-Condensable Gas

$$\frac{\left[\left(\alpha_g\rho_\alpha\right)_j^{n+1}-\left(\alpha_g\rho_\alpha\right)_j^{n}\right]}{\Delta t}+\nabla_j\cdot\left[\left(\alpha_g\rho_\alpha\right)^{n+1}u_g^{n+1}\right]=0 \tag{3-163}$$

Liquid

$$\frac{(\alpha_\ell\,\rho_\ell)_j^{n+1}-(\alpha_\ell\,\rho_\ell)_j^{n}}{\Delta t}+\nabla_j\left\{(\alpha_\ell\,\rho_\ell)^{n+1}\cdot u_\ell^{n+1}\right\}=-\tilde{\Gamma}_j^{n+1} \tag{3-164}$$

Liquid Solute

$$\frac{(\alpha_{\ell j}^{n+1}\tilde{m}_j^{n+1}\rho_{\ell j}^{n+1}-\alpha_{\ell j}^{n}m_j^{n}\rho_{\ell j}^{n})}{\Delta t}+\nabla_j\cdot(\alpha_\ell^{n+1}\tilde{m}^{n+1}\rho_\ell^{n+1}u_\ell^{n+1})=0 \tag{3-165}$$

$$m_j^{n+1}=\min\left[\tilde{m}_j^{n+1}+\frac{S_{cj}^{n}}{\alpha_{\ell j}^{n+1}\rho_{\ell j}^{n+1}},m_{max}\right] \tag{3-166}$$

and

$$S_{cj}^{n+1}=\left(\tilde{m}_j^{n+1}-m_j^{n+1}\right)\alpha_{\ell j}^{n+1}\rho_{\ell j}^{n+1}+S_{cj}^{n} \tag{3-167}$$

Stabilizer Energy Equations

Combined Gas

$$\begin{aligned}&\frac{[(\alpha_g\rho_ge_g)_j^{n+1}-(\alpha_g\rho_ge_g)_j^{n}]}{\Delta t}+\nabla_j\cdot\left[(\alpha_g\rho_ge_g)^{n+1}u_g^{n+1}\right]\\&+\tilde{P}_j^{n+1}\left[\frac{\left(\tilde{\alpha}_{gj}^{n+1}-\alpha_{gj}^{n}\right)}{\Delta t}+\nabla_j\cdot\left(\alpha_g^{n}u_g^{n+1}\right)\right]\\&=\tilde{q}_{wg}^{n+1}+q_{dg}^{n}+\tilde{q}_{ig}^{n+1}+\tilde{\Gamma}_j^{n+1}\tilde{h}_{sg}^{n+1}\end{aligned} \tag{3-168}$$

Liquid

$$\begin{aligned}&\frac{(\alpha_\ell\rho_\ell e_\ell)_j^{n+1}-(\alpha_\ell\rho_\ell e_\ell)_j^{n}}{\Delta t}+\nabla_j\cdot\left\{(\alpha_\ell\rho_\ell e_\ell)^{n+1}u_\ell^{n+1}\right\}\\&+\tilde{P}_j^{n+1}\left\{\frac{\left(\alpha_{gj}^{n}-\tilde{\alpha}_{gj}^{n+1}\right)}{\Delta t}+\nabla_j\cdot\left[\alpha_\ell^{n}u_\ell^{n+1}\right]\right\}\\&=\tilde{q}_{w\ell}^{n+1}+q_{d\ell}^{n}-\tilde{q}_{ig}^{n+1}-\tilde{\Gamma}_j^{n+1}\tilde{h}_{sg}^{n+1}\end{aligned} \tag{3-169}$$

The code does not directly solve all of the above stabilizer equations. The actual equations solved are differences between these equations and their corresponding equations from the semi-implicit step. For the case of solute transport, no corresponding equation exists in the semi-implicit step. As a result, the stabilizer solute-transport equation, Equation 3-165, is solved exactly as listed above. The final forms of the other equations as set in subroutine STBME follow:

Stabilizer Mass Equations

Combined Gas

$$\frac{\left[(\alpha_g\rho_g)_j^{n+1}-\tilde{\alpha}_{gj}^{n+1}\tilde{\rho}_{gj}^{n+1}\right]}{\Delta t}+\nabla_j\cdot\left[(\alpha_g\rho_g)^{n+1}u_g^{n+1}\right]=\nabla_j\cdot\left[(\alpha_g\rho_g)^{n}u_g^{n+1}\right] \tag{3-170}$$

Non-Condensable Gas

$$\frac{\left[(\alpha_g\rho_a)_j^{n+1}-\tilde{\alpha}_{gj}^{n+1}\tilde{\rho}_{gj}^{n+1}\right]}{\Delta t}+\nabla_j\cdot\left[(\alpha_g\rho_a)^{n+1}u_g^{n+1}\right]=\nabla_j\cdot\left[(\alpha_g\rho_a)^{n}u_g^{n+1}\right] \tag{3-171}$$

Liquid

$$\frac{(\alpha_\ell\rho_\ell)_j^{n+1}-\tilde{\alpha}_{\ell j}^{n+1}\tilde{\rho}_{\ell j}^{n+1}}{\Delta t}+\nabla_j\cdot\left[(\alpha_\ell\rho_\ell)^{n+1}u_\ell^{n+1}\right]=\nabla_j\cdot\left[(\alpha_\ell\rho_\ell)^{n}u_\ell^{n+1}\right] \tag{3-172}$$

Stabilizer Energy Equations

Combined Gas

$$\frac{\left[(\alpha_g\rho_g e_g)_j^{n+1}-\tilde{\alpha}_{gj}^{n+1}\tilde{\rho}_{gj}^{n+1}\tilde{e}_{gj}^{n+1}\right]}{\Delta t}+\nabla_j\cdot\left[(\alpha_g\rho_g e_g)^{n+1}u_g^{n+1}\right]=\nabla_j\cdot\left[(\alpha_g\rho_g e_g)^{n}u_g^{n+1}\right] \tag{3-173}$$

Liquid

$$\frac{\left\{(\alpha_\ell\rho_\ell e_\ell)_j^{n+1}-\left(1-\alpha_{\ell j}^{n+1}\right)\tilde{\rho}_{\ell j}^{n+1}\tilde{e}_{\ell j}^{n+1}\right\}}{\Delta t}+\nabla_j\cdot\left[(\alpha_\ell\rho_\ell e_\ell)^{n+1}u_\ell^{n+1}\right] = \nabla_j\cdot\left[(\alpha_\ell\rho_\ell e_\ell)^{n}u_\ell^{n+1}\right] \tag{3-174}$$

Source terms in the SETS equations follow the definitions provided during the discussion of the semi-implicit methods. They are redefined below to clarify the use of intermediate variables.

$$\tilde{q}_{w\ell}^{n+1}=h_{w\ell}^{n}A_w\left(T_w^{n}-\tilde{T}_\ell^{n+1}\right)/\text{vol} \tag{3-175}$$

$$\tilde{q}_{wg}^{n+1}=h_{wg}^{n}A_w\left(T_w^{n}-\tilde{T}_g^{n+1}\right)/\text{vol} \tag{3-176}$$

and

$$\tilde{\Gamma}^{n+1} = \frac{-\left(\tilde{q}_{ig}^{n+1} + \tilde{q}_{i\ell}^{n+1}\right)}{\left(h'_v\right)^{n+1} - \left(h'_\ell\right)^{n+1}} \tag{3-177}$$

where:

$$\tilde{q}_{ig}^{n+1} = \left(\frac{P_v}{P}\right)^n h_{ig}^n A_i^n \frac{\left(\tilde{T}_{sat}^{n+1} - \tilde{T}_g^{n+1}\right)}{vol} \tag{3-178}$$

and

$$\tilde{q}_{i\ell}^{n+1} = h_{i\ell}^n A_i^n \frac{\left(\tilde{T}_{sat}^{n+1} - \tilde{T}_\ell^{n+1}\right)}{vol} \tag{3-179}$$

As mentioned in Section 3.5.3.1.3, an important subtlety in the SETS application is the use of thermodynamic variables in the evaluation of specific terms. The current form of the SETS solution provides only final new-time values for void fraction (α), macroscopic densities $[\alpha_g\rho_g, \alpha_g\rho_a, \alpha_\ell\rho_\ell]$, and macroscopic energies $[\alpha_g\rho_g e_g, \alpha_g\rho_a e_a, \alpha_\ell\rho_\ell e_\ell]$. A final call to the thermodynamics subroutine does not occur after the solution of the stabilizer mass and energy equations. As a result, when basic thermodynamic variables are needed for evaluation properties such as viscosity or heat-transfer coefficients, values obtained from the previous semi-implicit step are used.

Equations 3-141 and 3-142 do not involve any implicit coupling between cells and can be solved directly for the gas and liquid velocities at each mesh-cell interface. Equations 3-143 and 3-144 are not coupled to each other. Each of these systems is implicitly coupled in space through the momentum-convection term, and each requires the solution of a tridiagonal linear system. Equations 3-145 through 3-159, combined with the necessary thermodynamic and constitutive equations, form a coupled system of nonlinear equations. Equations 3-145 and 3-146 are solved directly to obtain u_g^{n+1} and u_ℓ^{n+1} as linear functions of $\tilde{P}^{n+1}$. After substituting these equations for velocity into Equations 3-155 through 3-159, the resulting system is solved for the independent variables $\tilde{P}^{n+1}, \tilde{P}_a^{n+1}, \tilde{T}_g^{n+1}, \tilde{T}_\ell^{n+1}$, and $\tilde{\alpha}^{n+1}$ with a standard Newton iteration, including all coupling between cells. In practice, the linearized equations solved during this Newton iteration are reduced easily to a tridiagonal system involving only total pressures. The final eight stabilizer mass and energy Equations 3-162 through 3-169 also are simple tridiagonal linear systems because u_g^{n+1} and u_ℓ^{n+1} are known after solving Equations 3-145 through 3-159.

3.5.3.1.5 Summary of SETS Calculation Procedure

1) Pre-pass Calculations

In the pre-pass calculations, an estimate step and a stabilization step for the momentum equations are performed.

The estimate step of the momentum:

$$\frac{\hat{u}_k^{n+1}-u_k^n}{\Delta t}+\underbrace{u_k^n\nabla\tilde{u}_k^n}_{\text{given}}+\beta_k\cdot(\hat{u}_k^{n+1}-u_k^n)\nabla\tilde{u}_k^n+\frac{1}{\rho_k^n}\cdot\nabla P^n$$
$$=\underbrace{-M_k^d(\hat{u}_g^{n+1},\hat{u}_\ell^{n+1})+\left\{M_k^\Gamma(\hat{u}_g^{n+1},\hat{u}_\ell^{n+1})-\frac{\Gamma_k^n}{(\alpha_k\rho_k)^n}\cdot\hat{u}_k^{n+1}\right\}}_{\text{unknown}}-F_{wk}(\hat{u}_k^{n+1})-G_k$$

where

$$\beta_k=\begin{cases}1 & \text{if} \quad \nabla\tilde{u}_k^n\geq 0 \quad \text{and} \quad u_k^n\tilde{u}_k^n\geq 0\\ 0 & \text{if} \quad \nabla\tilde{u}_k^n<0 \quad \text{or} \quad u_k^n\tilde{u}_k^n<0\end{cases}$$

$$M_g^d(u_g,u_\ell)=\frac{C_i}{(\alpha_g\rho_g)}\cdot\left|u_g-u_\ell\right|\cdot(u_g-u_\ell)$$

$$M_\ell^d(u_g,u_\ell)=\frac{C_i}{(\alpha_\ell\rho_\ell)}\cdot\left|u_\ell-u_g\right|\cdot(u_\ell-u_g)$$

$$M_g^\Gamma(u_g,u_\ell)=\begin{cases}\dfrac{\Gamma_g}{(\alpha_g\rho_g)}\cdot u_\ell & \text{if} \quad \Gamma_g\geq 0\\ \dfrac{\Gamma_g}{(\alpha_g\rho_g)}\cdot u_g & \text{if} \quad \Gamma_g<0\end{cases}$$

$$M_g^\Gamma(u_g,u_\ell)-\frac{\Gamma_g}{(\alpha_g\rho_g)}\cdot u_g=\frac{\max(\Gamma_g,0)}{(\alpha_g\rho_g)}\cdot(u_\ell-u_g)$$
$$=-\frac{\Gamma^+}{(\alpha_g\rho_g)}\cdot(u_g-u_\ell)$$

$\because \quad \max(\Gamma_g,0)=\max(\Gamma,0)=\Gamma^+$

$$M_\ell^\Gamma(u_g,u_\ell)=\begin{cases}\dfrac{\Gamma_\ell}{(\alpha_\ell\rho_\ell)}\cdot u_g & \text{if} \quad \Gamma_\ell \geq 0\\ \dfrac{\Gamma_\ell}{(\alpha_\ell\rho_\ell)}\cdot u_\ell & \text{if} \quad \Gamma_\ell < 0\end{cases}$$

$$M_\ell^\Gamma(u_g,u_\ell)-\frac{\Gamma_\ell}{(\alpha_\ell\rho_\ell)}\cdot u_\ell=\frac{\max(\Gamma_\ell,0)}{(\alpha_\ell\rho_\ell)}\cdot(u_g-u_\ell)$$

$$=\frac{\Gamma^-}{(\alpha_\ell\rho_\ell)}\cdot(u_\ell-u_g)$$

$$\because \quad \max(\Gamma_\ell,0)=-\min(\Gamma,0)=-\Gamma^-$$

$$F_{wk}(u_k)=\frac{C_{wk}}{(\alpha_k\rho_k)}\cdot|u_k|\cdot u_k$$

$$G_k=g\cdot\cos\theta$$

The stabilization step of the solution of momentum equations:

$$\frac{\tilde{u}_k^{n+1}-u_k^n}{\Delta t}+\underbrace{u_k^n\nabla\tilde{u}_k^{n+1}}_{\text{unknown}}+\beta_k\cdot(\tilde{u}_k^{n+1}-u_k^n)\nabla\tilde{u}_k^n+\frac{1}{\rho_k^n}\cdot\nabla P^n$$

$$=\underbrace{-M_k^d(\hat{u}_g^{n+1},\hat{u}_\ell^{n+1})+\left\{M_k^\Gamma(\hat{u}_g^{n+1},\hat{u}_\ell^{n+1})-\frac{\Gamma_k^n}{(\alpha_k\rho_k)^n}\cdot\hat{u}_k^{n+1}\right\}}_{\text{given}}-F_{wk}(\tilde{u}_k^{n+1})-G_k$$

2) Outer Iterations

In the outer iterations, each conservation equation of mass/momentum/energy is calculated using the usual semi-implicit method. The unknowns in this calculation are updated with Newton iterations.

(a) Conservation of Momentum

$$\frac{u_k^{v+1}-u_k^n}{\Delta t}+\underbrace{u_k^n\nabla\tilde{u}_k^{n+1}}_{\text{given}}+\beta_k\cdot(u_k^{v+1}-u_k^n)\nabla\tilde{u}_k^n+\frac{1}{\rho_k^n}\cdot\nabla P^{v+1}$$

$$=-M_k^d(u_g^{v+1},u_\ell^{v+1})+\left\{M_k^\Gamma(u_g^{v+1},u_\ell^{v+1})-\frac{\Gamma_k^n}{(\alpha_k\rho_k)^n}\cdot u_k^{v+1}\right\}-F_{wk}(u_k^{v+1})-G_k$$

(b) Conservation of Mass

$$\frac{(\alpha_k \rho_k)^{v+1} - (\alpha_k \rho_k)^n}{\Delta t} + \nabla\left[(\alpha_k \rho_k)^m u_k{}^{v+1} \right] = \Gamma_k{}^{v+1}$$

(c) Conservation of Energy

$$\frac{(\alpha_k \rho_k e_k)^{v+1} - (\alpha_k \rho_k e_k)^n}{\Delta t} + \nabla\left[(\alpha_k \rho_k e_k)^m u_k{}^{v+1} \right] + P^{v+1} \cdot \left[\frac{\alpha_k{}^{v+1} - \alpha_k{}^n}{\Delta t} + \nabla(\alpha_k{}^n u_k{}^{v+1}) \right]$$

$$= L_k{}^{v+1} + Q_k{}^{v+1}$$

where,

L_k Interfacial heat transfer between gas and liquid

Q_k wall heat transfer

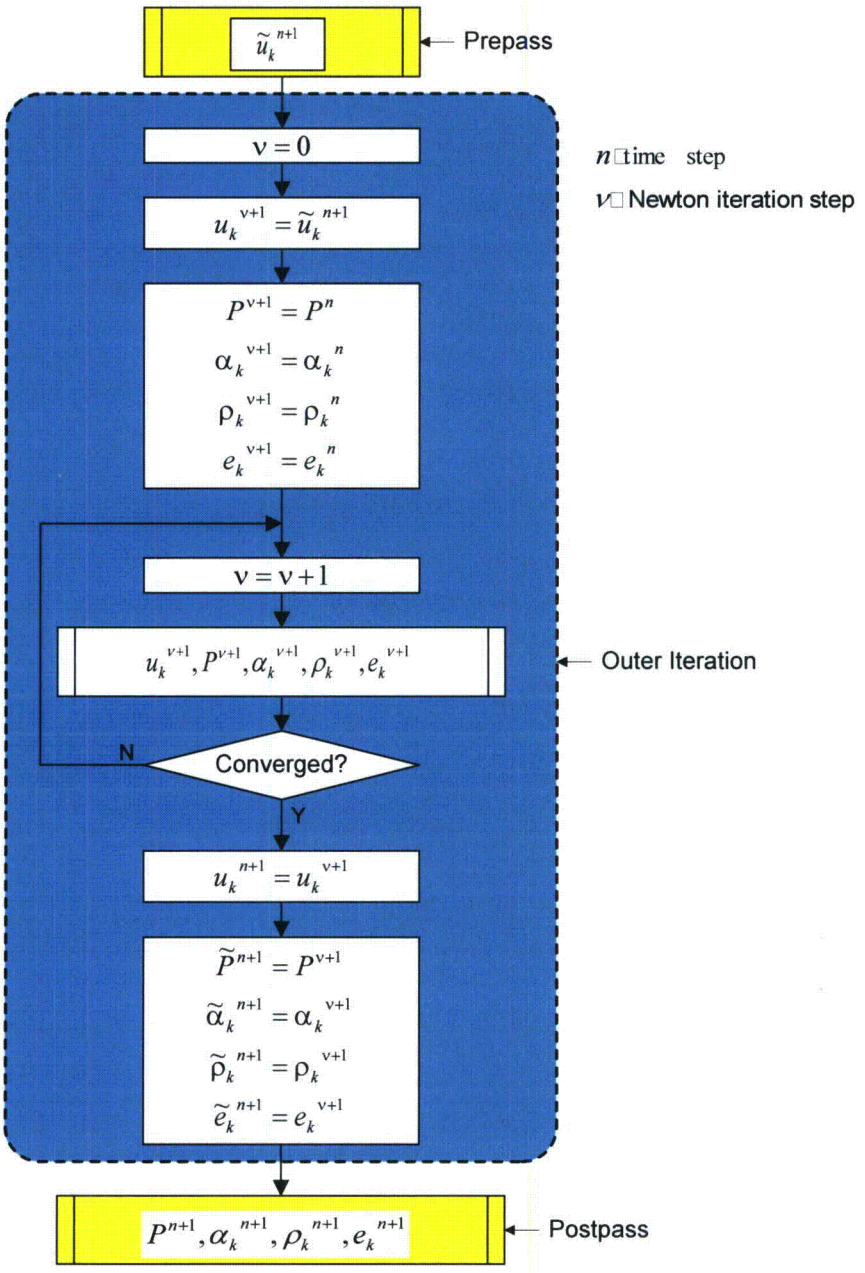

Outer iterations using the Newton Method

2) Postpass Calculations

After calculating the stabilization step of mass and energy conservation equations, final pressure, void fraction and temperature values are obtained by solving the linearized mass and energy equations.

(a) Stabilization step of mass equations

$$\frac{(\alpha_k\rho_k)^{n+1}-(\alpha_k\rho_k)^{n}}{\Delta t}+\nabla\left[(\alpha_k\rho_k)^{n+1}\underline{u_k}^{n+1}\right]=\tilde{\Gamma}_k^{n+1}$$

given (for $\tilde{\Gamma}_k^{n+1}$); given ($\underline{u_k}^{n+1}$)

which can be re-written in terms of the basic step as:

$$\frac{(\alpha_k\rho_k)^{n+1}-(\tilde{\alpha}_k\tilde{\rho}_k)^{n+1}}{\Delta t}+\nabla\left[(\alpha_k\rho_k)^{n+1}\underline{u_k}^{n+1}\right]=\nabla\left[(\alpha_k\rho_k)^{m}u_k^{n+1}\right]$$

given ($(\tilde{\alpha}_k\tilde{\rho}_k)^{n+1}$); given ($\underline{u_k}^{n+1}$); given ($\nabla\left[(\alpha_k\rho_k)^{m}u_k^{n+1}\right]$)

(b) Stabilization step of energy equations

$$\frac{(\alpha_k\rho_k e_k)^{n+1}-(\alpha_k\rho_k e_k)^{n}}{\Delta t}+\nabla\left[(\alpha_k\rho_k e_k)^{n+1}\underline{u_k}^{n+1}\right]+\tilde{P}^{n+1}\cdot\left[\frac{\tilde{\alpha}_k^{n+1}-\alpha_k^{n}}{\Delta t}+\nabla(\alpha_k^{n}u_k^{n+1})\right]$$
$$=\tilde{L}_k^{n+1}+\tilde{Q}_k^{n+1}$$

given ($\tilde{L}_k^{n+1}+\tilde{Q}_k^{n+1}$); given ($\underline{u_k}^{n+1}$); given ($\tilde{P}^{n+1}\cdot\left[\frac{\tilde{\alpha}_k^{n+1}-\alpha_k^{n}}{\Delta t}+\nabla(\alpha_k^{n}u_k^{n+1})\right]$)

which can be re-written in terms of the basic step as:

$$\frac{(\alpha_k\rho_k e_k)^{n+1}-(\tilde{\alpha}_k\tilde{\rho}_k\tilde{e}_k)^{n+1}}{\Delta t}+\nabla\left[(\alpha_k\rho_k e_k)^{n+1}\underline{u_k}^{n+1}\right]=\nabla\left[(\alpha_k\rho_k e_k)^{m}u_k^{n+1}\right]$$

given ($(\tilde{\alpha}_k\tilde{\rho}_k\tilde{e}_k)^{n+1}$); given ($\underline{u_k}^{n+1}$); given ($\nabla\left[(\alpha_k\rho_k e_k)^{m}u_k^{n+1}\right]$)

(c) Additional mass conservation equation:

$$(\alpha_k\rho_k)^{n+1} = \tilde{\alpha}_k^{\,n+1}\cdot\rho_k^{\,n+1} + \alpha_k^{\,n+1}\cdot\tilde{\rho}_k^{\,n+1} - (\tilde{\alpha}_k\tilde{\rho}_k)^{n+1}$$

unknown

(d) Additional energy conservation equation:

$$(\alpha_k\rho_k e_k)^{n+1} = \tilde{\alpha}_k^{\,n+1}\cdot\tilde{\rho}_k^{\,n+1}\cdot e_k^{\,n+1} + \tilde{\alpha}_k^{\,n+1}\cdot\rho_k^{\,n+1}\cdot\tilde{e}_k^{\,n+1} + \alpha_k^{\,n+1}\cdot\tilde{\rho}_k^{\,n+1}\cdot\tilde{e}_k^{\,n+1} - 2(\tilde{\alpha}_k\tilde{\rho}_k\tilde{e}_k)^{n+1}$$

unknown

3.6 NUMERICAL SOLUTION METHOD

3.6.1 Introduction

The conservation equations and computational mesh used by WCOBRA/TRAC-TF2 for the vessel and one-dimensional components were described in Sections 3.1 through 3.5. This section describes the numerical methods used to generate a solution to those sets of equations.

3.6.2 Vessel Component Numerical Solution

The equations shown in Sections 3.3 and 3.5 form a set of algebraic equations that must be solved simultaneously to obtain a solution for the flow fields involved. These equations must be simultaneously satisfied not only for each cell, but for the entire computational mesh. The methods used to solve these equations will now be described.

3.6.2.1 Solution of the Momentum Equations

The momentum equations are solved for first, using currently known values for all of the variables, to obtain an estimate of the new-time flow. All explicit terms and variables in the momentum equation are computed in this step and are assumed to remain constant during the remainder of the timestep. The semi-implicit momentum equations have the following form:

Vertical Liquid Momentum

$$F_\ell = A_1^F + B_1^F\Delta P + C_1^F F_\ell + D_1^F F_{gas} \tag{3-180}$$

Vertical Combined-Gas Momentum

$$F_{gas} = A_2^F + B_2^F\Delta P + C_2^F F_\ell + D_2^F F_{gas} + E_2^F F_e \tag{3-181}$$

Vertical Entrainment Momentum

$$F_e = A_3^F + B_3^F \Delta P + D_3^F F_{gas} + E_3^F F_e \tag{3-182}$$

Lateral Liquid Momentum

$$W_\ell = A_1^W + B_1^W \Delta P + C_1^W W_\ell + D_1^W W_{gas} \tag{3-183}$$

Lateral Combined-Gas Momentum

$$W_{gas} = A_2^W + B_2^W \Delta P + C_2^W W_\ell + D_2^W W_{gas} + E_2^W W_e \tag{3-184}$$

Lateral Entrainment Momentum

$$W_e = A_3^W + B_3^W \Delta P + D_3^W W_{gas} + E_3^W W_e \tag{3-185}$$

A_1, A_2, and A_3 are constants that represent the explicit terms in the momentum equations such as the momentum efflux terms and the gravitational force. B_1, B_2, and B_3 are the explicit portion of the pressure gradient force term. C_1 and C_2 are the explicit factors that multiply the liquid flow rate in the wall and the interfacial drag terms. D_1, D_2, D_3, E_2, and E_3 are the corresponding terms that multiply the combined-gas and entrained liquid flow rates.

The Equations 3-180 through 3-182 are written in matrix form as:

$$\begin{bmatrix} C_1 - 1 & D_1 & 0 \\ C_2 & D_2 - 1 & E_2 \\ 0 & D_3 & E_3 - 1 \end{bmatrix} \begin{Bmatrix} F_\ell \\ F_{gas} \\ F_e \end{Bmatrix} = \begin{Bmatrix} -A_1 - B_1 \Delta P \\ -A_2 - B_2 \Delta P \\ -A_3 - B_3 \Delta P \end{Bmatrix} \equiv \begin{Bmatrix} F_1 \\ F_2 \\ F_3 \end{Bmatrix} \tag{3-186}$$

A similar expression is obtained for the Equations 3-183 to 3-185.

The system (3-186) is solved by Gaussian elimination to obtain a solution for the phasic mass flow rates (both vertical and lateral) as a function of the pressure gradient across the momentum cell, ΔP. In particular:

Vertical Flow

$$\begin{Bmatrix} F_\ell \\ F_{gas} \\ F_e \end{Bmatrix}^{m+1} = \begin{Bmatrix} G_1^F \\ G_2^F \\ G_3^F \end{Bmatrix} + \begin{Bmatrix} H_1^F \\ H_2^F \\ H_3^F \end{Bmatrix} (P_{J+1} - P_J)^{m+1}$$
$$= \begin{Bmatrix} G_1^F \\ G_2^F \\ G_3^F \end{Bmatrix} + \begin{Bmatrix} H_1^F \\ H_2^F \\ H_3^F \end{Bmatrix} (P_{J+1} - P_J)^n + \begin{Bmatrix} H_1^F \\ H_2^F \\ H_3^F \end{Bmatrix} (dP_{J+1} - dP_J)^{m+1} = \begin{Bmatrix} F_\ell \\ F_{gas} \\ F_e \end{Bmatrix}^* + \begin{Bmatrix} dF_\ell \\ dF_{gas} \\ dF_e \end{Bmatrix}^{m+1} \quad (3\text{-}187)$$

Lateral (Gap) Flow

$$\begin{Bmatrix} W_\ell \\ W_{gas} \\ W_e \end{Bmatrix}^{m+1} = \begin{Bmatrix} G_1^W \\ G_2^W \\ G_3^W \end{Bmatrix} + \begin{Bmatrix} H_1^W \\ H_2^W \\ H_3^W \end{Bmatrix} (P_{JJ} - P_{II})^{m+1}$$
$$= \begin{Bmatrix} G_1^W \\ G_2^W \\ G_3^W \end{Bmatrix} + \begin{Bmatrix} H_1^W \\ H_2^W \\ H_3^W \end{Bmatrix} (P_{JJ} - P_{II})^n + \begin{Bmatrix} H_1^W \\ H_2^W \\ H_3^W \end{Bmatrix} (dP_{JJ} - dP_{II})^{m+1} = \begin{Bmatrix} W_\ell \\ W_{gas} \\ W_e \end{Bmatrix}^* + \begin{Bmatrix} dW_\ell \\ dW_{gas} \\ dW_e \end{Bmatrix}^{m+1} \quad (3\text{-}188)$$

The iterative equations are solved for increments of independent variables. In particular the increments on the flow are related to the increments in the pressure from the following equations:

$$\begin{Bmatrix} dF_\ell \\ dF_{gas} \\ dF_e \end{Bmatrix}^{m+1} = \begin{Bmatrix} H_1^F \\ H_2^F \\ H_3^F \end{Bmatrix} (dP_{J+1} - dP_J)^{m+1} \quad (3\text{-}189)$$

and

$$\begin{Bmatrix} dW_\ell \\ dW_{gas} \\ dW_e \end{Bmatrix}^{m+1} = \begin{Bmatrix} H_1^W \\ H_2^W \\ H_3^W \end{Bmatrix} (dP_{JJ} - dP_{II})^{m+1} \quad (3\text{-}190)$$

The mass flow rates given by Equations 3-189 and 3-190 are computed based on the mass of each phase contained within the momentum control volume. Once the tentative flows have been obtained from the momentum equations, the continuity and energy equations can be solved.

3.6.2.2 Linearization of the Mass and Energy Equations

As stated in Sections 3.3.3.1 and 3.3.3.3 the mass and energy equations are written in the form of residual errors. The combined-gas mass equation, for example, has a residual error given by:

$$E_{c,gas,J}^{m+1} = \frac{\Delta x_J A_{c,J}}{\Delta t}\left[\left(\alpha_{gas}\rho_{gas}\right)_J^{m+1} - \left(\alpha_{gas}\rho_{gas}\right)_J^{n}\right] + \sum_{KA=1}^{NA}\left[\left(\alpha_{gas}\rho_{gas}\right)_{KA}^{\tilde{n}} \tilde{u}_{gas,KA}^{m+1} A_{m,KA}\right]$$
$$- \sum_{KB=1}^{NB}\left[\left(\alpha_{gas}\rho_{gas}\right)_{KB}^{\tilde{n}} \tilde{u}_{gas,KB}^{m+1} A_{m,KB}\right] - \Delta x_J \sum_{KL=1}^{NKK}\left[L_{KL}\left(\alpha_{gas}\rho_{gas}\right)_{KL}^{\tilde{n}} \tilde{w}_{gas,KL}^{m+1}\right] - \Gamma_J^{m+1} - S_{c,gas,J}^{m+1} \quad (3\text{-}191)$$

All terms are computed using currently known values for each of the variables. The tilde (~) over the velocities indicates that they are the tentative values computed from the momentum equations, Equations 3-189 and 3-190. In addition to the combined-gas mass, two mass equations for the liquid phase, non-condensable gas mass and the two energy equations also have residual errors: $E_{c,\ell}$, $E_{c,e}$, $E_{c,NC}$, $E_{e,gas}$, and $E_{e,\ell}$. The equations are simultaneously satisfied when $E_{c,gas}$, $E_{c,\ell}$, $E_{c,e}$, $E_{c,NC}$, $E_{e,gas}$, and $E_{e,\ell}$ for all cells in the mesh simultaneously approach zero. The variation of each of the independent variables required to bring the residual errors to zero can be obtained using the block Newton-Raphson method. This is done by linearizing the equations with respect to the independent variables P, α_{gas}, $\alpha_{gas}H_{gas}$, $(1-\alpha_{gas})H_\ell$, α_e, and P_{NC} to obtain the following equation for each cell.

The mass and energy equations for the m+1 Newton-iteration are approximated to the first order of increments **dX** of the independent variables:

$$\overline{E}_J^{m+1} = \overline{E}_J^{n} + \left[\frac{\partial \overline{E}_J}{\partial \overline{X}_J}\right]^m \left\{\overline{dX}_J\right\}^{m+1} + \sum_{ICON=1}^{NCONS}\left[\frac{\partial \overline{E}_J}{\partial P_{ICON}}\right]^m \left\{dP_{ICON}\right\}^{m+1} + \overline{dE}_{S,J} \quad (3\text{-}192)$$

where $\overline{E}_J$ is the vector of residual in the cell **J**:

$$\overline{E}_J = \begin{Bmatrix} E_{c,gas} \\ E_{c,\ell} \\ E_{e,gas} \\ E_{e,\ell} \\ E_{c,e} \\ E_{c,NC} \end{Bmatrix}_J \quad (3\text{-}193)$$

The vector of the increments of the independent variables is the following:

$$\overline{dX}_J = \begin{Bmatrix} dP \\ d\alpha_{gas} \\ d\left(\alpha_{gas}H_{gas}\right) \\ d\left[\left(1-\alpha_{gas}\right)H_\ell\right] \\ d\alpha_e \\ dP_{NC} \end{Bmatrix}_J \quad (3\text{-}194)$$

To be more specific, the updates in Equation 3-194 refer to the Newton iteration updates, i.e.:

$$\overline{dX_J} = \left(\overline{X_J}\right)^{m+1} - \left(\overline{X_J}\right)^{n} \tag{3-195}$$

The third term is the contribution from the convective terms which have dependency on the neighboring cell pressure. The index ICON is the connection index to neighboring cells.

$\mathbf{dE_S}$ represents the 1D/3D mass and energy source increments dS_C and dS_E. [
]^{a,c}

[a,c] (3-196)

[
]^{a,c}
[a,c] (3-197)

[
]^{a,c}
[a,c] (3-198)

(3-199)

(3-200)

$$\left[\quad\right]^{a,c} \tag{3-201}$$

(3-202)

Let's **NCONS** be the number of neighboring vessel cells connected to cell J

Setting $\bar{E}_J^{m+1}$ to 0, and recasting into a matrix form, Equation 3-192 becomes,

$$\begin{bmatrix}
\frac{\partial E_{c,gas}}{\partial P_J} & \frac{\partial E_{c,gas}}{\partial \alpha_{gas}} & \frac{\partial E_{c,gas}}{\partial(\alpha_{gas}H_v)} & \frac{\partial E_{c,gas}}{\partial[(1-\alpha_{gas})H_\ell]} & \frac{\partial E_{c,gas}}{\partial \alpha_e} & \frac{\partial E_{cv}}{\partial P_{NC}} & \frac{\partial E_{c,gas}}{\partial P_{i=1}} & \cdots & \frac{\partial E_{c,gas}}{\partial P_{i=NCONS}} \\
\frac{\partial E_{c,\ell}}{\partial P_J} & \frac{\partial E_{c,\ell}}{\partial \alpha_v} & \frac{\partial E_{c,\ell}}{\partial(\alpha_v H_v)} & \frac{\partial E_{c,\ell}}{\partial[(1-\alpha_v)H_\ell]} & \frac{\partial E_{c,\ell}}{\partial \alpha_e} & \frac{\partial E_{c,\ell}}{\partial P_{NC}} & \frac{\partial E_{c,\ell}}{\partial P_{i=1}} & \cdots & \frac{\partial E_{c,\ell}}{\partial P_{i=NCONS}} \\
\frac{\partial E_{e,gas}}{\partial P_J} & \frac{\partial E_{e,gas}}{\partial \alpha_{gas}} & \frac{\partial E_{e,gas}}{\partial(\alpha_{gas}H_v)} & \frac{\partial E_{e,gas}}{\partial[(1-\alpha_{gas})H_\ell]} & \frac{\partial E_{e,gas}}{\partial \alpha_e} & \frac{\partial E_{e,gas}}{\partial P_{NC}} & \frac{\partial E_{e,gas}}{\partial P_{i=1}} & \cdots & \frac{\partial E_{e,gas}}{\partial P_{i=NCONS}} \\
\frac{\partial E_{e,\ell}}{\partial P_J} & \frac{\partial E_{e,\ell}}{\partial \alpha_{gas}} & \frac{\partial E_{e,\ell}}{\partial(\alpha_{gas}H_v)} & \frac{\partial E_{e,\ell}}{\partial[(1-\alpha_{gas})H_\ell]} & \frac{\partial E_{e,\ell}}{\partial \alpha_e} & \frac{\partial E_{e,\ell}}{\partial P_{NC}} & \frac{\partial E_{e,\ell}}{\partial P_{i=1}} & \cdots & \frac{\partial E_{e,\ell}}{\partial P_{i=NCONS}} \\
\frac{\partial E_{c,e}}{\partial P_J} & \frac{\partial E_{c,e}}{\partial \alpha_{gas}} & \frac{\partial E_{c,e}}{\partial(\alpha_{gas}H_v)} & \frac{\partial E_{c,e}}{\partial[(1-\alpha_{gas})H_\ell]} & \frac{\partial E_{c,e}}{\partial \alpha_e} & \frac{\partial E_{c,e}}{\partial P_{NC}} & \frac{\partial E_{c,e}}{\partial P_{i=1}} & \cdots & \frac{\partial E_{c,e}}{\partial P_{i=NCONS}} \\
\frac{\partial E_{c,NC}}{\partial P_J} & \frac{\partial E_{c,NC}}{\partial \alpha_{gas}} & \frac{\partial E_{c,NC}}{\partial(\alpha_{gas}H_v)} & \frac{\partial E_{c,NC}}{\partial[(1-\alpha_{gas})H_\ell]} & \frac{\partial E_{c,NC}}{\partial \alpha_e} & \frac{\partial E_{c,NC}}{\partial P_{NC}} & \frac{\partial E_{c,NC}}{\partial P_{i=1}} & \cdots & \frac{\partial E_{c,NC}}{\partial P_{i=NCONS}}
\end{bmatrix}
\begin{Bmatrix}
dP_J \\ d\alpha_{gas} \\ d(\alpha_{gas}H_v) \\ d[(1-\alpha_{gas})H_\ell] \\ d\alpha_e \\ dP_{NC} \\ dP_{i=1} \\ \cdots \\ dP_{i=NCONS}
\end{Bmatrix}$$

$$= -\begin{Bmatrix} E_{c,gas} \\ E_{c,\ell} \\ E_{e,gas} \\ E_{e,\ell} \\ E_{c,e} \\ E_{c,NC} \end{Bmatrix} \quad \left[\quad\right]^{a,c} \tag{3-203}$$

The superscripts m and m+1 are omitted, since it is clear at this point that the unknown vector is dX_{IC}. However note that the vector dX_{IC} also includes the pressure updates, for the center cell J as well as the neighborhood (dPs). The matrix is re-evaluated at the m-level, while the derivatives with respect to the flow are evaluated only at the n-level.

In the semi-implicit formulation the implicit terms are the following:

1. Convective contributions
2. [ ]^{a,c}

The LHS of Equation 3-203 is also referred to as "cell Jacobian" or RJAC-matrix using the actual variable name in the code. This is equivalent to Equation 3-192 and re-arranged in matrix form. The RJAC matrix is directly solved with Gaussian Elimination.

3.6.2.3 Reduction of Cell Jacobian and Development of the Pressure Matrix

This cell Jacobian of the vessel component, Equation 3-203 is first normalized, reduced and put in an upper triangular form. Using the actual array names which contain source (AIRS) [ ]^{a,c} as,

$$\begin{bmatrix} 1 & 0 & 0 & 0 & 0 & 0 & g_{1,i=1} & \cdots & g_{1,i=NCONS} \\ 0 & 1 & 0 & 0 & 0 & 0 & g_{2,i=1} & \cdots & g_{2,i=NCONS} \\ 0 & 0 & 1 & 0 & 0 & 0 & g_{3,i=1} & \cdots & g_{3,i=NCONS} \\ 0 & 0 & 0 & 1 & 0 & 0 & g_{4,i=1} & \cdots & g_{4,i=NCONS} \\ 0 & 0 & 0 & 0 & 1 & 0 & g_{5,i=1} & \cdots & g_{5,i=NCONS} \\ 0 & 0 & 0 & 0 & 0 & 1 & g_{6,i=1} & \cdots & g_{6,i=NCONS} \end{bmatrix} \begin{Bmatrix} dP_j \\ d\alpha_{gas} \\ d(\alpha_{gas} H_v) \\ d[(1-\alpha_{gas}) H_\ell] \\ d\alpha_e \\ dP_{NC} \\ dP_{i=1} \\ \cdots \\ dP_{i=NCONS} \end{Bmatrix}$$

$$= \begin{Bmatrix} AIRS(1) \\ AIRS(2) \\ AIRS(3) \\ AIRS(4) \\ AIRS(5) \\ AIRS(6) \end{Bmatrix} \begin{bmatrix} \quad \end{bmatrix}^{a,c} \tag{3-204}$$

Where the content of the arrays AIRS [ ]^{a,c} have been modified because of the Gaussian elimination. [ ]^{a,c}

$$\begin{bmatrix} \quad \end{bmatrix}^{a,c} \tag{3-205}$$

[

]^{a,c}

3.6.2.4 Solution for the Remainder of the Independent Variables

Once the pressure field update is obtained, the solution process can proceed with the unfolding of the other independent variables. In particular we have:

$$d\alpha_{gas} = a_2 - \sum_{i=1}^{NCONS} g_{2,i} dP_i \tag{3-206}$$

$$d\left(\alpha_{gas}H_v\right) = a_3 - \sum_{i=1}^{NCONS} g_{3,i}dP_i \quad (3\text{-}207)$$

$$d\left[\left(1-\alpha_{gas}\right)H_\ell\right] = a_4 - \sum_{i=1}^{NCONS} g_{4,i}dP_i \quad (3\text{-}208)$$

$$d\alpha_e = a_5 - \sum_{i=1}^{NCONS} g_{5,i}dP_i \quad (3\text{-}209)$$

$$dP_{NC} = a_6 - \sum_{i=1}^{NCONS} g_{6,i}dP_i \quad (3\text{-}210)$$

3.6.2.5 Cells Connected to One-Dimensional Components

[

]a,c

[a,c (3-211)

(3-212)

[

]a,c

[a,c (3-213)

[

]a,c

[a,c (3-214)

[

]a,c

[ ] a,c (3-215)

[

]a,c

[ ] a,c (3-216)

[

]a,c

[ ] a,c (3-217)

[ ]a,c

[ ] a,c (3-218)

[
]a,c

[ ] a,c

3.6.3 One-Dimensional Component Numerical Solution

The outcome of the solution of the momentum equation is a relationship between the update of the gas/liquid velocities and the update on the pressure in the adjacent cells. This is expressed by:

$$(u_g)^{v+1}_{j+1/2} = (u_g)^{v}_{j+1/2} - \left(\frac{du_g}{dP}\right)^{n}_{j+1/2} \cdot \left((\delta P)^{v+1}_{j+1} - (\delta P)^{v+1}_{j}\right) \tag{3-219}$$

$$(u_\ell)^{v+1}_{j+1/2} = (u_\ell)^{v}_{j+1/2} - \left(\frac{du_\ell}{dP}\right)^{n}_{j+1/2} \cdot \left((\delta P)^{v+1}_{j+1} - (\delta P)^{v+1}_{j}\right) \tag{3-220}$$

The expression is obtained by setting to zero the L.H.S of Equation 3-145 and Equation 3-146, and solving for the gas/liquid velocities at the new Newton iteration level:

$$\begin{pmatrix} (1+A)+B & -B \\ -D & (1+C)+D \end{pmatrix} \cdot \begin{Bmatrix} (u_g)^{v+1}_{j+1/2} \\ (u_\ell)^{v+1}_{j+1/2} \end{Bmatrix} = \begin{Bmatrix} (RHS_g)^{v}_{j+1/2} \\ (RHS_\ell)^{v}_{j+1/2} \end{Bmatrix} - \begin{Bmatrix} \frac{(\Delta t)^n}{(\rho_g)^n} \cdot \frac{1}{\Delta x_{j+1/2}} \\ \frac{(\Delta t)^n}{(\rho_\ell)^n} \cdot \frac{1}{\Delta x_{j+1/2}} \end{Bmatrix} \cdot \left((\delta P)^{v+1}_{j+1} - (\delta P)^{v+1}_{j}\right) \tag{3-221}$$

Thus:

$$\begin{Bmatrix} (u_g)^{v} \\ (u_\ell)^{v} \end{Bmatrix}_{j+1/2} = \left[\overline{\overline{M}}\right]^{-1} \cdot \begin{Bmatrix} (RHS_g)^{v} \\ (RHS_\ell)^{v} \end{Bmatrix}_{j+1/2} \tag{3-222}$$

and

$$\begin{Bmatrix} \left(\frac{du_g}{dP}\right)^{n} \\ \left(\frac{du_\ell}{dP}\right)^{n} \end{Bmatrix}_{j+1/2} = \left[\overline{\overline{M}}\right]^{-1} \cdot \begin{Bmatrix} \frac{(\Delta t)^n}{(\rho_g)^n} \cdot \frac{1}{\Delta x_{j+1/2}} \\ \frac{(\Delta t)^n}{(\rho_\ell)^n} \cdot \frac{1}{\Delta x_{j+1/2}} \end{Bmatrix} \tag{3-223}$$

$$\left[\overline{\overline{M}}\right] \equiv \begin{pmatrix} (1+A)+B & -B \\ -D & (1+C)+D \end{pmatrix} \tag{3-224}$$

After substituting Equations 3-219 and 3-220 for velocity into Equations 3-155 through 3-159, the resulting system is solved for the independent variables $\tilde{P}^{n+1}$, $\tilde{P}_a^{n+1}$, $\tilde{T}_g^{n+1}$, $\tilde{T}_\ell^{n+1}$, and $\tilde{\alpha}^{n+1}$ with a standard Newton iteration, including all coupling between cells. In practice, the linearized equations solved during this Newton iteration are reduced easily to a tridiagonal system involving only total pressures.

The five independent variables beside the gas/liquid velocities are collectively denoted by a vector:

$$d\overline{X}_j = \begin{pmatrix} \delta P \\ \delta \alpha_g \\ \delta T_g \\ \delta T_\ell \\ \delta P_a \end{pmatrix}_j \tag{3-225}$$

The mass and energy equations are structured in the following vector:

$$\overline{E}_j = \begin{pmatrix} E_{gc} \\ E_{\ell c} \\ E_{ge} \\ E_{me} \\ E_{ac} \end{pmatrix}_j \tag{3-226}$$

For each cell j, the vector of mass and energy equations is expanded into a first order Taylor series:

$$\begin{aligned}
(E_{gc})_j^{v+1} &= c_{11} + \bar{a}_1 \cdot d\overline{X}_j + c_{12} \cdot (\delta u_g)_{j+1/2}^{v+1} - c_{13} \cdot (\delta u_g)_{j-1/2}^{v+1} \\
(E_{\ell c})_j^{v+1} &= c_{21} + \bar{a}_2 \cdot d\overline{X}_j + c_{22} \cdot (\delta u_\ell)_{j+1/2}^{v+1} - c_{23} \cdot (\delta u_\ell)_{j-1/2}^{v+1} \\
(E_{ge})_j^{v+1} &= c_{31} + \bar{a}_3 \cdot d\overline{X}_j + c_{32} \cdot (\delta u_g)_{j+1/2}^{v+1} - c_{33} \cdot (\delta u_g)_{j-1/2}^{v+1} \\
(E_{me})_j^{v+1} &= (c_{31} + c_{41}) + (\bar{a}_3 + \bar{a}_4) \cdot d\overline{X}_j + c_{32} \cdot (\delta u_g)_{j+1/2}^{v+1} - c_{33} \cdot (\delta u_g)_{j-1/2}^{v+1} \\
&\quad + c_{42} \cdot (\delta u_\ell)_{j+1/2}^{v+1} - c_{43} \cdot (\delta u_\ell)_{j-1/2}^{v+1} \\
(E_{ac})_j^{v+1} &= c_{51} + \bar{a}_5 \cdot d\overline{X}_j + c_{52} \cdot (\delta u_g)_{j+1/2}^{v+1} - c_{53} \cdot (\delta u_g)_{j-1/2}^{v+1}
\end{aligned} \tag{3-227}$$

The equation above is expressed in term of pressure substituting the results from the solution of the momentum equation. The equation is expressed by:

$$\overline{E}_j^{v+1} = \bar{b}_j + \bar{\bar{a}}_j \cdot d\overline{X}_j + \bar{c}_j \cdot \left((\delta P)_{j+1}^{v+1} - (\delta P)_j^{v+1}\right) - \bar{d}_j \cdot \left((\delta P)_j^{v+1} - (\delta P)_j^{v+1}\right) + \bar{e}_j \cdot \left((\delta P)_{NC2}^{v+1} - (\delta P)_j^{v+1}\right) \tag{3-228}$$

where $(\delta P)_{NC2}$ is the pressure at the first cell of TEE branch.

The solution corresponds on setting the L.H.S. to zero. Therefore the previous equation can be expressed in the following matrix form:

$$\overline{\overline{A}}_j \cdot d\overline{X}_j = \overline{B}_j + \overline{C}_j \cdot \left((\delta P)_{j+1} - (\delta P)_j\right) - \overline{D}_j \cdot \left((\delta P)_j - (\delta P)_{j-1}\right) + \overline{T}_j \cdot \left((\delta P)_{NC2} - (\delta P)_j\right) \quad (3\text{-}229)$$

where A_j is the cell jacobian matrix for 1D cell-j.

Equation 3-229 can be solved by direct matrix inversion as follows:

$$d\overline{X}_j = \begin{Bmatrix} C'_{11} \\ C'_{21} \\ C'_{31} \\ C'_{41} \\ C'_{51} \end{Bmatrix} + \begin{Bmatrix} C'_{12} \\ C'_{22} \\ C'_{32} \\ C'_{42} \\ C'_{52} \end{Bmatrix} \cdot \left((\delta P)_{j+1} - (\delta P)_j\right) - \begin{Bmatrix} C'_{13} \\ C'_{23} \\ C'_{33} \\ C'_{43} \\ C'_{53} \end{Bmatrix} \cdot \left((\delta P)_j - (\delta P)_{j-1}\right) + \begin{Bmatrix} C'_{1T} \\ C'_{2T} \\ C'_{3T} \\ C'_{4T} \\ C'_{5T} \end{Bmatrix} \cdot \left((\delta P)_{NC2} - (\delta P)_j\right) \quad (3\text{-}230)$$

where:

$$\begin{Bmatrix} C'_{11} \\ C'_{21} \\ C'_{31} \\ C'_{41} \\ C'_{51} \end{Bmatrix} = \left[\overline{\overline{A}}^{-1}\overline{B}\right]_j, \quad \begin{Bmatrix} C'_{12} \\ C'_{22} \\ C'_{32} \\ C'_{42} \\ C'_{52} \end{Bmatrix} = \left[\overline{\overline{A}}^{-1}\overline{C}\right]_j, \quad \begin{Bmatrix} C'_{13} \\ C'_{23} \\ C'_{33} \\ C'_{43} \\ C'_{53} \end{Bmatrix} = \left[\overline{\overline{A}}^{-1}\overline{D}\right]_j, \text{ and } \begin{Bmatrix} C'_{1T} \\ C'_{2T} \\ C'_{3T} \\ C'_{4T} \\ C'_{5T} \end{Bmatrix} = \left[\overline{\overline{A}}^{-1}\overline{T}\right]_j.$$

3.6.4 Network Matrix Equation

The variation of the new-time pressure is obtained from the variation of the junction pressure difference. This process starts from Equation 3-230 and considering only the first element (pressure) of the vector dX. Equation 3-230 is reduced to:

$$(\delta P)_j = C'_{11} + C'_{12} \cdot \left((\delta P)_{j+1} - (\delta P)_j\right) - C'_{13} \cdot \left((\delta P)_j - (\delta P)_{j-1}\right) \quad (3\text{-}231)$$

Equation 3-231 can be written for all cells in the component. The treatment at the component boundaries requires some special attention.

At the left boundary (j=1), Equation 3-231 is written as follows:

$$(\delta P)_j = C'_{11} + C'_{12} \cdot \left((\delta P)_{j+1} - (\delta P)_j\right) - C'_{13} \cdot \Delta(\delta P)_L \quad (3\text{-}232)$$

At the right boundary (j=N), we have:

$$(\delta P)_j = C'_{11} + C'_{12} \cdot \Delta(\delta P)_R - C'_{13} \cdot \left((\delta P)_j - (\delta P)_{j-1}\right) \quad (3\text{-}233)$$

And at a TEE branch (j=T), we have:

$$(\delta P)_j = C'_{11} + C'_{12}\cdot\left((\delta P)_{j+1} - (\delta P)_j\right) - C'_{13}\cdot\left((\delta P)_j - (\delta P)_{j-1}\right) + C'_{1T}\cdot\Delta(\delta P)_T \tag{3-234}$$

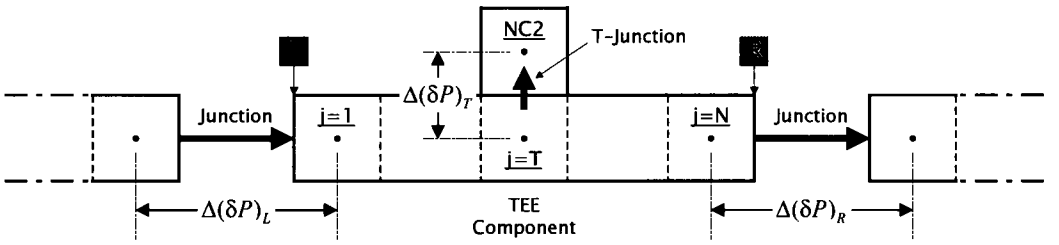

The system of pressure equations for the entire component can be summarized in the following tri-diagonal matrix form:

$$[\mathbf{M}]\cdot\begin{Bmatrix}(\delta P)_1\\ \vdots\\ \vdots\\ \vdots\\ (\delta P)_N\end{Bmatrix} = \{\mathbf{a}\} - \begin{Bmatrix}b_1\\ 0\\ \vdots\\ \vdots\\ 0\end{Bmatrix}\cdot\Delta(\delta P)_L + \begin{Bmatrix}0\\ \vdots\\ \vdots\\ 0\\ c_N\end{Bmatrix}\cdot\Delta(\delta P)_R + \begin{Bmatrix}0\\ \vdots\\ e_T\\ \vdots\\ 0\end{Bmatrix}\cdot\Delta(\delta P)_T \tag{3-235}$$

where:

$$[\mathbf{M}] = \begin{bmatrix} 1+C'_{12} & -C'_{12} & 0 & \cdots & 0 & 0\\ -C'_{13} & 1+C'_{13}+C'_{12} & -C'_{12} & \cdots & 0 & 0\\ \vdots & \vdots & \vdots & \vdots & \vdots & \vdots\\ 0 & 0 & \cdots & -C'_{13} & 1+C'_{13}+C'_{12} & -C'_{12}\\ 0 & 0 & \cdots & 0 & -C'_{13} & 1+C'_{13}\end{bmatrix}$$

$$\equiv \begin{bmatrix} d_1 & -u_1 & 0 & \cdots & 0 & 0\\ -l_2 & d_2 & -u_2 & \cdots & 0 & 0\\ \vdots & \vdots & \vdots & \vdots & \vdots & \vdots\\ 0 & 0 & \cdots & -l_{N-1} & d_{N-1} & -u_{N-1}\\ 0 & 0 & \cdots & 0 & -l_N & d_N\end{bmatrix} \tag{3-236}$$

The construction of the network equation starts from Equation 3-236. The solution of Equation 3-236 provides the relationships between the update on the pressure in each cell of the component and the update on the pressure difference at the boundary of the components. In other words the coefficients in the following equation are obtained:

$$(\delta P)_j = a''_j - b''_j\cdot\Delta(\delta P)_L + c''_j\cdot\Delta(\delta P)_R + e''_j\cdot\Delta(\delta P)_T \tag{3-237}$$

In particular it is noted that this equation is valid at the boundary nodes of the component. Usually, several components are joined for modeling of a complex system by connecting boundaries of the components and connecting the components to the vessel component, i.e., the 1D/3D junction. The connected boundary conditions between the components are determined by a network equation in TRAC-PF1, which is the subject of this section.

[

]^{a,c}

[a,c

(3-238)

(3-239)

(3-240)

(3-241)

(3-242)

(3-243)

(3-244)

(3-245)

(3-246)

[ ]^{a,c}

[a,c

(3-247)

(3-248)

(3-249)

(3-250)

(3-251)

(3-252)

[

]a,c

[a,c

(3-253)

(3-254)

(3-255)

(3-256)

]

or

[a,c

(3-257)

(3-258)

(3-259)

(3-260)

(3-261)

(3-262)

]

This can be re-arranged in the following matrix form:

[a,c

(3-263)

]

[

]a,c

[

]^{a,c}

[a,c]

(3-264)

3.6.5 WCOBRA/TRAC-TF2 Solution Routines

The WCT-TF2 calculational sequence involves several stages: input processing; initialization; pre-pass, outer-iteration, and post-pass calculations; timestep advancement or back-up; and output processing. Each of these stages is discussed in greater detail from a programmer's point of view in the sections that follow. First, a summary of the overall calculational sequences for transient and steady-state calculations is given.

3.6.5.1 General Summary

Depending on the values of the input parameters STDYST and TRANS1, TRAC may perform a steady-state calculation, a transient calculation, or both. The general control sequences of each type of calculation are outlined below, and specific details of the calculational sequence are discussed in more detail in the subsections that follow. For typical PWR and test facility calculations, only transient calculations are performed; a steady-state is achieved within the transient calculation scheme.

The transient calculation is directed by subroutine TRANS. The system state is advanced through time by a sequence of pre-pass, outer-iteration, and post-pass calculations that TRANS requests by calling subroutines PREP, HOUT, and POST, respectively. In these calculations, one or more sweeps are made through all the components in the system. To provide the output requested by the user, TRANS calls the EDIT, DUMP, and NSAPLOT routines by calling subroutine PSTEPQ. Subroutine TRANS is structured as shown in Figure 3-8. The major control variables within the timestep loop are: NSTEP, the current timestep number; TIMET, the time since the transient began; DELT the size of the current timestep; and OITNO, the current outer-iteration number. The timestep loop in Figure 3-9 begins with the selection of the timestep size, DELT, by subroutine TIMSTP.

A pre-pass is performed for each component by routine PREP to evaluate the stabilizer motion equation and phenomenological coefficients. At this point, if the current timestep number is zero, TRANS calls the EDIT routine to print the system state and the NSAPLOT routine to generate a graphics edit at the beginning of the transient. Subroutine TRANS then calls subroutine HOUT, which performs one or more outer iterations to solve the basic hydrodynamic equations. Each outer iteration is performed by routine OUTER and corresponds to one iteration of a Newton-method solution procedure for the fully coupled difference equations of the flow network. The outer-iteration loop ends when the outer-iteration convergence criterion (EPSO) is met. This criterion is applied to the maximum fractional change in the pressures throughout the system during the last iteration. The outer-iteration loop alternatively may terminate when the number of outer iterations reaches a user-specified limit (OITMAX). In this case, TRAC restores the state of all components to that at the beginning of the timestep, reduces the timestep

size (with the constraint that DELT be greater than or equal to DTMIN), and continues the calculation with the new timestep size. This represents a back-up situation and is discussed in greater detail in Section 3.6.5.3. When the outer iteration converges, TRANS calls the POST routine to perform a post-pass evaluation of the 1D component stabilizer mass and energy equations and the 1D component heat-transfer calculation. Then the timestep number is incremented and TIMET is increased by DELT. The calculation is complete when TIMET reaches the last TEND time specified on the timestep data.

3.6.5.2 Pre-pass, Outer-Iteration, and Post-pass Calculations

One complete timestep calculation consists of a pre-pass, outer-iteration, and post-pass stage. Each stage of the timestep calculation is detailed below.

3.6.5.2.1 Pre-pass Calculation

The pre-pass calculation uses the modeled-system solution state at the completion of the previous timestep to evaluate numerous quantities to be used during the outer-iteration calculation. The pre-pass begins by evaluating signal variables and control block, and determining the set status of all trips. Each component begins the pre-pass by moving the values calculated during the last timestep into the storage area for old-time values. Next, wall and interfacial friction coefficients are calculated, and an initial forward elimination on the 1D component stabilizer motion equations is performed. For 1D components that require heat-transfer calculations, the pre-pass also evaluates material properties and heat-transfer coefficients (HTCs). A second pass through all one-dimensional components is required to do the backward substitution on the stabilizer equations of motion. The pre-pass for heat-structure components can be more complex. Besides calculating material properties and HTCs for both average and additional rods, the pre-pass evaluates quench-front positions and fine-mesh properties if the reflood model has been activated.

The pre-pass calculation is controlled by routine PREP (Figure 3-10). Subroutine TRIPS controls the evaluation of signal-variable, control-block, and trip data. This is in contrast to subroutine TRIP that interrogates the trip set status in preparation for specific consequences of trips. Then subroutine PREP performs the first pass of the PREP stage for all one-dimensional components by calling PREP1D with IBKS set to 1. All heat-structure components are processed by calling HTSTR1. The pre-pass is completed with a call to C_PREP3D to perform heat transfer calculations including the fine-mesh renoding for quenching in reflood process in the VESSEL component.

Subroutine TRIPS calls subroutines SVSET, CBSET, and TRPSET. Subroutine SVSET uses current values of system-state variables to define the signal variables. Subroutine CONBLK, which is called by subroutine CBSET, evaluates control-block function operators. Subroutine TRPSET uses the current signal-variable and control-block values to determine the set status of trips. The one-dimensional pre-pass driver PREP1D calls one-dimensional component pre-pass routines to perform both steps of the pre-pass for each one-dimensional component type. The component driver routines have names which typically end with the numeral 1. For example, the PIPE component pre-pass subroutine is called PIPE1. On the first pass through the PREP stage, during which the stabilizer motion equations are set up, the one-dimensional component subroutines utilize the common low-level routines SAVBD, PREPER, and SETBD to avoid redundant coding. On the second pass, during which the stabilizer motion equations are solved, the common low-level routine BKMOM is used. The flag index IBKS (1 or 2) indicates the pass

being performed. Subroutine SAVBD retrieves BD-array boundary data from adjacent components, stores it in the appropriate array locations, and moves data for the last completed timestep into the old-time arrays. Subroutine PREPER evaluates wall friction by calling FWALL, evaluates material properties by calling MPROP, evaluates HTCs by calling HTPIPE, and evaluates interfacial-shear coefficients and begins the solution of the stabilizer equations of motion by calling FEMOM. For a specific component, any or all of these steps may occur under the control of the PREPER argument list. Subroutine SETBD uses the information in the component data arrays to reset the BD-array boundary data at both ends of the component. Subroutine BKMOM solves the stabilizer equations of motion for the stabilizer velocities for one-dimensional components.

The vessel component pre-pass calculation is performed by C_PREP3D, which updates boundary conditions and calls HEAT to determine the wall heat flux using heat transfer coefficients from HCOOL. The rod conduction equations are solved by subroutine TEMP and the quench front location and noding is controlled by subroutine QFRONT.

3.6.5.2.2 Outer Iteration Calculation

The hydrodynamic state of the modeled system is analyzed in TRAC by a sequence of Newton iterations that use full inversion of the linearized equations for all one-dimensional component loops and the VESSEL during each iteration (Figure 3-11). Throughout the sequence of iterations that constitute a timestep (each called an outer iteration), the properties evaluated during the pre-pass and the previous post-pass remain fixed. These include wall (SLAB and ROD) temperatures, HTCs, wall and interfacial shear coefficients, stabilizer velocities, and quench-front positions. The remaining fluid properties can vary to obtain the hydrodynamic-model solution. Each call to routine OUTER completes a single outer (Newton) iteration. Subroutine HOUT controls the overall structure of an outer iteration, as presented in Figure 3-12. Both the forward-elimination and backward-substitution sweeps through the one-dimensional component loops are performed by subroutine OUT1D and the associated outer-iteration routines. The calculations that these routines perform are controlled by the common variable IBKS, which is set by subroutine OUTER.

All one-dimensional components in a particular loop are handled by a single call to subroutine OUTID. This routine loads the data blocks for a component into memory, then calls the appropriate component outer-iteration subroutine. Component outer-iteration subroutines have names that end with the numeral 2. For example, the PIPE component outer-iteration subroutine is called PIPE2. The outer-iteration subroutines for one-dimensional components utilize subroutine INNER to perform common functions. Subroutine INNER retrieves boundary information from the BD boundary array, tests other boundary information for consistency, calls subroutine TF1D to perform the appropriate hydrodynamic calculation, and resets the BD boundary array by calling subroutine J1D. Subroutine TF1D calls subroutines TF1DS1, TF1DS, and TF1DS3 to solve the basic semi-implicit finite-difference equations to obtain the next approximation to the new-time pressures, temperatures, and void fractions. In C_OUT3D, the one-dimensional component data are transferred to vessel calculations by the 1D/3D boundary velocity change, and PSNEW with the pressure change rate in the one-dimensional component cell adjacent to the 1D/3D junction. Including mass, energy, and momentum sources at the junctions, XSCHEM computes coefficient matrices of the vessel momentum, mass, and energy equations. The coefficient matrix is reduced then the pressure coefficients are added to the system pressure matrix at the stage of cell by cell computation. When the entire cell in the vessel is processed, the system pressure

matrix is constructed. In subroutine GSSOLV, the pressure matrix is subjected to the 1D/3D coupling, and is solved by direct inversion method. Then the computed vessel component data are transferred to the one-dimensional network by OUTER, completing the forward elimination. Subroutine OUTER sets IBKS = 1 for signaling the IBKS-backward substitution process. First, the boundary velocities at 1D/1D and 1D/3D junctions are updated taking into account the pressure changes in each vessel component cell at a 1D/3D junction. Then, the remaining independent variables in one-dimensional components are computed. With the computed pressure and fluid temperatures, subroutine THERMO is called to generate other hydraulic properties. Finally, C_OUT3D is called to renew the boundary data, at 1D/3D junctions.

3.6.5.2.3 Post-pass Calculations

After the modeled-system hydrodynamic state has been evaluated by a sequence of outer iterations, TRAC performs a post-pass to solve the stabilizer mass and energy equations and to determine both mixture properties and wall temperatures. Routine POST performs this post-pass. POST also triggers the timestep back-up procedure, which is explained in detail in the next section. As shown in Figure 3-13, subroutine POST first processes all one-dimensional components by calling the appropriate one-dimensional component post-pass subroutine. These subroutines have names that end with the numeral 3 (e.g., PIPE3). Subroutine C_POST3D is called to handle the three-dimensional VESSEL component, and subroutine HTSTR3 is called to handle all heat-structure components. The one-dimensional component post-pass subroutines use the low-level routines SAVBD, POSTER, and SETBD to retrieve BD-array boundary conditions; to evaluate the stabilizer equations, wall temperatures, mixture properties, and transport properties; and to reset the BD boundary array, respectively.

The VESSEL post-pass routine, C_POST3D unfolds the values of the independent variables from the system matrix, updates the fluid densities and mass flow rates, and solves the drop interfacial area concentration equation. The hydrodynamic variables are unfolded in subroutines SAT, VOLLIQ, and VOLVAP for the vessel component. Boundary arrays are updated in SPLITIT. The neutronic point kinetics equation is solved in LUCIFER, and subroutine BACOUT unfolds vessel component independent variables.

Subroutine HTSTR3 controls the post-pass for the heat-structure components by calling subroutine CORE3. From within subroutine CORE3, subroutine FROD is called to evaluate temperature profiles and gap heat-transfer coefficients using subroutines RODHT and GAPHT, respectively.

When a containment component is present, after the TRAC 1D and 3D calculations are completed, TRANS calls CONTAIN to perform containment pressure calculation using the break flow rate computed from the current timestep, and update the pressure boundary condition at the break.

3.6.5.3 Timestep Advancement or Back-up

WCOBRA/TRAC-TF2 contains logic to control the timestep size and the rate at which it changes. Control of the timestep size is accomplished through user specified convergence criteria. Upon the successful completion of one timestep calculation (performed by the pre-pass, outer-iteration, and post-pass stages), the modeled-system state is updated to reflect the new-time conditions. This is accomplished at the start of the next PREP stage, and is handled on a component by component basis within the "1" subroutines, e.g., PIPE1. During this step, all dual-time variables are updated by copying

the values of the new-time variables into the old-time variables. The pre-pass, outer-iteration, and post-pass steps that follow then attempt to assign new values to the new-time variables, allowing the process to be repeated as time is advanced. The computed results of the outer iterations are evaluated by the following convergence criterion:

$$VARERM < EPSO$$

where VARERM is the maximum pressure change rate of all components in an iteration, and EPSO is the user specified maximum pressure change in a single iteration.

If this condition is satisfied, the iteration is completed and the computation is allowed to proceed to the next timestep.

If the outer iteration does not converge within an input specified maximum number of iterations, OITMAX, the outer iteration, is considered to have failed. All fluid conditions are reset to the previous timestep value, the timestep size is reduced by half, and the calculation is repeated.

Calculation of a new timestep size takes place just prior to the PREP stage and is controlled by subroutine TIMSTP. Two types of algorithms, inhibitive and promotional, are implemented in subroutine NEWDLT to evaluate the next timestep size. The inhibitive algorithms limit the new timestep size to ensure stability and to reduce finite-difference error. The promotional algorithm increases the timestep size to improve computational efficiency. The timestep size is regulated by convergence criteria selected by the user and several internal controls by the code. The internal controls on the timestep size are a result of limits based on each of the following conditions:

- The one-and three-dimensional Courant limits;
- The VESSEL and total mass error limits;
- The iteration count;
- The maximum allowable fractional change in void fraction, temperature, and pressure;
- The diffusion number for heat transfer;
- The maximum allowable fractional change in reactor power and valve area.

The actual new timestep size selected is the minimum imposed by the above conditions and the maximum timestep size specified by the user in the timestep data. Each of the conditional maximum timestep sizes are calculated in subroutine NEWDLT with the exception on valve adjustment. The valve adjustment maximum timestep size is evaluated by subroutine VLVEX with subroutine HOUT defining those maximum timestep sizes. In the event that a timestep is not successfully completed, TRAC will back up and try to reevaluate the new-time modeled-system state. Back-ups may occur when either the outer iteration does not converge (necessitating a reduction in the current timestep size) or when a flag indicating an extraordinary condition is activated, thereby requiring the outer iteration to be reevaluated. It is important to understand that there are two types of back-up, one corresponding to each of these scenarios. When the outer iteration fails to converge during the OUTER routine, the current timestep size is reduced and the calculation backs up to the start of the PREP stage. This is necessary because any variable calculated during the pre-pass and dependent on the timestep size was computed for the original timestep size and not the newly-reduced timestep size. In addition, all new-time variables are reset to reflect their beginning-of-timestep values. This enables TRAC to begin again from the PREP stage in a

manner no different than for any other timestep calculation except for having reduced the timestep size during the back-up. If repeated back-ups are performed for the same timesteps, the timestep size is halved for each of the first three back-ups, quartered for the fourth and fifth back-up, and tenth thereafter. The second type of back-up is initiated by a flag being set signaling an extraordinary condition such as a water pack. This indicates that the outer iteration needs to be repeated to account for the extraordinary condition. TRAC resets any new-time variables, that have been potentially evaluated incorrectly by the current attempt through subroutine OUTER, with their old-time values and repeats the outer iteration anew. For this type of back-up, the timestep size does not change, making it unnecessary to repeat the PREP-stage calculation. The difference between the two types of back-ups is that for a back-up to the start of the PREP stage, the timestep size is adjusted, all new-time variables are reset to their beginning-of-timestep values, and variables evaluated during the PREP stage are reevaluated using the newly adjusted timestep size. For a back-up to the start of the outer iteration, no change occurs in the timestep size and only new-time variables calculated during the outer iteration are reset to reflect their beginning-of-timestep values.

User selected convergence criteria include specifications of vessel and one-dimensional component pressure change limits, phasic enthalpy change limits (vessel), phasic temperature change limits (one-dimensional components), a fuel rod clad temperature change limit and a one-dimensional component heat structure temperature change limit. The effects of these limits on timestep size are as follows.

Pressure-Temperature Change Limits

[

]^{a,c}

Void Fraction Change Limit

[

]^{a,c}

These limits restrict the timestep size when fluid conditions are rapidly changing and increase the timestep for a slower transient. At the beginning of a steady-state calculation, the timestep size is set to the minimum allowable timestep size, DTMIN. Often, at the start of a large break LOCA, the Courant

limits and pressure change simulation become timestep controlling parameters. The timestep size typically increases with the promotional algorithm to the maximum allowable timestep size, DTMAX, or the size limited by the Courant condition.

3.6.6 Numerical Stability

To achieve numerical stability while maintaining reasonable computing time, discontinuities both in time and space must be eliminated. Several ramps are applied generally within WCOBRA/TRAC-TF2. One type of ramp eliminates discontinuities in calculated physical quantities as the void fraction varies from 0 to 1.0. Since different physical models for interfacial shear and heat transfer are used, for example, ramps are applied to assure a smooth transition in the calculated variable as the void fraction changes. Different ramps are used, as described in the following sections.

Generally, all phasic constitutive variables, such as shear and heat transfer coefficients, are ramped to zero as the phase is depleted in a cell. The ramps are applied over a small range of void fraction, usually less than one percent.

In addition to smoothing over void fraction, smoothing over time is also implemented. This is done by applying the following formula to constitutive variables:

$$y(t+\Delta t)=y_c^a\, y(t)^{1-a} \tag{3-265}$$

where $y(t + \Delta t)$ is the quantity which will be used in the new timestep, y_c is the quantity as calculated by models and correlations, $y(t)$ is the quantity as used in the previous timestep, and a is a number between 0 and 1.0.

[

]^{a,c}

3.7 REFERENCES

1. Bajorek, S. M., et al., 1998, "Code Qualification Document for Best Estimate LOCA Analysis," WCAP-12945-P-A, Volume 1, Revision 2, and Volumes 2 through 5, Revision 1, and WCAP-14747 (Non-Proprietary).

2. Ishii, M., 1977, "One-Dimensional Drift-Flux Model and Constitutive Equations for Relative Motion Between Phases in Various Two-Phase Flow Regimes," ANL-77-47.

3. Takeuchi, K. and Young, M. Y., 1988, "A Coupling Method of 1-D/1-D and 1-D/3-D Junctions for an Implicit WCOBRA/TRAC," *ANS Trans.*, Vol. 57, pg. 353.

4. Thurgood, M. J., et al., 1983, "COBRA/TRAC – A Thermal-Hydraulics Code for Transient Analysis of Nuclear Reactor Vessels and Primary Coolant Systems," Vol. 1, PNL-4385, NUREG/CR-3046.
5. Spore, J.W., et al., 2000, "TRAC-M/FORTRAN 90 (Version 3.0) Theory Manual," LA-UR-00-910.

Table 3-1	Timestep Size Reduction Limits

a,c

Table 3-2 Code Backup Limits

a,c

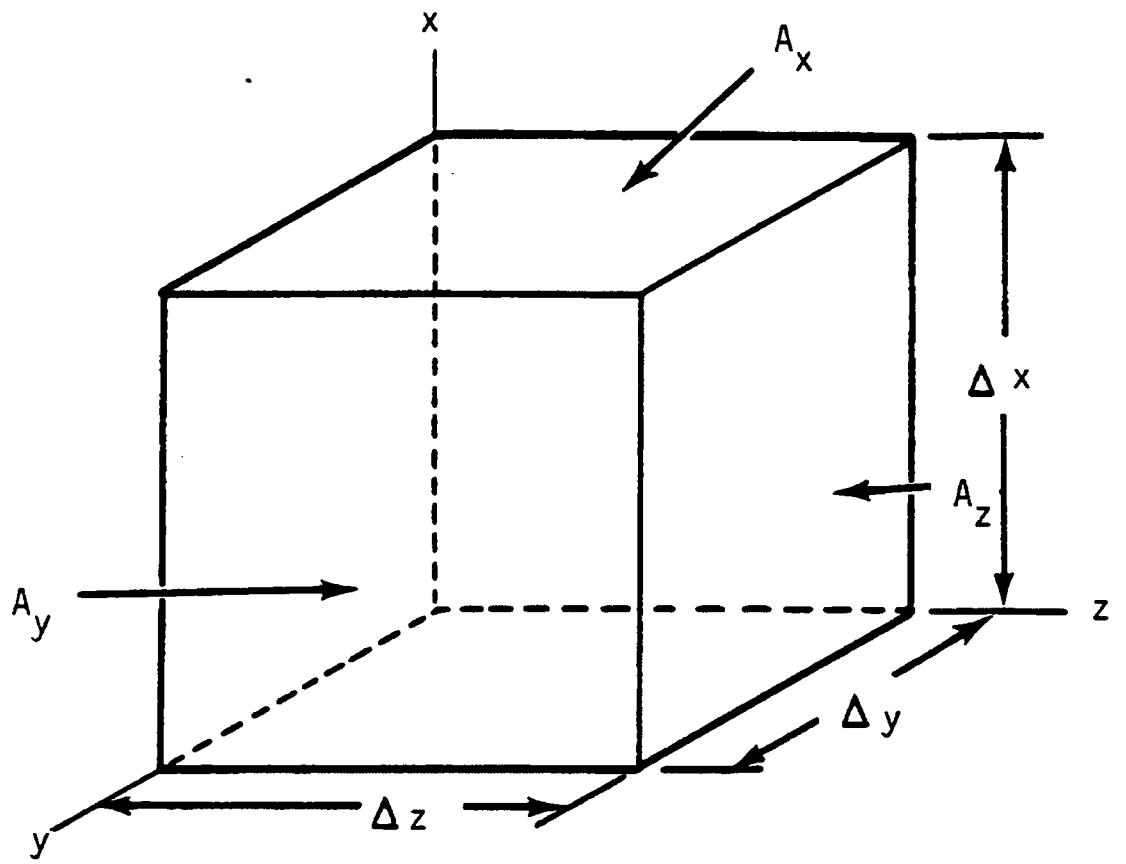

Figure 3-1 Control Volume for Cartesian Coordinates

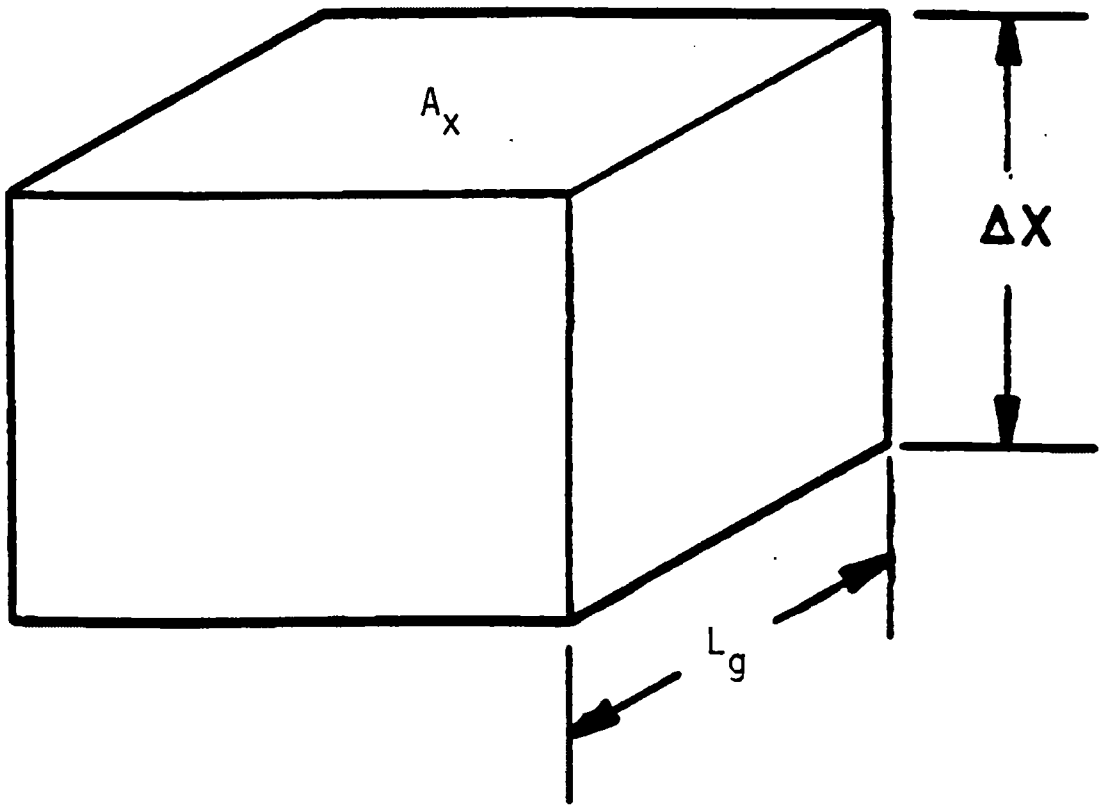

Figure 3-2 Basic Mesh Cell

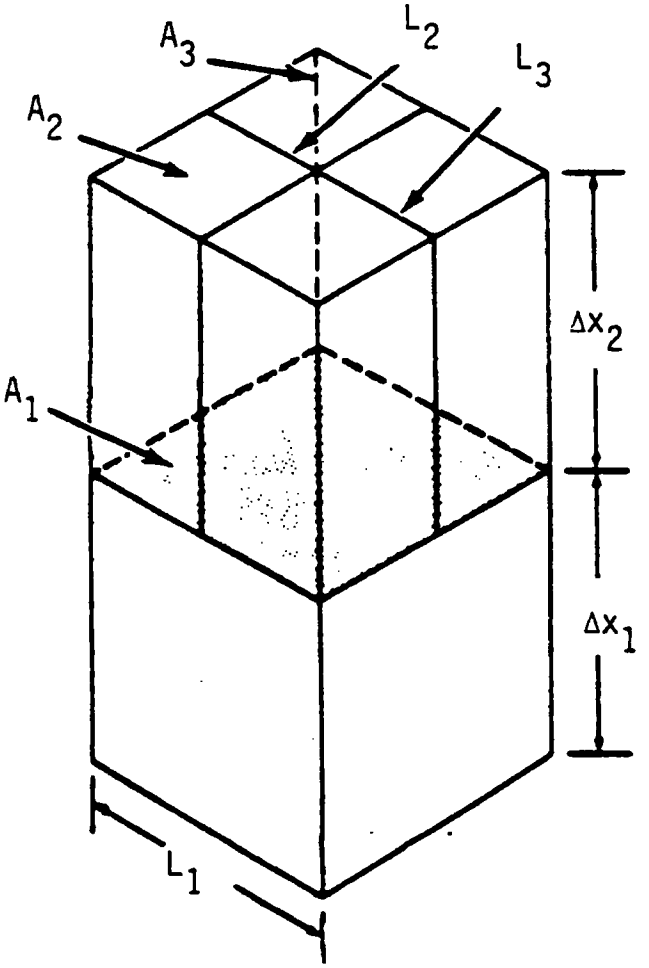

Figure 3-3 Variable Mesh Cell

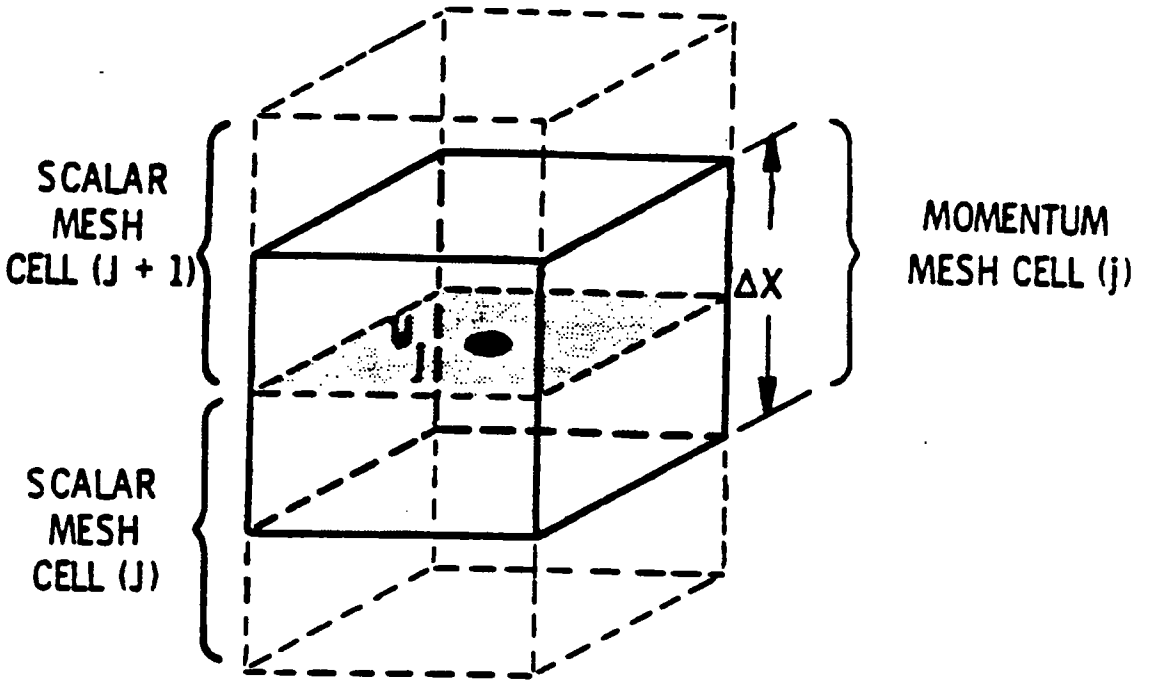

Figure 3-4 Mesh Cell for Vertical Velocities

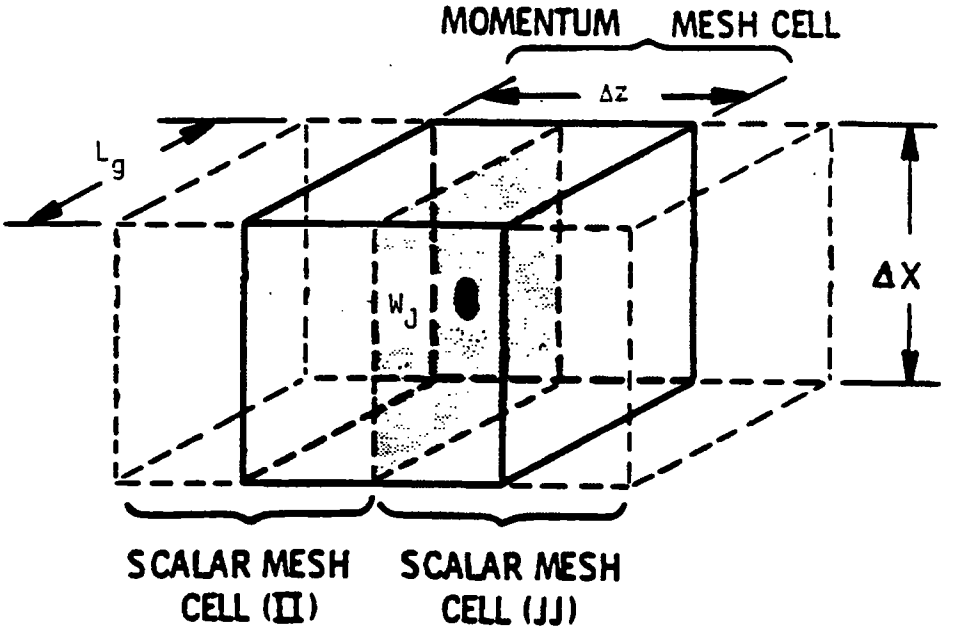

Figure 3-5 Mesh Cell for Transverse Velocities

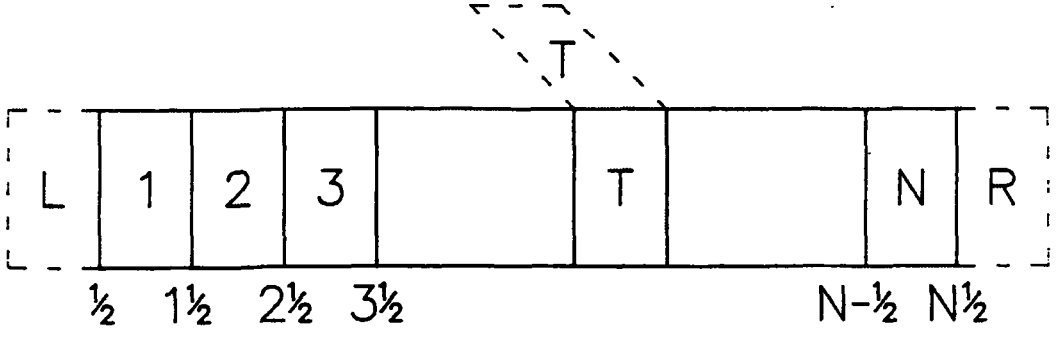

Figure 3-6 One-Dimensional Computational Cell Structure

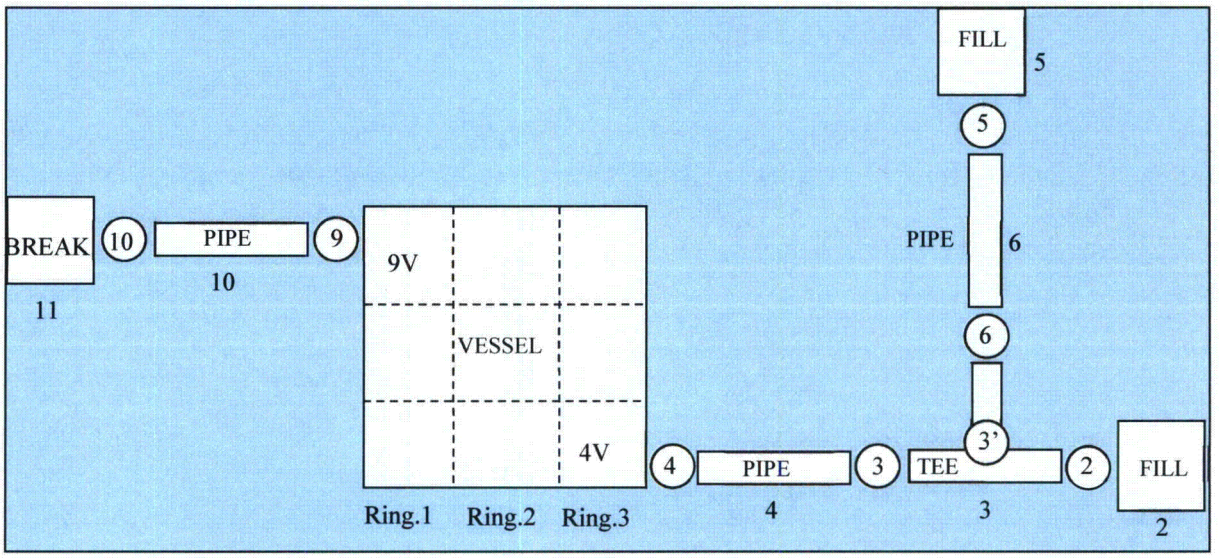

Figure 3-7 A Simple TRAC-PF1 Network

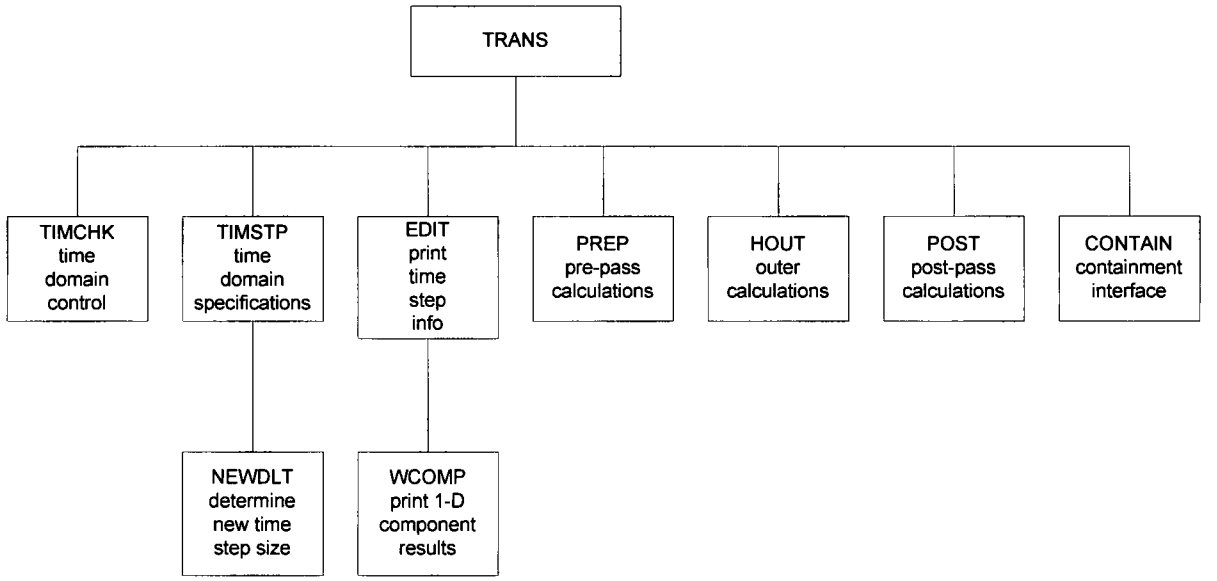

Figure 3-8 WCOBRA/TRAC-TF2 Numerical Solution Routines

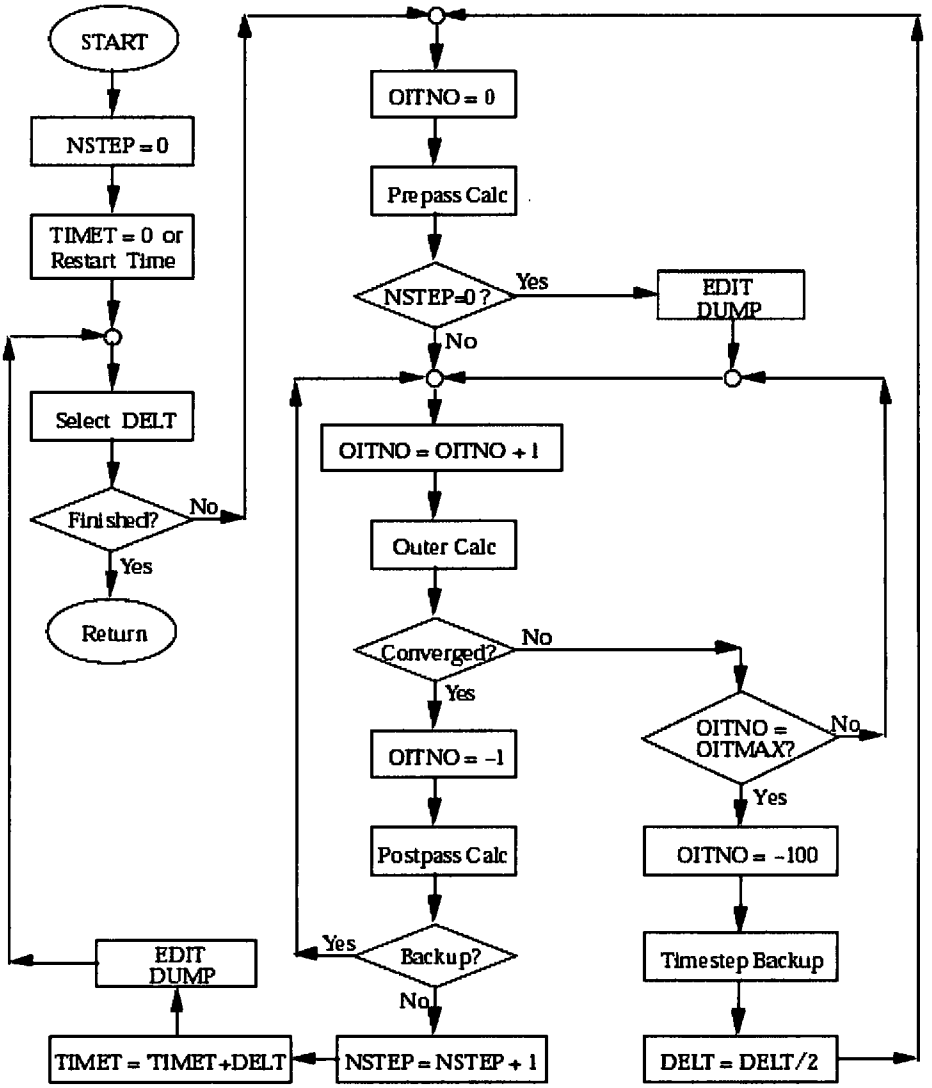

Figure 3-9 Transient Calculation Flow Diagram

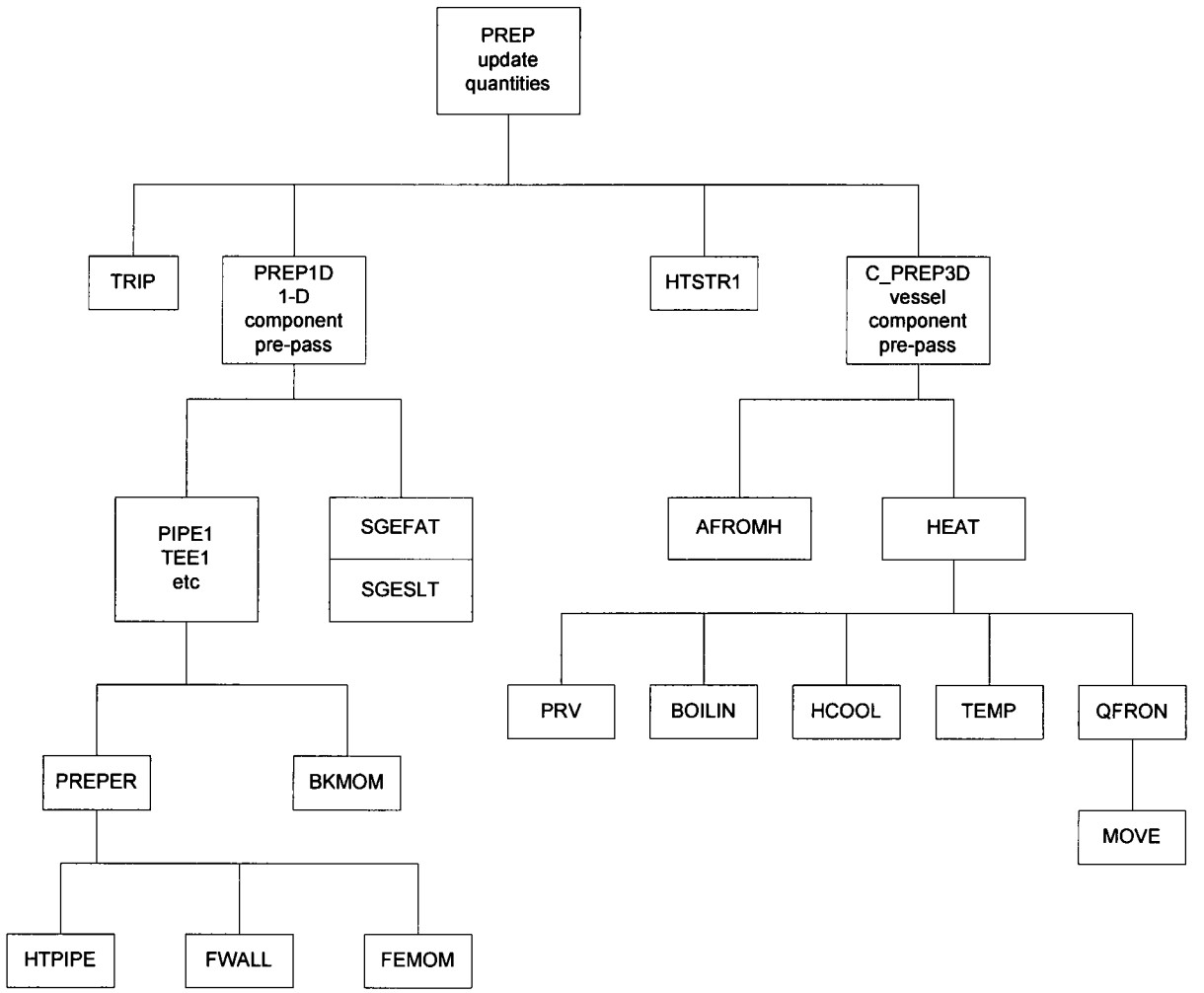

Figure 3-10 WCOBRA/TRAC-TF2 Pre-pass Calculation Routines

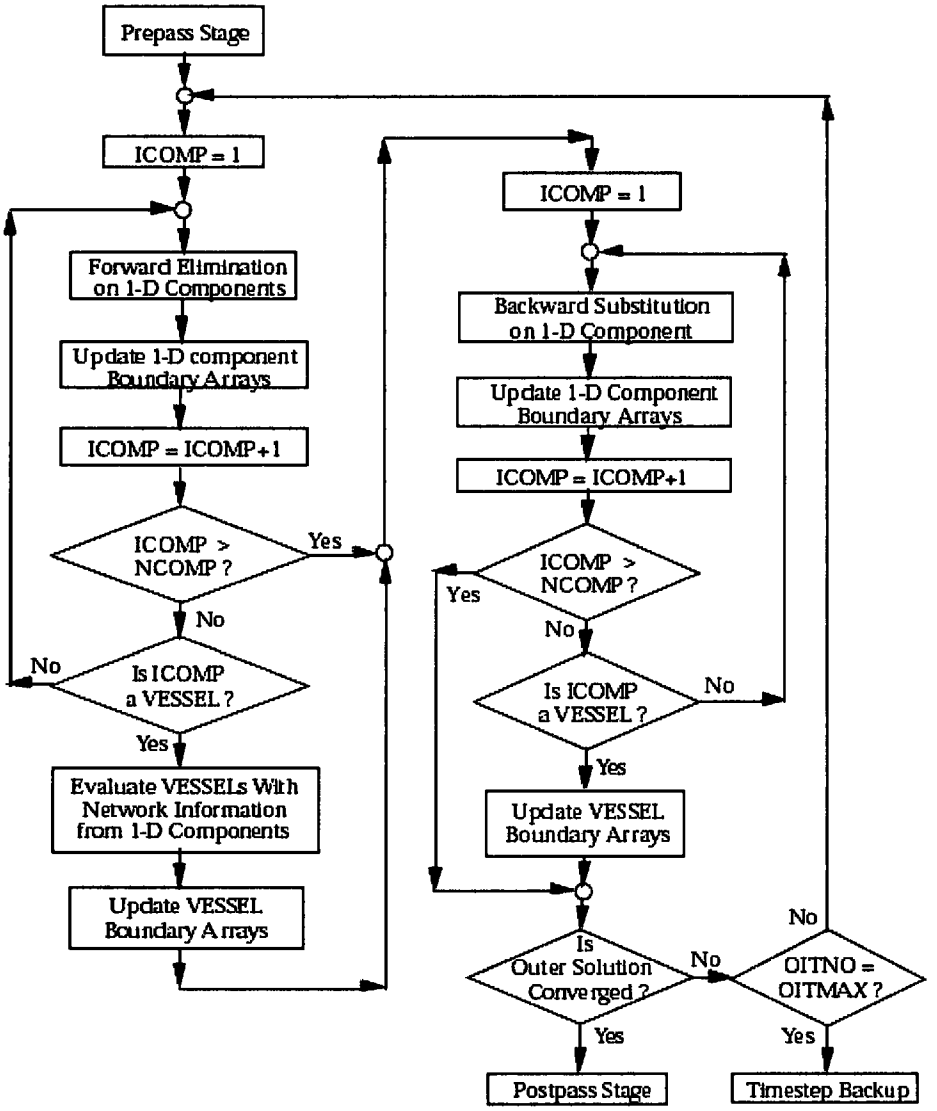

Figure 3-11 Outer Calculation Flow Diagram

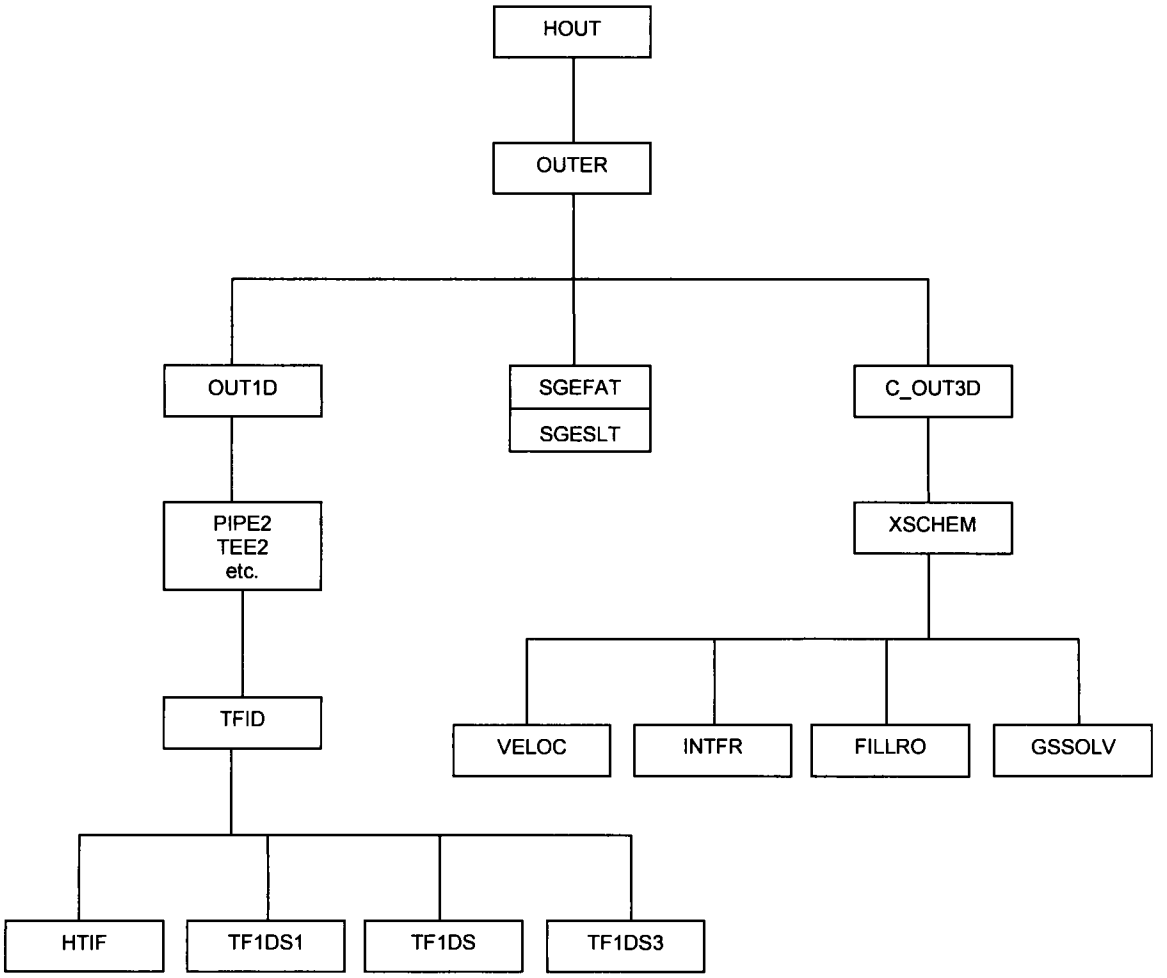

Figure 3-12 WCOBRA/TRAC-TF2 Outer Iteration Routines

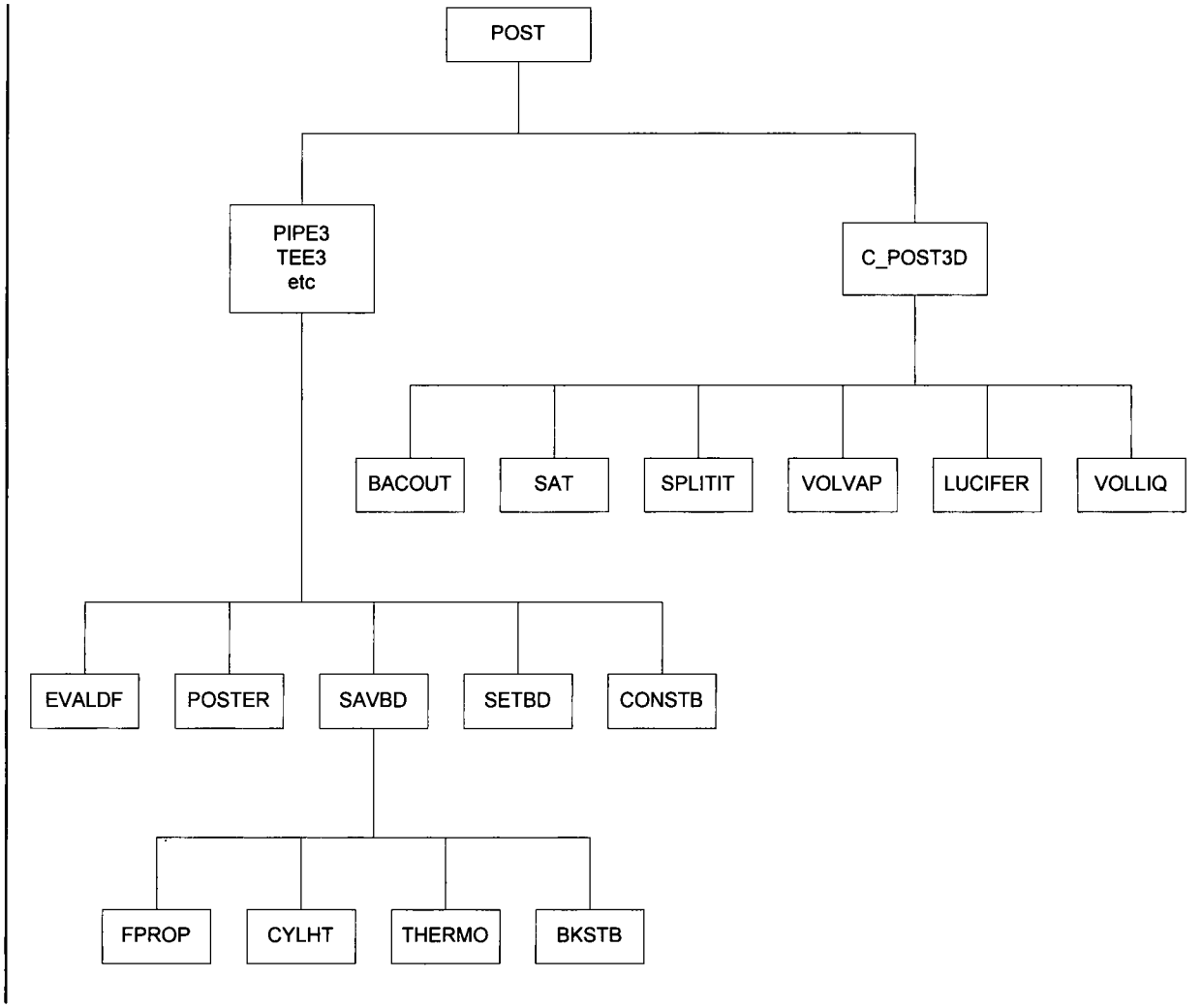

Figure 3-13 WCOBRA/TRAC-TF2 Routines for Post-Pass Calculations

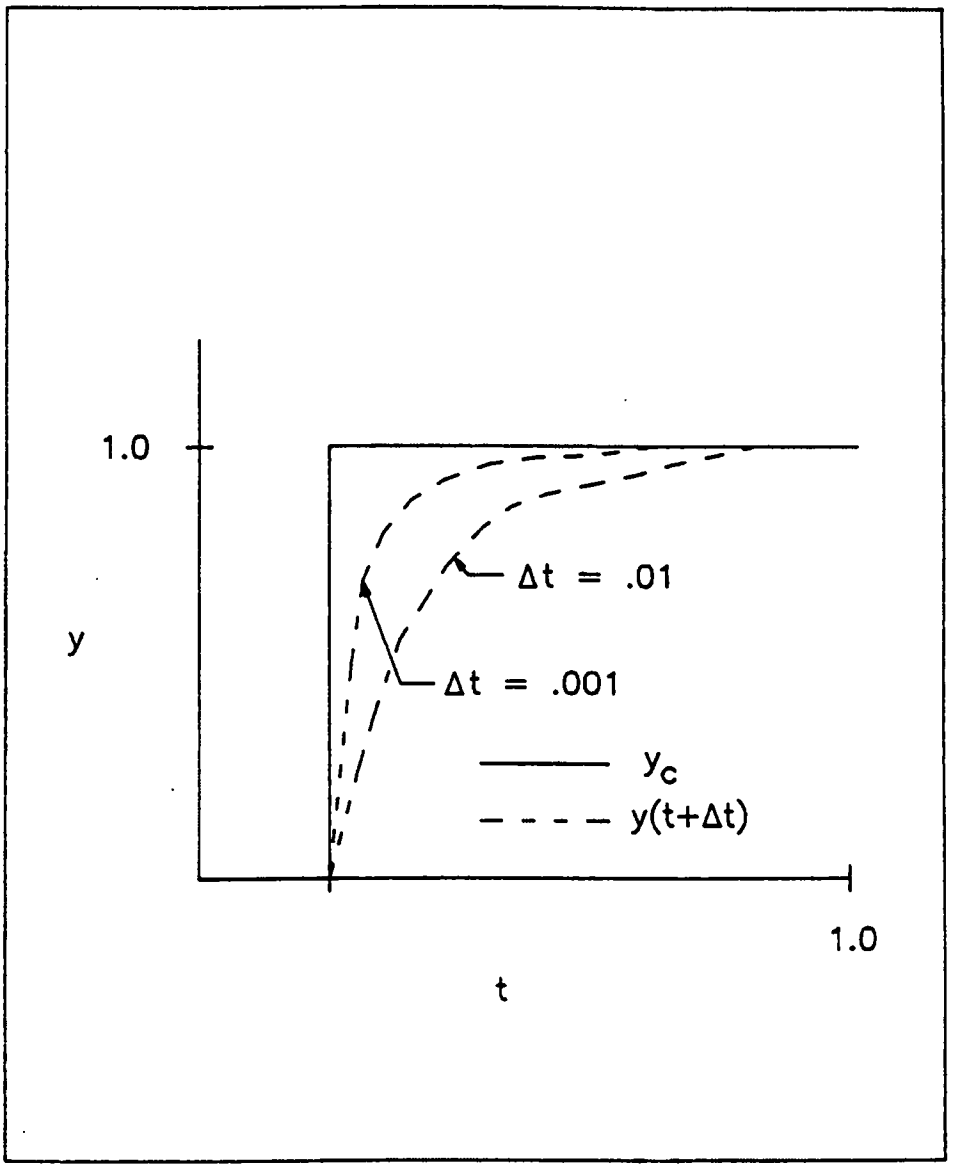

Figure 3-14 Effect of Numerical Damping on Transient Value of y

4 WCOBRA/TRAC-TF2 FLOW REGIME MAPS AND INTERFACIAL AREA

4.1 INTRODUCTION

Two-phase flow patterns are described by the use of flow regime maps. Subsequent calculations for interfacial heat and mass transfer, interfacial drag, and wall drag depend on the flow regime indicated by the flow regime maps. The WCOBRA/TRAC-TF2 code uses three flow regime maps to determine the type of two-phase flow in the reactor coolant system. Two flow regime maps are used in the vessel component. These are the "hot wall" flow regime map and the "normal wall" flow regime map. The normal wall flow regimes are also referred to as the "cold wall" flow regimes. The hot wall flow regime map is selected when a wall surface temperature exceeds the critical heat flux temperature, while the normal wall flow regime map is used when the wall is expected to be fully wetted. A third flow regime map, similar to the vessel component normal wall flow regime map, is used for the one-dimensional components. This section includes descriptions of the flow regimes and the calculations of interfacial areas in the vessel and one-dimensional components.

4.2 VESSEL COMPONENT NORMAL WALL FLOW REGIMES

4.2.1 Introduction

The vessel component normal wall flow regime selection logic is used when there are no heated structures within the computational cell with a surface temperature exceeding:

$$T_w = \begin{cases} 705.3°F \\ T_{CHF} \end{cases} \quad (4\text{-}1)$$

This temperature selection criterion assumes that below the critical heat flux temperature, the wall is fully wet-able and the surface temperature at the critical heat flux is approximated by $T_{CHF} \approx (T_{sat} + 75)$ °F. The upper limit of 705.3°F corresponds to the critical temperature of water. It is assumed that for cells in which a metal surface temperature exceeds the criterion given by Equation 4-1, liquid can only partially wet the wall and the hot wall flow regime is used.

The normal wall flow regimes, shown in Figure 4-1, are the following: small bubble (SB), small-to-large bubble (SLB), churn-turbulent (CT), and film/drop (FD). Selection logic for the normal wall flow regimes is shown in Figure 4-2.

The following subsections describe each regime in the vessel component and specify the range of conditions for which each regime can occur. In addition, the interfacial area estimated for each regime is described. The interfacial area is used in the calculation of interfacial drag and interfacial heat transfer, which are described in Sections 5 and 6.

Before selecting a flow regime and performing calculations, a check is made to ensure that the local flow regime is consistent with the global flow pattern. This is done by checking the void fraction difference between two axial mesh cells. The void fraction difference between cells is:

$$\Delta\alpha_v = \alpha_v(i, j+1) - \alpha_v(i, j) \tag{4-2}$$

where i is a channel index and j is an axial node index.

If the void fraction difference $|\Delta\alpha_v| >$ [ ]^{a,c}, a ramp is identified as:

[ ]^{a,c} (4-3)

and the volume fractions of each field used in calculations of the interfacial quantities in determining flow regime transitions for mesh cell (i, j) are re-defined as:

[ ]^{a,c} (4-4)

(4-5)

and

[ ]^{a,c} (4-6)

where α_v, α_ℓ and α_e are the volume fractions for the vapor, continuous liquid and entrained liquid, respectively.

If the mesh cell (i, j-1) is in the film/drop or a hot wall regime, α_v and α_ℓ are reset for subsequent calculations as:

[ ]^{a,c} (4-7)

and

[ ]^{a,c} (4-8)

If [ ]^{a,c}, an inverted pool is assumed and the void fractions used to determine the flow regime and interfacial terms in cell (i, j) are:

[ ]^{a,c} (4-9)

[ ]^{a,c} (4-10)

and

[ ]^{a,c} (4-11)

When a large void gradient between two cells is not present, the void fractions at the momentum cell center are assumed to be [ ]^{a,c} That is:

[ ]^{a,c} (4-12)

(4-13)

and

[ ]^{a,c} (4-14)

After these volume fractions (α_v , α_ℓ , α_e) are determined, the flow regime and interfacial terms are calculated. The following sections describe the flow regimes and the determination of interfacial area for each regime. The subsections for each normal wall flow regime follow in order of increasing void fraction. First the small bubble regime is described, followed by the small-to-large bubble regime, the churn-turbulent regime, and then the film/drop regime.

The flow regime is indicated by the code for each computational node following the numbering scheme shown in Table 4.2-1:

Table 4.2-1 Summary of Flow Regime Number in Vessel Components

Flow Regime Indicator and Number	Flow Regime
ISIJ = 1:	Small Bubble
ISIJ = 2:	Large Bubble
ISIJ = 5:	Film/Drop
ISIJ = 6:	Hot Wall
ISIJ = 11:	Top Deluge

4.2.2 Small Bubble Regime

Model Basis

The WCOBRA/TRAC-TF2 small bubble flow regime is assumed to exist for void fractions up to [ ]^{a,c}. This regime models what is generally referred to as bubbly flow. In this flow regime, the vapor phase is assumed to consist of dispersed spherical bubbles in a continuous liquid phase. As the void fraction increases above [ ]^{a,c}, the small-to-large bubble flow regime is selected and the transition from bubbly flow to slug flow is modeled.

Transition from bubbly flow to slug flow occurs when the dispersed bubbles agglomerate. When the dispersed bubble density becomes sufficiently large, the bubbles become closely packed and the collision rate increases. Griffith and Wallis (1961) conducted experiments with an air-water mixture in tubes with diameters up to 1.0 inch and observed that below a void fraction of 0.18 there was no indication of slug formation. Additional experiments by Griffith and Snyder (1964) indicated that the void fraction where the bubbly to slug transition occurs is in the range of 0.25 to 0.30.

Other investigators obtained similar conclusions on the bubbly-slug flow transition point. In a semi-theoretical approach, Radovcich and Moissis (1962) postulated that the maximum void fraction for bubbly flow is attained when the bubble collision frequency becomes very large, which they concluded to be at a void fraction of 0.30. Mishima and Ishii (1984) used and also recommended a value of 0.30 for the transition point between the bubbly and slug flow.

Model as Coded

The selection of vessel flow regime takes place in subroutine INTFR. Calculations are performed to determine the interfacial drag and interfacial heat transfer coefficients, [

]^{a,c}.

The bubble size is determined assuming a critical Weber number of [ ]^{a,c}:

$$\left[\right]^{a,c} \qquad (4\text{-}15)$$

[

]^{a,c}

[1] Defined by equation 5-44 in Section 5, but without any additional limiter applied.

[ ]a,c (4-16)

The interfacial area used in the interfacial drag coefficient calculations is then estimated as:

[ ]a,c (4-17)

[[

]a,c

[ ]a,c (4-18)

[

]a,c

[ ]a,c (4-19)

where:

[ ]a,c (4-20)

or

[ ]a,c (4-21)

The interfacial area for interfacial heat transfer coefficient calculations is:

[ ]a,c (4-22)

Scaling Considerations

The model for the small bubble regime is based on motion of an individual bubble in a flow stream. Therefore, no scale bias is introduced. The transition point from bubbly flow to slug flow, α_{SB} ~ [ ]^{a,c}, is close to the theoretical transition, which is also scale independent. Therefore, although there is little

information on flow pattern transitions for large diameter pipes, the transition point $\alpha_{SB} \sim$ [ ]^{a,c} appears to be generally applicable. In the application of WCOBRA/TRAC-TF2 to pressurized water reactors, typical fuel assemblies have a hydraulic diameter of approximately 0.5 in., which is within the range of tube diameters that were used in determining the transition point between the bubbly and slug flow. The flow regime tests thus provide reasonable assurance that the transition boundary between bubbly and slug flow is appropriate for flow in a reactor core. Simulations of experimental tests of differing scale using WCOBRA/TRAC-TF2 are reported in Volume 2 of this report.

The effect of scale on the small bubble transition boundary was also considered by Chow et al. (1989). In that study, the WCOBRA/TRAC-TF2 normal wall flow regime map was converted to $j_\ell - j_g$ map in Figure 4-4, and assessed by comparing it to the vertical flow regime map by Taitel, Barnea, and Dukler (1980), shown in Figure 4-3. The Taitel-Barnea-Dukler map was found to have a small scale dependence on D_h for the bubbly flow boundaries. As described in the reference, these boundaries were obtained by assuming steady flow conditions, deriving the relative velocity obtained from a force balance, and using the interfacial shear models described in Section 5. The WCOBRA/TRAC-TF2 flow regime boundary between small bubble and the small-to-large bubble regime is seen to agree well with the map developed by Taitel, Barnea, and Dukler (1980).

Conclusions

The void fraction used in WCOBRA/TRAC-TF2 as the upper limit of the small bubble regime is consistent with the experimental observations of Griffith and co-workers. Slugs, referred to as large bubbles in WCOBRA/TRAC-TF2, are not permitted to form below α_{SB} = [ ]^{a,c}. This value is in general agreement with the proposed mechanisms of slug formation (suggested by Radovcich and Moissis, 1962, and by Mishima and Ishii, 1984). For void fractions above α_v = [ ]^{a,c}, WCOBRA/TRAC-TF2 assumes the small-to-large bubble regime, which provides a continuous transition from small to large bubbles (slugs). Thus, WCOBRA/TRAC-TF2 at a void fraction of α_v = [ ]^{a,c} still assumes that part of the flow consists of discrete small bubbles. Therefore, the transition point assumed in WCOBRA/TRAC-TF2 between the small bubble and small-to-large bubble regimes is in good agreement with the transition points reported in the published literature.

4.2.3 Small-to-Large Bubble Regime

Model Basis

The small-to-large bubble transition regime in WCOBRA/TRAC-TF2 models the transition from bubbly flow to slug flow. This flow regime is more commonly known as the slug flow or the bubbly/slug flow regime. In the WCOBRA/TRAC-TF2 normal wall flow regime map, this small-to-large bubble regime is assumed for void fractions [ ]^{a,c}. The lower limit for transition into this regime from the small bubble regime was discussed in the previous section. The upper limit is based on the postulate of Taitel, Barnea, and Dukler (1980), who considered spherical bubbles arranged in a cubic lattice. They reported that at a void fraction of $\alpha_v = 0.52$, stationary bubbles would begin to touch and implied that this void fraction must represent the theoretical upper limit of bubbly flow. WCOBRA/TRAC-TF2 uses a value of α_v = [ ]^{a,c} to approximate this condition.

The small-to-large bubble regime models the growth of large vapor slugs and thus approximates the transition from bubbly to slug flow. The flow in this regime is assumed to consist of several large bubbles and many small spherical bubbles in the continuous liquid. In the small-to-large bubble regime, the vapor is partitioned into a small bubble field with a void fraction α_{SB} = [ ]^{a,c}, and the remaining vapor is used to form one or more large bubbles. Figure 4-5 shows this process pictorially. As the vapor fraction increases, the size of the large bubble increases until it is equal to the hydraulic diameter of the computational cell or [ ]^{a,c}, whichever is less. The large bubble is held at this constant value as the vapor fraction continues to increase. Thus, there can be more than one large bubble in each computational cell, and the interfacial area is dependent on the cell size. Figure 4-5 shows a case where there is sufficient vapor to form 1 and 2/3 large bubbles in the computational cell.

Model as Coded

Calculations for the small bubble regime as described in Section 4.2.2 are performed assuming all of the vapor is in the form of small bubbles and the interfacial area is stored as a temporary variable. Calculations assuming that all of the vapor is in the form of large bubbles are performed next. The large bubble calculations and the interpolation of the small and large bubble values for the small-to-large bubble regime are described below.

The large bubble radius is selected to be:

[ ]^{a,c} (4-23)

where r_{SB} is the bubble radius assuming all of the vapor is in the form of small bubbles and r_{LB} is the bubble radius for the large bubbles. The expression for r^*_{LB} is coded in subroutine INTFR as:

[ ]^{a,c} (4-24)

[

]^{a,c}

[ ]^{a,c} (4-25)

where V_ℓ is the volume of liquid in the mesh cell:

[ ]^{a,c} (4-26)

[ ]^{a,c}

$$[\quad]^{a,c} \tag{4-27}$$

[ ]^{a,c}

$$[\quad]^{a,c} \tag{4-28}$$

Substituting Equation 4-27 into Equation 4-28 gives V_{LB} as:

$$[\quad]^{a,c} \tag{4-29}$$

[ ]^{a,c}

$$[\quad]^{a,c} \tag{4-30}$$

[ ]^{a,c}

$$[\quad]^{a,c} \tag{4-31}$$

[ ]^{a,c}

For large bubbles, the interfacial area in a computational cell is equal to the surface area of a single bubble times the number of bubbles in the cell. Expressing the number of large bubbles in the computational cell as:

$$[\quad]^{a,c} \tag{4-32}$$

and assuming all of the vapor is in the form of large bubbles, the large bubble interfacial area is:

$$[\quad]^{a,c} \tag{4-33}$$

or

[ ]a,c (4-34)

This expression is used in the calculation of the large bubble interfacial drag coefficient.

$A_{i,LB}$ is then modified to avoid a large dependence on the adjacent void fraction:

[ ]a,c (4-35)

[

]a,c

[ ]a,c (4-36)

[

]a,c

[ ]a,c (4-37)

[ ]a,c

Equation 4-37 can be shown to be the as-coded expression:

[ ]a,c (4-38)

Scaling Considerations

The small-to-large bubble regime, similar to the small bubble regime, is based on the behavior of a single bubble in a flow field. The use of mesh cell volume to determine the large bubble size, however, indicates that noding selection can influence calculations for this regime. Chow et al. (1989), however, found the small-to-large bubble flow regime boundaries in WCOBRA/TRAC-TF2 to be relatively scale independent, as shown in Figure 4-4. That finding is consistent with the Taitel-Barnea-Dukler map, which shows no scale dependence for the slug flow regime, as shown in Figure 4-3. Therefore, the WCOBRA/TRAC-TF2 small-to-large bubble regime does not contribute to a scale bias.

Conclusions

The WCOBRA/TRAC-TF2 model for the small-to-large bubble regime is consistent with experimental observations on the growth and agglomeration of large bubbles and the formation of slug flow. Simulations of separate and integral effects tests discussed in Volume 2 apply to this model when slug flow is considered possible in experimental tests.

4.2.4 Churn-Turbulent Flow Regime

Model Basis

As the vapor content of the flow increases, the large bubbles will begin to coalesce. This marks the beginning of the transition into churn-turbulent flow. The churn-turbulent flow regime is assumed to occur above a void fraction of α_{LB} = [ ]^{a,c}. This regime is assumed at void fractions above α_{LB} until a stable liquid film is achieved. The void fraction at which a stable liquid film will exist depends on the flow channel size and the vapor velocity. The critical void fraction α_{crit} is determined from a force balance between the disruptive force of the pressure gradient over the crest of waves on the film and the restraining force of surface tension and derived below.

Model as Coded

The critical film thickness at the point where the film became unstable and began to be entrained was given by [ ]^{a,c}

$$\left[\quad \right]^{a,c} \tag{4-39}$$

and the constant includes effects such as wave shape, and amplitude. A value of [ ]^{a,c} was found by Thurgood (1981) to produce reasonable agreement with onset of entrainment data from Dukler (1977). Since the film thickness can be related to the void fraction by:

$$\left[\quad \right]^{a,c} \tag{4-40}$$

It is therefore obtained that:

$$\left[\quad \right]^{a,c} \tag{4-41}$$

where α_e is the entrained liquid fraction and $\underline{U}_{v\ell}$ is the relative velocity between the continuous liquid and the vapor phase in the cell.

Calculations to determine the critical void fraction marking the upper limit of the churn-turbulent flow regime and the interfacial area are performed in subroutine INTFR. The critical void fraction α_{crit} is limited to a value no less than [ ]^{a,c}, and is given by:

[ ]^{a,c} (4-42)

If [ ]^{a,c} $< \alpha_v < \alpha_{crit}$, the churn-turbulent regime is assumed to exist. The droplet diameter is calculated in the film/drop regime as:

[ ]^{a,c} (4-43)

where $A_{i,d}^{///}$ is the drop interfacial area density and is determined from solution of the interfacial area transport equation, described in Section 4.3.7.

The interfacial area for continuous liquid-vapor interfacial drag is calculated assuming a [ ]^{a,c}:

[ ]^{a,c} (4-44)

and for droplets that occur, the interfacial area assumes [ ]^{a,c}:

[ ]^{a,c} (4-45)

For interfacial heat transfer, the interfacial area is [ ]^{a,c}:

[ ]^{a,c} (4-46)

where:

[ ]a,c (4-47)

[

]a,c

Scaling Considerations

The model of the churn-turbulent flow regime was assessed by Chow et al. (1989). The transition boundaries of the churn-turbulent flow regime were found to be relatively insensitive to scale, as shown in Figure 4-4.

Conclusions

The churn-turbulent flow regime model is applicable to conditions expected in a pressurized water reactor (PWR) during a loss-of-coolant accident (LOCA) event. Transition boundaries are relatively insensitive to scale.

4.2.5 Film/Drop Flow Regime

Model Basis

At a void fraction above $\alpha_v = \alpha_{crit}$, the flow is considered to consist entirely of film/drop flow. As long as the vapor velocity is sufficiently high to entrain drops, a drop field will be maintained. The transition between film and droplet flow is predicted based on the models used for entrainment and interfacial drag between the vapor and the drops.

Model as Coded

The interfacial areas for continuous liquid film and drops in the film/drop regime are calculated in the same way as they are for churn-turbulent flow. As before, in the film/drop regime the drop diameter is calculated as:

[ ]a,c (4-48)

where $A'''_{i,d}$ is the drop interfacial area density.

The interfacial area for continuous liquid-vapor interfacial drag is calculated as:

[ ]a,c (4-49)

and the drop interfacial area is:

[ ]a,c (4-50)

For the interfacial heat transfer, the interfacial area is adjusted to provide a smoother transition between two adjacent hydraulic cells and is calculated as:

[ ]a,c (4-51)

where:

[ ]a,c (4-52)

Scaling Considerations

The model for the film/drop flow regime was assessed by Chow et al. (1989). The transition boundary between the film/drop regime and the churn-turbulent regime was found to be somewhat dependent on scale, as shown in Figure 4-4. For large hydraulic diameters, the boundary agrees with that given by Taitel, Barnea, and Dukler (1980) in Figure 4-3.

Conclusions

The film/drop regime model is applicable to conditions expected in a PWR during a LOCA event. Transition boundaries are somewhat dependent on scale.

4.3 VESSEL COMPONENT HOT WALL FLOW REGIMES

4.3.1 Introduction

This section describes the hot wall flow regime map used in the WCOBRA/TRAC-TF2 vessel component.

During the initial part of blowdown in a PWR, departure from nucleate boiling (DNB) occurs and the core undergoes a rapid heatup. After DNB, liquid-wall contact is prevented by the rapid evaporation of water, and the flow regimes are significantly different from the two-phase flow regimes that occur for an unheated surface. This flow regime is available only for channels with heated structures.

The "hot wall" flow regimes are assumed when a momentum cell contains a heated surface with a temperature exceeding the value of T_w given by Equation 4-1 . These hot wall regimes describe the structure and hydrodynamics of the highly non-homogeneous, thermal non-equilibrium two-phase flow encountered during blowdown and reflood. The hot wall flow regimes include the subcooled inverted annular flow regime, the inverted liquid slug flow regime, the dispersed droplet flow regime, the falling film flow regime and the top deluge flow regime. Figure 4-6 presents an illustration of the hot wall flow regimes, and Figure 4-7 shows a schematic of the hot wall regime selection logic. The following sections describe each of these flow regimes, and determine the interfacial area used in interfacial drag and heat transfer calculations.

4.3.2 Inverted Annular Flow Regime

Model Basis

An inverted annular flow regime is assumed during upflow when the continuous liquid phase is subcooled. In the inverted annular flow regime, the continuous liquid is assumed to be separated from the wall by a thin film of vapor. This assumed flow structure is in agreement with that observed in the experiments conducted by DeJarlais (1983). The interfacial areas calculated for the liquid annular column and any droplets present in the flow are consistent with this flow structure. For the continuous liquid, the interfacial area density is:

[ ]^{a,c} (4-53)

and for droplets the interfacial area density, $A^{///}_{i,d}$, is determined from the solution of the drop interfacial area transport equation.

Model as Coded

For continuous liquid, the interfacial area for the subcooled inverted annular flow regime is coded as:

[ ]^{a,c} (4-54)

and for the droplets by:

[ ]^{a,c} (4-55)

[

]^{a,c}

Scaling Considerations

The inverted annular flow regime is applicable to conditions expected in a PWR during a LOCA event and no scaling limitation was identified.

Conclusions

The inverted annular flow regime can exist when liquid-wall contact is prevented by the rapid evaporation of water near the wall. The continuous liquid is assumed to be separated from the wall by a thin film of vapor. The model is developed assuming a liquid core in the center of channel separated from the wall by a steam blanket. The inverted annular flow regime is expected during some conditions in a PWR during a LOCA event. No scaling issue was identified.

4.3.3 Inverted Liquid Slug Flow Regime

Model Basis

The inverted liquid slug flow regime, also referred to as the liquid chunk regime, models the flow pattern following breakup of the continuous liquid column in the inverted annular regime. In this regime, the annular liquid column disintegrates due to growth of unstable waves that form on the interface. The liquid slugs that form are large, nearly filling the channel flow area, and are unstable. These slugs eventually break up into smaller discrete droplets.

The interfacial area for the liquid slugs is estimated assuming the continuous liquid slugs are spherical. The interfacial area of the slugs is:

$$A_{i,S}''' = N_S''' \pi D_S^2 \tag{4-56}$$

where D_S is the liquid slug diameter and N_S''' is the number density of slugs:

$$N_S''' = \frac{\alpha_\ell}{\frac{\pi D_S^3}{6}} \tag{4-57}$$

The interfacial area density of the slugs then becomes:

$$A_{i,S}''' = \frac{6\,\alpha_\ell}{D_S} \tag{4-58}$$

Assuming the slugs have a diameter [ ]^{a,c} yields for slug interfacial area:

$$\left[\quad\right]^{a,c} \tag{4-59}$$

The slug diameter is based on the assumption that an inverted annular column will break up initially into drops whose dimensions are approximately equal to the wavelength of the surface instability which forms on the liquid column. Data by DeJarlais (1983) indicates that for conditions typical of those in a PWR core channel during reflood, the characteristic surface wavelength is about 0.75 of the liquid column diameter. The liquid column diameter is assumed to be equal to the channel diameter, because the inverted liquid slug regime is expected to occur at low void fraction.

Model as Coded

The interfacial area of the liquid slug in the inverted slug flow regime is coded as:

$$\left[\qquad\right]^{a.c} \tag{4-60}$$

where A_X is the flow area in the momentum cell, and ΔX is the cell height.

The interfacial area for any droplets that may appear in the inverted liquid slug regime is:

$$\left[\qquad\right]^{a,c} \tag{4-61}$$

Scaling Considerations

Data by DeJarlais (1983) indicates that for conditions typical of those in a PWR core channel during reflood, the characteristic surface wavelength is about 0.75 of the liquid column diameter which is consistent to what assumed in Equation 4-59.

Conclusions

The inverted liquid slug flow regime models the flow pattern following breakup of the continuous liquid column in the inverted annular regime. The annular liquid column disintegrates due to growth of unstable waves that form on the interface. These slugs eventually break up into smaller discrete droplets. The model is derived assuming liquid slugs are spherical. The slug diameter is determined by assuming that the annular column breaks up into drops whose dimensions are approximately equal to the wavelength of the surface instability which forms on the liquid column. The characteristic surface wavelength is 0.746 which was found to be consistent with data reported by DeJarlais (1983) at conditions similar to those experienced in a PWR core channel during reflood.

4.3.4 Dispersed Droplet Flow Regime

Model Basis

The dispersed droplet flow regime is characterized by small liquid drops surrounded by a continuous vapor phase. Entrainment of continuous liquid in the inverted slug regime allows for a smooth transition into the dispersed droplet flow regime. The dispersed droplet regime can exist at all void fractions, if entrainment mechanisms create this field.

Model as Coded

The interfacial area in this regime is determined directly from solution of the drop interfacial area transport equation, as described in Section 4.3.7.

The interfacial area for the dispersed droplets is given by:

[ ]a,c (4-62)

The droplet diameter used to calculate the drop Reynolds number for the interfacial drag and heat transfer is given by Equation 4-48.

Scaling Considerations

No scaling issue was identified.

Conclusions

The dispersed droplet flow regime is characterized by small cylindrical liquid drops surrounded by a continuous vapor phase. The dispersed droplet regime can exist at all void fractions, if entrainment mechanisms create this field. No scaling issue was identified.

4.3.5 Falling Film Regime

Model Basis

Although the normal direction for reflood is from the bottom of the core, a top quench front is assumed to exist if the momentum cell above the cell in a hot wall flow regime (inverted annular, inverted liquid slug, dispersed droplet) contains no surfaces with a temperature greater than T_{CHF}. If the void fraction is greater than [ ]^{a,c}, the falling film flow regime is assumed.

The interfacial area and diameter of droplets in the flow field are determined in the same way as described in the dispersed droplet flow regime. As in other hot wall regimes, the vapor blankets the wall, thus the interfacial area per unit volume for the film is:

[ ]a,c (4-63)

Model as Coded

The interfacial area for the falling film is calculated as:

[ ]a,c (4-64)

and the interfacial area for the droplets is again given by:

[ ]a,c (4-65)

Scaling Considerations

No major scaling issue was identified.

Conclusions

The falling film flow regime was designed to model the top quench front and can exist if the void fraction is greater than [ ]a,c. The interfacial area and diameter of droplets in the flow field are determined in the same way as described in the dispersed droplet flow regime. The interfacial area per unit volume for the film is determined similarly to the inverted annular flow regime.

4.3.6 Top Deluge Flow Regime

Model Basis

The top deluge flow regime is similar to the falling film regime except that top deluge is assumed when the void fraction is less than [ ]a,c. Like the falling film regime, a top quench front is assumed to exist if the momentum cell above the cell in a hot wall regime contains rods with temperatures less than T_{CHF}. In the deluge flow regime the flow is assumed to consist of large liquid slugs having diameters equal to the flow channel hydraulic diameter.

Model as Coded

The interfacial area and drop size for droplets that occur in the top deluge regime are determined in the same way as described for the dispersed droplet flow regime. The interfacial area for the liquid slugs is:

[ ]a,c (4-66)

The interfacial area of the drops is:

[ ]a,c (4-67)

Scaling Considerations

No major scaling issue was identified.

Conclusions

The top deluge flow regime is similar to the falling film regime except that top deluge is assumed when the void fraction is less than [ ]^{a,c}. The flow is assumed to consist of large liquid slugs having diameters equal to the flow channel hydraulic diameter.

4.3.7 Interfacial Area Transport Equation

Model Basis

The interfacial area of the entrained droplet field is determined by solving an interfacial area transport equation:

$$\frac{dA_{i,d}^{///}}{dt} + \nabla \cdot (A_{i,d}^{///} \underline{U}_e) = \dot{A}_{i,E}^{///} + \dot{A}_{i,\Gamma}^{///} \tag{4-68}$$

where the physical meaning of each term is expressed as:

$$\begin{bmatrix} \text{Rate of} \\ \text{Change of} \\ \text{Interfacial Area} \\ \text{Concentration} \end{bmatrix} + \begin{bmatrix} \text{Rate of} \\ \text{Efflux of} \\ \text{Interfacial Area} \\ \text{Concentration} \end{bmatrix} = \begin{bmatrix} \text{Rate of} \\ \text{Interfacial Area} \\ \text{Concentration} \\ \text{Generation by} \\ \text{Entrainment and} \\ \text{Deposition} \end{bmatrix} + \begin{bmatrix} \text{Rate of} \\ \text{Interfacial Area} \\ \text{Concentration} \\ \text{Change Due to} \\ \text{Phase Change} \end{bmatrix}$$

Model as Coded

The interfacial area transport equation given by Equation 4-68 is solved in subroutine C_POST3D for $A_{i,d}^{///}$ with an explicit method. Equation 4-68 is written as:

$$\left[\qquad \right]^{a,c} \tag{4-69}$$

[.

]^{a,c}

The change in drop interfacial area due to phase change within the cell is calculated from a mass balance:

$$\left[\qquad \right]^{a,c} \tag{4-70}$$

[

]a,c

Since:

[ ]a,c (4-71)

[ ]a,c

[ ]a,c (4-72)

Thus,

[ ]a,c (4-73)

[ ]a,c

Multiplying Equation 4-73 by [ ]a,c

[ ]a,c (4-74)

Thus,

[ ]a,c (4-75)

[

]a,c

The drop interfacial area concentration is then calculated. The net contribution to interfacial area from incoming and out flowing streams is evaluated and added to Equation 4-75 along with the entrainment component, as shown below:

[ ]a,c (4-76)

The interfacial area concentration given by Equation 4-76 is then compared to possible lower limits, and the final value of $A_{i,d}^{///}$ is selected as:

[ ]a,c (4-77)

The drop interfacial area for entrained flow is given by:

[ ]a,c (4-78)

Scaling Considerations

The interfacial area transport equation is not dependent on scale. One of the lower limits imposed on $A_{i,d}^{///}$ depends on mesh size, but that limit is rarely applied. As a result, the calculation of $A_{i,d}^{///}$ is not considered to be scale dependent.

Conclusions

The interfacial area of the entrained droplet field is determined by solving an interfacial area transport equation which more mechanistically captures the evolution of the interfacial area of the dispersed field as droplets are entrained, de-entrained and evaporates.

4.4 ONE-DIMENSIONAL COMPONENT FLOW REGIMES

4.4.1 Introduction

This section describes the flow regime map used in the one-dimensional components. WCOBRA/TRAC-TF2 adopts a basic flow regime map that is assumed to apply for both the horizontal and vertical flow. This flow regime map assumes the existence of four flow regimes: bubbly, slug, churn, and annular-mist. The bubbly flow regime occurs for void fractions $\alpha \le 0.3$, the slug regime for $0.3 < \alpha \le 0.5$ with mass flux $G \le 2000$ kg/m^2-s, the churn regime for $0.5 < \alpha < 0.75$, and the annular-mist regime for $\alpha \ge 0.75$. In addition, the flow regimes of horizontal stratified flow (including wavy-dispersed flow) may be superimposed onto the basic flow regime map, subject to certain physical and phenomenological criteria. The basic WCOBRA/TRAC-TF2 one-dimensional component flow regime map defined on a mass flux versus void fraction plane is shown in Figure 4-8. The crosshatched sections represent interpolation regions between two flow regimes and/or between mass flux over the range $2000 < G < 2700$ kg/m^2-s. For the churn flow regime, values of the interfacial area are interpolated between values at $\alpha = 0.5$ and $\alpha = 0.75$ rather than using separate correlations for churn flow. The transition from slug to bubbly flow for mass flux higher than 2000 kg/m^2-s also use interpolation to

smoothly change regimes over the range $2000 < G < 2700$ kg/m^2-s. Single phase liquid is assumed if $\alpha < 1.0 \times 10^{-6}$ and single phase vapor is assumed when $\alpha > 0.999999$.

The flow regime map described below is applied to the calculation of interfacial area for heat transfer only. The interfacial drag force occurring as a result of the momentum interchange between the phases is assumed in WCOBRA/TRAC-TF2 to be proportional to the square of the relative velocity, and the interfacial drag coefficient is defined as the constant of proportionality.

The flow regime is flagged by the code for each node following the numbering scheme shown in Table 4.4-1.

Table 4.4-1 Summary of Flow Regime Number in 1D Components	
REGNM=1:	bubbly or bubbly-slug flow
REGNM=2:	horizontal stratified flow with void fraction ≤0.5
REGNM=1.0~2.0:	interpolation region between REGNMs 1 and 2.
REGNM=2.5:	wavy-dispersed flow with void fraction ≤0.5
REGNM=3:	churn (transition) flow
REGNM=4:	horizontal stratified flow with 0.5<void fraction ≤0.75
REGNM=3.0~4.0:	interpolation region between REGNMs 3 and 4.
REGNM=4.5:	wavy-dispersed flow with 0.5<void fraction ≤0.75
REGNM=5:	annular-mist flow
REGNM=6:	horizontal stratified flow with 0.75<void fraction
REGNM=5.0~6.0:	interpolation region between REGNMs 5 and 6.
REGNM= -1:	ERROR
REGNM=0:	REGNM=0 is the initial value of flow regime number. It exists for the cell face adjacent to a FILL component or with flow area FA<1.0E-10 m^2. There is no physical meaning for flow with REGNM=0.

4.4.2 Bubbly-Slug Flow Regime

Model Basis

This section will refer collectively to the bubbly, bubbly-slug transition, and bubbly-slug flow regimes labeled in Figure 4-8. An older version of WCOBRA/TRAC (Bajorek et al., 1998) documentation called the "bubbly slug" region in Figure 4-8 simply the "slug" flow region. With regard to the description of the interfacial area logic, it is more convenient to combine the three names in the figure under the single term "bubbly slug."

Bubbly flow occurs for the range of $0 \le \alpha \le 0.30$ in the entire mass flux range. The transition point $\alpha = 0.30$ between bubbly and slug flow is the value postulated by Radovcich and Moissis (1962), Ishii and Mishima (1980), and Mishima and Ishii (1984). Bubbly flow is also assumed when $0.30 < \alpha < 0.50$ and the mass flux is greater than 2700 kg/m^2-s. This mass flux limit is based on the work by Choe, Weinberg, and Weisman (1976). When the vapor void fraction is $0.3 < \alpha \le 0.5$ and the cell-average mass flux is less than 2000 kg/m^2-s, slugs and bubbles coexist in the flow. At the upper void fraction limit, $\alpha = 0.5$, 40 percent of the vapor is assumed to exist in the form of trailing bubbles with the remainder contained in the slug. If the mass flux is greater than 2700 kg/m^2-s, slug formation is prohibited and the entire vapor field is assumed to exist as a bubbly flow. The intermediate mass flux range is treated as a transition region between bubbly and bubbly-slug regimes.

Model as Coded

The interfacial area calculation for different flow regimes is coded in the subroutine HTIF. For the purpose of interfacial heat transfer calculation, the minimum void fraction is limited to [

$$\left[\right]^{a,c} \quad \left[\right]^{a,c} \tag{4-79}$$

Based on the work of Ishii and Mishima (1980), the interfacial area concentration is calculated as a function of the average void fraction within the liquid slug, α_{gs}, such that:

$$\left[\right]^{a,c} \tag{4-80}$$

for

$$\left[\right]^{a,c} \tag{4-81}$$

However, if the cell void fraction, α, is found to be [ ]^{a,c}

In the area concentration equation, the Sauter mean bubble diameter, D_b, is defined as a function of the Laplace coefficient, L_o (Lime 2001), where:

[ ]^{a,c} (4-82)

and

[ ]^{a,c} (4-83)

The bubble diameter is also subject to the constraint that [ ]^{a,c}.

Finally, the parameters C^* and D^* are included to account for the presence of cap bubbles or vapor slugs. The two parameters are defined as a function of hydraulic diameter such that:

[ ]^{a,c} (4-84)

(4-85)

where $D_{h,crit}$ is a critical hydraulic diameter for slug to cap bubble transition, calculated as:

[ ]^{a,c} (4-86)

The parameters C^* and D^* have been modified from the original reference to include large-diameter flow channels.

Scaling Considerations

The flow regime map is void fraction based, with some consideration to account for the observed presence/absence of slugs in bubbly flow. A void fraction based map can be shown to be similar to the Taitel-Dukler (Taitel and Dukler, 1976) and Mishima-Ishii (Mishima and Ishii, 1980) maps which have been shown to predict regimes in small pipes. The slug size is in fact known to be limited due to surface instability (Kitscha and Kocamustafaogullari, 1989). Though the database used to form the model is limited in scale, extension to larger pipes is possible by allowing two different sizes of bubbles to exist. The model was adapted to be applicable to large diameter pipes. For example, the parameters C^* and D^* are included to account for the presence of cap bubbles or vapor slugs and have been modified from the

original reference to include large-diameter flow channels. No major scaling bias is expected for the purpose of modeling two-phase flow in PWR reactor coolant system (RCS) piping.

Conclusions

This section will refer collectively to the bubbly, bubbly-slug transition, and bubbly-slug flow regimes. Flow regime is intended to be applicable at the conditions and geometry scale of PWR RCS loop piping during LOCA conditions.

4.4.3 Churn Flow Regime

Model Basis

The churn flow regime is assumed in the range $0.5 < \alpha < 0.75$. The churn flow regime is modeled in WCOBRA/TRAC-TF2 one-dimensional components as a simple transition between bubbly-slug and annular-mist flows. The interfacial area for the churn flow regime is estimated using interfacial areas calculated for the bubbly-slug and annular-mist regimes using a weighing factor to insure the regimes merge smoothly.

Model as Coded

Interfacial areas are first calculated for the bubbly-slug regime $A_{i,bs}$, and for the annular-mist regime $A_{i,am}$. The interfacial area for the churn flow regime is then calculated using a [ ]^{a,c}:

$$\left[\right]^{a,c} \tag{4-87}$$

The interfacial area for the annular-mist regime, $A_{i,am}$, is described in Section 4.4.4 and is given by Equation 4-103.

The weighting factor W_t is given by:

$$\left[\right]^{a,c} \tag{4-88}$$

Scaling Considerations

The Churn Flow Regime is designed to be a simple transition between bubbly-slug and annular-mist flows. Therefore, the same considerations to those regimes apply.

Conclusions

The Churn Flow Regime is intended to be applicable to the geometry of PWR RCS loop piping during LOCA conditions.

4.4.4 Annular-Mist Flow Regime

Model Basis

The annular-mist flow regime is assumed when $0.75 < \alpha < 0.999999$. The liquid flows as droplets in the gas core and also forms a liquid film on a solid wall.

The interfacial area concentration in the mist flow portion is given by Kataoka and Ishii (1982) as:

$$a_{i,drop} = \frac{\alpha}{1-\alpha_{d,c}}\left(\frac{6\cdot\alpha_{d,c}}{D_d}\right) \tag{4-89}$$

where D_d is the Sauter mean diameter of the droplet population; $\alpha_{d,c}$ is the droplet fraction in the gas core and α is the vapor phase fraction. The droplet fraction is estimated as a function of the entrainment fraction E (Ishii and Mishima, 1980 and Ishii and Mishima, 1989):

$$\alpha_{d,c} = E\frac{(1-\alpha)u_\ell}{\alpha u_g} \tag{4-90}$$

where u_g and u_ℓ are the vapor and liquid velocities, respectively.

The entrainment fraction E is defined as:

$$E = \frac{\dot{m}_e}{\dot{m}_\ell} = \frac{j_e}{j_\ell} \tag{4-91}$$

where $\dot{m}_e$, $\dot{m}_\ell$, j_e and j_ℓ are droplet mass flow rate, total liquid mass flow rate, droplet volumetric flux and total liquid volumetric flux, respectively, and:

$$E = \tanh\left(7.25\times10^{-7}\,We^{1.25}Re_\ell^{\,0.25}\right) \tag{4-92}$$

In Equation 4-92 the liquid Reynolds number Re_ℓ and the effective Weber number We are defined as:

$$Re_\ell = \frac{\rho_\ell(1-\alpha)u_\ell D_h}{\mu_\ell} \tag{4-93}$$

and

$$We = \frac{\rho_g(\alpha u_g)^2 D_h}{\sigma}\left(\frac{\rho_\ell-\rho_g}{\rho_g}\right)^{1/3} \tag{4-94}$$

Additionally, the Sauter mean droplet diameter is calculated as:

$$D_d = (0.796)D_{dl} \tag{4-95}$$

provided that $84\,\mu m \le D_d \le 4\,mm$. D_{dl} is based on the correlation of Kataoka, Ishii, and Mishima (1983), where:

$$D_{dl} = \frac{0.01\cdot\sigma}{\rho_g\cdot(\alpha u_g)^2}\cdot Re_g^{2/3}\cdot\left(\frac{\rho_g}{\rho_\ell}\right)^{-1/3}\left(\frac{\mu_g}{\mu_\ell}\right)^{2/3} \tag{4-96}$$

where μ is the fluid viscosity.

Other droplet diameter formulation such as one based on the work of Kataoka, and of Kitscha

and Kocamustafaogullari (1989) was considered (= D_{d2}) in the developmental stage. D_{d2} is expressed as:

$$D_{d2} = 0.254\cdot L_o\cdot\left(-0.13\cdot We_m + \sqrt{16+(0.13\cdot We_m)^2}\right) \tag{4-97}$$

In the above droplet relations, the Reynolds number and Weber number are given by:

$$Re_g = \frac{\rho_g\alpha u_g D_h}{\mu_g} \tag{4-98}$$

$$We_m = \frac{\rho_g(\alpha u_g)^2 L_o}{\sigma} \tag{4-99}$$

The droplet diameter formulation using Equation 4-97 was not selected for the current WCOBRA/TRAC-TF2. Finally, if all the liquid is entrained as liquid droplets, then $\alpha_{d,c} = 1-\alpha$ and:

$$a_{i,drop,max} = B_{cell}\cdot\frac{6\cdot(1-\alpha)}{D_d} \tag{4-100}$$

From purely geometric considerations, the liquid film interfacial area can be calculated as:

$$A_{i,film} = B_{cell}\cdot\frac{4\cdot Cr}{D_h}\sqrt{\frac{\alpha}{1-\alpha_{d,c}}} \tag{4-101}$$

where the parameter Cr is included to account for waviness of the liquid interface when the liquid film becomes very thin (<25 mm) and the film breaks down and rivulets form. It is defined by:

[ ] a,c (4-102)

where $l_{min} = 0.1\,mm$.

Model as Coded

In WCOBRA/TRAC-TF2, both liquid film and entrained droplets are modeled, and the characteristics of liquid droplets and film must be properly superimposed to represent the liquid flow field. Thus, the interfacial area is based on a [ ]^{a,c}

[ ] a,c (4-103)

The weighting factor, W_f, is introduced to account for the fact that beyond a certain limit in phasic velocities all the liquid will be entrained in the form of droplets, thus no liquid film will exist. The phasic velocities are compared to a critical velocity defined based upon a Helmholtz disturbance wave and given by:

[ ] a,c (4-104)

The weighting factor is obtained as:

[ ] a,c (4-105)

Scaling Considerations and Conclusions

A range of applicability and scaling assessment of the 1D annular-mist flow regime model is provided in Appendix F.1.2 of TRAC-M theory manual (Spore et al., 2000). As stated in that report both the diameter and the entrainment fraction correlations are based upon low-pressure air-water data. In the code, these relations are also used at high pressures and use steam-water properties. The trends follow physical expectations. Quantitative error committed by extrapolating these correlations beyond their parametric will be accounted for in the overall WCOBRA/TRAC-TF2 code bias and uncertainty discussed in Volume 2 of this report.

4.4.5 Horizontal Stratified Flow

Model Basis

At low liquid and vapor velocities, the individual phases may separate and form a relatively smooth interface. The schematic plot of horizontal stratified flow is shown in Figure 4-9. Due to the effect of gravity, the two-phase flow is separated with the heavier liquid phase at the bottom and the lighter gas phase at the top. A flat horizontal liquid-gas interface separates the two phases. One characteristic of the horizontal stratified flow is that the interfacial area between two phases is minimal compared with other flow regimes, such as bubbly-slug, annular-mist, etc. A low interfacial area consistent with stratified flow allows for increased gas venting capability during a small break LOCA scenario. However, the structure of horizontal stratified flow is unstable if the relative velocity between the two phases is large. According to the Kelvin-Helmholtz stability theory, a large relative velocity causes the interface to become unstable and interfacial waves to grow. The growing interfacial waves eventually destroy the stratified flow structure.

The transition criterion from horizontal stratification to other regimes is based on a modified version of the Kevin-Helmholtz theory and is discussed in the following. The theory presented is supported by theoretical studies and experiments (Taitel and Dukler, 1976; Anoda et al.,1989; Crowley et al., 1992; Barnea and Taitel, 1993). The criterion is based on dimensionless parameters and is shown to have a relatively minor dependence on the pipe diameter, system pressure, and fluid properties, as well as the fluid superficial velocities.

It is recognized that the transition criterion developed here is based on a steady state condition which lacks proper treatment relative to transient behavior such as an explicit relaxation model to account for settling of the separation process and changing of the interface level. Taitel et al. (1978) discussed a delay in transition to non-stratified flow due to gravity wave propagation when the level changes due to a liquid flow increase. They also demonstrated that the delay characteristics are different when the separated liquid flow is subcritical or supercritical. Transition from the non-stratified flow pattern to the stratified flow pattern also shows a delay, since it takes place when the two phases are completely separated. The settling of the separation process takes time, since the turbulence in liquid flow interferes with the merging and rising of the bubbles. These phenomena are not explicitly modeled in the transition model, although the transition criterion based on the local variables partially captures the transition process from the stratified flow to non-stratified flow. It is noted that the highly transient behavior, which likely happens in loop seal clearance, was simulated reasonably well for Integral Effects Tests, such as the Rig-of-Safety Assessment (ROSA) 0.5% break, 2.5% break, 5% break, and 10% break. Details are given in Section 21.

Transition Criteria

Taitel and Dukler (1976) represents the first complete semi-theoretical horizontal flow regime transition theory. In the original Taitel-Dukler work, boundaries of smooth stratified, wavy stratified, intermittent, annular, and dispersed bubbles regimes are derived assuming steady state flows.

The Taitel-Dukler stratification transition criterion was developed using Kelvin-Helmholtz stability theory. The Kelvin-Helmholtz theory provides a stability criterion for waves of infinitesimal amplitude

formed on a flat surface of liquid flow between horizontal parallel plates. Considering a round pipe geometry and pipe inclination angle, Taitel and Dukler gave a semi-empirical neutral stability condition for horizontal stratified flow.

$$u_g = \left(1 - \frac{h_l}{D}\right)\sqrt{\frac{(\rho_\ell - \rho_g) g \cos\beta A_g}{\rho_g S_i}} \tag{4-106}$$

where h_l is the depth of the liquid layer, D is the pipe diameter, ρ_ℓ and ρ_g are the respective liquid phase density and gas phase density, g is the gravitational constant, A_g and A_l are the areas of the pipe occupied by the respective gas phase and liquid phase, S_i is the interfacial length in the cross section of pipe (Figure 4-9), and β is the pipe inclination angle.

If the gas phase velocity is higher than the critical gas velocity given in Equation 4-103, the stratified flow is no longer stable and the transition happens. The critical gas velocity is determined by the pipe diameter, the void fraction, the pipe inclination angle, and fluid densities. However, Taitel-Dukler assumed liquid phase velocity is much smaller than the gas phase velocity in their criterion, which is only reasonable for low mass flux flow.

Asaka et al. (1991) analyzed Two-Phase Test Facility (TPTF) experiments using the TRAC-PF1/MOD1 code to assess the adequacy of the Taitel-Dukler flow regime transition criterion and code's interfacial drag models. The code predicted slug or transitional flow regime for tests conducted for relatively high flow rates, whereas the experimental flow regime was stratified flow. This resulted in a large over-prediction of the interfacial drag for these tests. As a result, Asaka suggested the use of a modified version of the Taitel-Dukler model to better describe the flow regime transition (Anoda et al., 1989). The difference between Equation 4-107 and Equation 4-106 is the gas phase velocity u_g is replaced by relative velocity $|u_g - u_\ell|$.

$$\Delta u_c = |u_g - u_\ell| = \left(1 - \frac{h_l}{D}\right)\sqrt{\frac{(\rho_\ell - \rho_g) g \cos\beta A_g}{\rho_g S_i}} \tag{4-107}$$

Beside TRAC-PF1/MOD1, the modified Taitel-Dukler (1976) criterion for the transition and its variations were also implemented in other LOCA safety evaluation codes. A similar approach was also implemented in the RELAP5/MOD3 code (INEL, 1995). The model included in CATHARE was described by Bestion (1990). A review of these models was presented in the paper by Yudov (2002) which in particular described how the horizontal stratified flow regime is formulated in the KORSAR code.

Asaka's (1991) approach, with the sound physical base of the modified Taitel-Dukler criterion, has been considered for the 1D module of WCOBRA/TRAC-TF2. There are other more sophisticated transition criteria (Barnea and Taitel, 1993; Crowley, et al., 1992) that consider viscous effects of the Kelvin-Helmholtz stability analysis. The viscous transition models improve accuracy of the transition criteria by incorporating the viscous Kelvin-Helmholtz instability into the two-fluid model. However, the implementation of the viscous transition model into a computer code is cumbersome. The original inviscid Taitel-Dukler (1976) criterion is suggested over the viscous transition model for

WCOBRA/TRAC-TF2. However, the predictions from the viscous transition model are utilized to calibrate the transition model developed here.

The modified Taitel-Dukler transition criterion can be presented in dimensionless form. A modified Wallis number $j_{g\ell}^*$ is defined using the liquid velocity, the vapor velocity, the void fraction, the pipe diameter, gravitational constant, and fluid densities.

$$j_{g\ell}^* = \frac{|u_g - u_\ell|\alpha}{\sqrt{\frac{\rho_\ell - \rho_g}{\rho_g} Dg}} \tag{4-108}$$

Therefore, Equation 4-107 is regrouped as:

$$j_{g\ell,c}^*(\alpha) = \left(1 - \frac{h_l}{D}\right)\sqrt{\frac{\alpha^3 \pi D \cos\beta}{4S_i}} \tag{4-109}$$

Here $\cos\beta$ is the effect of pipe inclination angle on the transition criterion. In the WCOBRA/TRAC-TF2 regime map, horizontal flow is only allowed when the pipe inclination angle is less than [ ]^{a,c}. Since [ ]^{a,c} the value can be approximated as 1.0 for simplicity, and $\cos\beta$ is removed from the stratification transition criterion. This simplification will slightly stabilize the stratified flow in an inclined pipe flow. The new transition criterion is given by:

$$j_{g\ell,c}^*(\alpha) = \left(1 - \frac{h_l}{D}\right)\sqrt{\frac{\alpha^3 \pi D}{4S_i}} \tag{4-110}$$

In Equation 4-110, $j_{g\ell}^*$ is only a function of void fraction for a round pipe since h_l/D and S_i/D are both functions of void fraction. Trends with pressure and hydraulic diameter are shown in Figure 4-10 and Figure 4-11. Figure 4-12 shows the modified Taitel-Dukler transition line in the $j_{g\ell}^*$-α plot together with various transition boundary data. The data points in Figure 4-12, and also used in Figure 4-13, Figure 4-14, and Figure 4-17, include the stratified flow to slug flow transition boundary observed in the TPTF tests (Nakamura et al., 1995), the transition boundaries from the offtake experiments of Moon (Moon and No, 2003), and from Smoglie, which data points were presented by Moon and No (2003), gas-liquid experimental data from Crowley et al. (1992). The data sources for Figure 4-13 are summarized in Table 4.4.5-1. The data considered include pressures from 0.1 MPa to 7.3 MPa as well as pipe diameter up to 0.7 m.

The transition boundary data of Crowley et al (1992) were given in the format of gas superficial velocity and liquid superficial velocity. The superficial velocities are transformed to the modified Wallis number by assuming the equilibrium state void fraction.

The transition boundaries of Moon and Smoglie were obtained from offtake experiments (Moon and No, 2003). The offtake phenomenon is the process that occurs in the proximity of the break in a horizontal pipe when the two-phase mixture is stratified. For instance, if a break is at the top of a pipe and the flow in the pipe is in stratified condition, only steam will be vented at the top of the pipe, unless the liquid layer in the pipe is high enough to cause liquid to be entrained. The conditions at which the flow transitions from stratified flow to slug or bubbly flow were reported. It is inferred that in offtake experiments, the liquid phase velocity is zero.

In Figure 4-12, most of the experimental data are bound in a narrow band which ranges from half to twice the modified Taitel-Dukler critical relative velocity for the stratified to intermittent flow regime transition. However, the modified Taitel-Dukler model tends to [

]^{a,c}

The constants in both models are adjusted to better match experimental data. [

]^{a,c} The modified criterion is:

$$\left[\right]^{a,c} \qquad (4\text{-}111)$$

[

]^{a,c} The curve of predicted $j^*_{g\ell,c}$ as function of void fraction is plotted in Figure 4-14 together with experimental transition data.

[

]^{a,c}

Model as Coded

The horizontal stratification criterion is met if the phasic relative velocity is below the following critical relative velocity Δu_c :

[ ]^{a,c} (4-112)

Note, the piecewise function in Equation 4-115 is replaced by an equivalent function [ ]^{a,c}. Once the criteria of horizontal stratified flow are met, the code calculates the interfacial area as follows. With concern for interfacial instability at extremely low void fractions, horizontal stratification is prohibited when void fraction is less than [ ]^{a,c}.

For fully horizontal stratified flow, the interfacial area can be calculated from the cell geometry. For horizontal stratified flow, the interfacial area is given by:

$$A_i = A_{i,st} = S_i \cdot \Delta x = D_h \cdot \Delta x \sqrt{1 - \left(1 - \frac{2\,h_l}{D_h}\right)^2} \tag{4-113}$$

where h_l and Δx represent the stratified liquid level and the cell length, respectively, S_i is the width of the stratified interface, and D_h is the hydraulic diameter of the pipe. For a cylindrical channel cross-section (Figure 4-15), the h_l is calculated from the void fraction using a polynomial curve fit as follows:

$$\begin{aligned} &\text{if } \alpha \le 0.5 \quad \text{then} \quad X = \alpha \quad \text{and} \\ &\qquad\qquad\qquad\quad h_l = Y, \quad \text{or} \\ &\text{if } \alpha > 0.5 \quad \text{then} \quad X = 1.0 - \alpha \quad \text{and} \\ &\qquad\qquad\qquad\quad h_l = D_h - Y, \end{aligned} \tag{4-114}$$

where:

$$\begin{aligned} &\text{if } X \le 0.001 \quad \text{then} \\ &\quad Y = (1.0 - 7.612668 \cdot X) \cdot D_h, \quad \text{or} \\ &\text{if } 0.001 < X \le 0.5 \quad \text{then} \\ &\quad Y = (1.0 - 0.70269591 \cdot X^{0.6666666667} - 0.034146667 \cdot X - 0.161023911 \cdot X^{2.0}) \cdot D_h \end{aligned} \tag{4-115}$$

These interfacial area models are based on the idealized geometry of the interface depicted in Figure 4-15.

The stratified flow regime is superimposed on the basic flow regime map. Thus, when the flow is not fully stratified, the code interpolates between the interfacial area determined for stratified flow, calculated as above, and the value otherwise determined with respect to the basic flow regime map. In other words,

[ ]^{a,c} (4-116)

where $0 \le W_{st} \le 1$.

The weighting factor W_{st} is calculated as a function of critical velocity in Equation 4-112.

[ ]^{a,c} (4-117)

where C_{stfru} and C_{hs_slug}[2] are adjustable constants. C_{hs_slug} (HS_SLUG) = 1.0 is the default value in WCOBRA/TRAC-TF2. The allowable input range of C_{hs_slug} (HS_SLUG) is from [ ]^{a,c}. The size of the interpolation region can be adjusted by the input variable, C_{stfru}. The default value of C_{stfru} is [ ]^{a,c}. The allowable input range of C_{stfru} is from [ ]^{a,c}. At C_{hs_slug} = 0.5, the transition occurs at one-half of the nominal transition relative velocity.

Scaling Considerations

[

]^{a,c}

[2] Note that C_{hs_slug} and HS_SLUG define the same quantity, and are used interchangeably.

[

]^{a,c}

$$\begin{bmatrix} \end{bmatrix}^{a,c} \quad (4\text{-}118)$$

[

]^{a,c}

[

]a,c

Conclusions

A hybrid transition model [

]a,c The model was developed assuming a cylindrical pipe. The uncertainty of these models is accounted for in the overall WCOBRA/TRAC-TF2 code bias and uncertainty discussed in Section 29.

Table 4.4.5-1 [ ]a,c

a,c

4.4.6 Wavy-Dispersed Flow

Model Basis

A wavy-dispersed flow regime is a particular horizontal stratified flow characterized by a significant amount of liquid entrained in a vapor core (pictorial representation below). This flow was observed in high pressure (3~12 MPa) steam/water experiments using the TPTF facility (Nakamura, 1995). It was observed that when pressure is above 8.6 MPa, the slug flow regime could not be established and was completely replaced by the wavy-dispersed flow instead. The occurrence of wavy-dispersed flow instead of slug flow potentially has a significant influence on the coolant distribution during a small break LOCA.

The continuous vapor core in wavy-dispersed flow allows better steam venting than slug/bubbly flow, which separates the steam phase into bubbles.

Pictorial Representation of Wavy-Dispersed Flow

Both wavy-dispersed flow and horizontal stratified flow have a relatively flat interface between the bulk liquid and the vapor, and the bulk liquid is located at the bottom of the pipe. The difference between the wavy-dispersed flow regime and the horizontal stratified flow regime is that wavy-dispersed flow regime [ ]^{a,c}

The similarity of the wavy-dispersed flow and annular-mist flow is the existence of an entrained droplets core and that the perimeter of the pipe wall is wetted. The difference between the wavy-dispersed flow regime and the annular-mist flow regime is that [

]^{a,c}

Transition Criteria

[

]^{a,c}

[ ] a,c (4-119)

[

]^{a,c}

[

]a,c

Model as Coded

If the conditions for the wavy-dispersed flow regime are satisfied, the next step is to determine what fraction of liquid is in the form of droplets (dispersed phase) and what remains in the form of bulk liquid. Based on the process previously discussed, the equilibrium entrainment liquid fraction in the wavy-dispersed flow regime can be calculated, [

]a,c

[ ]a,c (4-120)

[

]a,c

Similar to the strategy to define the flow regime numbers for stratified flow, the flow regime identifiers for the wavy-dispersed flow are REGNM=2.5 ($0.0<\alpha\leq 0.3$) and 4.5 ($0.5<\alpha\leq 0.75$), corresponding to different basic flow regimes with void fraction less than 0.75.

The wavy-dispersed flow regime shares similar characters with the annular-mist flow regime. [

]^{a,c}

Because of the similarity between the wavy-dispersed flow and the annular-mist flow, the closure relations for wavy-dispersed flow are similar to the closure relations for annular-mist flow in WCOBRA/TRAC-TF2. The major differences are:
[

]^{a,c}

For wavy-dispersed flow, the interfacial area is combined from the bulk liquid layer and droplet fields such that:

$$\left[\qquad\qquad\right]^{a,c} \tag{4-121}$$

The interfacial area term for the droplets is defined by:

$$A_{i,drop} = \left(\frac{6\alpha_d}{D_d}\right)\cdot B_{cell} \tag{4-122}$$

where α_d represents the droplet fraction in the cell, D_d is the Sauter mean droplet diameter, and B_{cell} is the volume of the cell. Equation 4-122 is developed by combining all the surface of N droplets with diameter of D_d, where $N = \frac{\alpha_d B_{cell}}{\frac{1}{6}\pi D_d^3}$. The droplet fraction is estimated as a function of the entrainment fraction, η, thus,

$$\left[\qquad\qquad\right]^{a,c} \tag{4-123}$$

The entrainment fraction is calculated by Equation 4-120. Additionally, the Sauter mean droplet diameter [ ]^{a,c}:

[ ]^{a,c} (4-124)

provided that [ ]^{a,c}.

In the above droplet relations, the Reynolds number is given by:

[ ]^{a,c} (4-125)

The interfacial area term for the bulk liquid layer is similar to the interfacial area term for fully stratified flow,

$$A_{i,layer} = D_h \cdot \Delta x \sqrt{1-\left(1-\frac{2h_l}{D_h}\right)^2} \tag{4-126}$$

If the interfacial area is applied to calculate interfacial heat transfer, the interfacial area for the liquid layer is made from two portions, the arc portion and the flat chord portion. The chord portion is the interface of the bulk liquid layer, and the arc portion is the additional wetted perimeter caused by the deposition of liquid droplets on the pipe wall. Per Figure 4-21, the interfacial area for the bulk liquid is given by:

[ ]^{a,c} (4-127)

where:

[ ]^{a,c} (4-128)

Note, the interfacial area model assumes liquid existence on the arc portion of the pipe.

Scaling Considerations

The modeling of the wavy-dispersed flow regime is consistent with observation by Nakamura (1995) in the TPTF experiments. The onset of entrainment was observed to prevent the transition to slug by breaking the developing waves and cause transition to wavy-dispersed flow. This is particularly important at relatively high pressure which can be encountered during postulated small break LOCA in PWRs. The onset of entrainment is calculated by the [ ]^{a,c}.

Conclusions

The model for the wavy-dispersed regime is verified through its use in the 1D components of the ROSA and LOFT integral effects tests, as documented in Volume 2. The uncertainty in modeling this regime is accounted for in the overall WCOBRA/TRAC-TF2 code bias and uncertainty.

4.5 REFERENCES

1. Anoda, Y., Kukita, Y., Nakamura, H. and Tasaka, K., 1989, "Flow Regime Transition in High-Pressure Large-Diameter Horizontal Two-Phase Flow," *Proceeding of 26th ASME/AICHE/ANS National Heat Transfer Conference*, Philadelphia, pp 61-68.

2. Asaka, H., Kukita, Y., Anoda, Y., Nakamura, H. and Tasaka, K., 1991, "Improvement of TRAC-PF1 Interfacial Drag Model for Analysis of High-Pressure Horizontally-Stratified Two-Phase Flow," *Journal of Nuclear Science and Technology*, Vol. 28, No. 1, pp. 33-44.

3. Bajorek, S. M., et al., 1998, "Code Qualification Document for Best Estimate LOCA Analysis," WCAP-12945-P-A, Volume 1, Revision 2, and Volumes 2 through 5, Revision 1, and WCAP-14747 (Non-Proprietary).

4. Barnea, D. and Taitel, Y., 1993, "Kelvin-Helmholtz Stability Criteria for Stratified Flow: Viscous versus Non-viscous (Inviscid) Approaches," *Int. J. Multiphase Flow*, Vol. 19, No. 4, pp. 639-649.

5. Bestion, D., 1990, "The physical closure laws in the CATHARE code," *Nuclear Engineering and Design*, Vol. 124, pp. 229-245.

6. Choe, W. G., Weinberg, L. and Weisman, J., 1976, "Observation and Correlation of Flow Pattern Transitions in Horizontal, Cocurrent Gas-Liquid Flow," Two-Phase Transport and Reactor Safety, Veziroglu, T. N. and Kakac, S., editors, Vol. IV, pp. 1357-1393.

7. Chow, S. K., et al., 1989, "Assessment of Scaling Uncertainties for PWR Plant Large-Break LOCA Analysis," EPRI NP-6602.

8. Crowley, C. J., Wallis, G. B. and Barry, J. J., 1992, "Validation of a One-Dimensional Wave Model for the Stratified-to-Slug Flow Regime Transition, with Consequences for Wave Growth and Slug Frequency," *Int. J. Multiphase Flow*, Vol. 18, No. 2, pp. 249-271.

9. DeJarlais, G., 1983, "An Experimental Study of Inverted Annular Flow Hydrodynamics Utilizing an Adiabatic Simulation," ANL-83-44, NUREG/CR-3339.

10. Dukler, A. E., 1977, "Two Phase Interactions in Countercurrent Flow Studies of the Flooding Mechanism," NUREG-0214.

11. Griffith, P. and Snyder, G. A., 1964, "The Bubbly-Slug Transition in a High Velocity Two Phase Flow," MIT Report 5003-29 (TID-20947).

12. Griffith, P. and Wallis, G. B., 1961, "Two-Phase Slug Flow," *J. Heat Transfer*, Vol. 83, pp. 307-320.

13. INEL, 1995, "RELAP5/MOD3, Code Manual, Volume IV: Models and Correlations," NUREG/CR-5535, Volume IV.

14. Ishii, M. and Mishima, K., 1980, "Study of Two-Fluid Model and Interfacial Area," ANL-80-111, NUREG/CR-1873.

15. Ishii, M. and Mishima K., 1989, "Droplet entrainment correlation in annular two-phase flow," *Int. J. Heat Mass Transfer*, Vol. 32, No. 10, pp. 1835-1846.

16. Kataoka, I. and Ishii, M., 1982, "Mechanism and Correlation of Droplet Entrainment and Deposition in Annular Two-Phase Flow," ANL 82 44, NUREG/CR-2885.

17. Kataoka, I., Ishii, M. and Mishima, K., 1983, "Generation and Size Distribution of Droplet in Annular Two-Phase Flow," *Trans. ASME, J. Fluids Engineering*, Vol. 105, pp. 230-238.

18. Kitscha, J. and Kocamustafaogullari, G., 1989, "Breakup Criteria for Fluid Particles," *Int. J. Multiphase Flow*, Vol. 15, No. 4, pp. 573-588.

19. Lime, J. F., 2001, "Memorandum on Interfacial Drag from M. Ishii to R. Nelson, July 28, 1987," LA UR 01 1591.

20. Lovell, T. W., 1977, "The Effect of Scale on Two-Phase Counter-Current Flow Flooding in Vertical Tubes," Masters Thesis, Thayer School of Engineering, Dartmouth College.

21. Mishima, K. and Ishii, M., 1980, "Theoretical Prediction of Onset of Horizontal Slug Flow," *J. Fluids Eng.*, Vol. 102, pp. 441-445.

22. Mishima, K. and Ishii, M., 1984, "Flow Regime Transition Criteria for Upward Two-Phase Flow in Vertical Tubes," *Int. J. Heat Mass Transfer*, Vol. 27, No. 5, pp. 723-737.

23. Mandhane, J.M., Gregory, G.A. and Aziz, K., 1974, "A Flow Pattern Map for Gas-Liquid Flow in Horizontal Pipes," *Int. J. Multiphase Flow*, Vol. 1, pp. 537-553.

24. Moon, Y. M. and No, H. C., 2003, "Off-take and Slug Transition at T-junction of Vertical-up Branch in the Horizontal Pipe," *Journal and Nuclear Science and Technology*, Vol. 40, No 5, pp. 317- 324.

25. Nakamura, H., Anoda, Y. and Kukita, Y., 1991, "Flow Regime Transitions in High-Pressure Steam-Water Horizontal Pipe Two-Phase Flow," *ANS Proceeding of 1991 National Heat Transfer Conference*, Minneapolis, 269-276.

26. Nakamura, H., Kukita, Y. and Tasaka, K., 1995, "Flow Regime Transition to Wavy Dispersed Flow for High-Pressure Steam/Water Two-Phase Flow in Horizontal Pipe," *J. Nuclear Science and Technology*, Vol. 32, No. 7, pp.641-652.

27. Radovcich, N. A. and Moissis, R., 1962, "The Transition from Two Phase Bubble Flow to Slug Flow," MIT Report 7-7673-22.

28. Spore, J. W., et al., 2000, "TRAC-M/Fortran 90 (Version 3.0) Theory Manual," LA-UR-00-910.

29. Taitel, Y., Bornea, D. and Dukler, A. E., 1980, "Modelling Flow Pattern Transitions for Steady Upward Gas-Liquid Flow in Vertical Tubes," *AIChE Journal*, Vol. 26, No. 3, pp. 345-354.

30. Taitel, Y. and Dukler, A. E., 1976, "A Model for Predicting Flow Regime Transitions in Horizontal and Near Horizontal Gas-Liquid Flow," *AIChE Journal*, Vol. 22, No. 1, pp. 47-55.

31. Taitel, Y., Lee, N. and Dukler, A. E., 1978, "Transient Gas-Liquid Flow in Horizontal Pipes: Modeling the Flow Pattern Transitions," *AIChE Journal*, Vol. 24, No. 5, pp. 920-934.

32. Thurgood, M. J., et al., 1981, "COBRA/TRAC, A Thermal Hydraulics Code for Transient Analysis of Nuclear Reactor Vessels and Primary Coolant Systems," NUREG/CR-3046.

33. Wallis, G. and Dobson, J., 1973, "The Onset of Slugging in Horizontal Stratified Air-Water Flow," *Int. J. Multiphase Flow*, Vol. 1, pp 173-193.

34. Yudov, Y. V., 2002, "The KORSAR Computer Code Modeling of Stratified Two-Phase Flow Hydrodynamics in Horizontal Pipes," *Proceedings of 10th International Conference on Nuclear Engineering*, Arlington, VA, April 14-18.

a,c

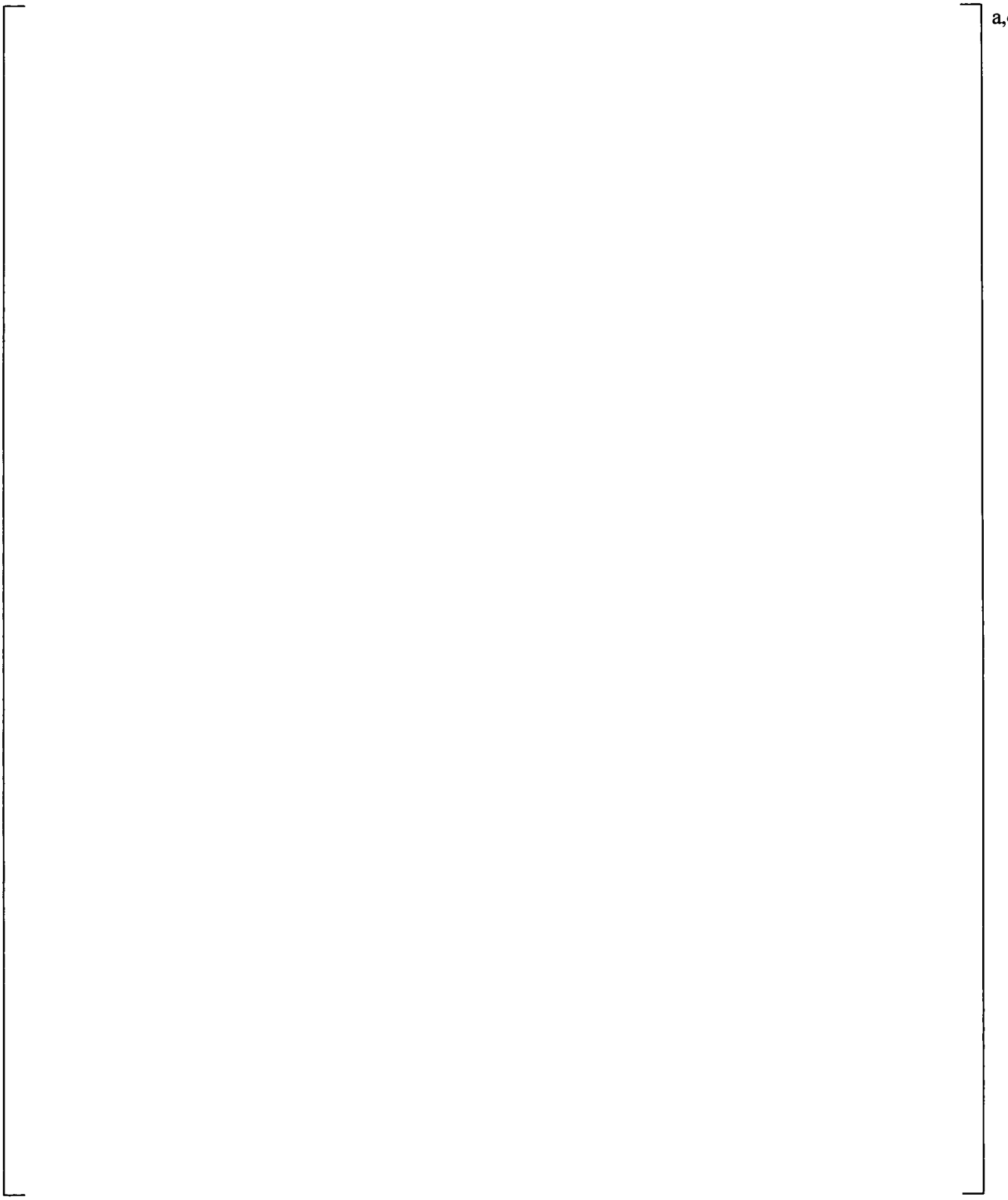

Figure 4-1 Vessel Component Normal Wall Flow Regimes

a,c

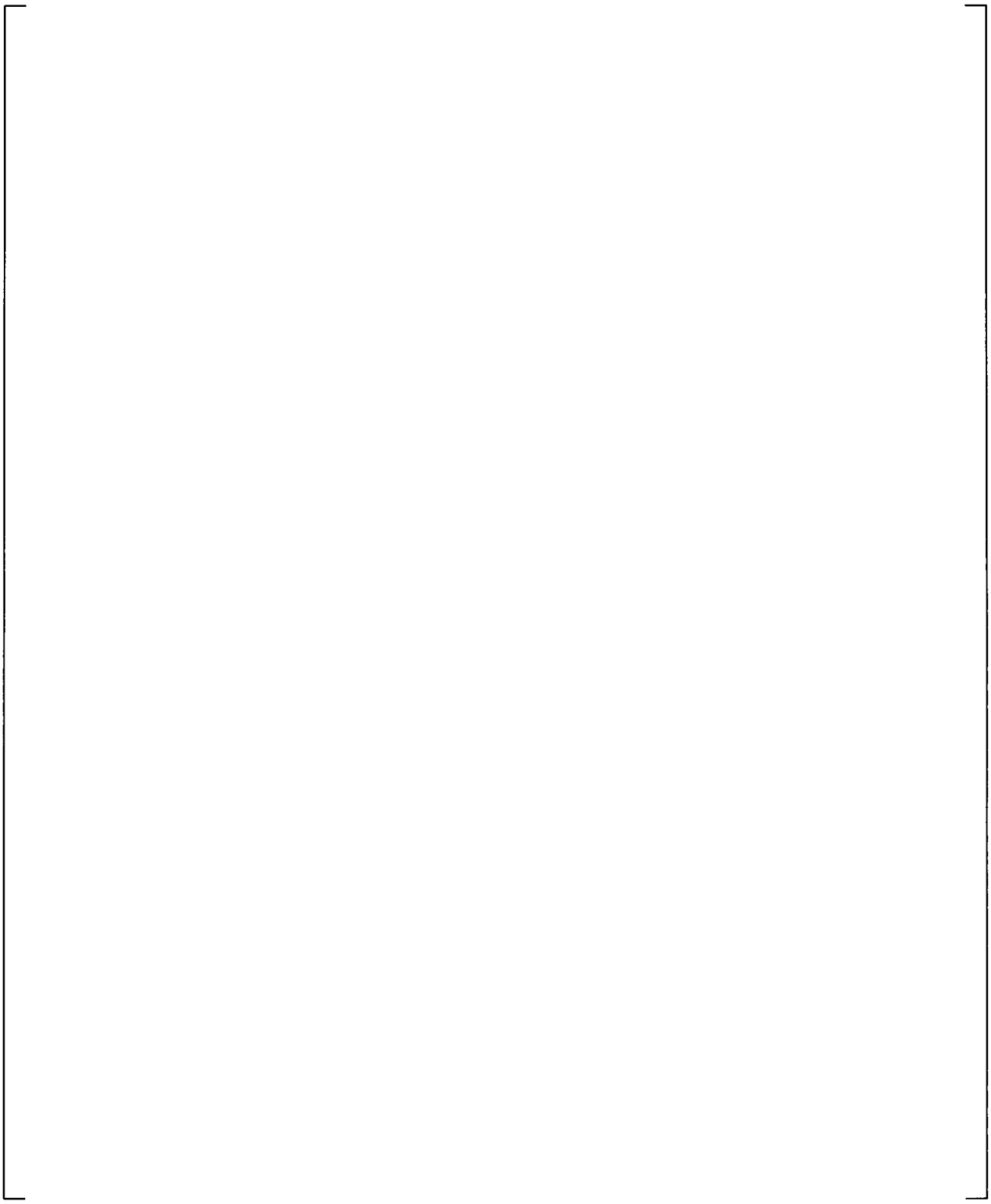

Figure 4-2 Vessel Component Normal Wall Flow Regime Selection Logic

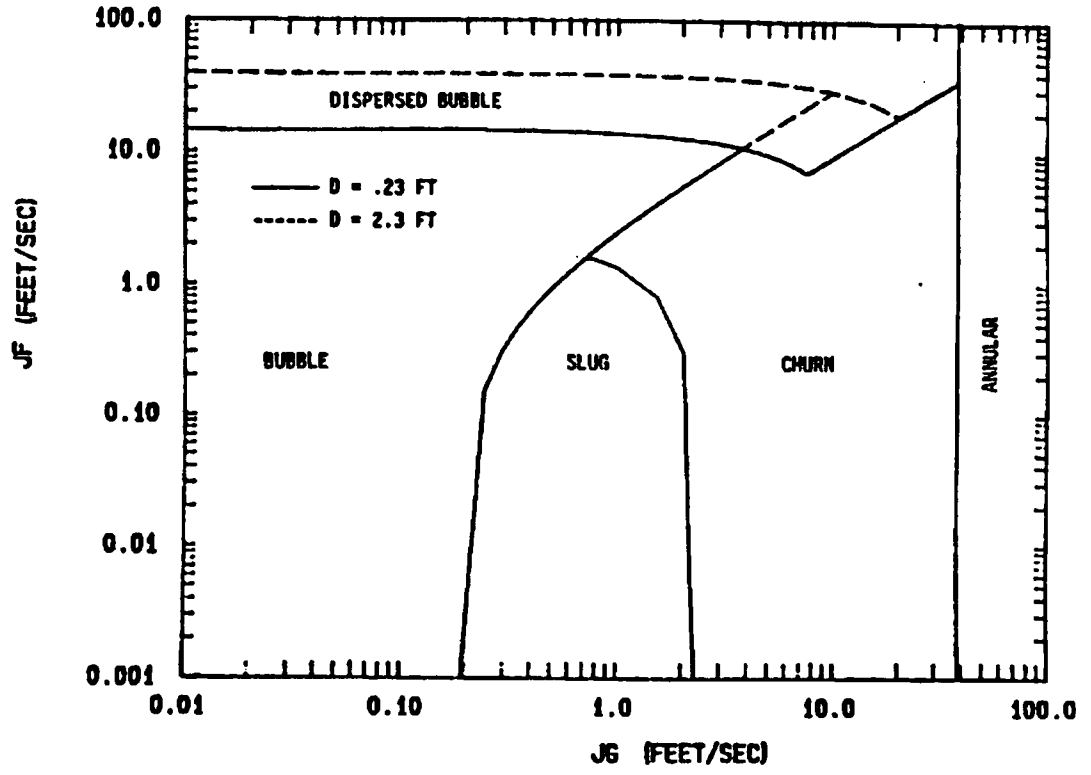

Figure 4-3 Effect of Scale on Vertical Upflow Regime Transitions Predicted by Taitel, Barnea, and Dukler (1980)

a,c

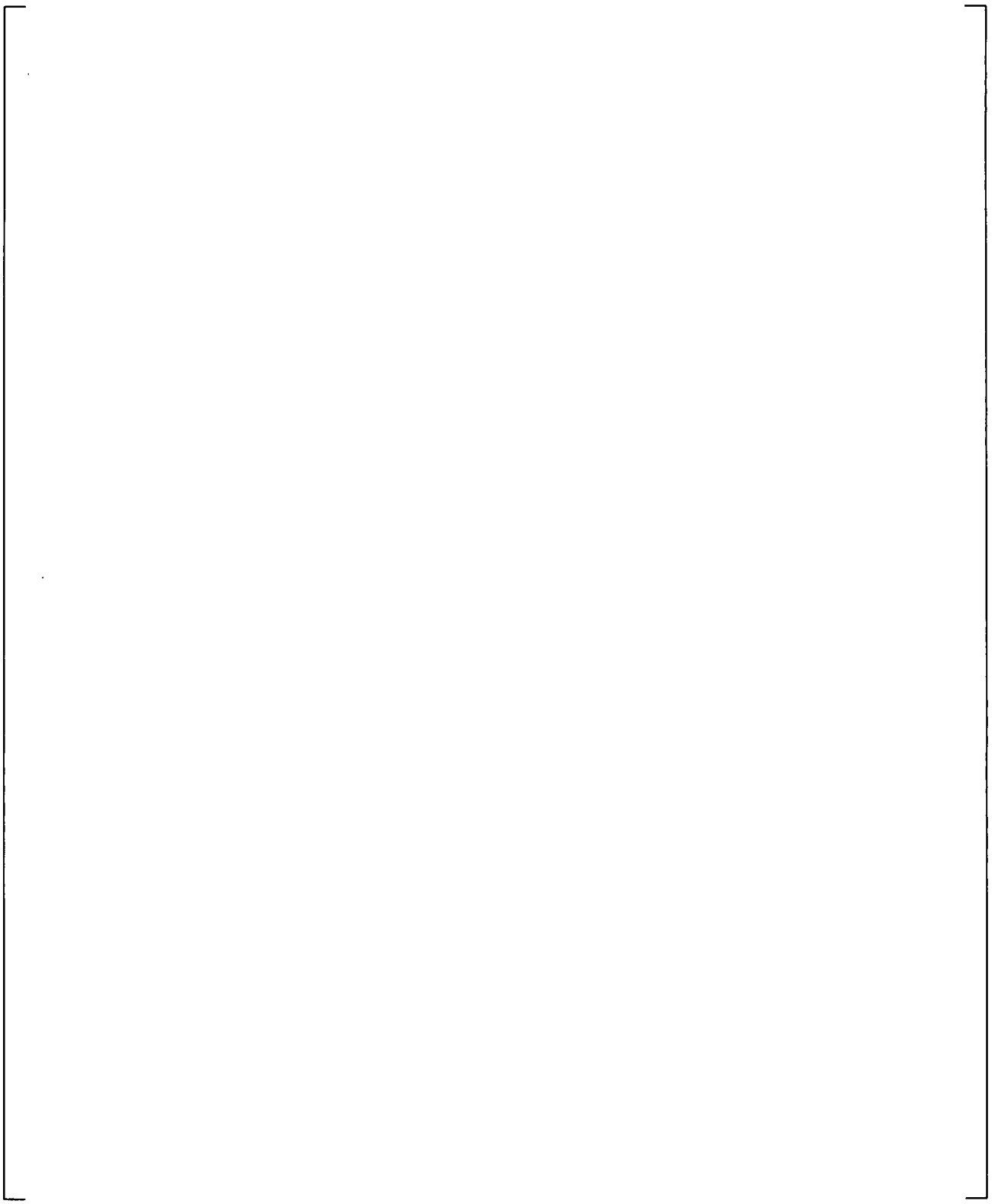

Figure 4-4 Effect of Scale on Vertical Upflow Regime Transitions (Chow, 1989)

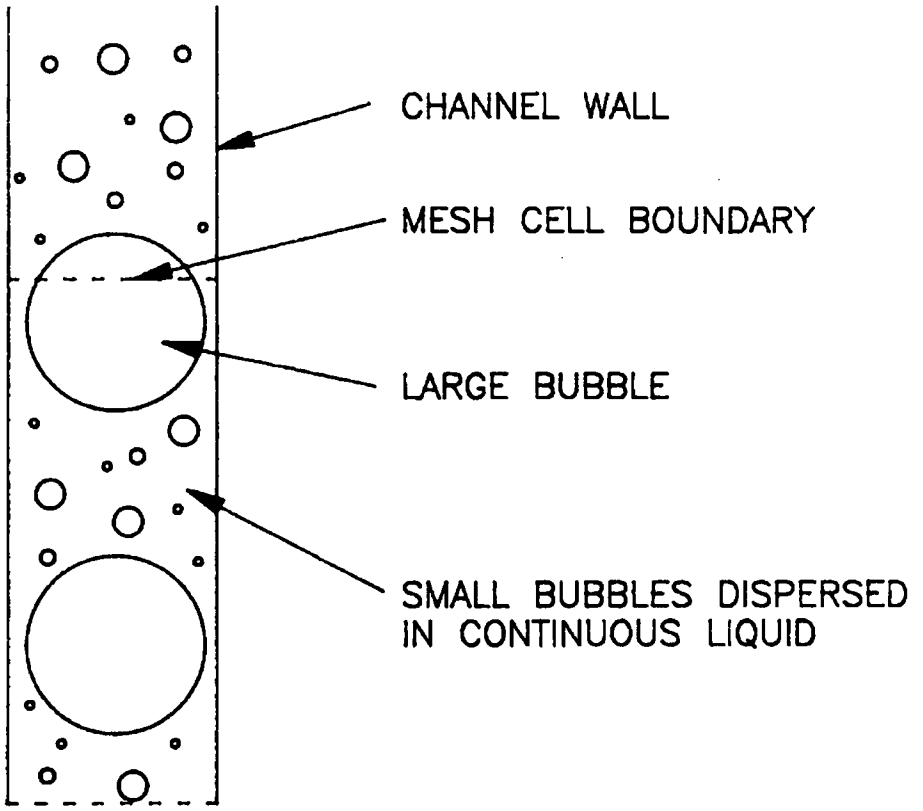

Figure 4-5 Small-to-Large Bubble Regime – Formation of Large Bubbles

a,c

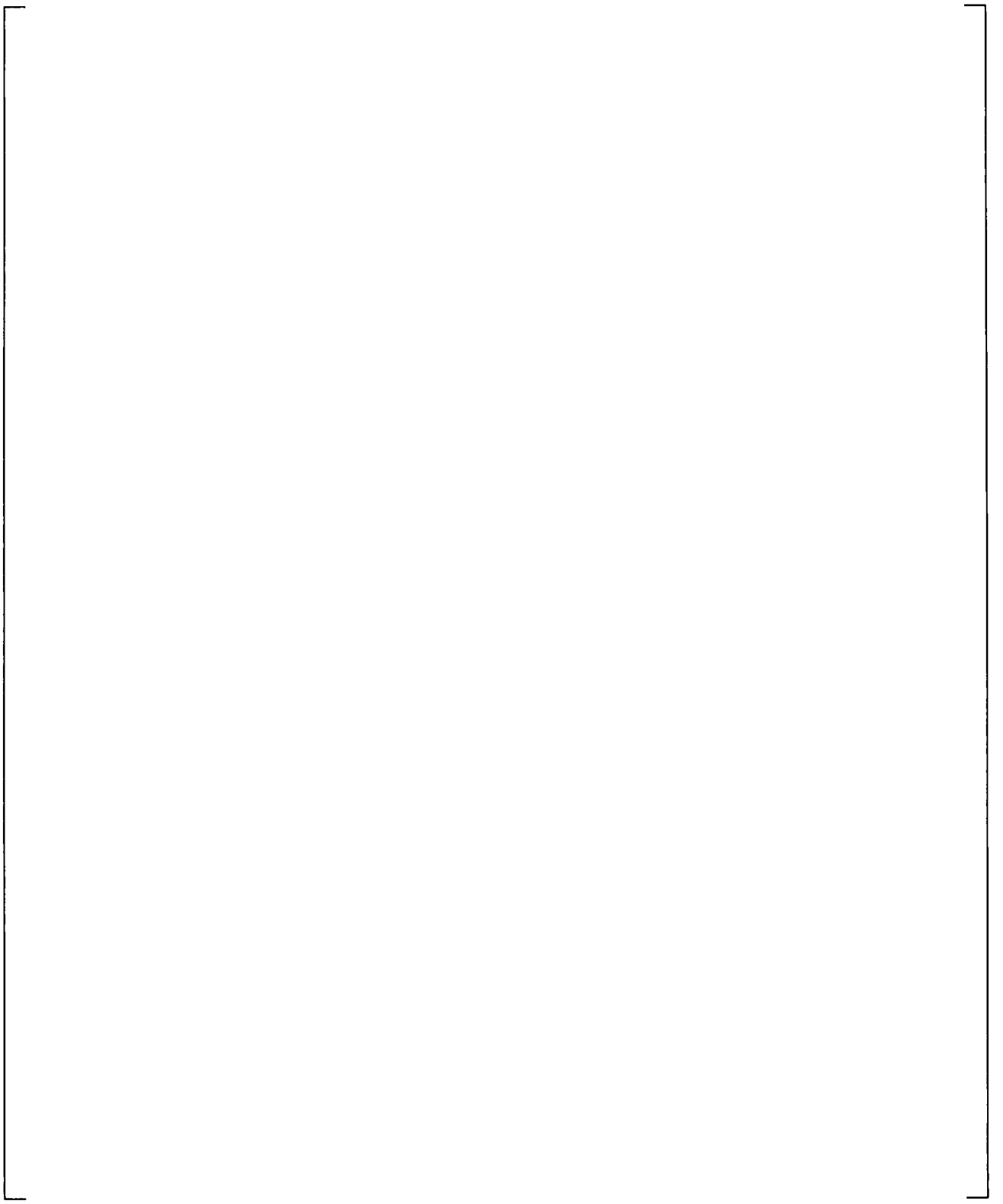

Figure 4-6 Vessel Component Hot Wall Flow Regimes

a,c

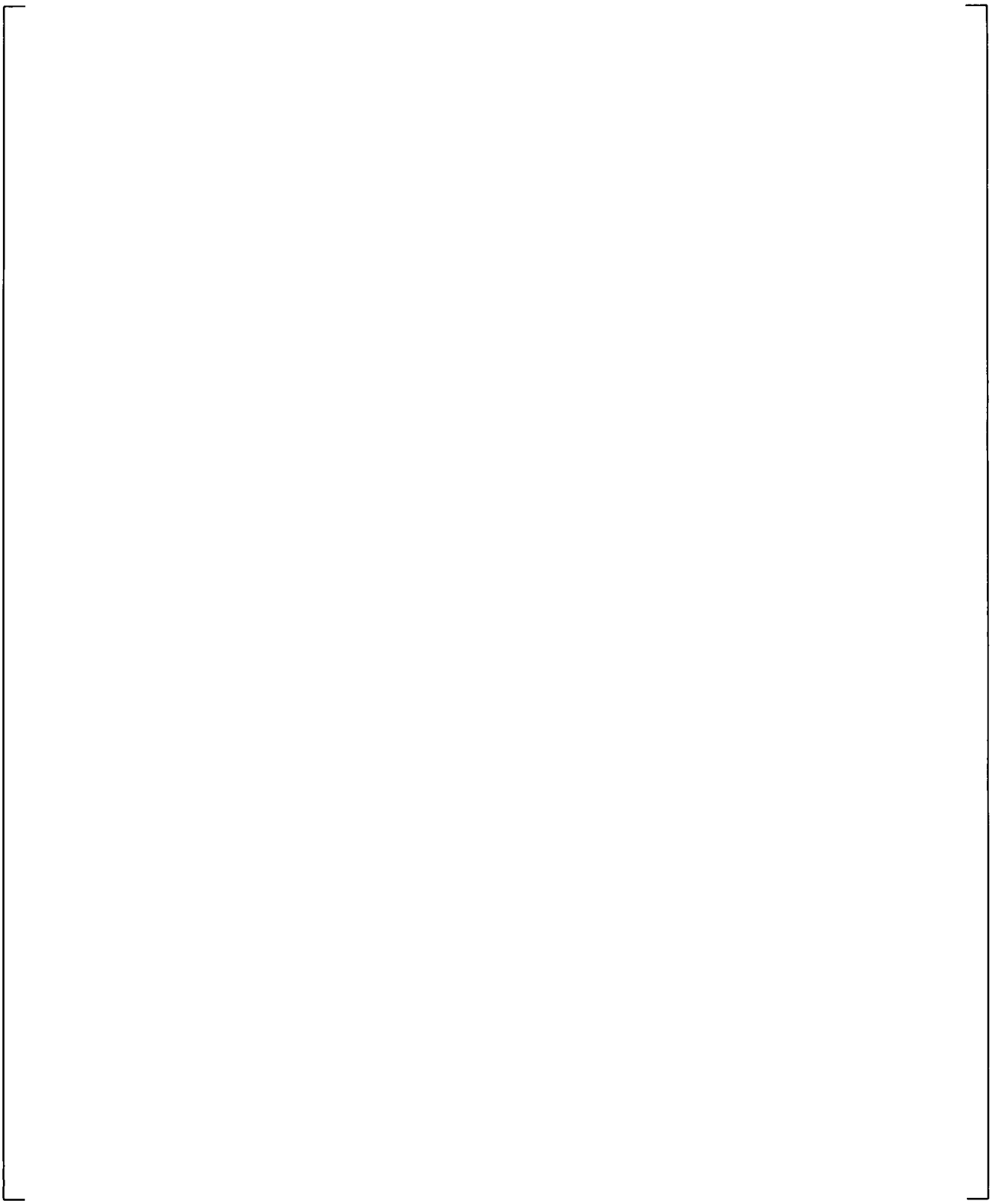

Figure 4-7 Hot Wall Flow Regime Selection Logic

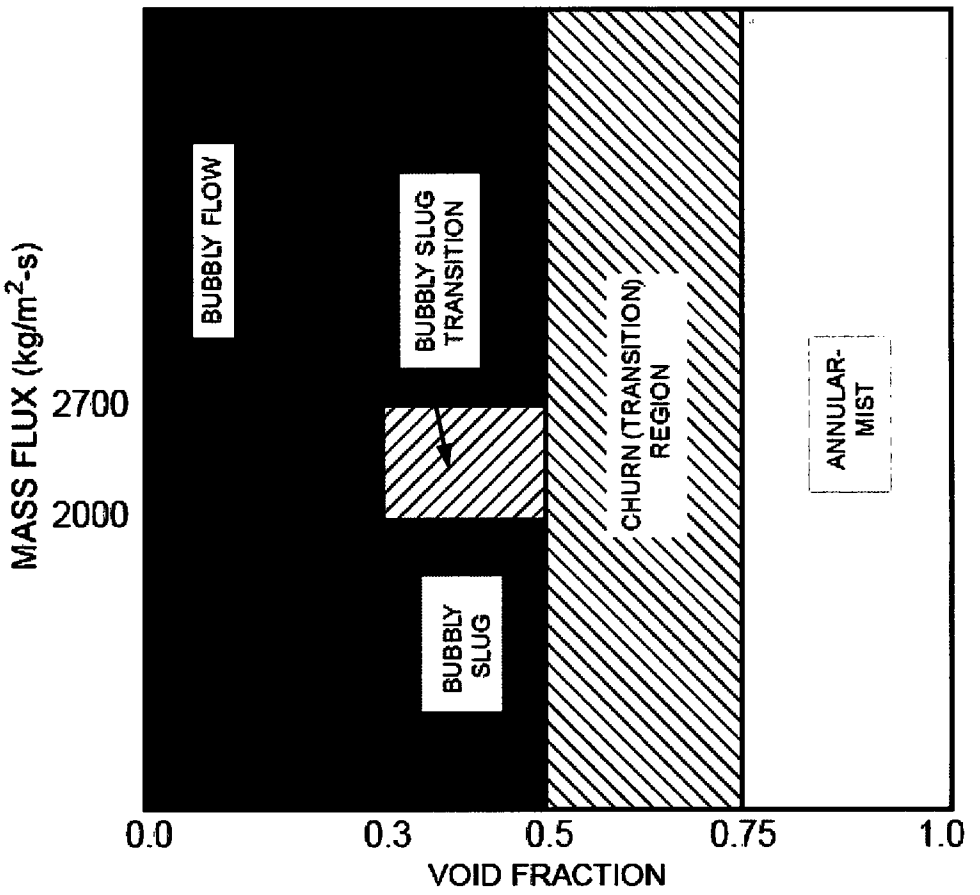

Figure 4-8 One-Dimensional Component Flow Regime Map

a,c

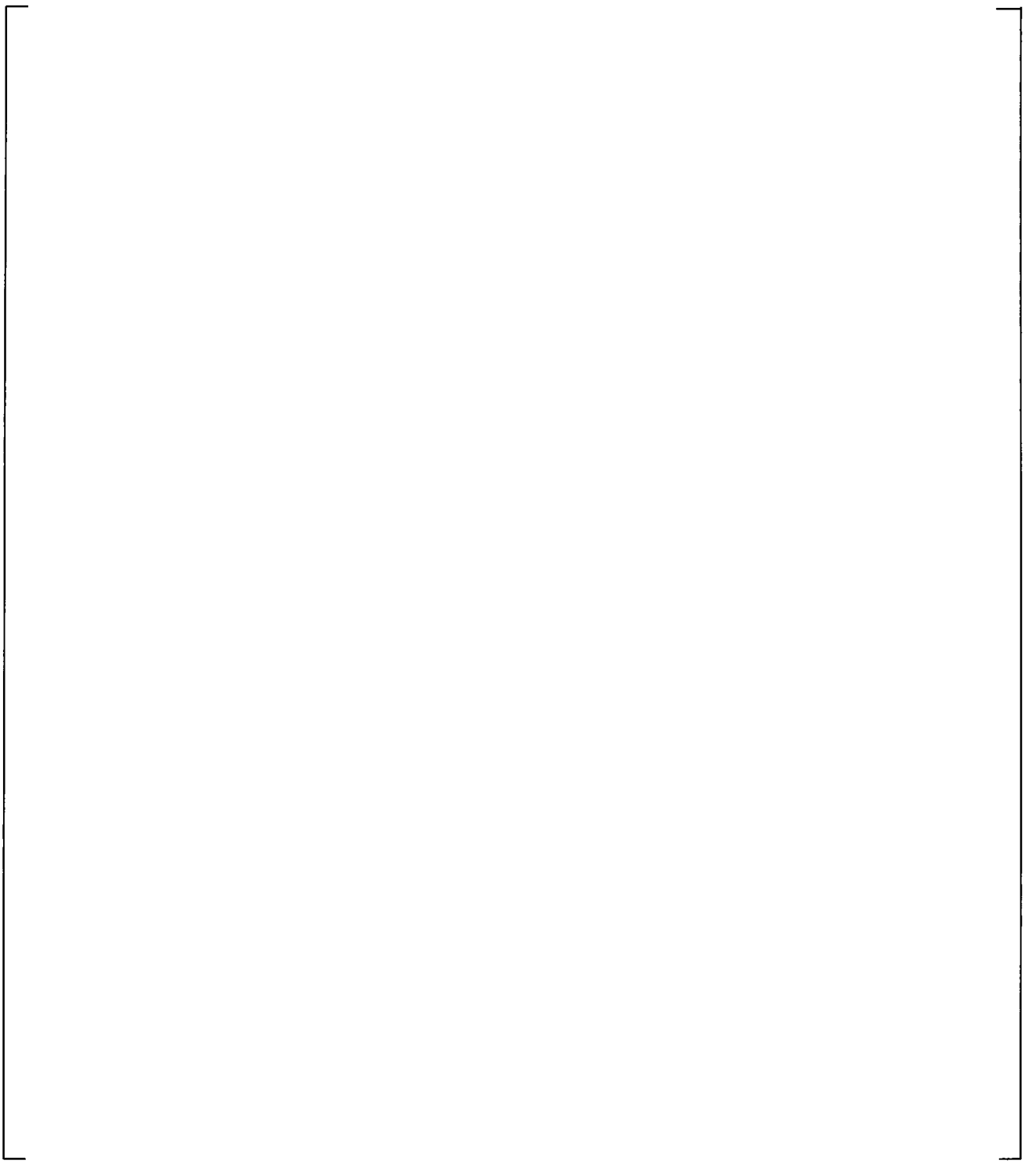

Figure 4-9 One-Dimensional Horizontal Stratified Flow

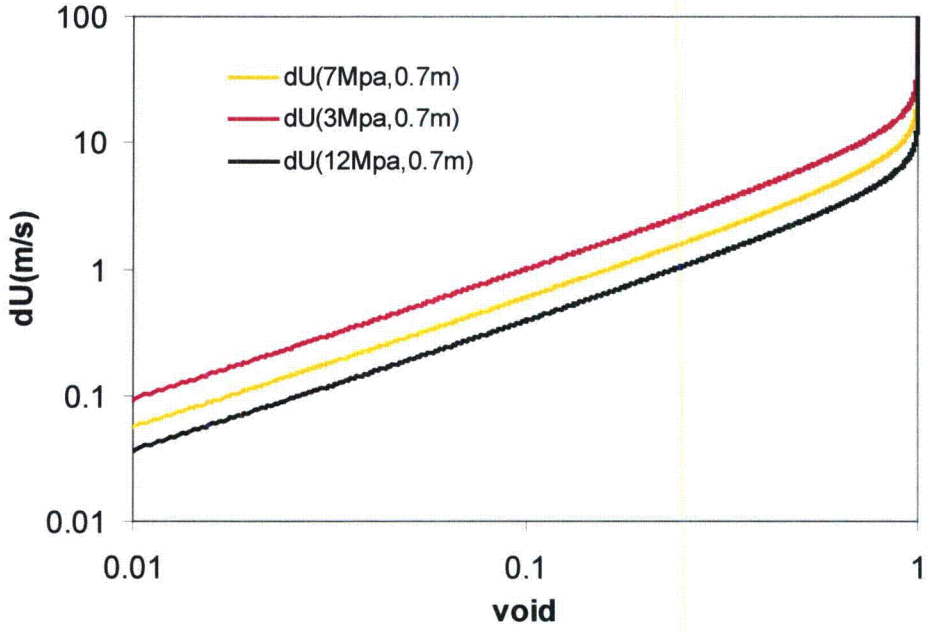

Figure 4-10 Taitel-Dukler Transition Criteria as a Function of Pressure

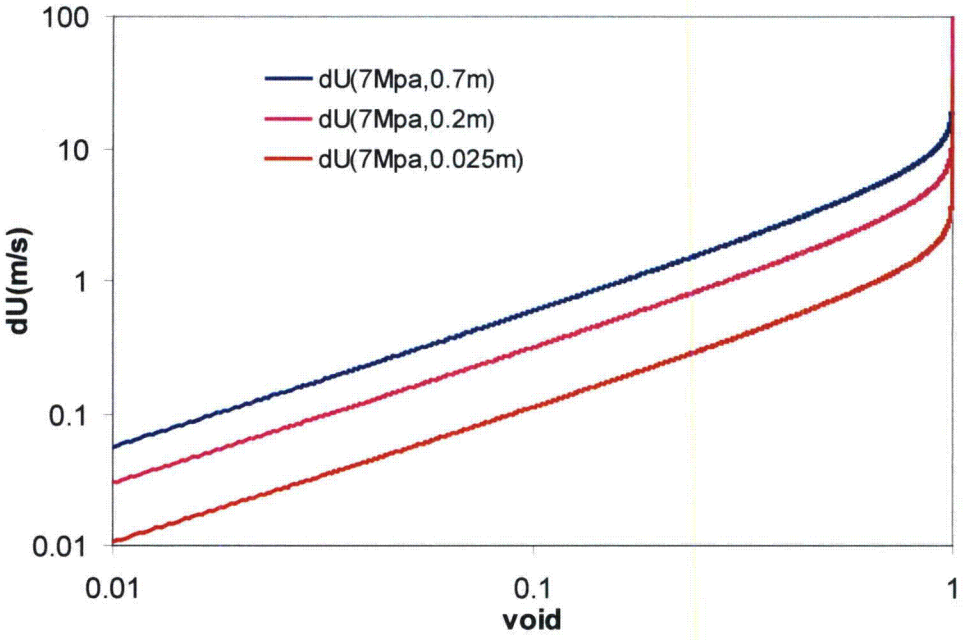

Figure 4-11 Taitel-Dukler Transition Criteria as a Function of Pipe Diameter

[a,c

]

Figure 4-12 [ ][a,c]

[a,c

]

Figure 4-13 [ ][a,c]

a,c

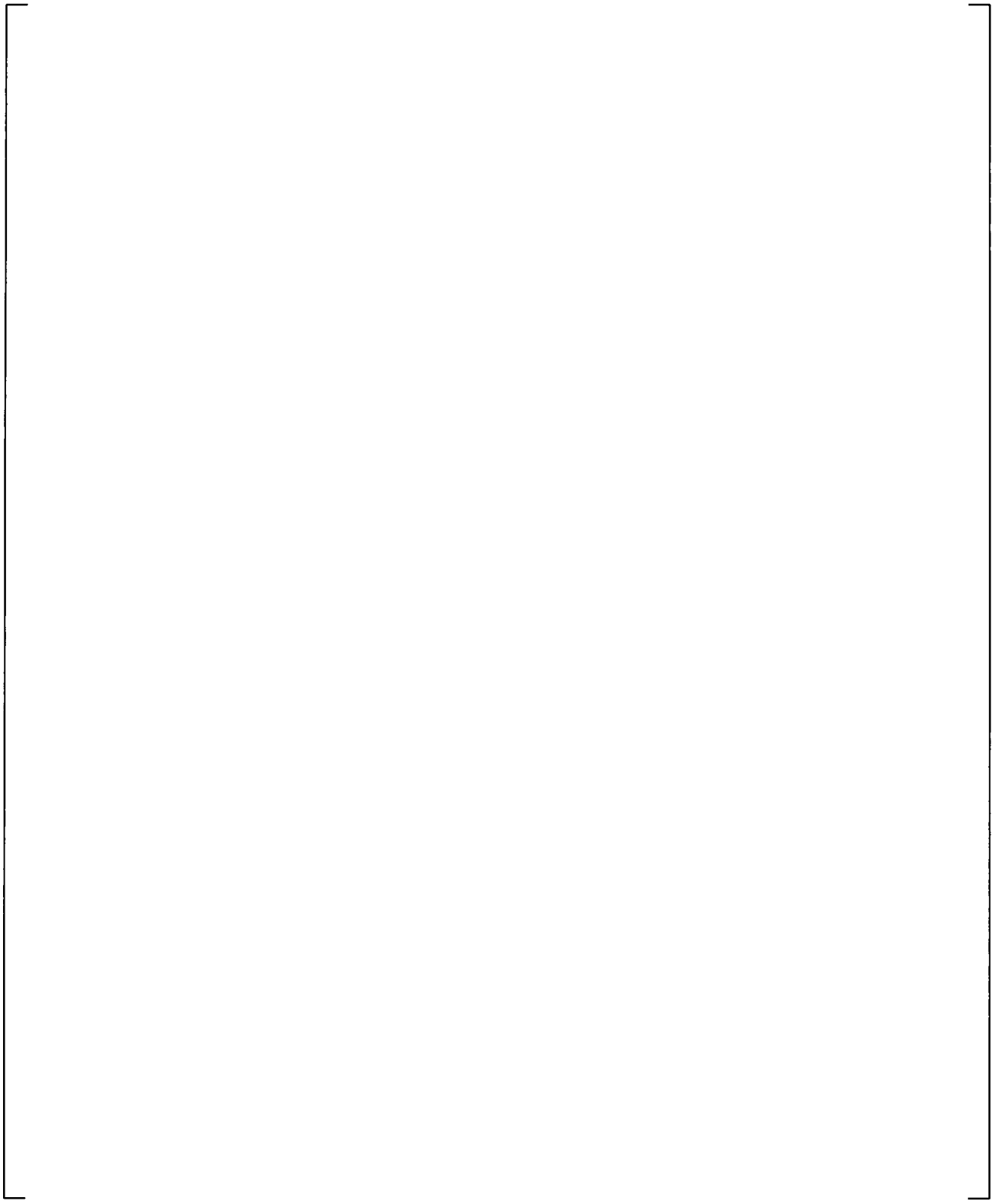

Figure 4-14 The Hybrid Horizontal Stratification Criterion

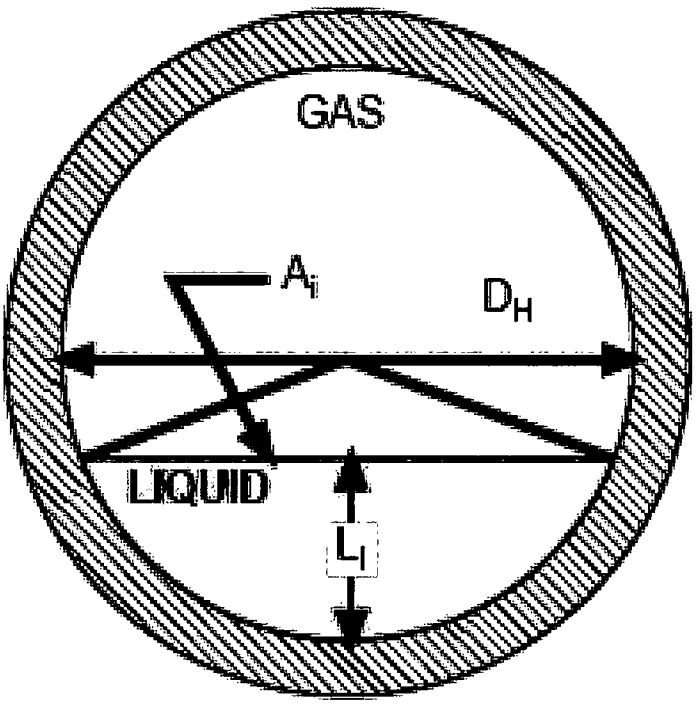

Figure 4-15 Cross Section of Horizontal Stratified Flow

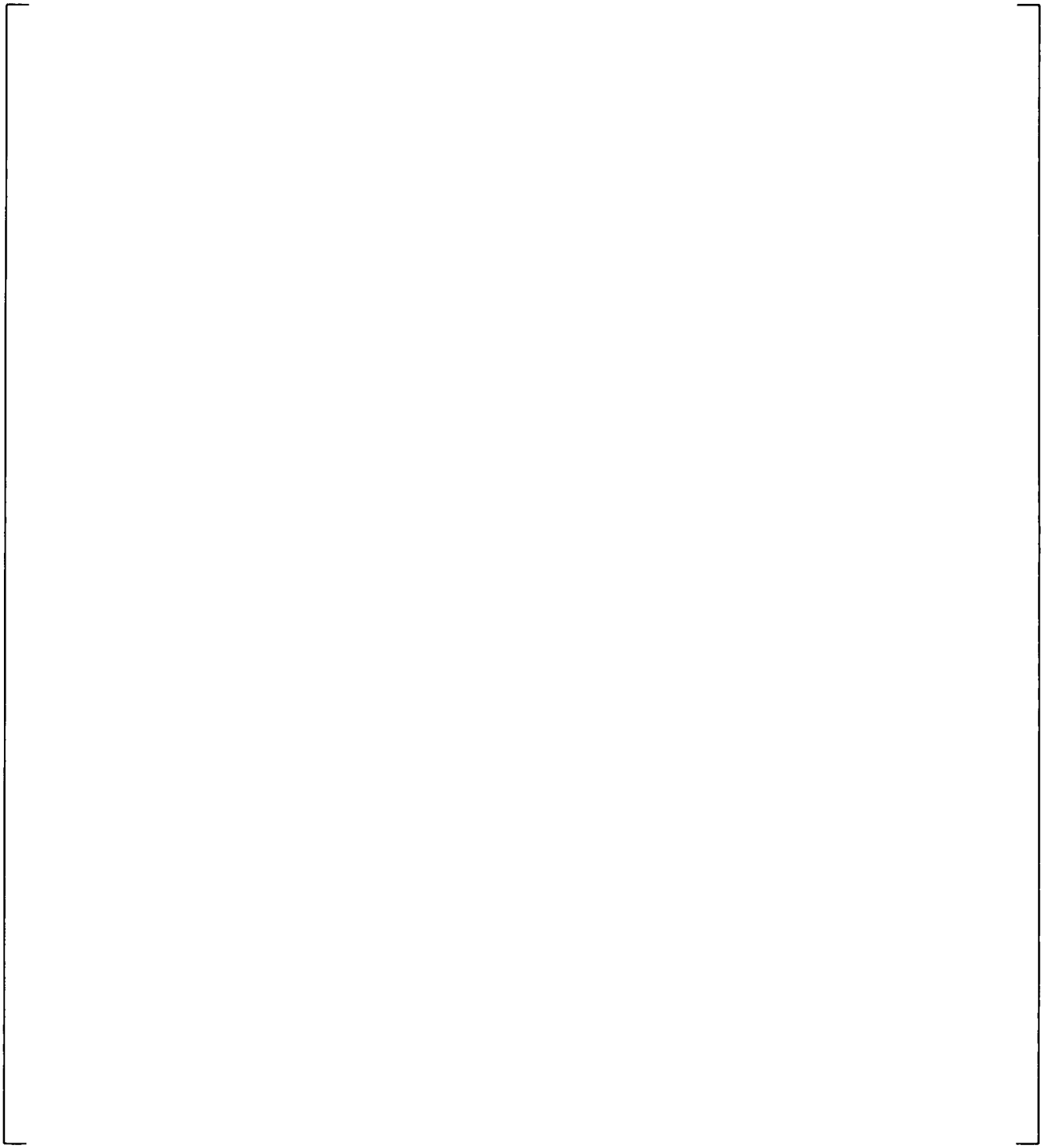

a,c

Figure 4-16 Transition Boundary for Various Tests (Continuous Line is Transition Deduced from Data, While Dashed Line is Prediction of Modified Taitel-Dukler Criterion). Note, the Ridge of Taitel-Dukler Boundary of the 0.18 m and 7.3 MPa at Low Jg* Represents a Singularity Point at Zero Relative Velocity.

a,c

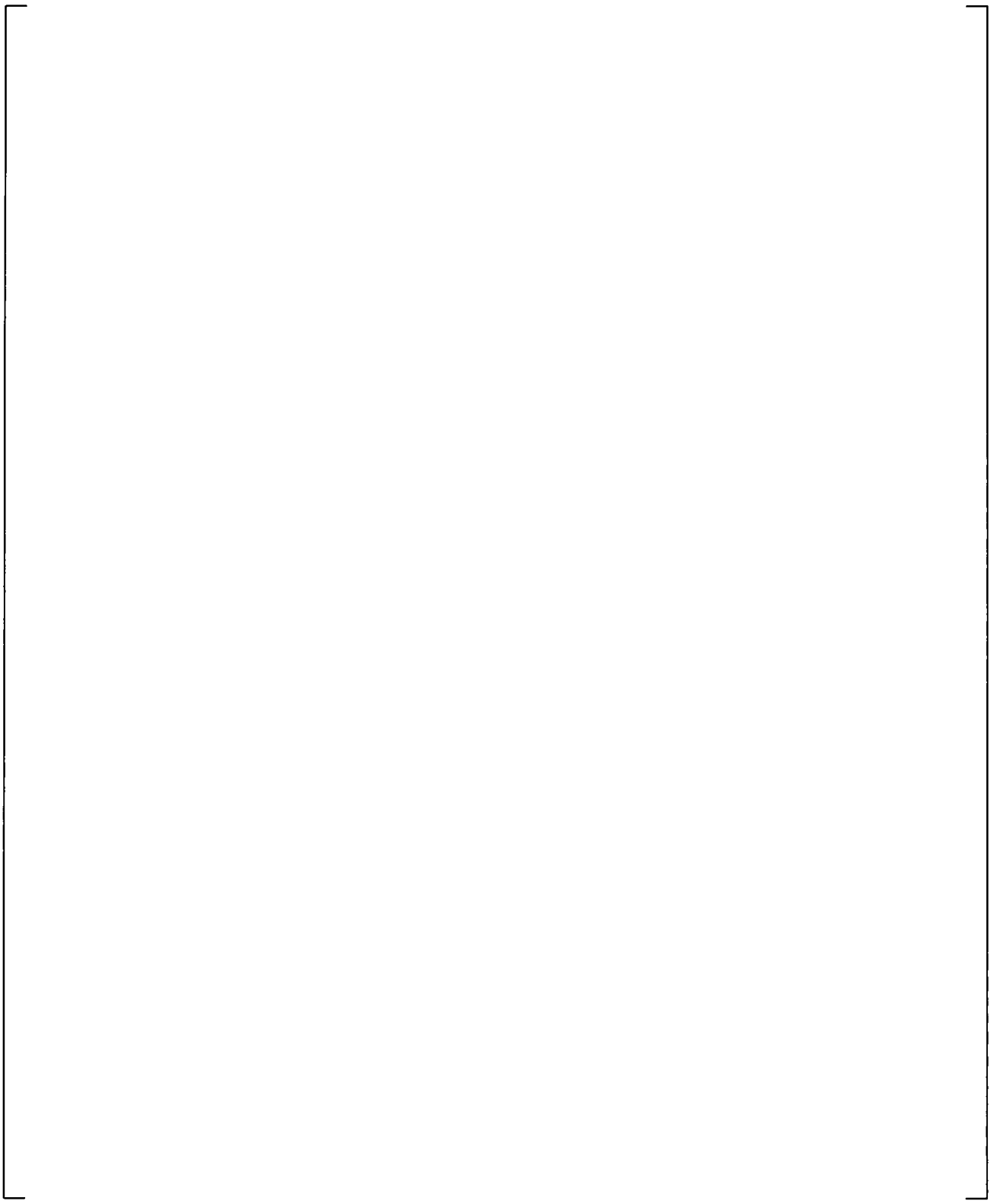

Figure 4-17 Horizontal Stratified Flow Regime Transition and Relevant Data

a,c

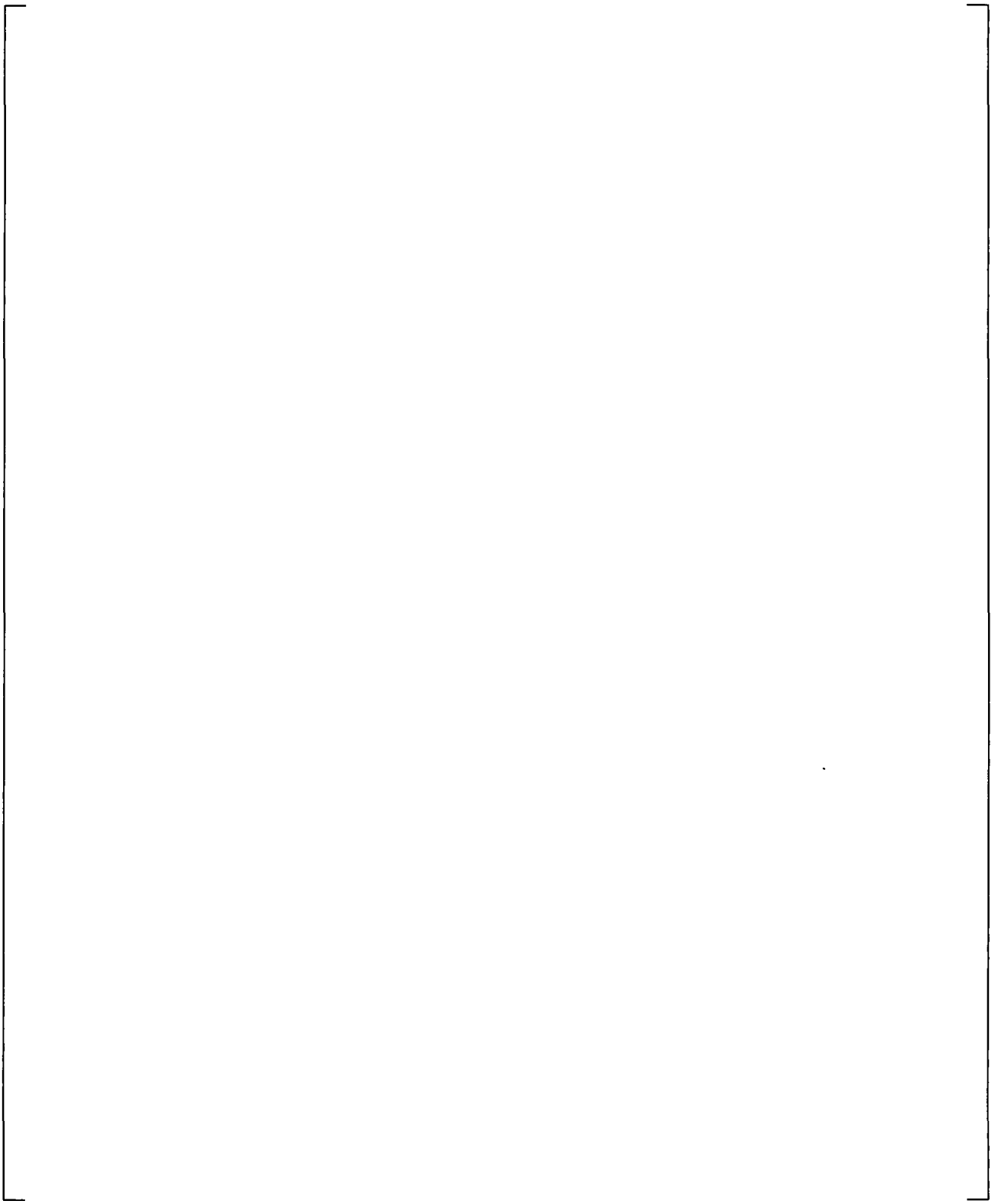

Figure 4-18 Comparison Between Hybrid Horizontal Stratification Criterion and Viscous Kelvin-Helmholtz Models at Various Pressures and Pipe Diameters

a,c

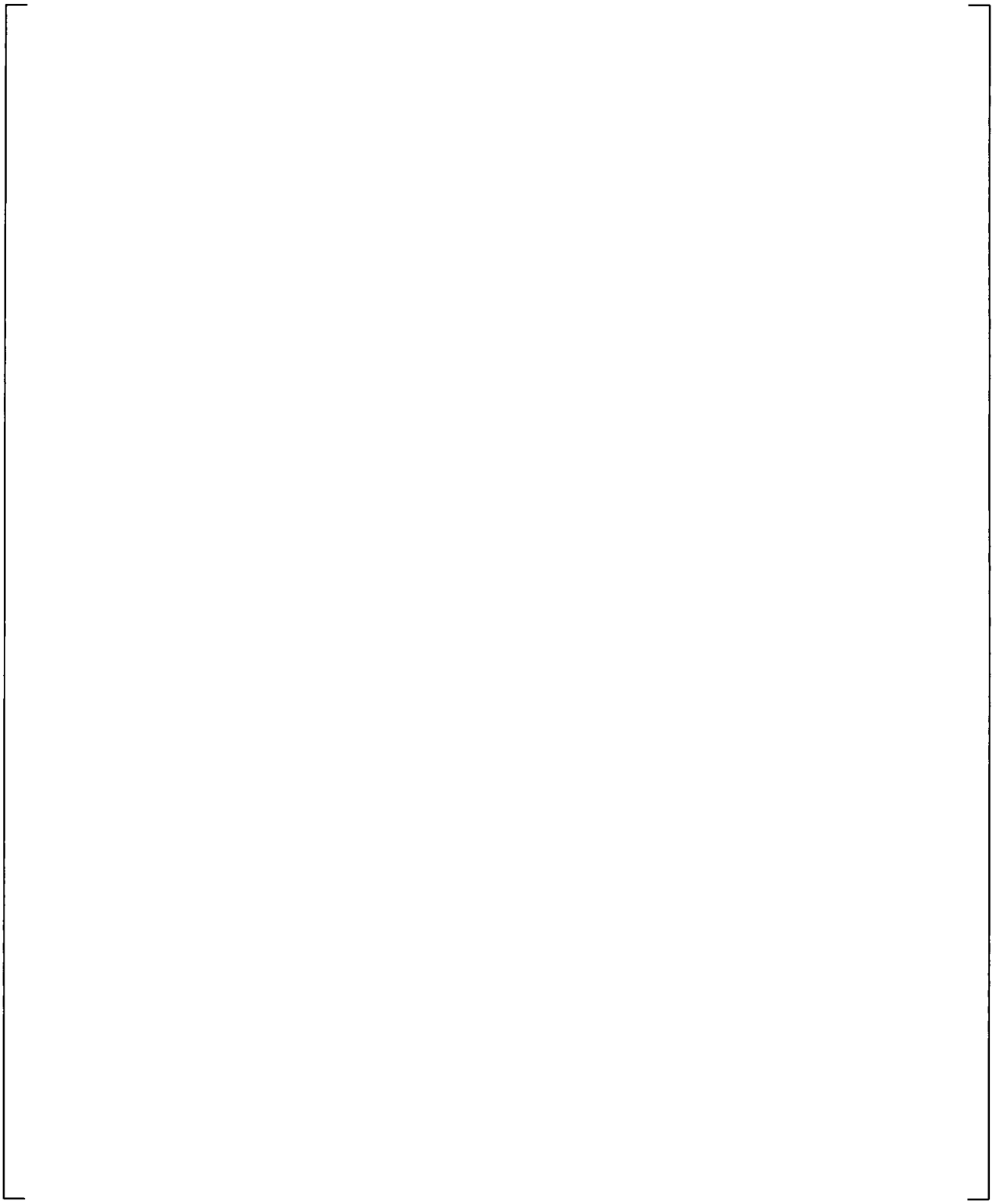

Figure 4-19 Horizontal Flow Regime Map Including Wavy-Dispersed Regime

a,c

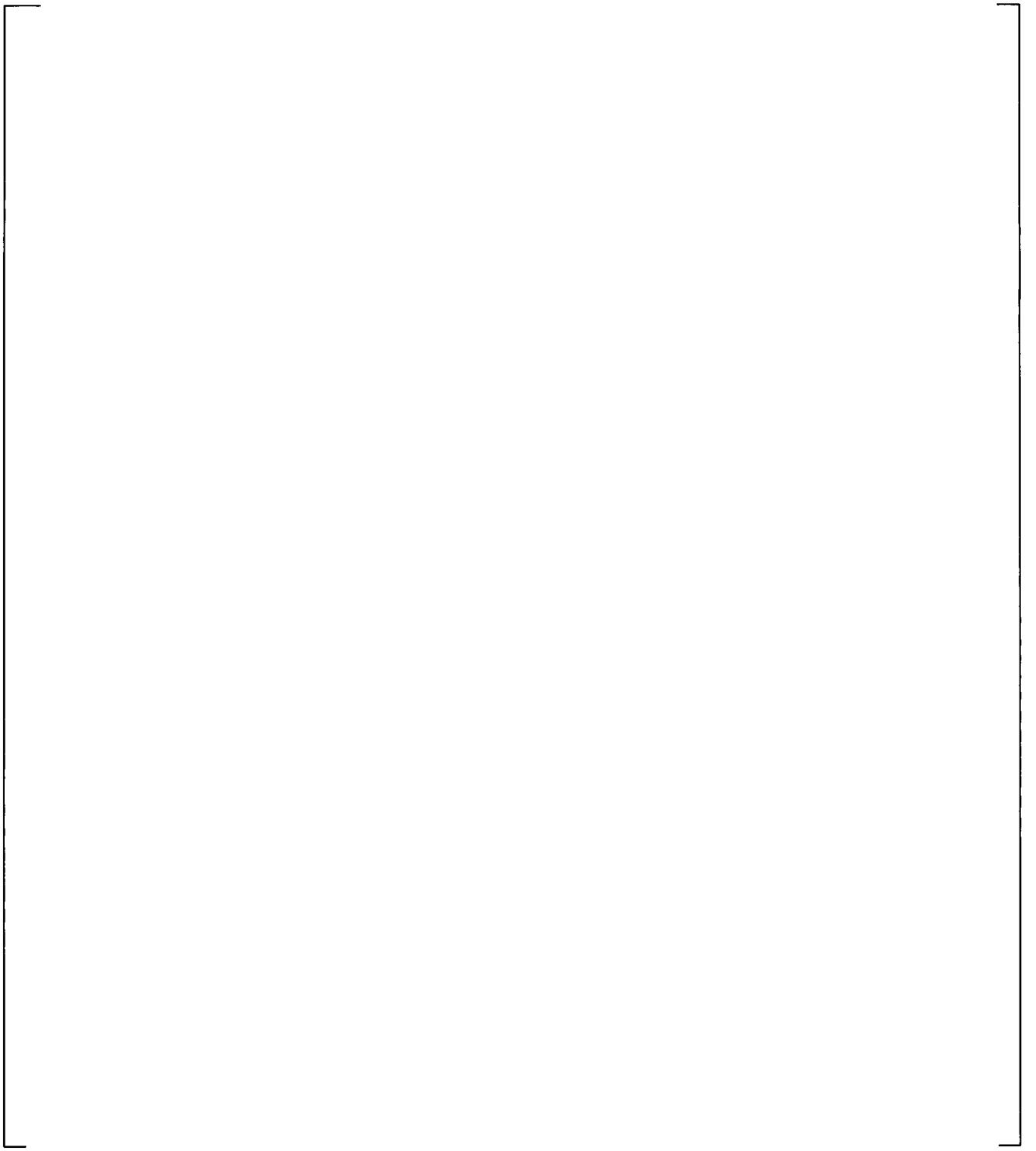

Figure 4-20 Illustration of Calculation of Entrainment Fraction in Wavy-Dispersed Regime. Example for Pressure 12 MPa and Diameter 0.18 m. Note, Flow Regime Map Is Simplified to Emphasize the Entrainment in Wavy-Dispersed Flow.

a,c

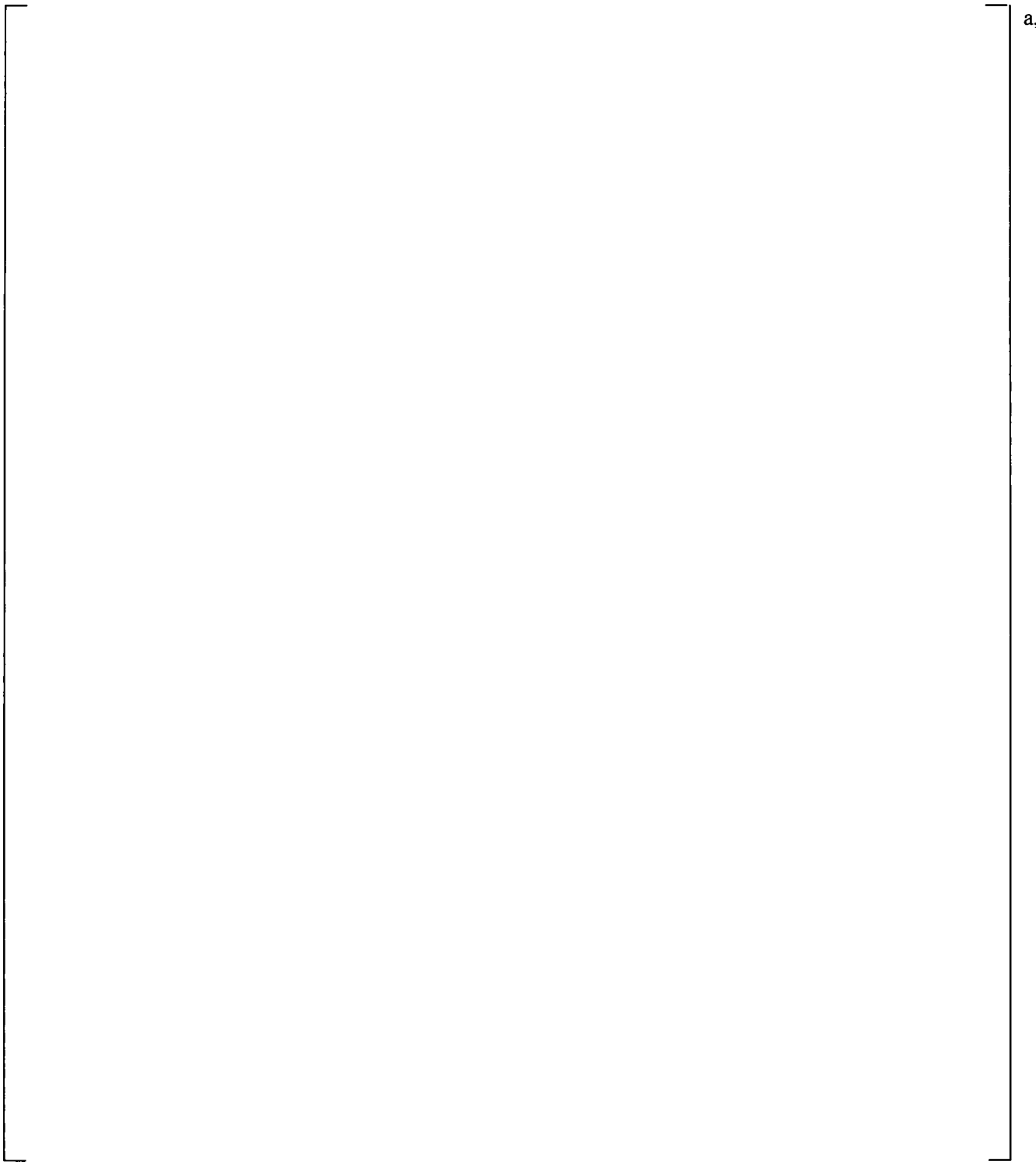

Figure 4-21 Schematic View of Wavy-Dispersed Flow in Cross Section

5 WCOBRA/TRAC-TF2 MOMENTUM TRANSFER MODELS

5.1 INTRODUCTION

The momentum equations used for the WCOBRA/TRAC-TF2 vessel component and loop components have been described in Section 3. There are specific terms in these equations that model the wall-to-fluid drag for each phase and the vapor-to-liquid drag. The constitutive relationships which characterize the wall and interphase drag account for the wall frictional force on the fluid, as well as the interfacial forces which occur as a result of momentum exchange between the phases flowing together within a channel. The interfacial drag models and correlations used in WCOBRA/TRAC-TF2 are flow regime dependent. These expressions for the interfacial drag force also assume that the force is proportional to the square of the relative velocity between the phases. In the WCOBRA/TRAC-TF2 vessel model, there exist two liquid fields such that different expressions are used to calculate the interfacial drag term for the entrained droplet and the continuous liquid fields within a computational cell.

As mentioned above, the interfacial drag relationships are flow regime dependent. Thus, the interfacial area, liquid content, and resulting frictional relationships between the phases will change as the flow regime changes. As a result, the interfacial drag relationship will be dependent on the cell void fraction and the total local mass flux through the cell at any one time. The flow regimes used in WCOBRA/TRAC-TF2 have been discussed in Section 4 of this report and the interfacial drag models and their basis for each flow regime are described in this section.

Since the WCOBRA/TRAC-TF2 vessel component uses the formulation of two separate liquid fields, entrained and continuous film flow, this permits the use of more basic, microscopic models to describe the interfacial drag. In addition, the use of two liquid fields permits more accurate modeling of the reactor vessel geometric details such as spacer grids, top and bottom fuel nozzles (tie plates), downcomer, lower plenum, and the complex flow passages in the upper core plate and structures. More detailed modeling of these geometries allows the code to calculate, more accurately, a variety of hydraulic conditions such as countercurrent flow, flooding, entrainment and de-entrainment.

WCOBRA/TRAC-TF2 vessel component also has the capability of modeling turbulent effects within the continuous phases. The turbulence model in the original COBRA/TRAC code uses a simplified version of the Ishii (1975) mixing length model. The effects of the turbulence models are to reduce gradients within the continuous liquid or vapor between adjacent subchannels thereby promoting heat transfer without mass transfer by mixing. The coarse noding used in WCOBRA/TRAC-TF2 precludes the use of those models because the lateral length scale between adjacent channels greatly exceeds the subchannel hydraulic diameter which is used as the basis for the mixing length. If the code were used in a true subchannel basis, then the turbulence formulation given in the original COBRA/TRAC code would be applicable. As discussed in Section 3.2.3 WCOBRA/TRAC-TF2 turbulence model was not used in the Loss-of-Coolant Accident (LOCA) analysis application nor in the validation package presented in this document.

The WCOBRA/TRAC-TF2 one-dimensional loop components use an eight equation two fluid formulation to solve the system of two-phase flow equations as described in Section 3. The constitutive correlations for the wall (independent of flow regime) and interfacial drag (flow regime-dependent) assume that the frictional drags are proportional to the phase velocities (wall drag for individual phases)

and phase relative velocities (interfacial drag) and enable the hydraulic solution of the phase velocities, void fraction and the pressure gradient.

5.2 VESSEL COMPONENT WALL SHEAR MODELS

Model Basis

The vessel momentum equations described in Section 3.3.3.2 define the wall drag coefficient in units which, when multiplied by the new time phasic velocity, will yield force per unit volume of the momentum cell. However, as described in Section 3.6.2, the phasic mass flow rates are the actual solution variables. The wall drag coefficients described here are defined in terms of the units in which they are derived in subroutine INTFR. The wall shear stress components for axial flow in the vessel are expressed as:

$$\underline{\tau}'_{wX,\ell} = K_{wX,\ell}\,\rho_\ell\,\alpha_\ell\,\underline{U}_\ell\,A_X \tag{5-1a}$$

$$\underline{\tau}'_{wX,v} = K_{wX,v}\,\rho_v\,\alpha_v\,\underline{U}_v\,A_X \tag{5-1b}$$

$$\underline{\tau}'_{wX,e} = K_{wX,e}\,\rho_\ell\,\alpha_e\,\underline{U}_e\,A_X \tag{5-1c}$$

and for lateral flow by:

$$\underline{\tau}'_{wZ,\ell} = K_{wZ,\ell}\,\rho_\ell\,\alpha_\ell\,\underline{W}_\ell\,A_Z \tag{5-2a}$$

$$\underline{\tau}'_{wZ,v} = K_{wZ,v}\,\rho_v\,\alpha_v\,\underline{W}_v\,A_Z \tag{5-2b}$$

$$\underline{\tau}'_{wZ,e} = K_{wZ,e}\,\rho_\ell\,\alpha_e\,\underline{W}_e\,A_Z \tag{5-2c}$$

where:

$\underline{\tau}'_{wX,k}, \underline{\tau}'_{wZ,k}$ = wall frictional force per unit length

$K_{wX,k}, K_{wZ,k}$ = wall drag coefficient

ρ_k = phasic density

α_k = phasic volumetric fraction

$\underline{U}_k, \underline{W}_k$ = phasic velocity $\underline{U}_k$ for axial velocity and $\underline{W}_k$ for lateral velocity

A_X, A_Z = flow area

subscript = X for axial flow; Z for lateral flow; k = ℓ, v, e for liquid, vapor and entrainment phase

The wall shear stress is assumed to be carried by the continuous liquid field when the wall is wet, except at very high vapor fractions. [

]^{a,c}

[a,c

(5-3)

(5-4)

]

[

]^{a,c}

[a,c

(5-5)

]

[

]^{a,c}

The friction factors for the liquid and vapor fields are:

$$f_{w\ell} = \text{maximum}\begin{cases} 64/\text{Re}_\ell & \text{(laminar)} \\ 0.0055 + 0.55\,\text{Re}_\ell^{-1/3} & \text{(turbulent)} \end{cases} \quad (5\text{-}6a)$$

$$f_{wv} = \text{maximum}\begin{cases} 64/\mathrm{Re}_v & \text{(laminar)} \\ 0.0055 + 0.55\,\mathrm{Re}_v^{-1/3} & \text{(turbulent)} \end{cases} \quad (5\text{-}6b)$$

The Reynolds number for each phase is based on the phasic mass velocity:

$$\mathrm{Re}_\ell = \frac{D_h \left| G_{X,\ell} \right|}{\mu_\ell} \quad (5\text{-}7a)$$

$$\mathrm{Re}_v = \frac{D_h \left| G_{X,v} \right|}{\mu_v} \quad (5\text{-}7b)$$

The wall shear models for the lateral directions are similar to those for the axial or vertical direction. The same friction factor relationships given in Equations 5-6a and 5-6b are used, and the form loss coefficients for lateral flow are user input.

For all flow regimes, a shear term associated with an input form loss (Kx) is also considered. [

]^{a,c}

[ ]^{a,c} (5-8a)

(5-8b)

(5-8c)

Similar expressions hold for the lateral flow equations.

In summary, the wall drag coefficient is defined as follows for the continuous liquid in the cold wall regime:

[ ]^{a,c} (5-9)

(5-10)

Combining and using Equations 5-8a, 5-9, and 5-10,

[ ] a,c (5-11)

Similarly, in the hot wall regime,

[ ] a,c (5-12)

Model as Coded

For bubbly, film, and single-phase liquid, the wall-vapor friction factor (f_{wv}) is set equal to zero. For single-phase vapor, and inverted annular and droplet (no film flow) flow regimes, the wall-liquid friction factor ($f_{w\ell}$) is set equal to zero.

The axial flow models are described first. The liquid and vapor Reynolds numbers are calculated using Equations 5-7a and 5-7b, and the friction factors by Equations 5-6a and 5-6b. The phasic frictional pressure drops are calculated as:

[ ] a,c (5-13a)

(5-13b)

where:

$\bar{\rho}_\ell$ = average liquid density between mesh cells
$\bar{\rho}_v$ = average vapor density between mesh cells

The axial wall drag coefficient for the liquid phase is calculated as:

[ ] a,c (5-14)

and the axial wall drag coefficient for the vapor phase is calculated as:

[ ]a,c (5-15)

The first term of Equation 5-15 is zero except at vapor fractions near one. For the entrained field, the wall drag coefficient has only the form loss term:

[ ]a,c . (5-16)

[

]a,c

[ ]a,c (5-17)

and

[ ]a,c (5-18)

where F_{SPV} and F_{SPL} are defined as:

[ ]a,c (5-19)

and

[ ]a,c (5-20)

The functions F_{SPV} and F_{SPL} provide a smooth transition of the wall friction term from one field to another as a phase is depleted.

In the hot wall flow regime, the axial wall drag coefficient is calculated as:

[ ] a,c (5-21)

The continuous liquid phase coefficient is:

[ ] a,c (5-22)

[
]a,c

[ ] a,c (5-23)

[

]a,c The single-phase friction factor for transverse flow is calculated using the same correlations for friction factors given in Equations 5-6a and 5-6b for each phase. For transverse flow, the phasic Reynolds numbers are calculated as:

[ ] a,c (5-24a)

(5-24b)

[

]a,c

The single-phase frictional pressure drop between two adjacent channels through the gap becomes:

[ ] a,c (5-25a)

[ ] a,c (5-25b)

[

]a,c

For the cold wall flow regimes, lateral drag coefficients are calculated as:

[ ] a,c (5-26)

(5-27)

(5-28)

[

]a,c

[ ] a,c

and

[ ] a,c

The values of F_{SPV} and F_{SPL} are given by Equations 5-19 and 5-20.

For the hot wall flow regime,

[a,c] (5-29)

(5-30)

[ ]a,c

[a,c] (5-31)

The next section discusses the use and calculation of form loss coefficients in more detail.

Scaling Considerations

The wall friction models, as defined in the above subsections, are scale independent. The friction factor relationships given in Equations 5-6a and 5-6b agree with existing friction factor relationships found in text books (Vennard, 1961). The laminar friction factor is obtained from a momentum balance in laminar flow and the turbulent relationship agrees with the smooth pipe data of Nikuradse (1933) and with Moody friction model for typical loop piping. The void fraction weighting of the form losses as shown in Equations 5-8a to 5-8c was justified in Andreycheck (1988).

Conclusions

The WCOBRA/TRAC-TF2 vessel wall shear models use a system of consistent correlations for the friction and form loss components for axial and lateral flow. The WCOBRA/TRAC-TF2 use of an entrained liquid field in addition to a continuous liquid field results in partitioning the form losses by each fraction of the flow for the total loss. This particular feature of the vessel wall shear models has been verified on full-scale, two-phase flow experiments on simulated reactor hardware.

5.3 VESSEL COMPONENT FORM LOSS

Model Basis

The WCOBRA/TRAC-TF2 vessel component models a form loss as defined in Section 5.2. The form loss coefficient is directly input into the code for both axial and lateral flows. The user has two options when modeling an unrecoverable pressure loss due to area changes: to model the true area change, or to use the nominal area and input a loss coefficient that has been adjusted for the area change. Both methods are used in WCOBRA/TRAC-TF2 when modeling true area changes. However, the WCOBRA/TRAC-TF2 numerics will calculate an unrecoverable pressure loss which is nearly the same as that which one would

normally input. Therefore, care must be used when modeling true area changes such that unrecoverable losses are not accounted for twice in the calculation.

Model As Coded

WCOBRA/TRAC-TF2 solves the momentum equations on a control volume extending from the midpoint of one continuity cell to the midpoint of the next continuity cell as seen with the shaded cells in Figure 5-1. The momentum equations from Section 3.3 can be reduced to the one-dimensional, single-phase, steady, frictionless form, and applied to the one-dimensional mesh shown in Figure 5-1. For simplicity it will be assumed that the flow is upward, so that the donor cell is the cell below. Since the lateral momentum equations are differenced in a similar manner, the conclusions which will be drawn below apply to the lateral flow through the gaps as well.

The expression for the axial pressure difference across a momentum cell neglecting friction and density changes is:

[ ] a,c (5-32)

This equation can be applied to a sudden expansion, a sudden contraction, or a combination of both where successive pressure differences across several cells are combined to get the total pressure difference. For example, for a sudden contraction, Equation 5-32 applied successively across two consecutive cells in Figure 5-1 yields:

Sudden Contraction:

[ ] a,c (5-33)

Adding the pressure drops for each cell in Equation 5-33 results in:

[ ] a,c (5-34)

From Figure 5-1, $A_2 = A_3 = A_T$ and $A_1 = A_p$, and $U_1 = U_0 = U_p$, while $U_2 = U_3 = U_T$

Using the continuity equation,

$$A_T \rho U_T = A_P \rho U_P \quad (5\text{-}35)$$

or:

$$U_P = \frac{A_T}{A_P} U_T = R U_T \tag{5-36}$$

such that Equation 5-34 becomes:

[ ] a,c (5-37)

Rearranging, Equation 5-37 yields:

[ ] a,c (5-38)

Normalizing the pressure change to the dynamic head at the minimum area gives:

[ ] a,c (5-39)

for a sudden contraction. Similarly, for a sudden expansion in which the expansion occurs across one cell:

[ ] a,c (5-40)

and for a combination contraction/expansion in which the contraction occurs across one cell,

[ ] a,c (5-41)

The expression for the expansion is the same as would be predicted by the Bernoulli equation. The other expressions are more complicated and result from the differencing technique used. In Table 5-1 to Table 5-3, the pressure difference predicted by Equations 5-39, 5-40 and 5-41 is compared to data from King and Brater (1963) and Archer (1913).

[

]a,c

[

]^{a,c}

Scaling Considerations

The loss coefficients that are normally used in codes like WCOBRA/TRAC-TF2 are derived from full-scale and scaled experimental test data, and in many cases are standardized and available in handbooks of hydraulic resistance (Crane, 1969). For specific nuclear reactor geometries and area changes in the reactor vessel, loss coefficients and unrecoverable pressure drop information is obtained from scale model experiments. These experimental loss coefficients and pressure drops are used as a guide to adjust the form loss coefficients in regions of the vessel where the geometries are complex.

The WCOBRA/TRAC-TF2 method of applying the form loss coefficients is verified by comparing the WCOBRA/TRAC-TF2 steady-state flow and pressure distributions to calculated pressurized water reactor (PWR) steady-state conditions.

Conclusions

The form loss coefficients are user inputs to the calculation and are dependent on the geometry and the method of modeling the area changes in the model. Explicitly modeled area changes require a small adjustment of the form loss coefficient using the guidance provided above. For cases where no area change is modeled, explicitly standard experimentally determined loss coefficients are used.

5.4 VESSEL COMPONENT INTERFACIAL SHEAR MODELS

Flow regime maps used in the vessel component of WCOBRA/TRAC-TF2 are described in Section 4. The vessel momentum equations described in Section 3 require the interfacial drag coefficient in units which, when multiplied by the new time velocity difference between the phases, will yield force per unit length for that phase. During the numerical solution, these coefficients are divided by the appropriate phasic densities, when the phasic mass flow rate is solved for. In subroutine INTFR, the interfacial drag coefficients are defined based on phasic velocity, as shown below. The average interfacial drag force per unit length between the vapor and continuous liquid is defined as:

$$\tau'_{iX,v\ell} = K_{iX,v\ell}\,\underline{U}_{v\ell} \tag{5-42}$$

where:

$\tau'_{iX,v\ell}$	=	the force per unit length on the liquid by the vapor
$K_{iX,v\ell}$	=	the flow regime dependent interfacial drag coefficient
$\underline{U}_{v\ell}$	=	the axial relative velocity between the vapor and the continuous liquid

A similar expression exists for the drag force between the vapor and entrained liquid. This expression is given as:

$$\tau'_{iX,ve} = K_{iX,ve}\,\underline{U}_{ve} \tag{5-43}$$

where:

$\tau'_{iX,ve}$	=	the force per unit length on the entrained liquid phase by the vapor
$K_{iX,ve}$	=	the flow regime dependent interfacial drag coefficient
$\underline{U}_{ve}$	=	the axial relative velocity between the vapor and the entrained phase

When accounting for the relative velocity between the phases in some calculations, for example the Reynolds number in Equation 5-51, the relative velocity value generally assumed is the [

]^{a,c}:

$$\left[\qquad\qquad\right]^{a,c} \tag{5-44}$$

where $\underline{W}_{v\ell,max}$ is the maximum lateral relative velocity and $\underline{U}_{v\ell}$ is the axial relative velocity for the cell. However, in some cases, this value is modified as described in the Model as Coded sections. When the value has been modified, it is expressed as U_r.

5.4.1 Small Bubble Flow Regime Interfacial Drag

5.4.1.1 Non-Rod Bundle Geometry

Model Basis

For the bubbly regime, the general form of the interfacial drag coefficient is:

$$K_{iX,v\ell} = C_{Db}\frac{\rho_\ell\,|\underline{U}_{v\ell}|}{2}A_{p,b}/\Delta X \tag{5-45}$$

where $A_{p,b}$ is the total projected area of the bubbles in the volume. For spherical bubbles, this results in:

$$A_{p,b} = N_b \pi r_b^2 \tag{5-46}$$

where N_b is the number of bubbles in the cell, and r_b is the bubble radius. This can be shown to be equivalent to:

[a,c] (5-47)

where $A_{i,b}$ is the bubble interfacial area, described in Section 4. Two alternate forms of the interfacial drag coefficient are obtained:

[a,c] (5-48a)

(5-48b)

Similarly, for lateral flow,

[a,c] (5-49a)

(5-49b)

Expressions for the bubble drag coefficient (C_{Db}) are discussed by Ishii (1977) and Ishii and Chawla (1979). The drag coefficients are Reynolds number dependent and closely related to the drag coefficients for single bubbles and drops in an infinite medium. The drag coefficient for a single bubble in an infinite liquid medium is shown in Figure 5-2. The bubble is considered to behave as a solid sphere in the viscous regime. At a higher Reynolds number, the bubble is characterized by a distorted shape and irregular motion. In this distorted particle regime the drag coefficient decreases with the Reynolds number. As the Reynolds number further increases, the bubble becomes spherical-cap shaped and the drag coefficient becomes constant.

As discussed by Ishii (1979), in the viscous regime the drag coefficient of a single particle in a multi-particle system may be assumed to have the same functional form as that of a single particle in an infinite medium, provided that the Reynolds number is computed using the appropriate mixture viscosity. Therefore, in the viscous regime the drag coefficient on a bubble is given by:

$$C_{Db} = \frac{24}{Re_b}(1.0 + 0.1 Re_b^{0.75}) \quad (5\text{-}50)$$

where:

$$Re_b = \frac{2r_b \rho_\ell \underline{U}_{v\ell}^*}{\mu_{m_b}} \tag{5-51}$$

and

$$\mu_{m_b} = \mu_\ell (1-\alpha_v)^{-2.5\frac{(\mu_v+0.4\mu_\ell)}{(\mu_v+\mu_\ell)}} \tag{5-52}$$

In the distorted particle regime, it is again assumed that the drag coefficient for a particle in a multi-particle system is the same as that of a single particle in an infinite medium with the Reynolds number based on a mixture viscosity. In addition, it is assumed that churn-turbulent flow always exists in the distorted particle regime. Under these conditions, a particle tends to move in the wake caused by other particles. Therefore, the velocity used in the drag coefficient and Reynolds number should be the drift velocity, $\underline{U}_{vj} = (1-\alpha_v)\underline{U}_{v\ell}$. The drag coefficient in the distorted particle regime is then,

$$C_{Db} = \frac{\sqrt{2}}{3} N_\mu Re_b' (1-\alpha_v)^2 \tag{5-53}$$

where:

$$N_\mu = \frac{\mu_\ell}{\left[\rho_\ell \sigma \sqrt{\frac{\sigma}{g(\rho_\ell - \rho_v)}}\right]^{1/2}} \tag{5-54}$$

$$Re_b' = \frac{2r_b \rho_\ell (1-\alpha_v) \underline{U}_{v\ell}^*}{\mu_m} \tag{5-55}$$

and

$$\mu_m = \frac{\mu_\ell}{(1-\alpha_v)} \tag{5-56}$$

The $(1-\alpha_v)^2$ in the expression for the drag coefficient results from using the drift velocity to compute the drag force.

Churn-turbulent flow is also assumed for the cap bubble regime where:

$$C_{Db} = \frac{8}{3}(1-\alpha_v)^2 \tag{5-57}$$

For the large-bubble flow regime, Equation 5-50 is assumed to apply down to the limit of Newton's regime where the drag coefficient for a single solid sphere becomes constant at a value of 0.45. Within Newton's regime the large bubbles are assumed to move with respect to the average volumetric flux and,

therefore,

$$C_{Db} = 0.45 (1 - \alpha_v)^2 \tag{5-58}$$

The mixture viscosity is used in Re'_b in Equation 5-55 because a particle moving in a multi-particle system experiences a greater resistance than a single particle in an infinite medium. As it moves it must deform not only the fluid, but the neighboring particles as well. The effect is seen by the particle as an increased viscosity.

The terminal relative velocity between the bubble and liquid is also calculated from a bubble rise model given by Ishii (1977) as:

$$U_{rb} = 1.414 \left[\sigma g g_c (\rho_\ell - \rho_v) / \rho_\ell^2\right]^{0.25} / (1 - \alpha_v) \tag{5-59}$$

The bubble size is assumed to depend on a Weber number criterion:

$$r_b = 0.5 \, We_b \, \sigma g_c / (\rho_\ell \underline{U}^{*2}_{v\ell}) \tag{5-60}$$

where:

We_b = 10

[

]^{a,c}

[ ] a,c (5-61)

where the relative velocity $\underline{U}_{v\ell}$ is defined as the vapor phase velocity in the high void cell subtracted by the liquid phase velocity in the low void cell.

If large heat releases exist at a solid boundary within the cell, then vapor is assumed to concentrate as a film at the wall. The interfacial shear between the vapor film and the bulk liquid is then determined by assuming a transition inverted slug regime described in Section 5.4.6.

Model as Coded

The WCOBRA/TRAC-TF2 coding logic uses the above correlations for non-rod bundle geometry with consistency checks to establish limits on parameters such as relative velocities and bubble size before the interfacial drag is calculated. The relative velocity is compared using different methods and the minimum value is used in the bubble Weber number and drag coefficient. The reason for this is that in the small bubble regime the interfacial area is large and would lead to excessively large forces if a large relative velocity were used.

The relative velocity to be used in Equation 5-45 is limited as follows.

The first limit is calculated by [

]^{a,c}:

[ ] a,c (5-62)

[

]^{a,c}

[ ] a,c (5-63)

and the drift velocity is determined by:

[ ] a,c (5-64)

The second limit is calculated by [ ]^{a,c}:

[ ] a,c (5-65)

[

]^{a,c}

The value of $\underline{U}_{v\ell}$ used in Equation 5-45 is then:

[ ] a,c (5-66)

[

]^{a,c}

[

]a,c

Next, the bubble drag coefficient is calculated, using Equations 5-50, 5-53, 5-57, and 5-58. [

]a,c

The interfacial drag between the continuous liquid and the vapor in the small bubble regime is calculated as:

[ ]a,c (5-67a)

where the interfacial area $A_{i,SB}$ is given in Equation 4-17. If there is significant vapor generation at the wall, the interfacial drag is ramped between the small bubble value calculated from Equation 5-67a and the inverted slug value as:

[ ]a,c (5-67b)

The hot wall drag coefficient, $K_{iX,v\ell,HW}$ is calculated similar to Equation 5-109 as:

$$K_{iX,v\ell,HW} = \text{maximum}\begin{cases} K_{iX,IVS} \text{ as defined by Equation 5-107} \\ 0.125\,\rho_v A_{i,IVS} \end{cases} \quad (5\text{-}67c)$$

The value of F'_Γ is given as:

[ ]a,c (5-68a)

Where, [ ]a,c (5-68b)

[

]^{a,c}

U_{rb} in Equation (5-68b) is calculated from Equation 5-59 and:

$$\left[\right]^{a,c} \tag{5-69}$$

where A_x is the cell momentum area in the axial direction and $Q_{w\ell}$ and Q_b are the heat flow from wall to liquid and the subcooled boiling heat flow, respectively (Section 7.2). To illustrate the effect of the ramps and limits described above, Equation 5-67b was evaluated as a function of $\underline{U}_{v\ell}$ for typical fluid conditions, and plotted in Figure 5-3a. It can be seen that, at high heat flux and high relative velocities, the interfacial drag factor approaches a value more typical of separated, rather than bubbly, flow.

For lateral flow through gaps, the procedure is similar, with the following differences: the relative velocity is limited to a maximum value of [ ]^{a,c}. The more complicated channel model is not used because, in general, gaps tend to have a large flow area, and the flow velocities are relatively small.
[

]^{a,c}

The lateral flow interfacial drag uses the same expression for bubble drag coefficient except that the vector sum relative velocity is used in the Reynolds number as described earlier. The bubble drag coefficient for lateral flow uses the same logic as the axial or vertical flow. The interfacial area is calculated in the same fashion for the lateral flow as the axial flow, except the velocity is the lateral relative velocity for the gap flow. The lateral flow interfacial drag is given as:

$$\left[\right]^{a,c} \tag{5-70}$$

[ ]^{a,c}

Scaling Considerations

The formulation used in the small bubble regime is scale independent, since it is based on an individual bubble in the flow stream. Therefore, no scale dependence or bias would be introduced into the calculation by this model.

Conclusions

The small bubble regime models for non-rod bundle geometry are based on the work of Ishii and Chawla (1979). The same coding logic is used to represent the axial bubble behavior as well as the gap or lateral bubble effects.

5.4.1.2 Rod Bundle Geometry

Model Basis

The small bubble flow regime interfacial drag for axial flow in rod bundle geometry is based on Bestion's drift velocity. The Bestion drift correlation in rod bundles was presented in (Bestion, 1990). The model performance against relevant rod bundle tests and other correlations were studied in (Coddington and Macian, 2002). Coddington and Macian concluded that the Bestion drift correlation resulted in very good prediction of the experimental data.

According to (Bestion, 1990), the drag force using the drift-flux model can be expressed as:

$$\tau_i = \alpha \cdot (1-\alpha)\frac{1}{C_m^2}\frac{\rho_m}{L_m}(1 - C_0 \cdot \alpha)^2 \left[V_V - \frac{C_0(1-\alpha)}{1-C_0\cdot\alpha}V_L\right]^2 \quad (5\text{-}71)$$

When V_{gj} is expressed as:

$$V_{gj} = C_m \left[\frac{g\cdot\Delta\rho\cdot L_m}{\rho_m}\right]^{1/2} \quad (5\text{-}72)$$

where:

C_m = 0.188 for rod bundle geometry,

g = gravitational constant,

$\Delta\rho$ = $\rho_\ell - \rho_v$,

ρ_ℓ = liquid density,

ρ_v = vapor density,

L_m = D_h (hydraulic diameter) for rod bundle geometry,

ρ_m = ρ_v for rod bundle geometry,

α = void fraction,

C_0 = distribution parameter,

V_V = vapor velocity,

V_L = liquid velocity

Model as Coded

The Bestion drift correlation is coded as described in the model basis discussion. The distribution parameter is defined as C_0=1 consistent with the optimum value from the comparison presented in (Coddington and Macian, 2002). The interfacial drag for the small bubble flow regime in rod bundle geometry is then:

$$\tau'_{iX,v\ell,SB} = K_{iX,v\ell,SB} \cdot \underline{U}_{v\ell} = \alpha_v (1-\alpha_v) \frac{1}{0.188^2} \frac{\rho_g}{D_h} (1-\alpha_v)^2 (V_V - V_L)^2 A_{mom} \quad (5\text{-}73)$$

Since $\underline{U}_{v\ell} = V_V - V_L$ the small bubble drag coefficient, $K_{iX,vl,SB}$, in rod bundle channels is:

$$K_{iX,v\ell,SB} = \alpha_v (1-\alpha_v)^3 \frac{1}{0.188^2} \frac{\rho_g}{D_h} |\underline{U}_{v\ell}| A_{mom} \quad (5\text{-}74)$$

If there is significant vapor generation at the wall, the bubble drag coefficient is ramped according to Equation 5-67b, where $K_{iX,v\ell,SB}$ is given by Equation 5-74 and $K_{iX,v\ell,HW}$ is given by Equation 5-67c.

Scaling Considerations

The formulation used in the small bubble regime is full scale relative to the PWR bundle. Therefore, no scale bias would be introduced into the calculation by this model. The model is assessed against prototypical rod bundle data in Volume 2 of this report.

Conclusions

The small bubble regime model for axial flow in a rod bundle geometry is based on the work of Bestion (1990), which has been found to well-predict rod bundle geometry data.

5.4.2 Small-to-Large Bubble Flow Regime Interfacial Drag

Model Basis

The approach used for the large bubble regime is similar to that for the small bubble regime. The small bubbles are primarily in the viscous regime where $1.0 \le Re_b \le 1000$ whereas the larger bubbles may be in Newton's Regime where $Re_b \ge 1000$. In the Newton Regime the large bubbles are assumed to move with the average volumetric flux in the flow.

[

]a,c

As discussed by Ishii (1977) the presence of other particles affects the resulting drag for a multi-particle system. This effect is corrected by using the appropriate mixture viscosity for multi-particle systems. As a single bubble moves in a multi-particle system, it deforms not only the neighboring fluid, but the other particles as well. The individual particle or bubble is, in turn, distorted by its neighbors as it moves through the fluid. This effect is seen as an increased fluid viscosity. The bubble Reynolds number is defined as Equation 5-51 with the mixture viscosity correction given as Equation 5-52.

[

]a,c In the Newton regime, the large bubbles are assumed to move relative to the average volumetric flux such that:

$$C'_{Db} = C_{Db}(1-\alpha_v)^2 \tag{5-75}$$

where the $(1-\alpha_v)^2$ term results from using the drift velocity to calculate the drag force, and C_{Db} is the maximum drag from Equation 5-50 or a value of [ ]a,c.

The same basis is used for the transverse drag relationships in this regime. [

]a,c

Model as Coded

The interfacial drag between the continuous liquid and vapor in the small-to-large bubble regime is calculated as:

[ ]a,c (5-76)

where $A_{i,LB}$ is given by Equation 4-34. The calculation for the large bubble regime follows the same general procedure as the small bubble model, except the relative velocity $|\underline{U}_{v\ell}|$ is not modified by the limits described by Equation 5-66.

For conditions in which there is a large vapor generation rate at the wall, the [

]a,c :

[ ]a,c (5-77)

[ ]a,c

The interfacial drag coefficient between the continuous liquid and vapor for the small-to-large bubble regime is then calculated by [ ]a,c

[ ]a,c (5-78a)

or:

[ ]a,c (5-78b)

[

]a,c

[ ]a,c (5-79)

which can be shown to be the as-coded expression:

[ ]a,c (5-80)

The term α_{SB} represents the upper bound of the small bubble regime, assumed to be [ ]a,c.

The bubble drag relationship for the lateral flow through the gaps for the small-to-large bubble and large bubble regime are the same as the axial flow coding logic. As mentioned earlier, the lateral relative velocity along with the gap bubble radius is used to calculate the bubble Reynolds number for the bubble drag coefficient. The small-to-large bubble range is the same for the lateral flow as the axial flows given in Equation 5-76.

The effect of the models, ramps, and limits on the axial interfacial drag factor for this flow regime is shown in Figure 5-3b, and indicates similar trends as the small bubble regime.

Scaling Considerations

As described in Section 5.4.1, the noding selection could influence this flow regime and how it is weighted with other regimes. The verification of this model with noding similar to PWR noding is considered in the code assessment presented in Volume 2.

Conclusions

The bubble drag coefficient and interfacial drag relationships are consistent between lateral flow and axial flow in the WCOBRA/TRAC-TF2 model. The drag relationships are based on the extensive work by Ishii and Chawla (1979). A number of prototypical rod bundle experiments with different rod array sizes are considered in Volume 2 to assess the interfacial drag model in the small-to-large bubble flow regime.

5.4.3 Churn-Turbulent Flow Regime Interfacial Drag

Model Basis

The churn-turbulent regime is assumed to be a combination of the small-to-large bubble regime and the film/drop regime. The model basis for the film/drop regime is described in Section 5.4.4.

Model as Coded

The small-to-large bubble interfacial drag coefficient is calculated from the selected drag coefficient and the relative velocity as previously described in Section 5.4.2.

The interfacial drag relationships for the film/drop component are described in Section 5.4.4. For the interpolation in the Churn-Turbulent regime, the film drag value corresponding to the value at the Churn-Turbulent/Film-Drop regime boundary ($\alpha = \alpha_{CRIT}$ defined by Equation 5-84) is used.

For the churn-turbulent regime, a [ ]^{a,c}:

[ ]^{a,c} (5-82)[1]

where:

[ ]^{a,c} (5-83)

where α_{LB} = [ ]^{a,c}, and α_{crit} is given as:

[ ]^{a,c} (5-84)

[1] Equation 5-81 is intentionally omitted.

The same linear interpolation logic is used in the lateral direction to combine large bubble and film/drop components.

Scaling Considerations

This model for interfacial drag has some scale dependence. Ishii (1977) attempted to compensate for the interaction effects of one bubble or groups of bubbles on each other through adjustments of the effective viscosity.

Conclusions

Although the model has some scale dependence, the coding logic will limit the bubble sizes based on the true physical dimensions for the problems.

5.4.4 Film/Drop Flow Regime

Model Basis

This section describes the interfacial drag models between the vapor and continuous liquid for the wetted wall film flow regime. The interfacial drag between the vapor and entrained liquid for this regime is the same as that for the hot wall dispersed droplet flow regime, and is discussed in Section 5.4.7. As shown in Section 4, when the vapor content in the flow exceeds a critical void fraction, and the wall is below the wetted wall temperature criteria, the film is assumed to become stable and liquid can no longer bridge the channel.

In the film regime, the general form of the interfacial drag coefficient is, for axial flow,

[ ] a,c (5-85)

where $A_{iX,film}$ is the interfacial area in the volume. For a thin liquid film, the interfacial area is:

[ ] a,c (5-86)

For lateral flow, the expression for interfacial area is:

[ ] a,c (5-87)

where the gap is viewed as a series of N_g vertical slots of height ΔX.

With the above equations, alternate versions of Equation 5-85 are defined:

[ ]a,c (5-88)

(5-89)

The friction factor ($f_{i,FD}$) for film flow is dependent on whether the film is stable or unstable. It has been observed experimentally that the onset of film instability causes a sudden increase in system pressure drop. This is a result of increased roughness of the liquid film caused by large, unstable waves. The film friction factor for stable film flow in tubes has been studied by Wallis (1969), and Henstock and Hanratty (1976) have correlated a large amount of co-current and countercurrent film flow data for unstable films.

Henstock and Hanratty's correlation is of the form,

$$f_{i,HH} = f_s\left\{1+1400F\left[1-\exp\left(-\frac{1}{G}\cdot\frac{(1+1400F)^{3/2}}{13.2F}\right)\right]\right\} \tag{5-90}$$

where:

$$G = \frac{\rho_\ell g D_h}{\rho_v U_v^2 f_s} \tag{5-91}$$

and

$$F = \frac{m^+}{Re_v^{0.9}}\frac{\mu_\ell}{\mu_v}\sqrt{\frac{\rho_v}{\rho_\ell}} \tag{5-92}$$

with:

$$m^+ = [\,(0.707\,Re_\ell^{0.5})^{\,2.5} + (0.0379\,Re_\ell^{0.9})^{\,2.5}\,]^{\,0.40} \tag{5-93}$$

and

[ ]a,c (5-94)

[ ]a,c The single-phase friction factor is different from that given in the Henstock and Hanratty (1976) paper which was:

$$f_s = 0.046\,Re_v^{-.20} \tag{5-95}$$

[

]^{a,c}

For stable films, the annular flow interfacial correlation developed by Wallis (1969) is used:

$$f_{i,W} = 0.005\left[1 + 75\left(1 - \alpha_v\right)\right] \tag{5-96}$$

[

]^{a,c}

As discussed in Section 4, the transition to churn-turbulent (large bubble) regime begins at a void fraction of [ ]^{a,c} percent and continues until a stable film is achieved. The void fraction at which a stable liquid film will exist depends on the flow channel size and the vapor velocity. The critical void fraction is determined from a force balance between the disruptive force of the pressure gradient over the crest of waves on the film and the restraining force of surface tension. The resulting expression for the critical vapor fraction is:

[ ] a,c (5-97)

The critical void fraction is limited to a minimum value of [ ]^{a,c}, the value below which waves can be expected to bridge across the flow channel and cause a transition to churn-turbulent flow.

The interfacial drag logic for the lateral flow is simplified relative to the vertical flow since the film flow between the gaps is assumed to be stable and the Wallis interfacial friction factor given in Equation 5-96 is used. [

]^{a,c}

Model as Coded

[

]^{a,c}

[

]^{a,c} The interfacial drag is calculated as,

$$[\quad]^{a,c} \tag{5-98}$$

where the interfacial area $A_{i,film}$ is given by Equation 4-51.

For lateral flow through the gaps, the interfacial friction factor is calculated using:

$$[\quad]^{a,c} \tag{5-99}$$

where the factor of 2 in Equation 5-89 has been taken into account, and giving a lateral drag coefficient of:

$$[\quad]^{a,c} \tag{5-100}$$

Scaling Considerations

The Wallis friction factor for film, Equation 5-96 has been examined for horizontal and vertical flow from pipe sizes ranging from 1-inch to 3-inch diameter as shown in Figure 5-4. The Hanstock and Hanratty film friction model has also been compared to vertical film flow data on diameter of 0.503 inches to 2.5 inches over a range of different fluid velocities and pressures. The comparison of their correlation to data is shown in Figure 5-5. This comparison shows that the correlation provides a good fit to the data over a range of scales.

Conclusions

The film wall drag models have been compared for both horizontal and vertical flows over a range of geometries and hydraulic diameters. WCOBRA/TRAC-TF2 has been used with these models to calculate the two-phase pressure drops in an annular film flow regime.

5.4.5 Inverted Annular Flow Regime

Model Basis

An inverted annular flow regime is assumed if the continuous liquid phase is subcooled and the surrounding surface is hot and dry. This regime consists of a liquid core surrounded by a vapor film.

For inverted annular flow, the interfacial friction factor is [ ]^{a,c}:

$$[\quad]^{a,c} \tag{5-101}$$

Model as Coded

WCOBRA/TRAC-TF2 calculates the continuous liquid enthalpy and compares it to the saturated liquid enthalpy in the cell. If the liquid is subcooled and the wall is in the hot wall regime, the flow regime is inverted annular. If the liquid enthalpy is saturated or superheated, the code assumes the inverted liquid slug regime.

The interfacial drag for the axial momentum equation then is set to:

$$K_{iX,v\ell,IVA} = f_{iX,IVA} \frac{\rho_v |\underline{U}_{v\ell}|}{2} A_{i,film} / \Delta X \qquad (5\text{-}102)$$

where the interfacial area $A_{i,film}$ is given by Equation 4-54 and equal to $\frac{4\sqrt{\alpha_\ell} A_X \Delta X}{D_h}$.

The interfacial drag and friction models are simplified for the lateral flow in the inverted annular and inverted annular slug regimes. [

]^{a,c} A drag coefficient in the lateral direction of:

[ ]^{a,c} (5-103)

is used, and the radius of the chunk of liquid is:

[ ]^{a,c} (5-104)

The interfacial drag coefficient becomes:

[ ]^{a,c} (5-105)

where $|\underline{W}_{v\ell}|$ is the lateral relative velocity between the continuous liquid and the vapor.

Scaling Considerations

Inverted annular flow can most commonly occur during a rapid reflood process when subcooled liquid is forced into the core either at the beginning of reflood, or when the nitrogen pressurizes the downcomer. When this situation occurs, the subcooled continuous liquid is forced into the bundle at a much higher velocity than the quench front velocity on the rods, and a thin vapor film exists on the rods' surface, separating it from the liquid core. Inverted annular flow was observed in the Full Length Emergency Cooling Heat Transfer (FLECHT) and FLECHT- Separate Effects and System Effects Test (SEASET) rod bundle experiments (Sections 14 and 15). These experiments are full-length tests using prototypical rod dimensions and spacing such that the geometric effects for this flow regime are preserved, and there are

no scaling effects. The experimental conditions were varied over wide ranges to ensure that the PWR plant conditions were covered.

Conclusions

The inverted annular interfacial drag model used in WCOBRA/TRAC-TF2 is derived from the annular film flow model used for high void fraction wetted wall flows. The inverted annular interfacial drag model is assessed with full-scale prototypical rod bundle experiments for different rod arrays.

5.4.6 Inverted Liquid Slug Regime

Model Basis

As the liquid flow in the inverted annular flow regime is heated by wall heat transfer, the liquid core is accelerated by the increased vapor content of the flow. When the liquid reaches the saturation temperature, it no longer can condense the vapor and the liquid begins breaking into ligaments or chunks into a dispersed droplet flow as it progresses up along the heated channel. The interfacial friction is calculated assuming an unstable liquid film surface exists on the large liquid ligaments or drops as:

[ ]^{a,c} (5-106)

This equation is [ ]^{a,c} times the Wallis (1969) equation for stable liquid films discussed earlier, given as Equation 5-96.

The interfacial area is calculated assuming that the liquid slugs are spherical, and have a diameter [ ]^{a,c} of the channel diameter, as described in Section 4.3.3.

Model as Coded

The axial flow interfacial drag coefficient is calculated as:

$$K_{iX,IVS} = f_{i,IVS} \frac{\rho_v |\underline{U}_{v\ell}|}{2} A_{i,IVS} / \Delta X \tag{5-107}$$

where the friction factor is calculated from Equation 5-106 and the interfacial area $A_{i,IVS}$ for the liquid slug regime is from Equation 4-60 as:

$$A_{i,IVS} = \frac{8.04\alpha_\ell}{D_h} A_X \Delta X \approx \frac{8\alpha_\ell}{D_h} A_X \Delta X \tag{5-108}$$

where α_ℓ is the minimum of the liquid void fraction in the mesh cell $\alpha_\ell(i,j)$ and the average liquid void is given by Equation 4-13.

This is further modified by:

[ ]^{a,c} (5-109)

The lower limit is necessary to allow for [

]^{a,c}.

The lateral flow interfacial drag for the inverted slug regime is calculated in the same fashion as the inverted annular regime, as described in the previous section.

Scaling Considerations

As mentioned earlier in this subsection, the inverted annular flow regime is an evolution of the inverted annular flow regime as heat is transferred by the wall to the fluid. The inverted slug regime is a transition from the inverted annular flow regime, where the liquid column breaks up into ligaments or large liquid slugs, and into the dispersed droplets.

The interfacial drag in the inverted liquid slug regime will be somewhat sensitive to the number of heated surfaces per unit volume since the vapor layers along the heated rods will be growing. The liquid will not be continuous, but will still be trapped between the heated surfaces. Reflood experiments used to validate the WCOBRA/TRAC-TF2 code have full-height and full-scale subchannel dimensions prototypical of PWR fuel bundles. The inverted annular flow regime is expected to exist in those experiments so scaling effects if present will be evaluated as part of the code assessment.

Conclusions

The inverted slug regime is a transition hot wall regime where the liquid is breaking up into a dispersed droplet flow regime.

5.4.7 Dispersed Droplet Flow Regime

Model Basis

As discussed in Section 3, WCOBRA/TRAC-TF2 has a separate entrained liquid field. The droplet drag model is based on the work by Ishii (1977) using the analogy of a single drop in an infinite vapor medium to a single bubble in an infinite liquid field. The droplet drag models discussed in this section are used for both the hot wall and cold wall flow regimes. The interfacial friction coefficient used is:

$$K_{iX,ve,DD} = C_{Dd} \frac{\rho_v |\underline{U}_{ve}|}{2} A_{p,d} / \Delta X$$

$$= C_{Dd} \frac{\rho_v \underline{U}_{ve}^{*}}{2} \frac{A_{i,drop}}{4} / \Delta X \quad (5\text{-}110)$$

where:

C_{Dd} = the droplet drag coefficient

$\underline{U}_{ve}^{*}$ = the vector sum relative velocity between the vapor and the entrained droplet, and is given as

$$\underline{U}_{ve}^{*} = \sqrt{\underline{W}_{ve,max}^{2} + \underline{U}_{ve}^{2}} \tag{5-111}$$

$A_{p,d}$ = total projected area of the droplets, $\frac{3\alpha_e}{4r_d} A_X \Delta X$

$A_{i,drop}$ = interfacial area of the droplets, $\frac{3\alpha_e}{r_d} A_X \Delta X$

and

$\underline{W}_{ve,max}$ = the maximum lateral relative velocity between the vapor and the entrained droplet of all gaps connected to the fluid cell

r_d = the droplet radius

α_e = the entrained liquid fraction in the flow,

It can be see that $A_{p,d} = \frac{A_{i,drop}}{4}$.

It is assumed that the drops are in the Newton Regime where the droplet Reynolds number is large. The droplet drag coefficient that is used in this is assumed to be:

[ ] a,c (5-112)

Bird, Stewart, and Lightfoot (1960) recommend a value of 0.44 for the droplet drag in the Newton Regime while Ishii and Chawla (1979) recommend a value of 0.45.

The droplet sizes used in WCOBRA/TRAC-TF2 are discussed in Section 4. The drop size is calculated as:

[ ] a,c (5-113)

Model As Coded

The current droplet diameter is first established via Equation 5-113.

The droplet interfacial drag is then calculated as:

$$K_{iX,ve,DD} = \left(C_{Dd} \frac{\rho_v \underline{U}_{ve}^{*}}{2} \frac{A_{i,drop}}{4} \right) / \Delta X \tag{5-114}$$

where:

$$A_{i,drop} = A_{i,d}''' A_X \Delta X \tag{5-115}$$

The droplet drag relationships for a cold wall are identical, except that there is no check on the drop size relative to the hydraulic diameters. If the drops were as large as the hydraulic diameter, they would intersect the liquid films on the wall and the channel would be filled with liquid. This would result in a different flow regime.

The lateral flow droplet calculation uses the average droplet radius calculated in each of the adjacent cells from Equation 5-113. The droplet drag coefficient for lateral flow is a constant value, C_{Dd} = [ ]^{a,c}, and the lateral droplet drag coefficient is calculated as:

$$K_{iZ,ve,DD} = C_{Dd} \frac{\rho_v |\underline{W}_{ve}|}{2} \frac{3\alpha_e}{4r_d} L_g \Delta X \tag{5-116}$$

Scaling Considerations

The droplet sizes have as their basis drop sizes measured in the FLECHT-SEASET program (Lee, N. et al., 1981). The interfacial drag is based on assuming spherical droplets to be in the Newton Regime (droplet Reynolds number is large). Since the rod bundle experiments have been performed on full-scale bundle simulations, the droplet interfacial drag models are applicable to the PWR.

Conclusions

There is consistency in how the droplet flow is modeled both axially and laterally. The same relationships for droplet drag are used for each drag coefficient formulation. Droplet size is derived from observations in prototypical rod bundle (FLECHT-SEASET) during reflood conditions, therefore the droplet interfacial drag models are applicable to the PWR.

5.4.8 Falling Film Flow Regime

Model Basis

As fuel rods quench from the top, a liquid film is formed on the rods behind the quench and sputtering front. Liquid is de-entrained from the upward flowing dispersed droplet flow to provide liquid source for the film on the rods. The interfacial drag relationships on the film behind the top quench front are the same as those for annular film flow except that the interfacial friction uses the Wallis (1969) friction factor given in Equation 5-96. [ ]^{a,c}

[

]^{a,c} Therefore, the interfacial friction coefficient for falling films is:

$$f_{iX,FF} = 0.005\left(1 + 75\alpha_\ell\right) \tag{5-117}$$

In the falling film regime, the gap or transverse flow film interfacial drag is calculated in the same fashion as the annular film flow drag discussed earlier in Section 5.4.4. The lateral flow of drops which are sputtered from the top down quench front would be handled in the same fashion as the droplet flow discussed in Section 5.4.7.

Model as Coded

The interfacial drag coefficient is given as:

$$\left[\qquad\qquad\right]^{a,c} \tag{5-118}$$

where $f_{iX,FF}$ is from Equation 5-117 and $A_{i,film}$ is calculated from Equation 4-64.

The interfacial drag is always calculated if a cold wall is present in the cell. If the cell void fraction is greater than [ ]^{a,c}, then the flow regime is a falling film regime with upward flowing entrained droplets. If the void fraction is below [ ]^{a,c} and the liquid flow is from the top, then the interfacial drag is ramped between the top deluge regime and the falling film regime. The top deluge interfacial drag coefficients will be discussed in Section 5.4.9.

Scaling Considerations and Conclusions

No major scaling issue was identified. The falling film flow regime was designed to simply approximate the behavior of the top quench front. The model is exercised as part of the assessment against prototypical rod bundle tests presented in Sections 14 and 15.

5.4.9 Top Deluge Flow Regime

Model Basis

When the walls are hot and a large amount of liquid flows downward into a computational cell, the flow regime is called the top deluge. This flow regime is similar to the liquid slug regime for upflow as discussed in Section 5.4.6. The top deluge regime is assumed present at void fractions less than [ ]^{a,c}. Physically, the top deluge regime could occur with large liquid injection rates in a PWR upper plenum due to upper plenum injection or upper head injection. The top deluge regime would also occur during blowdown when the core flow reverses and large amounts of liquid either drain out of the upper head or plenum and are forced into a hot core. PWR with combined injection, hot leg, and cold leg accumulators, where the hot leg accumulators inject large liquid flows in the upper plenum, could also experience the top deluge flow regime.

Model As Coded

The droplet drag coefficient is calculated as the maximum of:

$$C_{Dd} = \frac{24}{Re_v}\left[1.0 + 0.1 Re_v^{.75}\right] \tag{5-119}$$

where Re_v is the vapor Reynolds number in the cell based on local vapor properties; and:

$$\left[\qquad\qquad\right]^{a,c} \tag{5-120}$$

The interfacial drag coefficient for top deluge regime is calculated as:

$$K_{iX,v\ell,TD} = C_{Dd}\frac{\rho_v |\underline{U}_{v\ell}| A_{i,film}}{2}\frac{}{4} / \Delta X \tag{5-121}$$

where the interfacial area is given by Equation 4-66.

The low vapor fraction for this regime implies that the liquid is filling most of the channel. Note that the velocity used in Equation 5-121 is the relative velocity between the continuous liquid and the vapor, rather than the entrained liquid to vapor, since the liquid slugs are modeled by the continuous liquid field. Again, the model represents large liquid slugs or chunks which would nearly fill the channel and would capture any small droplets in the channel.

[

]^{a,c}

Scaling Considerations and Conclusions

The top deluge model is similar to the liquid slug model for upflow. The basic correlations that are used are scale dependent because they depend on the channel hydraulic diameter. However, models have been assessed against prototypical rod bundle tests as discussed in Sections 14 and 15.

5.5 VESSEL COMPONENT INTERCELL DRAG

Model Basis

WCOBRA/TRAC-TF2 calculates an additional interfacial drag force for interfacial shear that occurs at mesh cell boundaries. These interfaces are detected by changes in void fraction between adjacent cells, and can occur on either horizontal or vertical cell boundaries.

The intercell drag model is used to help calculate counter current flow limitation (CCFL) situations where there is liquid flowing downward against vapor upflow, as expected in the multi-dimensional downcomer

during refill for example. The intercell drag models are applied between channels where liquid can pool, such as on the top of the upper core plate in the reactor upper plenum, and channels representing vapor jets through holes in the upper core plate, for example. The intercell drag models will calculate a drag force on the pooled liquid in the adjacent cell as well as the reaction force on the vapor jet. The details of the model are given below.

For two cells, i and j, connected to each other by a vertical or lateral connection, an intercell interface is assumed when [ ]^{a,c}, so that cell i is on the vapor side of the interface and cell j is on the liquid side. The drag force is a function of the difference between the vapor velocity in cell i and the liquid velocity in cell j, and is given by:

$$F_{I,X} = f_i \frac{1}{2} \rho_v \left| \left(U_{v,i} - U_{\ell,j}\right) \right| \left(U_{v,i} - U_{\ell,j}\right) A_{I,X} \tag{5-122}$$

for the vertical direction and:

$$F_{I,Z} = f_i \frac{1}{2} \rho_v \left| \left(W_{v,i} - W_{\ell,j}\right) \right| \left(W_{v,i} - W_{\ell,j}\right) A_{I,Z} \tag{5-123}$$

for the lateral direction, where:

$$\left[\qquad \right]^{a,c} \tag{5-124}$$

In these equations $A_{I,X}$ and $A_{I,Z}$ are the appropriate intercell areas. The intercell interfacial force is added to the liquid momentum equation in cell j (on the liquid side of the interface) and subtracted from the vapor momentum equation in cell i (on the vapor side).

Model as Coded

The code logic checks [

]^{a,c} If such cells are identified, the code will calculate an intercell drag force. [

]^{a,c}

$$\left[\qquad \right]^{a,c} \tag{5-125}$$

where $\Delta\alpha_\ell$ is the difference in liquid fraction between adjacent cells. This difference is an estimate of the contact area between vapor and liquid at the cell interface. Since the absolute value is used, the area is always a positive number. The intercell drag force becomes:

[ ]a,c (5-126)

where $\Delta U_{i,j}$ is the difference between the vapor velocity in cell j and the liquid velocity in cell i, and is used as the relative velocity for the interfacial drag as given in Equation 5-122. This additional drag component will be added or subtracted depending on the cell void fraction. For the liquid rich cell, the interfacial force is added to the liquid momentum equation in that cell. For the adjacent vapor rich cell, this interfacial drag force is subtracted from the vapor momentum equation in the cell.

The code also checks for void differences on horizontal interfaces. In this case, the lateral velocity components are used for the liquid and vapor velocities. The interfacial area for the horizontal calculation is:

[ ]a,c (5-127)

where ΔZ is the lateral distance between the centerlines of the two adjacent cells. [

]a,c

Scaling Considerations

The intercell drag model has no direct scale dependence, but it can be noding dependent since the geometric areas, cell sizes, gaps, and interfacial areas are all directly used in the drag calculations. The use of a constant interfacial friction factor such as f_i = [ ]a,c simulates a rough surface for all Reynolds numbers of interest, and has an equivalent roughness of ϵ / D_h = [ ]a,c. This roughness would simulate surface waves which are roughly [ ]a,c of the pipe or channel hydraulic diameter. The use of this friction factor is an assumption which is verified by comparisons to experimental data. The experiments which can be used to confirm the intercell drag model are experiments such as the UPTF and Cylindrical Core Test Facility (CCTF) which measure liquid levels in the upper plenum above a simulated core plate. The results of these experiments are discussed in Section 19. To address the scalability question, the experiments are modelled in the same manner as the PWR such that the geometry effects, which enter the intercell frictional drag calculation, are preserved between the PWR and the experiments. Also, the UPTF used full-scale reactor hardware components such that this intercell frictional drag model was verified at full-scale.

Conclusions

The intercell drag model relationships can depend on the method of modeling critical areas where counterflow can occur. The modeling and noding technique used on the large scale systems tests, such as Loss-of-Fluid Test (LOFT), UPTF, CCTF, and others, is the same as is used for the PWR.

5.6 VESSEL COMPONENT ENTRAINMENT AND DE-ENTRAINMENT MODELS

5.6.1 Introduction

The drag between the vapor and continuous liquid results in either liquid entrainment, where the liquid moves from the continuous liquid field to the entrained liquid field due to the interfacial shear forces of the vapor acting on the liquid, or liquid de-entrainment caused by the entrained liquid interacting with the continuous liquid in the form of liquid film on structures. For liquid de-entrainment, the liquid moves from the entrained phase to the continuous liquid phase. The models for the different entrainment and de-entrainment mechanisms will be discussed below.

5.6.2 Entrainment in Film Flow

Model Basis

Entrainment of liquid drops from the continuous liquid phase can occur under a variety of conditions. The physical models used to determine the average net mass rate of entrainment and the entrained drop size will be different for each condition. Entrainment mechanisms that may have a significant influence on reactor thermal-hydraulics include entrainment from liquid films, reflood entrainment, entrainment resulting from vapor bubbling through liquid pools, and entrainment resulting from vapor flow across rod structures such as the upper plenum internals of a PWR.

The net mass entrainment rate is defined as:

$$S = S'''V \tag{5-128}$$

where V is the cell volume and S''' is the net entrainment rate per unit volume.

The net mass entrainment rate (S) has units of mass per unit time and is the net result of the opposing mechanisms of entrainment (S_E) and de-entrainment (S_{DE}). Models for the entrainment rate, de-entrainment rate, and drop formation size are discussed below.

In addition to the entrainment rate, the rate of change of interfacial area of the entrained liquid field must be determined for use in the interfacial area transport equation (Section 4). The rate of change of total droplet area due to entrainment and de-entrainment is:

$$\dot{A}_{i,E} = \frac{3S_E}{\rho_\ell r_{d,E}} - \frac{3S_{DE}}{\rho_\ell r_{d,DE}} \tag{5-129}$$

where $r_{d,E}$ is the radius of the entrained droplet, and $r_{d,DE}$ is the radius of the de-entrained droplet. $r_{d,DE}$ is assumed to be the cell average droplet diameter, while $r_{d,E}$ depends on the entrainment mechanism.

The contribution to droplet area resulting from droplet breakup mechanisms is also calculated. This term is calculated as:

$$\left[\qquad\qquad\right]^{a,c} \tag{5-130}$$

where S_{BR} is the mass flow of drops being broken, $r_{d,0}$ is the original drop size, and $r_{d,1}$ is the new drop size. This equation is derived in subsequent sections.

[

]^{a,c}

The void fraction at which a stable liquid film will exist depends on the flow channel size and the vapor velocity. The critical void fraction is determined from a force balance between the disruptive force of the pressure gradient over the crest of waves on the film and the restraining force of surface tension, as described in Section 4. The resulting expression for the critical vapor fraction is,

$$\alpha_{crit} = 1.0 - 2.0\sigma/(\rho_v |\underline{U}_{v\ell}|^2 D_h) \tag{5-131}$$

The critical void fraction is limited to a minimum value of [ ]^{a,c}, the value below which waves can be expected to bridge across the flow channel and cause a transition to churn flow. The interfacial geometry of the churn-turbulent flow is treated as a linear interpolation between bubbly flow and film flow. The flow is considered to consist entirely of bubbly flow as described above at a void fraction of [ ]^{a,c}, and entirely of film flow at the critical void fraction. Entrainment of liquid from the continuous liquid field into the droplet field is allowed in this flow regime. The entrainment rate is interpolated between 0.0 at a void fraction of [ ]^{a,c} to the full value given by the entrainment correlations at the critical void fraction. This provides a smooth transition into film or film mist flow. It should be noted that as long as the vapor velocity is sufficiently high to carry liquid drops away, the film mist flow regime will be maintained. This is consistent with Dukler's et al. (1979) explanation for the transition to film flow. This transition is predicted by the code based on the models used for the entrainment rate and interfacial drag between the vapor and drops.

Liquid entrainment is generated from the random perturbations in the flow which cause the development of a wavy interface on the film. These waves will grow as a result of the hydrodynamic and surface tension forces acting on the wave. Eventually the amplitude of the wave becomes so large that the

pressure differential over the wave exceeds the restraining force of surface tension, and the wave breaks toward the gas core. The resulting drops are then carried along with the vapor. The shape and size of the wave depends on whether the film flow is co-current or countercurrent. Lower-amplitude roll waves with drops being sheared off of the wave crest are typical of co-current flow (Ishii and Grolmes, 1975). Abrupt, large-amplitude waves are typical of countercurrent flow (Lovell, 1977). This may be partially attributed to the fact that higher vapor velocities are required to cause vertical co-current upflow. As a result, the film thickness and wave amplitudes are generally smaller than those found in countercurrent vertical flow, which occurs at lower vapor velocities. Also, in countercurrent flow the shear forces act in opposition to gravity, causing larger wave amplitudes.

In countercurrent flow, the entrainment rate (S_E) is taken to be [

$$\left[\right]^{a,c} \quad \text{a,c} \tag{5-132}$$

The critical liquid fraction is defined as:

$$\alpha_{\ell,crit} = (1 - \alpha_{crit}) \tag{5-133}$$

where α_{crit} is given by Equation 5-131.

It is assumed that all liquid in excess of that required for a stable film is removed from the film and enters into the entrained liquid phase, where it is treated as drops. In reality, some of this liquid may be in the form of waves which travel upward while the bulk of the film flows down. The gross flow split between the amount of liquid flowing down and that flowing up in the form of drops and waves is obtained by the above assumption.

For co-current film flow, Whalley et al. (1973) have correlated entrainment data with the parameter:

$$S_k = k_S \tau_i / \sigma \tag{5-134}$$

where k_S, the equivalent sand roughness, is used as the length scale for the entrainment force due to surface tension, and τ_i is the interfacial shear stress. Wurtz (1978) later modified the above correlation by multiplying it by the dimensionless velocity $|\underline{U}_v| \mu_\ell / \sigma$ to compare with a larger variety of data. This velocity was also used by Paleev and Filippovich (1966) to correlate air-water entrainment data. This resulting correlating parameter became:

$$S_u = \frac{k_s \tau_i |\underline{U}_v| \mu_\ell}{\sigma^2} \tag{5-135}$$

and was then used to obtain a relationship for the entrainment rate. This relationship is:

$$S_E = 0.41 S_u P_W \Delta X \tag{5-136}$$

where ΔX is the vertical dimension of the mesh cell and P_W is the wetted perimeter. This empirical correlation is used to determine the entrainment rate for co-current film flow. The equivalent sand roughness is given as:

$$k_s = [0.57]\delta + [6625.0\text{ft}^{-1}]\delta^2 - [3.56\text{x}10^6\,\text{ft}^{-2}]\delta^3 + [1.5736\text{x}10^9\,\text{ft}^{-3}]\delta^4 \qquad (5\text{-}137)$$

where δ is the film thickness and:

$$\tau_i = \frac{f_i}{2}\rho_v |\underline{U}_{v\ell}|^2 \qquad (5\text{-}138)$$

The interfacial friction factor (f_i) has been given with the interfacial drag models discussed in Section 5.4.4, and is calculated using [

]^{a,c}

The size of drops formed by entrainment from films has been characterized by Tatterson et al. (1977). Their results are used for both co-current and countercurrent flow. The drop formation radius is given by:

$$r_{d,E} = 0.0056\left(\frac{D_h\sigma}{\frac{f_s}{2}\rho_v |U_v|^2}\right)^{1/2} \qquad (5\text{-}139)$$

where f_s is defined in Equation 5-95.

Model as Coded

[

]^{a,c}

A modified relative velocity is calculated as:

[ ] a,c (5-140)

where α_ℓ is the average liquid fraction between adjacent axial cells J and J+1.

The entrainment rate is calculated by assuming that all liquid in excess of the liquid fraction when the film thickness is at its critical value (the critical liquid fraction calculated from Equation 5-133) is entrained. The entrainment rate is then calculated as the [ ]^{a,c}

[

]^{a,c} :

$$\left[\qquad\qquad\right]^{a,c} \tag{5-141}$$

where $\alpha_{\ell,crit}$ is calculated from Equation 5-131 using U_{Rl} :

$$\alpha_{\ell,crit} = 4C_1\sigma/\left(\rho_v U_{Rl}^2 D_h\right) \tag{5-142}$$

where [ ]^{a,c}

[

]^{a,c}

Scaling Considerations and Conclusions

The basis for these film entrainment models is small-scale experiments which isolate each phenomenon. The entrainment rate formulation given by Equation 5-141 is mesh cell length dependent. However, this dependence reflects the length of the surfaces with films which are generating the entrained liquid. Other parameters in the entrainment model given in Equation 5-141 are local flow, interfacial friction, and the channel geometry. Sources of verification of the film entrainment model are the UPTF emergency core cooling (ECC) bypass tests. In these experiments, the walls were cold and had liquid films from which entrainment could be generated. Also, these experiments had co-current flows as well as countercurrent flows. The UPTF experiments were full-scale, so there were no scaling distortion effects. These experiments and the calculated results are reported in Section 19.

5.6.3 Entrainment During Bottom Reflood

Model Basis

This model is available for channels with heated structures only. When the cladding temperature is above the surface rewetting temperature, a film boiling heat transfer mechanism will be established. This may correspond to either a dispersed flow regime or an inverted-annular, two-phase flow regime, depending upon the liquid content of the flow, the liquid subcooling, and the vapor velocity. As the cladding temperature is reduced because of the cooling provided by film boiling, the cladding will enter a transition boiling, and finally a nucleate boiling regime. High flow rates of superheated vapor result from the steam generated as the rods are quenched. Vapor velocities are usually high enough to entrain

significant fractions of the liquid in the form of drops. This droplet entrainment is beneficial since it enhances heat transfer downstream of the quench front by de-superheating the steam and contributing to the total steam flow rate as the drops evaporate.

Several mechanisms for the formation of droplets during reflood can be postulated. The droplets may be formed by the breakup of the inverted annular liquid core because of surface instabilities if the liquid is subcooled. If the liquid is saturated, droplets may be formed by bubbles breaking through the surface of the liquid.

In COBRA/TRAC and WCOBRA/TRAC-TF2, the entrainment rate is given (Thurgood et al., 1983) by:

$$S_E = (\alpha_v U_v / U_{crit})^2 \dot{m}_v \tag{5-143}$$

where $\dot{m}_v$ is the vertical vapor mass flow rate and U_{crit} is the vertical vapor velocity required to lift a droplet, with radius defined by the critical Weber criterion against gravity. The critical velocity is obtained from a balance between the drag force and gravity force acting on the drop,

$$U_{crit} = \left(\frac{4We_d}{3C_{Dd}} \right)^{1/4} \left(\frac{\sigma g \Delta\rho}{\rho_v^2} \right)^{1/4} \tag{5-144}$$

A Weber number of [ ]^{a,c} (typical of reflood in the FLECHT tests) and a droplet drag coefficient of [ ]^{a,c} are used. The use of the vapor flow rate, $\dot{m}_v$, in Equation 5-143 reflects the effect of vapor generation at the quench front on droplet formation.

In Kataoka (1983), models for entrainment from pools were developed, and several correlations were presented. Entrainment is defined as:

$$E = \frac{\rho_\ell j_{\ell e}}{\rho_v j_v} \tag{5-145a}$$

where the entrainment ' E ' was expressed as the ratio of the mass flux of the entrained droplets to the mass flux of the gas. Kataoka and Ishii noted that E depends on the gas flux and the height above the top of the liquid pool. For a given height above the pool, the entrainment was reported as proportional to the gas flux as:

$E \propto j_v$ for low gas flux

$E \propto j_v^{3-4}$ for intermediate gas flux

$E \propto j_v^{7-20}$ for high gas flux

Equation 5-145a can be recast and written in terms of Kataoka and Ishii's definition for entrainment as,

[ ]a,c (5-145b)

This shows that the entrainment model in WCOBRA/TRAC-TF2 for bottom reflood is proportional to j_v^2, and is consistent with the work by Kataoka and Ishii for low gas flux. For reflood, with high vapor generation, the high and intermediate gas flux regimes are likely. What this implies, is that the WCOBRA/TRAC-TF2 model has a weaker dependence on j_v than should be expected.

In addition, Kataoka and Ishii provide information that suggests that the upper limit of 4.0 in the as-coded original expression may be too restrictive at low pressure. Kataoka and Ishii give:

$$E = 0.00484 \frac{\Delta\rho}{\rho_g} \tag{5-145c}$$

as appropriate for an upper limit on entrainment. This becomes greater than 4.0 below about 30 psia and increases rapidly with lower pressures. Thus, even if there is sufficient vapor flow at low pressure, the 4.0 upper limit could impose too low a limit on the entrainment.

The work by Kataoka and Ishii resulted in two modifications to the prior WCOBRA/TRAC model that would increase entrainment. First, the exponent of the αU_v term should be increased from 2 to something higher. Second, the upper limit of 4.0 could be increased, which would allow more entrainment at low pressure. The final expression for bottom reflood entrainment used in WCOBRA/TRAC-TF2 is the same as that for WCOBRA/TRAC:

[ ]a,c (5-145d)

[

]a,c

The droplet formation diameter for bottom reflood entrainment is taken as:

[ ]a,c (5-146)

where:

[ ]a,c (5-147a)

and

[ ]a,c (5-147b)

where:

W_e = 7.5

The droplet size Equations 5-147a and 5-147b are estimates of the reflood droplet size based on FLECHT data. Equation 5-147a is based on an equation originally developed for the BART code (Young et al., 1984); and then adapted to an earlier version of the vessel model called COBRA-TF, which was then used to assess FLECHT tests (Paik and Hochreiter, 1986). In the BART code, the initial droplet size is defined by (after combining Equations 2-115 and 2-71 in Young):

[ ]a,c (5-147c)

This equation was simplified by using a hydraulic diameter which was an average of the "large" and "small" Westinghouse fuel rod designs. The following table shows rod pitch, rod diameter, and hydraulic diameter for 15x15 and 17x17 fuel (the same geometry was used in FLECHT COSINE and FLECHT SEASET), and the average of the two.

Array Type	Rod Pitch (in)	Rod Diam (in)	D_h (ft)
15x15	0.563	0.422	0.0334
17x17	0.496	0.374	0.0386
		AVERAGE D_h:	0.036

If the averaged value of D_h is used in Equation 5-147c, and is combined with the constant, the value [ ]^{a,c} is obtained, which compares with the value coded of [ ]^{a,c}. This equation is also used in Paik and Hochreiter (1986), Equation 2-50, the only difference being that the g term is also combined with the constant: [ ]^{a,c}, which compares with the reported value of [ ]^{a,c}.

The simplification of using an average hydraulic diameter, while unnecessary, reflects the fact that the scatter in droplet diameters is such that the effect of hydraulic diameter cannot be discerned over the narrow range of interest.

Equation 5-147b uses the Weber number criterion to establish the maximum droplet size which can be entrained.

The liquid which is being shattered into drops is assumed to be suspended above a pool through which vapor is flowing at a flux j_v $(=\alpha U_v)$. The relative velocity between the vapor and the liquid above the pool is therefore the vapor velocity above the pool, which is approximated by j_v.

The droplet size data is tabulated in Lee et al., (1982). The droplet size data ranges from 0.002 to 0.006 feet. When the data was plotted against droplet velocity, no clear trend was observed. The various equations, and the minimum allowed value from Equation 5-146 are compared to this data range in Figure 5-6a for 40 psia. Equation 5-147a estimates the midpoint of the data range, and includes a pressure effect through the vapor density. Equation 5-147b assures that if vapor volumetric flux is high, the predicted droplet size approaches the minimum of the range. A second comparison at 20 psia is shown in Figure 5-6b.

Near the quench front, the measured droplet size was somewhat larger, with a minimum value of 0.0033 ft. This value is used as a lower bound in Equation 5-146 for bottom reflood.

Model as Coded

Entrainment due to bottom flooding is assumed if the flow regime in the cell is a hot wall regime, and if the vapor velocity in the cell is upward.

Equation 5-145d is evaluated as follows:

[[ ] a,c (5-148)

[

]a,c

[

]a,c

The value of U_Γ is given by

[ ] a,c (5-149)

Where A_x is the cell momentum area in the axial direction and Γ_v (Equation 6-101) is the cell vapor generation rate and $Q_{w\ell}$ and Q_b are the heat flow from wall to liquid and the subcooled boiling heat flow, respectively (Section 7.2).

A further check on the entrainment is made by calculating a minimum velocity needed to lift a droplet upward against gravity. In this case, the minimum vapor velocity is given as:

[ ]^{a,c} (5-150)

where the drop diameter is given in Equation 5-146 and is the minimum of these choices. The droplet drag coefficient is [ ]^{a,c} in Equation 5-150. If the vapor velocity is less than [ ]^{a,c} times $U_{v,min}$, then the entrainment rate calculated in Equation 5-148 is modified by:

[ ]^{a,c} (5-151)

[

.]^{a,c}

Equation 5-151 gives the incremental amount of entrained liquid which should be added to the entrained liquid field in the cell. Once the flow is entrained, the droplet drag relationships discussed in Section 5.4.7 will convect the entrained droplets axially as well as in the transverse directions.

Scaling Considerations and Conclusions

The basic model formulation for entrainment has no scale dependent parameters, and the droplet Weber numbers given in Equations 5-144 to 5-147c come from high speed movies of FLECHT reflood experiments which were performed using prototypical geometries, flow, pressures, and powers. However the calculated entrainment rate has shown some node size dependency. The impact of such dependency is minimized by replicating the noding scheme used for the code assessment presented in Section 15 in the simulation of the PWR.

5.6.4 Entrainment During Top Down Reflood

Model Basis

There are two mechanisms for entrainment in top down reflood, upper plenum injection, or top spray situations. The first mechanism is the breakup of pooled liquid films on reactor internal hardware as the liquid falls through holes, slots, or slits in the hardware, into the core. The second mechanism is entrainment from falling films at the top quench front where the film flow exceeds the quench rate of the rod and the excess liquid is sputtered off the hot surface. The model for entrainment from the top down quench front will be discussed first.

When the top ends of a fuel or heater rod quench, a quench front moves down the rods by axial conduction. A liquid film follows the quench front down the rods toward the sputtering or quench front. It is assumed that the entrainment rate from a falling film top quench front is equal to the liquid film flow rate reaching the quench front, $(\dot{m}_\ell)$, minus the vapor generation rate at the quench front,

$$S_E = \dot{m}_\ell - \Gamma_q''' \cdot V \tag{5-152}$$

Droplets are assumed to be generated at the sputtering front (quench front) with a drop size which is selected as:

a,c

[ ]

(5-153)

The falling liquid film behavior is handled using the models previously discussed in Section 5.4.8 for both vertical and lateral flow. The droplet behavior is handled using the dispersed droplet models for vertical and lateral flow discussed in Section 5.4.7.

The model for the breakup of pooled liquid films is discussed next.

The drop size model for the sputtering quench front is based on top spray heat transfer experiments, typical of a boiling water reactor (BWR). When Westinghouse began analysis of the Westinghouse G-2 refill experiments (Hochreiter et al., 1976), which were low pressure rod bundle film boiling experiments with significant liquid injection into the upper plenum, it was found that the entrained droplet size, using a

sputtering front model, would yield drops which were too small, resulting in excess over cooling compared to the G-2 test data.

When examining the tests and the code predictions, it was felt that the main reason for the higher predicted heat transfer was the drop size the code was choosing. The flows in these experiments were sufficiently small that the injected water would de-entrain, pool and fall, or be forced through the upper fuel nozzle simulator which was a plate with several small diameter holes. This plate was designed to be hydraulically similar to a PWR top fuel nozzle plate.

It was felt that the dominant drop size which would fall through the rod bundle would be determined from drops which were formed at the fuel nozzle simulation plate or top spacer grid as the liquid fell or was forced through the holes in the plate. Therefore, a drop size model was developed to calculate the size of droplets which would be formed as the liquid flowed through hardware at the top of the fuel assembly into the heated portion of the core. Wallis (1969) presented a model for a single drop falling through an area restriction, or orifice. For liquid velocity less than the critical velocity derived from Equation 9.8 of Wallis (1969),

$$V_{L,LIM} = \frac{2.5}{D_h}\left(\frac{\sigma^3}{\rho_\ell^2 g(\rho_\ell - \rho_v)}\right)^{\frac{1}{4}} \tag{5-154a}$$

Equation 12.1 of Wallis (1969) is used to estimate the drop diameter.

$$\frac{D_d}{2} = \left(\frac{\sigma(D_h/2)}{g(\rho_\ell - \rho_v)}\right)^{\frac{1}{3}} \tag{5-154b}$$

For liquid velocity greater than this limit, the liquid will form an unstable liquid jet which breaks up to form drops with a radius equal to:

$$r_{OR} = 1.9R_o \tag{5-154c}$$

from Wallis, Equation 12-3,

where:

r_{OR} = the drop radius formed from the liquid jet as the water flows through the orifice, and

R_o = the radius of the orifice plate or hole size

For plates which have multi-hole geometries such as the G-2 top fuel nozzle simulation, a PWR top fuel nozzle core plate, or a top spacer grid, this formulation was generalized to:

$$D_{OR} = 1.9D_h \tag{5-155}$$

where:

D_{OR} = the droplet diameter formed at the orifice or area reduction, and

D_h = the hydraulic diameter which characterizes the plates or hardware where the liquid pools and flows through

Again, the above formulation is valid for situations in which the vapor-to-liquid velocities are small, such that there is small interfacial shear on the liquid as it flows through the area reduction or orifice.

If the liquid flow is being accelerated through the plate holes by steam, there is a possibility that the liquid will be shattered into smaller drops by the large relative liquid and vapor velocities. The dimensionless group which describes the largest stable droplet size to be formed under these conditions is the Weber number given as:

$$We_{crit} = \frac{\rho_v (U_v - U_\ell)^2 D_{OR}}{\sigma} \tag{5-156}$$

Experiments have shown that $We_{crit} \cong 12$ for this situation (Wallis, 1969).

In a situation where there is top down flooding with a top quench front, two different drop sizes will be calculated: the large drops which are generated from the hardware at the top of the rod bundle with drop sizes calculated with Equation 5-155, and drop sizes generated at the quench front which are calculated using Equation 5-153. The drops from the hardware will flow down into the channel between the heated rods, while the smaller drops will sputter off the heated surface into the channel flow area. It is assumed that these drops can be treated as a single droplet field of average diameter as determined by the interfacial area transport equation. The large drop sizes, which are generated from the hardware, will dominate so that the resulting drop size is closer to the large hardware generated drops, not the very small sputtering front drops. The model then represents the sweeping up of the smaller drops, or the coalescence of the smaller drops by the large droplets in the channel. The effect of this model for top down flooding is to reduce the interfacial area between the liquid and vapor such that reduced interfacial heat transfer occurs, the steam superheats to higher temperatures, and the overall heat transfer from the heated surface decreases.

The above models are used for downflow at void fractions above $\alpha_v \geq [\quad]^{a,c}$.

Model as Coded

For the entrainment from the sputtering front the code calculates the maximum liquid available for entrainment as given in Equation 5-152 as:

$$\left[\quad\right]^{a,c} \tag{5-157}$$

where $\alpha_{\ell,J+1}$ is the upstream cell liquid fraction, $\dot{m}_{X,\ell,j}$ is the liquid downflow, and $\alpha_{\ell,j}$ is the averaged liquid fraction between the current cell and the donor cell.

This is further modified by comparing the void fraction for the liquid film to the critical liquid void fraction for a stable liquid as:

[ ]a,c (5-158)

The coding logic chosen for the top down flooding droplet size model chooses a maximum droplet size as specified in Equation 5-153. [

]a,c

For the breakup of pooled liquid films, the code examines changes in the momentum area along the channel to determine if the drop size should be recalculated with the drop orifice equation given in Equation 5-155. For momentum area changes greater than [ ]a,c, the drop size is recalculated using the hydraulic diameter in the reduced area channel. Fuel rod grid locations are also checked to see if the grid area reduction is significant relative to the channel area, and the drop size can be calculated at the grid locations using the grid hydraulic diameter.

For the orifice droplet equation, drops are assumed to be formed by the reactor hardware where an area reduction of greater than [ ]a,c occurs. [

]a,c

That is:

[ ]a,c (5-159)

If a grid exists in the cell, the incoming drop size is compared to that calculated with Equation 5-155 using the grid hydraulic diameter, and the minimum drop size is used.

That is:

[ ]a,c (5-160)

The rate of change of the interfacial area due to the droplet diameter change is given as:

$$\dot{A}_{i,OR} = \frac{dA_i'''}{dt} A_X \Delta X \quad (5\text{-}161)$$

where A_i''' is the interfacial area/volume. Equation 5-161 can be approximated as:

[ ] a,c (5-162)

[ ]a,c

The interfacial area upstream of the restrictive plate is:

[ ] a,c (5-163)

where:

N_d = the number of drops/volume, and
D_{UP} = the drop size upstream of the plate

The plate will reform the drops with a new drop diameter given from Equations 5-159 or 5-160, depending on whether the plate or grid is more limiting. The interfacial area downstream of the plate or grid is:

[ ] a,c (5-164)

where D_{OR} is the new drop size, and $N_{d,new}$ is the new number of droplets. The volume of drops are preserved such that the new number of drops becomes:

[ ] a,c (5-165)

The interfacial area change across the plate or grid then becomes:

[ ] a,c (5-166)

or:

[ ] a,c (5-167)

However, the entrained void fraction upstream of the plate or grid is:

[ ]a,c (5-168)

Substituting Equation 5-168 into Equation 5-167, the interfacial area change becomes:

[ ]a,c (5-169)

The rate of change of interfacial area from Equation 5-162 then becomes:

[ ]a,c (5-170)

which is programmed as:

[ ]a,c (5-171)

for downflow.

[

]a,c

A further test is used on the calculated drop size (D_{OR}) for large drops. [

]a,c

becomes:

[ ]a,c (5-172)

The model described above causes entrained droplets flowing through the orifice plate to change size. Continuous liquid flowing through the orifice is also assumed to be completely entrained into the droplet field. This is done by calculating an orifice entrainment rate as:

[ ]a,c (5-173)

where $\alpha_{\ell,J}$ is the upstream cell liquid fraction. The droplet size associated with this entrainment is D_{OR}, calculated from Equation 5-159 or 5-160.

Using Equation 5-129, the contribution to the entrainment interfacial area density change is:

[ ]^{a,c} (5-174)

This equation assumes that, in a cell containing an orifice plate, entrainment from all sources leads to drops of size D_{OR}.

The interfacial area shifts to a larger or smaller value depending on the drop size generated by the models described above. If drops generated in the cell are one half the original size or smaller, this is reflected in the interfacial area source term as an increase in the interfacial area. This increase in area will usually improve the interfacial heat transfer in a dispersed flow situation by de-superheating the steam temperature such that the wall is exposed to a lower sink temperature.

The above model and approach are for downflow. The code logic is applied in the dispersed flow film boiling regime, [ ]^{a,c}. The interfacial area generation term is added to other sources of interfacial area generation as a source term for the total interfacial area transport equation, which is solved for the next time step.

Scaling Considerations

No scaling dependency was identified in the development of the falling film entrainment model. This model is used for all reflood and blowdown situations and has been verified on full-length heated rod bundles with prototypical dimensions and rod arrays, such that there should be no scaling effects. The droplet entrainment model for top down flooding uses a generalized Wallis orifice droplet formulation which models the complex flow passages with a hydraulic diameter. This model has been validated against the G-1 blowdown data as described in Sections 14 and 15. This model generalizes the Wallis equation and uses the hydraulic diameter of the structure as the dimension to set the droplet diameter for the entrained flow coming into the core from the upper plenum. Using the hydraulic diameter will permit the modeling of all the wetted surfaces and flow passages found in the complex upper core plate, top fuel nozzle, and spacer grids. Normally either the top nozzle or the top most spacer grid is limiting and results in the smallest droplet diameter being formed. This particular model will set the initial drop size entering the bundle. The drops can be further broken up by the grids as they are accelerated down through the bundle.

Conclusions

The generalization of the Wallis orifice equation for drop formation has been verified on several different hardware geometries which are similar to real PWR hardware. The G-1 blowdown experiments use prototypical Westinghouse mixing vane and non-mixing vane grids, and a fuel assembly tie plate similar to an actual fuel assembly. The CCTF tests use hardware which is also similar to actual PWR fuel assembly components.

5.6.5 Spacer Grid Droplet Breakup Model

Model Basis

Spacer grids are structural members in the reactor core which support the fuel rods at a prescribed rod-to-rod pitch. Fuel assemblies may have grids at different elevations across the core. Because the grids are modeled explicitly at their physical elevations, flow bypass or flow redistribution are taken into consideration by the code. Since the grid reduces the fuel assembly flow area, the flow is contracted and accelerated, and then expands downstream of each gridded layer in the core. As the flow is accelerated within the grid and then expands downstream, it reestablishes the thermal boundary layers on the fuel rod, which increases local heat transfer within and downstream of the grid.

Several single-phase experiments clearly showed that the continuous phase heat transfer downstream of a spacer grid can be modeled on entrance effect phenomena where the abrupt contraction and expansion result in establishment of a new thermal boundary layer on the heated surface downstream of the grid. This entrance effect heat transfer decays exponentially downstream of the grid, and the local Nusselt number decreases exponentially downstream of the grid. The enhancement of the convective heat transfer is described in Section 7.2.7.

When the flow is a two-phase dispersed droplet flow, characteristic of a calculated PWR blowdown or reflood, the grids can promote additional heat transfer effects. Since the grids are unpowered, they can quench before the fuel rods. If the grids quench, they can create additional liquid surface area, which can help de-superheat the vapor temperature in the non-equilibrium two-phase droplet flow. A wetted grid will have a higher interfacial heat transfer coefficient compared to the droplets, since the relative velocity for the vapor flow relative to the liquid film is larger. The models accounting for the wetted grid effect are described in Section 6.2.10.

In addition to grid rewetting, the grids can also cause shattering of the entrained droplets into smaller, more easily evaporated droplet fragments. The evaporation of the smaller shattered droplets provides an additional steam source, which decreases the stream superheated temperature and also increases the convective heat transfer coefficient. This section describes how the droplet breakup at grids is accounted for in WCOBRA/TRAC-TF2.

Wachters and Westerling (1966) studied drops impinging on a plate and classified the droplet fragmentation in terms of the perpendicular Weber number:

$$We_d = \frac{\rho_\ell D_0 U_p^2}{\sigma} \tag{5-175}$$

where U_p is the drop velocity perpendicular to the plate and D_0 is the incoming drop size. Extensive experiments were also performed by Takeuchi et al. (1982) on droplets normally impacting on a hot plate. Liquid deforms as a circular sheet, then disintegrates into fine droplets. The splashed droplet diameter was also reported as a function of the droplet's perpendicular Weber number.

Since the grid thickness is usually less than the droplet diameter during a typical reflood transient, the impact phenomena for a droplet on a grid should be different from that found by Wachters (1966) and Takeuchi (1982). From movies of reflood tests conducted by Japan Atomic Energy Research Institute (Okubo and Sugimoto, 1984), the entrained droplets were clearly observed to break into finer sizes after impaction on the grid structure. However, no further study was performed on droplet breakup phenomena. Experiments which concentrated on the study of the droplet impingement on the spacer grid can be found from the tests conducted by the Central Electricity Generating Board (CEGB) of the United Kingdom, (Adams and Clare (1983, 1984)), by S. L. Lee et al. (1982, 1984a,b) at the University of New York at Stony Brook, and by Yao, Hochreiter, and Cai (1988) from Westinghouse/Carnegie-Mellon University.

When an entrained droplet impacts on the grid strap, the droplet is split into two liquid sheets flowing along each side of the grid strap, as shown in Figure 5-7(a). Detailed photographic studies from the above references indicated the mass and the trajectory angle of the split liquid sheet varied with the impact conditions, such as the incoming drop velocity, grid strap-to-droplet thickness ratio, and the degree of asymmetry between the droplet and grid center. For a high velocity droplet impacting on a wide grid, the resulting trajectory angle is large, which results in significant generation of microdrops. A low velocity droplet impacting on a thin grid will be sliced into two liquid sheets which reform into two large drops with very few micro drops being generated. For high velocity droplets the splashed liquid sheet expands and a cylindrical rim forms at the free edge of the liquid sheet. The cylindrical rim was observed to be a source of small droplets. A thinner liquid sheet will generate finer droplets. Based on these observations, the size of broken droplets should be a function of two major dimensionless parameters, namely the droplet Weber number (We_d) as defined in Equation 5-175 and the ratio of grid thickness to incoming droplet diameter w/D_0.

The droplet off-set parameter, Δ defined in Figure 5-7 (b), was also reported by Yao, Hochreiter, and Cai (1988) as a parameter affecting the size of the generated small droplets. However, the off-set parameter can be absorbed in the parameter w/D_0 and the break-up efficiency in the droplet break-up correlation to be described below.

Following the first impact, the shattered droplets will either flow away with the steam and provide some grid cooling by film boiling if the grid is non-wettable, or help in quenching of the grid and formation of a liquid film on the grid surface if the grid is wettable. If a liquid film is formed, new drops may be generated through entrainment mechanisms either from the liquid film on the grid or from the liquid sheet flowing away from the trailing edge of the grid. Adams and Clare (1984) also observed that the drop size entrained from liquid sheets flowing away from the trailing edge of a wetted grid is similar to the drop size before the impact, which is consistent with the WCOBRA/TRAC-TF2 film entrainment model for quenched grids. It is concluded that the small droplet formation occurs primarily at the first impact rather than from subsequent droplet entrainment off the grid.

The leading edge of a wetted grid may be covered by a thick film, if the local vapor velocity is low, or a thin film if the local vapor velocity is high enough to push the liquid film upward (Figure 5-7c). The droplet breakup mechanism is expected to be different in these two situations. Droplet breakup into sizes significantly smaller than the incoming droplet size was observed to occur at droplet Weber numbers of 80 or higher (Yao, Hochreiter, and Cai, 1988, Figure 11). This Weber number corresponds to a droplet velocity of approximately 15 ft/s; the minimum vapor velocity for droplet breakup is therefore expected

to be 25 ft/s or greater, which, in addition to evaporation of the liquid to superheated steam, would lead to a thin film on the grid. This likely situation is further supported by measurements in Lee et al. (1982) which indicated that the shattered droplets were of similar size whether the grid was wet or dry. In the case of a wet grid with a thin film or a dry grid, the droplet breakup mechanism was found to result primarily from the impact of the droplet on the grid leading edge. In experiments by Yao, Hochreiter, and Cai (1988), the leading edge condition for the wet grid cases was similar to the thin film case (Figure 5-7c), since the test was designed to let the droplets fall onto the grid. The film would then drain from the grid strap away from the leading edge.

The broken small droplets measured by Lee et al. (1982, 1984a,b), either with dry grid or wet grid were found to be of similar size, supporting the conclusion that a thin film covers the grid. Yao, Hochreiter, and Cai also observed that the small droplet sizes under a cold grid impact were only slightly larger than that when the grid was hot. In the test by Yao, Hochreiter, and Cai, since the droplet was falling downward, the leading edge condition for both cold grid and hot grid for high vapor velocity were very close to that shown in Figure 5-7c. The leading edge impact is the most important break-up mechanism; the drop size distributions for either cold or hot (i.e., wet or dry) grids should be similar since the condition of the leading edges are similar.

As the entrained droplets impact a grid spacer, some may pass through without contact while some will impact on the grid structure. The droplets which impact on the grid will be broken into many or few microdrops depending on how the drop hit the grid. The size of the shattered droplets is represented by the following formula:

[ ]^{a,c} (5-176)

[

]^{a,c}

D_{small} is the Sauter mean diameter of the shattered drop, D_0 is the diameter of incoming drop, and w is the grid strap width.

The correlation given by Equation 5-176 is a refinement to earlier models which reflects the effects of different grid thickness to droplet diameter ratios at high Weber numbers. [

]^{a,c}

[

]^{a,c}

Model as Coded

WCOBRA/TRAC-TF2 has the coding and input logic to locate the grid structure within the core channels for any PWR fuel design. Once the grid is located, the drop size approaching the grid is calculated from the entrained flow and the droplet number density in the upstream cell,

$$D_d = \frac{6\alpha_e}{A'''_{i,d}} \tag{5-177}$$

If the calculated drop size from Equation 5-177 is less than [ ]^{a,c} feet in diameter, the drops are not allowed to be further broken up by the grids and the grid droplet logic is bypassed. A droplet Weber number is calculated for the incoming droplets in the cell using Equation 5-175. If the droplet Weber number is less than [ ]^{a,c}, it is assumed that the drops do not have sufficient inertia to be broken-up by the grids and the grid logic is bypassed. For droplet Weber numbers greater than [ ]^{a,c}, the droplet breakup model given in Equation 5-176 is used to calculate the shattered drop-to-incoming-drop ratio after the drops pass though the grid. This ratio is then used to calculate the small droplet diameter after passing through the grid, by multiplying the calculated droplet ratio by the incoming droplet diameter.

The rate of change of the interfacial area due to the droplet breakup is given as:

$$\dot{A}_{i,GR} = \frac{dA'''_{i,d}}{dt} A_X \Delta X \tag{5-178}$$

where $A'''_{i,d}$ is the interfacial area/volume.

Equation 5-178 can be approximated as:

$$\left[\qquad \right]^{a,c} \tag{5-179}$$

where $\Delta A'''_i = A'''_{i_{new}} - A'''_i$ is the change in the interfacial area.

The interfacial area upstream of the grid is:

$$A'''_{i,d} = \pi D_d^2 N_d \tag{5-180}$$

where:

N_d = the number of drops/volume

D_d = the drop size upstream of the grid and is determined from the interfacial area transport equation, described in Section 4

The grid will shatter a fraction of the drops which impact the grid. The drop volume is preserved such that if a fraction (F_s) of the drops are shattered, the number of new small drops are given as:

[ ] a,c (5-181)

such that the new interfacial area downstream of the grid is:

[ ] a,c (5-182)

The change in the interfacial area $\Delta A_i'''$ is calculated by using Equation 5-182 and subtracting Equation 5-180 as:

[ ] a,c (5-183)

but:

[ ] a,c (5-184)

such that by substituting Equation 5-184 into Equation 5-183, and then putting the result into Equation 5-179, the rate of change of the interfacial area becomes:

[ ] a,c (5-185)

Equation 5-185 is programmed as:

[ ] a,c (5-186)

The value of F_S is [

]^{a,c}. This area is input and depends on the grid design and the fuel type.

Unlike the orifice breakup model, only the entrained droplet field is considered for breakup through grids. This is because the grid droplet breakup mechanism occurs only in dispersed droplet flow in the hot wall regime.

Scaling Considerations

The grid droplet breakup model is a basic model which accounts for the physical geometry of the fuel assembly spacer grids and is not scale dependent. However, the droplet breakup model is empirical and does depend upon the specified geometry of the spacer grid in the fuel assembly. The grid droplet breakup model development was based on droplet size data which is characteristic of PWR reflood situations as well as prototypical spacer grid structures. The total model was verified by comparing the resulting film boiling heat transfer in rod bundles for different types of spacer grids. In particular, the Flooding Experiment with Blocked Arrays (FEBA) experiments were modeled with and without a mid-plane spacer grid, the FLECHT and FLECHT-SEASET experiments were modeled using simple egg-crate spacer grids, and the G-1 and G-2 blowdown and reflood experiments were modeled using 15x15 and 17x17 Westinghouse production mixing vane grids. Inclusion of the spacer grid droplet breaking model improved the WCOBRA/TRAC-TF2 predictions of these experiments. These experiments were all based on full-length with prototypical rod array geometries and grids.

Conclusions

A droplet breakup model for spacer grids has been developed to represent the actual effects of the grids on the entrained two-phase flow at high void fractions, $\alpha_v \geq$ [ ]^{a,c}. The model has been verified against a range of full-length rod bundle experiments with prototypical geometries and different grid designs in blowdown and reflood situations.

5.6.6 De-entrainment in Film Flow

Model Basis

Liquid film flow can exist on any structural surface which is in the wetted wall regime, such as the reactor upper plenum structures, vessel wall, core barrel wall, the ends of the fuel rods which are quenched, and other structures.

The deposition of entrained drops on this liquid film occurs as a result of random turbulent motions that impart transverse velocity to the drops, bringing them into contact with the solid surfaces or liquid films within the flow channel. The rate at which this occurs has been correlated by Cousins et al. (1965) using a drop concentration gradient diffusion model in which the concentration at the wall is assumed to be zero. Cousins' model is used to determine the de-entrainment rate for film flow as:

$$S_{DE} = k_\sigma \Delta C P_w \Delta X \qquad (5\text{-}187)$$

where:

k_σ	=	the mass transfer coefficient
P_w	=	the wetted perimeter
ΔX	=	the cell height

and where ΔC is the concentration gradient for the channel as given by:

$$\Delta C = \frac{\alpha_e \rho_\ell}{\alpha_e + \alpha_v} \tag{5-188}$$

The mass transfer coefficient, (k_σ), has been found to be a function of surface tension (Whalley, 1973). This function is represented by:

$$k_\sigma = \text{maximum}\begin{cases} 3.0492\left(10^{12}\right)\sigma^{5.3054} \\ 12.491\sigma^{0.8968} \end{cases} \tag{5-189}$$

and is compared with the Whalley data in Figure 5-9.

The de-entraining flow is assumed to carry with it droplets of average size as calculated from the cell interfacial area transport equation (Section 4.3.7).

Model as Coded

[

]^{a,c}

[

]^{a,c}

The mass flow of de-entrained droplets goes into the liquid film flow field. The de-entrainment rate also is reflected as a loss of interfacial area in the interfacial area transport equation discussed in Section 4.3.7, using Equation 5-129.

Scaling Considerations and Conclusions

The de-entrainment model, as developed from small scale data, does have the surface geometric effects directly included in the formulation through the wetted perimeter and the cell length. The use of the cell length can make the model noding sensitive. The droplet de-entrainment is most critical for ECC bypass calculations and reflood calculations since de-entrainment can represent liquid mass that is retained in the reactor vessel. The model was assessed against full scale UPTF data as discussed in Section 19.

Applicability to the PWR is ensured by applying the same noding strategy in modeling the full scale test facility and the PWR.

5.6.7 Crossflow De-entrainment

Model Basis

Entrained liquid carried into the reactor upper plenum during reflood can de-entrain on the reactor structures as the two-phase mixture flows across these structures and out of the hot legs of the reactor. This cross flow de-entrainment will result in creating liquid films on the structures which can flow downward to create a liquid pool at the horizontal upper core plate.

The model used in the code employs de-entrainment fractions obtained in the upper plenum de-entrainment experiments of Dallman and Kirchner (1980) where:

$$S_{DE} = \eta_{NR}\alpha_e\rho_\ell|U_e|L_g\Delta X \tag{5-190}$$

The de-entrainment fraction (η_{NR}) is user input and depends on the reactor design. Following the recommendations of Dallman and Kirchner (1980) the de-entrainment fraction for an array of tubes is given by:

$$\eta_{NR} = 1-(1-\eta_R)^N \tag{5-191}$$

with:

$$\eta_R = \eta_I(1+4.5\beta^2) \tag{5-192}$$

from Chen (1955) where:

η_R = the de-entrainment fraction for a single row of tubes

N = the number of rows of tubes

β = the diameter-to-pitch ratio of the array

η_I = the de-entrainment fraction for a single tube (0.19 for cylindrical tubes and 0.27 for square tubes)

In the reactor situation, the square cross section tubes represent control rod guide tube structures while the circular tubes represent support column structures.

The experiments performed by Dallman and Kirchner were for air/water flows and a single structure (either a cylinder or square tube). There were cylindrical structures of different sizes examined, ranging up to ~4.0 inches in diameter, with variations in air and droplet velocities. These authors obtained the

single structure de-entrainment data for cylinders or square tubes, which is the basis for Equation 5-192. They examined the effects of the droplet Weber number defined as:

$$We_d = \frac{\rho_\ell U_d^2 D_d}{\sigma} \tag{5-193}$$

which characterizes the drop splashing and splattering effects at high values of We_d and [ ]^{a,c}. The range of drop Weber numbers investigated ranged from 2500 to 7000 which compares to drop velocities from 10 m/sec to 18 m/sec. These drop velocities are more characteristic of the region close to the hot leg nozzle where the flow is accelerating toward the nozzle from the upper plenum. The data indicated that the single structure de-entrainment was independent of the drop Weber number over the range of the data, and a consistent value could be used for the de-entrainment fraction. The values given by the authors are best fit to the data.

The extrapolation of these de-entrainment measurements of isolated structures in air-droplet crossflow to multiple structures in close proximity, e.g., a row of cylinders, has been investigated by Chen (1955) and Davies (1952). The work of Chen is the most directly applicable to the PWR situation.

Chen used cylinders with very small diameters--a few millimeters. Therefore, application of Equation 5-191 to the present work must be verified at larger geometries. Chen assumed that for an array the flow is completely mixed between rows, and the changes in drop size and velocity spectra do not change the local de-entrainment efficiencies markedly from those of the first row. With these assumptions, Chen developed an equation for multi-row de-entrainment efficiency (η_{NR}) as:

$$\eta_{NR} = A[1 - C(1-\eta_{R1})\ldots(1-\eta_{RN})], \tag{5-194}$$

where C is a complicated geometric parameter dependent upon array pitch diameter ratios, staggered versus in-line arrays, etc., A has a value of unity for a staggered array with no line of sight through the array, and η_{RN} is the capture efficiency of the n^{th} row. Equation 5-192 is used to calculate η_R for the de-entrainment from the first row and Equation 5-194 or Equation 5-190 is used to calculate the de-entrainment from multi rows of tubes using $C = 1$ and $A = 1$ in Equation 5-194. Thus a prediction can be made of the multiple tube array de-entrainment efficiency using only isolated tube measurements.

Model as Coded

The de-entrainment fractions given in Equations 5-192 and 5-194 are geometry dependent since N, β, and $\eta_{l\alpha}$ which represent the crossflow de-entrainment geometry in that particular cell, are input.

The source term for de-entrainment is then calculated as:

$$\left[\qquad\qquad\right]^{a,c} \tag{5-195}$$

where η_{NR} is given in Equation 5-191 or 5-194 and:

[ ]a,c (5-196)

where $\dot{m}_{Z,e}$ is the mass flow of the entrained phase in the cross-flow or lateral directions. [

]a,c

Scaling Considerations

The experiments by Dallman and Kirchner (1980) were performed on scaled structures, but used typical droplet velocities and drop sizes. The key parameter is the blockage effects of these structures on the cross-flow, both the size and number of rows of structures. Other experiments such as CCTF have scaled reactor internal structures which can de-entrain the droplets from a two-phase mixture crossflowing toward the hot legs. In these experiments, there are competing effects of liquid de-entrainment as well as liquid entrainment from the falling films and pools that exist in the simulated upper plenum. Therefore, the data, in the form of pressure drop readings, give the net de-entrainment for the experiment as a function of time. Full-scale upper plenum de-entrainment data is also available from the UPTF test facility. In these experiments, the radial dimensions from the core to the hot legs are preserved, as well as the drop sizes, drop velocities, and the steam velocity. The structures in UPTF are actually larger than those in a Westinghouse PWR. The comparisons of WCOBRA/TRAC-TF2 to the pressure drop data from CCTF and UPTF is shown in Section 19. These simulations used the same noding as the PWR to address scale effects.

Conclusions

The cross-flow de-entrainment model was developed in the basis of scaled tests with fluid conditions, drop sizes, velocities, and vapor velocities, that are typical of PWR conditions. This model, in conjunction with other entrainment and de-entrainment models, has been compared to both scaled and full-scale data which covers the expected thermal-hydraulic conditions and geometries for a PWR.

5.6.8 De-entrainment at Area Changes

Model Basis

Droplets will de-entrain at area changes on the wetted wall flow regimes by contacting the walls or surfaces of the reduced area channel for axial and lateral flow. The drops are assumed to de-entrain anytime the area changes, regardless if the actual area is normal or inclined toward the flow. These drops will then form liquid films on those surfaces which will drain.

De-entrainment can be expected to occur as droplets, formed during reflood, flow through the upper tie plate. Droplets that strike the solid portions of the tie plate de-entrain and provide the initial liquid for the top quench front. This type of de-entrainment is accounted for using [ ]a,c

[ ]a,c (5-197)

[

]^{a,c} The reduced area acts to sweep the drops out of the entrained flow field since it is assumed the drops flow normal to the flow area and impact the area reduction.

De-entrainment is not calculated for cells in the hot wall flow regime. De-entrainment on spacer grids is separately accounted for in the spacer grid model. Most area de-entrainment will occur outside the core region since the core region has a constant flow area, and is usually in the hot wall regime.

The area change de-entrainment model is also generalized to treat droplets which are flowing vertically upward toward a horizontal surface or downward toward a pool that exists on a horizontal surface. In both cases, all the entrained flow flowing normal to these surfaces is de-entrained into the liquid field.

Model as Coded

The de-entrainment for an area change is calculated as:

[ ] a,c (5-198)

where $A_{X,j}$ is the momentum (cell edge) area, and $A_{X,J}$ is the cell nominal area.

This equation de-entrains some of the entrained liquid flow entering at the bottom of a cell if the top of the cell has a reduced flow area; it de-entrains some of the entrained liquid flow entering at the top of the cell if the bottom of the cell has a reduced flow area. As described previously, the cell centered entrained flow rate $\left(\dot{m}_{X,e,J}\right)$ is obtained from the cell edge flow rate $\left(\dot{m}_{X,e,j}\right)$ by taking the appropriate ratios of fluid properties (see for example, Equation 5-149).

Scaling Considerations

This model has no scale dependence as such and simply models the geometric changes seen in the flow channels. This particular model has been tested at different scales from the CCTF experiments for reflood, as well as the full-scale UPTF experiments for upper plenum de-entrainment, and the LOFT experiments. The CCTF has scaled prototypical hardware in the upper plenum and CCFL region above the fuel such that the area ratios were typical of a PWR. Similarity, the UPTF used full-scale hardware in the CCFL region, core plate, downcomer, and upper plenum, so not only was the area ratio preserved but the areas were prototypical. In LOFT, the fuel assembly hardware at the top of the assemblies was prototypical. The upper plenum structures were also prototypical, particularly the guide tubes. There is no direct verification of this particular model, since no instrumentation was available to measure liquid film flow at the area change locations. However, the model is logical since the drops would have sufficient inertia such that they would impact a flow structure rather than flow around such structures.

Conclusions

The area change de-entrainment model is a logical application of WCOBRA/TRAC-TF2 which uniquely models the entrained droplet field. There are experiments which have the same types of area reductions that occur in a PWR at the same locations in the simulated reactor vessel. Experiments such as LOFT, CCTF and UPTF all have area reductions and prototypical hardware designs.

5.6.9 De-entrainment at Solid Surfaces and Liquid Pools

Model Basis

Entrained liquid flow is assumed to de-entrain under the following additional conditions:

1. Flow of entrained droplets into a cell with a solid surface at the opposite cell face, and
2. Flow of entrained droplets into a cell which is in a bubbly flow regime.

Model as Coded

For the cases above the de-entrainment rate is calculated as:

[ ]^{a,c} (5-199)

[

]^{a,c}

Scaling Considerations and Conclusions

This model has no scale dependence as such since complete de-entrainment on either horizontal surfaces or low void fraction pools is assumed. The model assumptions are logical since the entrained drops should have sufficient inertia to impact a solid wall in a cell if one exists, rather than flowing around the obstruction. Drops flowing into a cell with a low void fraction, typical bubbly flow regime, would be expected to de-entrain since they would mix with the continuous liquid in the cell.

5.7 ONE-DIMENSIONAL COMPONENT INTERFACIAL DRAG MODELS

5.7.1 Introduction

The interfacial drag term in WCOBRA/TRAC-TF2 field equations assumes that it is proportional to the square of the relative velocity. In the calculation of the interfacial drag coefficient, the constant of proportionality depends on the flow regime that is determined by the local total mass flux and the void fraction (see Section 4 for the description of the flow regime map). The discussion that follows describes how the interfacial drag coefficient is calculated for bubbly slug flow, annular mist flow, stratified flow, and the transition among them.

5.7.2 Bubbly Slug Flow

Model Basis

The bubbly slug flow regime in this section refers collectively to the bubbly, bubbly slug transition and bubbly slug flow (see Section 4 for the flow regime map implemented in WCOBRA/TRAC-TF2). Accounting for only the forces of the skin friction and form drag on the bubble (ignoring apparent mass and the Basset force during bubble or slug acceleration), Ishii and Chawla (1979) defines the interfacial force for the dispersed phase as,

$$M_i = \frac{\alpha F_b}{vol_b} \tag{5-200}$$

$$F_b = \frac{1}{2} C_{Db} \cdot \rho_\ell \cdot V_r \cdot |V_r| \cdot A_{pb} \cdot P_s \tag{5-201}$$

where:

M_i	=	the interfacial drag force per unit volume
α	=	the void fraction
vol_b	=	the bubble volume
F_b	=	the force on the gas bubbles
C_{Db}	=	the bubbly flow drag coefficient
A_{pb}	=	the projected area of the bubble
ρ_ℓ	=	the liquid density
V_r	=	the relative velocity of bubble and liquid phases

The bubble redistribution due to the velocity profile in the channel is considered by a profile slip factor, P_s in Equation 5-201.

Combining Equation 5-200 and 5-201 with the relations for the projected area and the volume of a sphere, it is obtained that:

$$M_i = \frac{3}{4} \frac{C_{Db} \cdot \alpha \rho_\ell \cdot V_r \cdot |V_r| \cdot P_s}{D_b} \tag{5-202}$$

and

$$M_i = c_i \cdot V_r \cdot |V_r| \tag{5-203}$$

$$c_i = \frac{3}{4} \frac{C_{Db} \cdot \alpha \rho_\ell \cdot P_s}{D_b} \tag{5-204}$$

where c_i is the interfacial drag coefficient appearing in the 1D component momentum equations in Section 3. To determine the interfacial drag coefficient c_i from Equation 5-204, correlations are required for the bubble diameter D_b, the bubble drag coefficient C_{Db}, and the profile slip factor P_s.

The bubble diameter D_b in Equation 5-204 is calculated using the Laplace coefficient L_0 defined by Ishii (Lime, 2001), as follows:

$$D_b = 2 \cdot L_0 \tag{5-205}$$

where L_0 is the Laplace coefficient defined as:

$$L_0 = \sqrt{\frac{\sigma}{g(\rho_\ell - \rho_g)}} \tag{5-206}$$

D_b is suggested by Ishii as an approximate arithmetic average of the minimum and maximum bubble diameters observed experimentally. From Equation 5-204, it is shown that the bubble diameter has a direct effect on the interfacial drag.

The bubble drag coefficient C_{Db} in Equation 5-204 is determined by Reynolds number for the Stokes regime, viscous regime, and Newton's regime.

Stokes regime ($Re_b \leq 0.1031$),

$$C_{Db} = 240.0 \tag{5-207}$$

Viscous regime ($0.1031 < Re_b < 989.0$),

$$C_{Db} = \frac{24.0}{Re_b}\left(1.0 + 0.15 Re_b^{0.687}\right) \tag{5-208}$$

and Newton's regime ($Re_b \geq 989.0$),

$$C_{Db} = 0.44 \tag{5-209}$$

where the bubble Reynolds number $Re_b = \frac{D_b V_r \rho_\ell}{\mu_\ell}$.

The constant drag coefficients at two extremes of Re_b provide the upper and lower limit of the drag coefficient as Re_b approaches very small or very large values. The upper limit of the drag coefficient is equivalent to the well-known Stokes' law at $Re_b = 0.1$ and it avoids dividing by zero in case the relative velocity and therefore Re_b is zero. Different sources of literature define a slightly different transition Re_b between Stokes and viscous regime, and WCOBRA/TRAC-TF2 uses [ ]^{a,c} to enable continuous

drag coefficient at the transition value of Reynolds number. For reference, Bird, Stewart, and Lightfoot (1960) suggests Stokes flow can be assumed up to $Re_b = 0.1$ while Ishii and Chawla (1979) recommended 1.0. To make the drag coefficient continuous at the transition Reynolds number from the viscous regime to Newton's regime, WCOBRA/TRAC-TF2 adopts [ ]^{a,c} as the transition Reynolds number, which is slightly greater than the value of [ ]^{a,c}, as suggested by Shiller and Nauman (1933), and less than [ ]^{a,c} as used by Ishii and Chawla.

In Newton's regime, the drag force is approximately proportional to the square of the relative velocity between the bubbles and surrounding fluid, and the drag coefficient reaches an asymptotic constant value. WCOBRA/TRAC-TF2 uses [ ]^{a,c} as recommended in Bird, et al. Ishii and Chawla proposed 0.45 to be the constant of proportionality for the same purpose.

In WCOBRA/TRAC-TF2, the effect on the drag coefficient of bubble redistribution in channel flow due to the velocity profile is taken into consideration through a profile factor P_s in Equation 5-204. Physically, the lighter phase (bubbles) tends to migrate to a higher-velocity region of the channel, resulting in a higher void concentration in the central region. Ishii (Lime, 2001) introduced the profile factor to account for the additional slip between the phases as:

$$P_s = \frac{\left(C_1 V_g - C_0 V_\ell\right)^2}{V_r^2} \tag{5-210}$$

where the distribution parameters are given by:

$$C_0 = 1.2 + 0.2\sqrt{\frac{\rho_\ell}{\rho_g}} \tag{5-211}$$

$$C_1 = \frac{1.0 - C_0\alpha}{1.0 - \alpha} \tag{5-212}$$

In determining C_0 in Equation 5-211, fully developed turbulent flow in a circular channel is assumed.

For slug flow, the bubble diameter is calculated by linear interpolation between that calculated by Equation 5-205 and the minimum of $40L_0$ and $0.9D_h$. The basis for this upper limit is supported by the analysis of Kataoka and Ishii (Kataoka and Ishii, 1987) who argued that slug bubbles cannot be sustained for channels with a diameter much larger than $40L_0$ due to interfacial instability, and cap bubbles are formed instead. The same conclusion was drawn in the report of Grace et al. (Grace, Wairegi and Brophy, 1978) and Kitscha and Kocamustafaogullari (Kitscha and Kocamustafaogullari, 1989). The limit of $0.9D_h$ is proposed by Ishii and Chawla. Based on how the slug flow is defined on the flow regime map in Section 4, the void fraction is the independent parameter in the interpolation to determine the slug flow interfacial drag coefficient.

Model as coded

The calculation of the interfacial drag coefficient for 1D components is implemented in the subroutine FEMOM in WCOBRA/TRAC-TF2. Being flow regime dependent, the interfacial drag model in bubbly-slug flow regime, Equations 5-204 through 5-212, is coded explicitly when the local total mass flux and void fraction are in the specified range for bubbly slug flow.

The interfacial drag force is calculated at the cell edges at the centers of the momentum control volume. Since the input parameters required for the interfacial drag coefficient calculation, such as void fraction and fluid thermodynamic properties, are defined at the cell centers, interpolation is needed to obtain the value of these parameters at the cell edges.

The relative velocity in the interfacial drag calculation is defined as:

[ ]a,c (5-213)

where subscript $j+1/2$ is at the cell edge and g, l represent the gas (bubble) and liquid phases, respectively.

The void fraction used in Equation 5-204 is spatially averaged using the cell length, Δx, and is defined as:

[ ]a,c (5-214)

(5-215)

The determination of surface tension σ, liquid viscosity μ_ℓ and vapor viscosity μ_g adopts the donor cell scheme and is implemented in the code as:

[ ]a,c (5-216)

(5-217)

(5-218)

(5-219)

(5-220)

(5-221)

In the bubbly slug regime, the diameter is interpolated with a weighting factor between the bubble diameter determined from [

]^{a,c}.

[ ] a,c (5-222)

The weighting factor is [

]^{a,c} Therefore,

[ ] a,c (5-222a)

In order to avoid numerical difficulties caused by the unreasonably large or small numbers, several limits are imposed and implemented in the code. In bubbly flow regime, the bubble diameter is not allowed to be [ ]^{a,c} and is not allowed to be [ ]^{a,c}, i.e.,

[ ] a,c (5-222b)

The allowable change in the interfacial drag in WCOBRA/TRAC-TF2 is based on real time to eliminate the sensitivity to the time-step size. The maximum and minimum allowable changes in the interfacial drag are given by:

[ ] a,c (5-223)

(5-224)

Thus, the amount of transient time required for the interfacial drag to double or halve is [ ]^{a,c} s. The maximum allowable change is limited to be less than [ ]^{a,c}, and the minimum allowable change is limited to be greater than [ ]^{a,c}. For the special case of steady-state calculations, the new-time interfacial drag is a weighted average of [ ]^{a,c} to provide stable convergence.

If the flow area of the cell edge of interest is [
]^{a,c}, the interfacial drag is set to zero to avoid extra computation.

The void fraction used to calculate the interfacial drag is restricted to the range of [
]^{a,c} in all components.

Scaling consideration and Conclusions

The bubbly slug interfacial drag model used in the 1D module of WCOBRA/TRAC-TF2 is based on the TRAC-P [ ]^{a,c} interfacial drag package. Range and applicability of the model is presented in Appendix H.1.1 of the TRAC-M theory manual (LA-UR-00-910). In particular scaling considerations are provided in Appendix H.1.1.9 of the same report. It is shown that for large hydraulic diameters at high pressure, the bubbly flow regime interfacial drag predicted by the model is in reasonable agreement with the Chexal model, which is a full range model that extends to very large pipe (~ 1.0 m diameter).

5.7.3 Annular Mist

Model Basis

Annular mist flow is assumed to exist if the void fraction is greater than 0.75 on the basic flow regime map (Section 4) and the flow is not stratified. It implies the existence of the liquid phase as a combination of annular film and entrained droplets; however, since only one liquid field exists in the 1D component, the effective interfacial drag force for annular mist flow in WCOBRA/TRAC-TF2 is assumed to be a superposition of the separate drag forces caused by the entrained droplets and the annular film, and it therefore must represent the combined effect. Based on this assumption, the annular mist interfacial drag coefficient c_i is thus defined by:

$$c_i = \frac{M_i}{V_r \cdot |V_r|} \tag{5-225}$$

For:

$$M_i = M_{id} + M_{ia} \tag{5-226}$$

Where:

M_{id} = the drag forces caused by the droplet field per unit volume,
M_{ia} = the drag forces caused by the liquid film per unit volume,
V_r = $V_g - V_\ell$, the relative velocity of the gas and liquid phase.

The code calculates the amount of entrainment based on correlations from Kataoka and Ishii (Kataoka and Ishii, 1987). It calculates the amount of liquid existing as a film by subtracting the entrained liquid from the total amount of liquid. An interfacial drag coefficient is calculated for the droplets in a manner similar to bubbly flow by assuming there is no droplet distortion. Thus, it follows the theory developed by

Ishii and Chawla (Ishii and Chawla, 1979), Bird, Stewart, and Lightfoot (Bird, et al., 1960), and Shiller and Nauman (Shiller and Nauman, 1933). A separate interfacial drag coefficient is calculated for the liquid film using a correlation proposed by Wallis (Wallis, 1969).

For the component of the dispersed droplet flow, WCOBRA/TRAC-TF2 uses the drag force equation given by Ishii and Mishima (Ishii and Mishima, 1984):

$$M_{id} = a_i \left[\frac{C_d}{4} \left(\frac{r_{sm}}{r_d} \right) \cdot \frac{\rho_g \left(V_g - V_d \right)^2}{2} \right] \tag{5-227}$$

in which the droplet interfacial area per unit volume, a_i is defined as:

$$a_i = \frac{\alpha}{1-\alpha_{d,c}} \frac{3\alpha_{d,c}}{r_{sm}} \tag{5-228}$$

In Equations 5-227 and 5-228,

$\alpha_{d,c}$ = the area fraction of the droplet in the mixture of gas and droplet flow (not including the liquid film if it exists); therefore, the area fraction of the droplet in the total mixture area is $\frac{\alpha \cdot \alpha_{d,c}}{1-\alpha_{d,c}}$

r_{sm} = the Sauter mean radius ($r_{sm} = 0.796 \frac{D_d}{2}$)

r_d = the drag radius

The ratio of the Sauter mean radius to the drag radius in Equation 5-227 is defined as a shape factor, which is one for a spherical particle.

The required inputs to determine the drag force M_{id} include the droplet diameter D_d, area fraction of droplets α_d, and the droplet-drag coefficient C_d. In annular mist flow, as the liquid velocity that is solved for from the conservation equations (Section 3) is an effective liquid velocity representing both the entrained droplet and the liquid film, the term $\left(V_g - V_d \right)$ in Equation 5-227 also needs to be estimated to determine the drag force M_{id}.

For the droplet diameter, a correlation for the volume mean diameter of droplets was developed by Kataoka, Ishii, and Mishima (Kataoka et al., 1983). The mechanism assumed for the generation of the droplets is that of shearing from wave crests, such as those produced in annular-mist flow. The droplet diameter is given by:

$$D_d = \frac{2.0}{\rho_g \cdot j_g^{\,2}}\left[0.005 \cdot \sigma \cdot \left(\frac{\mu_g}{\mu_\ell}\right)^{2/3} Re_g^{\,2/3}\left(\frac{\rho_g}{\rho_\ell}\right)^{-1/3}\right] \tag{5-229}$$

To estimate the droplet-drag coefficient, WCOBRA/TRAC-TF2 uses a correlation recommended by Ishii and Chawla. The correlation is given by:

$$C_d = \frac{24.0}{Re_d}\left(1.0 + 0.1 Re_d^{\,0.75}\right) \tag{5-230}$$

where the droplet Reynolds number is given by:

$$Re_d = \frac{D_d \rho_g \left|V_g - V_d\right|}{\mu_m} \tag{5-231}$$

and the modified viscosity is:

$$\mu_m = \frac{\mu_g}{\left(1 - \alpha_{d,c}\right)^{2.5}} \tag{5-232}$$

In annular-dispersed flow, most droplets are in the wake regime because of their relatively small size. WCOBRA/TRAC-TF2 thus uses a relative velocity developed by Ishii (Ishii, 1977) based on the drift-flux formulation of the flow as follows.

$$V_g - V_d = \frac{D_d}{4}\left[\frac{(g\Delta\rho)^2}{\mu_g \rho_g}\right]^{1/3}\left(1 - \alpha_{d,c}\right)^{1.5} \text{ for} \tag{5-233}$$

$$|j| \geq 1.456\left[\frac{\sigma g \Delta\rho}{\rho_g^{\,2}}\right]^{1/4}\left[\frac{\mu_g^{\,2}}{\rho_g \sigma (\sigma / g\Delta\rho)^{1/2}}\right]^{-1/12} \tag{5-234}$$

If $|j|$ < the right-hand side of Equation 5-234:

$$V_g - V_d = \sqrt{2} \cdot \left[\frac{\sigma g \Delta\rho}{\rho_g^{\,2}}\right]^{1/4}\left(1 - \alpha_{d,c}\right)^{1.5} \tag{5-235}$$

To estimate the droplet area fraction, the entrainment correlation developed by Kataoka and Ishii (Kataoka and Ishii, 1982) is used. The correlation is given by:

$$E = \tanh\left(7.25 \times 10^{-7} We_d^{\,1.25} Re_\ell^{\,0.25}\right) \tag{5-236}$$

where the liquid Reynolds number is given by:

$$Re_\ell = \frac{\rho_\ell j_\ell D_h}{\mu_\ell} \tag{5-237}$$

and the droplet Weber number is:

$$We_d = \frac{\rho_g j_g^{\,2} D_h}{\sigma}\left(\frac{\rho_\ell - \rho_g}{\rho_g}\right)^{1/3} \tag{5-238}$$

For small droplets, the area fraction of droplets can approximately be related to the entrainment ratio by (Kataoka and Ishii, 1982, Equation 90):

$$\alpha_{d,c} = \frac{j_\ell E}{j_g} \tag{5-239}$$

For the annular film component, the basis for the interfacial-drag coefficient for the annular film follows a force balance for a segment of liquid film as shown in Figure 5-10. By integrating the shear stress at the core-to-film interface over a length Δz, it is obtained that:

[ ]^{a,c} (5-240)

In Equation 5-240, D_c is [

]^{a,c}. From geometric considerations, D_c is given as:

[ ]^{a,c} (5-241)

Where:[

]^{a,c}

Similar to the wall-shear stress in single-phase channel flow, the shear stress at the film to core interface is given by:

[ ]^{a,c} (5-242)

where the density term refers to the gas core and f_i is the film-interface friction factor obtained from a correlation of Wallis (Wallis, 1969), i.e.,:

$$f_i = 0.005 \cdot \left[1 + 75 \cdot \left(1 - \alpha_f\right)\right] \tag{5-243}$$

where, as previously noted, α_f is the film area fraction.

For annular-mist flow, the model developed by Ishii and Mishima is used. The total interfacial shear force denoted by M_i has two sources, namely, the generalized drag M_{id} and the interfacial shear and void gradient M_{ia}. The M_{id} for droplets is given by Equation 5-227. Ishii and Mishima showed that the interfacial shear and void gradient for annular flow in a tube is:

$$M_{ia} = \left(\nabla\alpha_k \cdot \tau_i\right) = \alpha_{if} \cdot \tau_f \tag{5-244}$$

where:

$$\alpha_{if} = \frac{4C_{an}}{D}\sqrt{\frac{\alpha}{1-\alpha_{d,c}}} \tag{5-245}$$

The term τ_f is given by Equation 5-242 and C_{an} is the roughness parameter due to waves in the film $\left(C_{an} \geq 1\right)$. By definition, we have:

$$M_i = C_{iam} \cdot \left(V_g - V_{fd}\right) \cdot \left|V_g - V_{fd}\right| \tag{5-246}$$

where C_{iam} is the overall interfacial-drag coefficient for annular-mist flow. In the above equation, a formulation for the relative velocity $\left(V_g - V_{fd}\right)$ is needed to calculate the interfacial-drag coefficient C_{iam}. Kataoka and Ishii (1982) developed a correlation for the relative velocity $\left(V_g - V_{fd}\right)$ based on the drift-flux model (Ishii, 1977). The correlation is given as:

$$\begin{aligned} V_g - V_{fd} = & \frac{1}{\alpha_c + \left[\frac{1+75\left(1-\alpha_c\right)}{\sqrt{\alpha_c}}\frac{\rho_g}{\rho_\ell}\right]^{1/2}}\left[j + \sqrt{\frac{\Delta\rho \cdot g_c D\left(1-\alpha_c\right)}{0.015\rho_\ell}}\right] \cdot \left(1-\alpha_c\right) \\ & + \frac{r_d}{2}\left[\frac{\left(\Delta\rho \cdot g_c\right)^2}{\mu_g\rho_g}\right]^{1/3} \cdot \alpha_{d,c}\left(1-\alpha_{d,c}\right)^{1.5} \end{aligned} \tag{5-247}$$

Model as Coded

The interfacial drag model for annular mist flow regime is coded as shown in Equations 5-227 through 5-247. To calculate the interfacial drag for annular mist using the model described, the void fraction,

hydraulic diameter, gas density, liquid density, surface tension, gas viscosity, liquid and vapor viscosity, and relative velocity need to be input. The void fraction is [ ]^{a,c}. The gas density and gas viscosity are [ ]^{a,c}. The liquid density, surface tension, and liquid viscosity are [ ]^{a,c}. The gas velocity used to calculate the entrainment is [ ]^{a,c}. The relative velocity used is [ ]^{a,c}.

In determination of the entrainment, the Weber number in the code is chosen to be [ ]^{a,c}. Liles et al. (1981) made tests on the sensitivity of TRAC-PD2 to the Weber number and found the results were not strongly influenced by variations of the Weber number between 2 and 12.

Limits are imposed on the allowable droplet size to prevent the calculation of excessively large drag coefficients. The droplet diameter is limited to the range [ ]^{a,c} m. The limits for the void fraction and the interfacial drag change rate during the iteration are [ ]^{a,c}.

The rate limits, i.e. allowable changes from one time step to the next are imposed after the interfacial drag coefficient calculation is complete. The restriction as described by Equations 5-223 and 5-224 is the same for all regimes.

Scaling Considerations and Conclusions

The droplet-drag component for the annular mist flow regime is not scale dependent if the droplet diameter and entrainment rate are assumed to be predicted properly. The Wallis correlation (Wallis, 1969) used in the liquid film drag component was developed based on a small-scale test, and its application to the large diameter hardware in a PWR is validated through the separate and integral tests documented in Volume 2 of this report.

5.7.4 Churn Turbulent Flow

Model Basis

In the void fraction range of 0.5 to 0.75, a transition flow referred to as churn-turbulent flow regime is made between the bubbly slug and annular mist flow regimes. Instead of a separate correlation for the interfacial drag, a weighted average interfacial drag coefficient of the bubbly slug and the annular mist flow regimes is calculated for the churn-turbulent regime.

Model as Coded

In the code, the interfacial drag coefficient for churn turbulent flow is calculated by [ ]^{a,c}. It is implemented as:

$$\left[\quad\right]^{a,c} \tag{5-248}$$

and

[ ] a,c (5-249)

where:[

]a,c

Scaling Considerations and Conclusions

The churn turbulent flow is modeled as a simple transition flow regime between the bubbly slug and annular mist flows, and there are no specific models for the churn turbulent flow other than the linear interpolations between the bubbly slug and annular mist regimes.

5.7.5 Horizontal Stratified Flow

Model Basis

In WCOBRA/TRAC-TF2, the code calculates a stratified flow interfacial drag coefficient if certain flow criteria in terms of phase velocities and flow inclination angle are met (Section 4). The calculation follows a hybrid horizontal stratification transition model derived from the Taitel and Dukler (1976) model and the Wallis-Dobson (1973) model and the interfacial friction factor based on the Ohnuki (Ohnuki, 1988) correlation.

Model as Coded

For fully stratified flow, the interfacial drag coefficient is defined by the method of Taitel and Dukler (1976). Specifically, the drag coefficient is calculated such that:

$$c_{i,st} = \frac{1}{2} f_i \rho_g \frac{S_i}{A_{flow}} \quad (5\text{-}250)$$

where f_i is the interfacial friction factor, S_i is the width of the stratified interface (see Equation 4-113), and A_{flow} is the flow area:

$$A_{flow} = \frac{\pi}{4} D_h^2 \quad (5\text{-}251)$$

The flow area and width of the stratified interface are determined assuming a circular channel cross section.

For horizontal stratified flow, the interfacial friction-factor is calculated based on the correlation from Ohnuki (1988):

$$f_i = 1.84\, f_{wg} \tag{5-252}$$

where f_{wg} is the assumed gas phase wall friction factor:

$$\begin{aligned} f_{wg} &= \frac{16}{Re_g}, && Re_g < 1189 \\ f_{wg} &= \frac{0.0791}{Re_g^{0.25}}, && 1189 < Re_g \le 1.145\times 10^5 \\ f_{wg} &= 0.0008 + \frac{0.05525}{Re_g^{0.237}}, && Re_g > 1.145\times 10^5 \end{aligned} \tag{5-253}$$

As discussed in Section 4, the stratified-flow regime is superimposed on the basic flow-regime map. Thus, when the flow is not fully stratified, the code interpolates between the drag coefficient determined for stratified flow, calculated as above, and the value otherwise determined with respect to the basic flow-regime map. In other words,

$$c_i = (1 - W_{st})\, c_{i,map} + W_{st} c_{i,st} \tag{5-254}$$

where the weighting factor W_{st}, with the range of $0.0 \le W_{st} \le 1.0$, is calculated as a function of critical velocity in Equation 4-117 in Section 4.

Scaling Considerations

Horizontal stratified flow exists in the hot leg during the natural circulation stage, in the cold leg during the boiling off stage and core recovery stage, and in the loop seal after loop seal clearance of a Small Break LOCA. Horizontal stratified flow also exists in the hot leg and the cold leg during the reflood stage of a Large Break LOCA (LBLOCA). The interfacial drag component for the horizontal stratified flow regime is not scale-dependent if the interfacial friction factor is predicted properly. The Ohnuki interfacial drag model (Ohnuki, 1988) was developed based on small-scale tests, and it was validated (Ohnuki, 1988) against the counter-current flow data in the UPTF experiment, which is a PWR-scale facility, in the range of low to medium pressure. The application of the Ohnuki interfacial drag model to high pressure and large scale facilities is validated through the Two-Phase Test Facility (TPTF) separate effect test in Section 16 of this report.

Conclusions

The interfacial drag model for the horizontal stratified flow regime is based on the work of Ohnuki (1988). In Section 16 of this report, the model is validated against the high pressure, large scale TPTF test. The predicted void fractions are in good agreement with the experimental data. Compared with the horizontal stratification transition criterion, the interfacial drag model is of less importance to the accuracy of the horizontal stratified flow model. The uncertainty in the interfacial drag model is accounted for in the uncertainty in the horizontal stratification transition criterion.

5.7.6 Wavy Dispersed Flow

Model Basis

The background and criteria for the wavy-dispersed flow were introduced in Section 4.4.6. The wavy-dispersed flow regime is predicted when the onset of entrainment precedes the onset of interfacial instability predicted [

]^{a,c}

Model as Coded

[ ]^{a,c}

[ ]^{a,c} (5-255)

[ ]^{a,c} (5-256)

and

[ ]^{a,c} (5-257)

[

]^{a,c}

[ ]^{a,c} (5-258)

[ ]^{a,c}

[

]^{a,c}

$$\left[\quad\right]^{a,c} \tag{5-259}$$

[ ]^{a,c}

$$\left[\quad\right]^{a,c} \tag{5-260}$$

[

]^{a,c}

$$\left[\quad\right]^{a,c} \tag{5-261}$$

for:

$$\left[\quad\right]^{a,c} \tag{5-262}$$

and

$$\left[\quad\right]^{a,c} \tag{5-263}$$

[ ]^{a,c}

$$\left[\quad\right]^{a,c} \tag{5-264}$$

[

]^{a,c}

$$\left[\quad\right]^{a,c} \tag{5-265}$$

[

]a,c

[a,c] (5-266)

[ ]a,c

[a,c] (5-267)

[ ]a,c

[a,c] (5-268)

[

]a,c

[a,c] (5-269)

[

]a,c

[a,c] (5-270)

[ ]a,c

[ ]a,c (5-271)

[

]a,c

[ ]a,c (5-272)

Scaling Considerations

The droplet interfacial drag component for the wavy-dispersed flow regime is not scale dependent if the droplet diameter, relative velocity and entrainment rate are assumed to be predicted properly. [

]a,c The entrainment model assumes the liquid fraction beyond the critical liquid fraction corresponding to the horizontal stratification boundary is entrained. The model for [

]a,c

Conclusions

The interfacial drag model for the wavy-dispersed flow regime is developed according to the similarity with the annular-mist flow regime and the horizontal stratified flow regime. The approach is judged to be adequate for the purpose of modeling the flow regime in PWR geometries and conditions.

5.8 ONE-DIMENSIONAL COMPONENT WALL DRAG MODELS

The pressure gradient caused by the wall drag of the two-phase one dimensional flow is given by the sum of the gas and liquid phase wall drag terms:

$$\left(\frac{dP}{dz}\right)_f = -c_{wg}|V_g|V_g - c_{w\ell}|V_\ell|V_\ell \tag{5-273}$$

where:

$$c_{wg} = \frac{\alpha_g \rho_g c_{fg}}{D_h} \tag{5-274}$$

$$c_{w\ell} = \frac{\alpha_\ell \rho_\ell c_{f\ell}}{D_h} \tag{5-275}$$

c_{fg} and $c_{f\ell}$ are the gas and liquid friction factors, α_g is the void fraction associated with the gas phase, and α_ℓ is the liquid fraction $\alpha_\ell = 1 - \alpha_g$. From these equations, it can be seen that the constant of proportionality is c_{fg}/D_h for the gas phase and that the momentum flux for the gas phase is $\alpha_g \rho_g |V_g| V_g$. For the liquid phase, the constant of proportionality is $c_{f\ell}/D_h$ and the momentum flux is $\alpha_\ell \rho_\ell |V_\ell| V_\ell$.

As the void fraction goes to zero, Equation 5-273 will result in the correct single phase liquid pressure gradient caused by wall drag consistent with c_{fl}, the liquid phase friction factor. As the void fraction goes to one, Equation 5-273 will result in the correct single phase gas pressure gradient caused by wall drag consistent with c_{fg}, the gas phase friction factor. Therefore, the single phase correlations for $c_{f\ell}$ and c_{fg} for laminar and turbulent flow will determine the single pressure gradient caused by wall shear.

For the purpose of comparison with correlations of known accuracy, the WCOBRA/TRAC-TF2 wall drag model will be rewritten in terms of a two-phase multiplier (Wallis, 1969, and Collier, 1972). Division of Equation 5-273 by the single phase liquid wall drag flowing at the total mass flux yields the following effective two-phase multiplier for WCOBRA/TRAC-TF2 (Wallis, 1969):

[ ]^{a,c} (5-276)

where [ ]^{a,c}. The gas and liquid friction factors in the above equation are based on different correlations depending upon the type of flow. The different correlations for each flow regime will be discussed in the following subsections.

NFF is the input parameter for selecting 1D wall drag options. Setting NFF equal to ± 1 selects the homogeneous wall drag option. Setting NFF to zero results in constant wall friction with only the user input values (FRIC array in input). A negative NFF results in the automatic calculation of an appropriate form loss coefficient in addition to the selected two-phase flow friction factor.

5.8.1 Homogeneous Flow

Model Basis

The friction factor model for single phase turbulent flow was chosen based on Churchill's model (Churchill, 1977):

$$f = 2 \cdot \left[\left(\frac{8}{Re} \right)^{12} + \frac{1}{(a+b)^{3/2}} \right]^{1/12} \tag{5-277}$$

where:

$$a = \left[2.457 \times \ln \left(\frac{1}{\left(\frac{7}{Re} \right)^{0.9} + \frac{0.27\varepsilon}{D_h}} \right) \right]^{16} \tag{5-278}$$

and

$$b = \left(\frac{37530}{Re} \right)^{16} \tag{5-279}$$

In Equation 5-278, ε is the wall surface roughness. Churchill's equation represents a fit to the Moody curves, which include the laminar, transition, turbulent, smooth, and rough regimes in a single equation. The Reynolds number in the Churchill correlation is not allowed to [

]^{a,c}.

The WCOBRA/TRAC-TF2 two-fluid momentum equations result in a two-phase multiplier that includes the effect of slip without the modification for the single-phase friction factor. The homogeneous wall-drag model alters the single-phase friction factor by using a two-phase viscosity (μ) defined in terms of the flow quality (X_f) (Collier, 1972) as:

$$\mu = \left[\frac{X_f}{\mu_g} + \frac{(1 - X_f)}{\mu_f} \right]^{-1} \tag{5-280}$$

According to Whalley (Whalley, 1981), of the different methods for defining the two-phase viscosity, this method is more accurate than the methods of Owens (Owens, 1981) or Cicchitti (Cicchitti, 1960), but is not as accurate as Dukler's method (Dukler, 1964). Whalley indicates that the standard deviation for the homogeneous wall-drag model with a two-phase viscosity based on Equation 5-280 is ~38% for steam/water systems.

The coefficient of friction for the liquid phase is related to the Fanning friction factor by Equation 5-281 and that for the gas phase by Equation 5-282, such that:

$$c_{f\ell} = 2f \tag{5-281}$$

$$c_{fg} = c_{f\ell} \tag{5-282}$$

Substitution of Equation 5-280, Equation 5-281, and Equation 5-282 into Equation 5-276 yields:

[ ]a,c (5-283)

From Equation 5-283, it can be seen that the effective two-phase multiplier in WCOBRA/TRAC-TF2 is [ ]a,c, as shown in Equation 5-284 below.

[ ]a,c (5-284)

It can be shown that [ ]a,c.

Therefore, for slip ratios close to unity, the model will [ ]a,c.

Model Basis

The homogeneous 1D wall drag model is coded in subroutine FWALL as outlined in Equations 5-277 through 5-282, the flow qualities in Equation 5-280 are [ ]a,c. More specifically,

[ ]a,c (5-285)

and

[ ]a,c (5-286)

where [ ]a,c. For slip ratios close to unity, [ ]a,c. As the slip ratio increases, [ ]a,c.

FWALL also sets the calculated quality to zero when [ ]a,c. This eliminates any division by zero in Equation 5-286.

FWALL calculates the mass flux to be used in the calculation of the Reynolds number as [

]^{a,c}

The mixture velocity is calculated in the PREPER routine with the following equation:

[ ]^{a,c} (5-287)

In this expression [

]^{a,c} given by:

[ ]^{a,c} (5-288)

where [ ]^{a,c}.

The WCOBRA/TRAC-TF2 1D homogeneous wall-drag model assumes [

]^{a,c}

Scaling Considerations and Conclusions

The WCOBRA/TRAC-TF2 wall shear homogeneous model is a function of Re, X_f, S_r, all of which are non-dimensional parameters that generally are accepted as independent of scale. It is also important to note that the wall shear is less important for a full-size plant (volume/surface area effect) than for the assessed experiments in which satisfactory overall results have been obtained. As the scale increases, the importance of wall shear decreases. Inspection of the wall-shear term in the momentum equations reveals that it has a $D^{-1.2}$ dependence (Table 5-4). No other term in the fluid momentum equations contains this inverse diameter effect (except for the interfacial drag during pure annular flow).

5.8.2 Horizontal Stratified Flow

Model Basis

The horizontal stratified-flow wall-shear model is based on the assumption that the wall shear for each phase can be determined by assuming smooth-pipe wall-shear models for each phase. The local-phase velocity and the hydraulic diameter based on the phasic flow area and wetted perimeters are used to determine the phase-dependent Reynolds number.

Model as Coded

The wall shear coefficients are coded in subroutine FEMOM. At the fluid/wall interface, closure of the liquid- and gas-field momentum equations requires two additional parameters: the wall drag coefficient for the liquid phase $c_{w\ell}$ and the wall drag coefficient for the combined-gas phase c_{wg}. These two drag coefficients are defined as follows:

$$c_{w\ell} = \frac{\rho_\ell c_{f\ell}}{D_\ell} \tag{5-289}$$

and

$$c_{wg} = \frac{\rho_g c_{fg}}{D_g} \tag{5-290}$$

where $c_{f\ell}$ and c_{fg} are the coefficients of friction for the liquid and gas phases, respectively. The hydraulic diameters D_ℓ and D_g are based on the flow area and wetted perimeter for each phase, which are based on the height of the liquid level in the horizontal pipe,

$$D_g = \frac{4A_g}{S_g + S_i} \tag{5-291}$$

and

$$D_\ell = \frac{4A_\ell}{S_\ell} \tag{5-292}$$

where,

$$S_\ell = D_h\left(\pi - \cos^{-1}\left(\frac{2h_\ell}{D_h} - 1\right)\right) \tag{5-293a}$$

$$S_g = \pi D_h - S_\ell \tag{5-293b}$$

The liquid- and gas-phase coefficients of friction are related to the Fanning friction factor as follows:

$$c_{f\ell} = c_{fg} = 2\,f_w \tag{5-294}$$

The friction factor f is determined considering the geometry of the horizontal stratified flow. For fully stratified flow, the Blasius model, Equation 5-295 is used to calculate the wall friction factor for both liquid and gas phases. The actual wall friction is interpolated between stratified flow and non-stratified

flow, if the flow is in the interpolation region. The code uses a Reynolds number of 1502 to obtain a smooth transition from the laminar to turbulent flow:

$$f_w = \frac{16}{Re}, Re < 1502$$
$$f_w = \frac{0.046}{Re^{0.2}}, Re > 1502 \quad (5\text{-}295)$$

The Reynolds numbers are based on the velocities for each phase as given below:

$$Re_g = \max\left(100, \frac{\rho_g |V_g| D_g}{\mu_g}\right) \quad (5\text{-}296)$$

and

$$Re_\ell = \max\left(100, \frac{\rho_\ell |V_\ell| D_\ell}{\mu_\ell}\right) \quad (5\text{-}297)$$

where D_ℓ and D_g are the hydraulic diameters based on the flow area and the wetted perimeter for each phase, which are based on the height of the liquid level in the horizontal pipe.

The interpolation between the non-stratified wall shear model defined in Section 5.8.1 and the horizontal stratified wall shear model described in this section is based on the stratified flow model transition logic explained in Section 4. The interpolation function is used in the following manner:

[ ]^{a,c} (5-298)

and

[ ]^{a,c} (5-299)

where $c_{w\ell}$ and c_{wg} are the coefficients to be used in Equation 5-273, $c_{w\ell,st}$ and $c_{wg,st}$ are the horizontal stratified wall shear coefficients, and $c_{w\ell,map}$ and $c_{wg,map}$ are the non-stratified wall shear coefficients (basic flow regime map).

The densities and void fractions used in the horizontal stratified-flow wall-drag correlation are based on a length-weighted average, as described by:

[ ]^{a,c} (5-300)

where ξ can be any cell-center fluid property. This process yields an averaged fluid property for the WCOBRA/TRAC-TF2 1D momentum cell. The length weighted averaging process is appropriate for properties that appear in the wall drag terms, since the wall drag is proportional to the cell length, not to the cell volume. The viscosity and surface tension are donor cell properties, with the surface tension and the liquid phase viscosity based on the liquid phase flow direction and the gas phase viscosity based on the gas phase flow direction.

Scaling Considerations

The wall drag component for the horizontal stratified flow regime is independent of scale if the friction factor is assumed to be predicted properly. The friction factor is predicted by the Blasius model. [

]^{a,c}

Conclusions

The wall drag model for the horizontal stratified flow regime is based on the Blasius model. The model is judged to be acceptable for application to PWR LOCA prediction. Compared with the horizontal stratification transition criterion, the wall drag model is of less importance to the accuracy of the horizontal stratified flow model. The uncertainty in the wall drag model is accounted for in the uncertainty in the horizontal stratification transition criterion.

5.9 ONE-DIMENSIONAL COMPONENT FORM LOSS

Model Basis

In addition to ordinary friction losses in a uniform straight pipe, other losses can occur because of sudden velocity changes resulting from abrupt area changes. In long pipes, these additional losses may be neglected in comparison to the normal friction loss of the pipe. In short pipes, however, these additional losses may actually be much larger than the ordinary friction loss.

In the case of abrupt area changes, the source of the loss is confined to a very short length of pipe, although the turbulence produced may persist for a considerable distance downstream. The flow after the

change may be exceedingly complex. For the purposes of analysis, however, it is assumed that the effects of ordinary friction and of the additional large-scale turbulence may be separated, and that the abrupt area change loss is concentrated at the location of the area change. The total head loss in a pipe may then be considered to be the sum of the ordinary friction for the length of pipe considered and the extra loss due to the abrupt area change.

For an abrupt expansion, a theoretical determination of the loss is possible. For an abrupt contraction, however, this is not true, and experimental results must be used to determine the flow loss. Because the losses have been found to vary as the square of the mean velocity, they are frequently expressed in the form:

$$\text{Head loss} = K\frac{V^2}{2g} \tag{5-301}$$

where K is the loss coefficient, V is the mean velocity, and g is the gravitational acceleration constant.

The corrective terms added to the WCOBRA/TRAC-TF2 momentum equations are determined by first considering the momentum equation for single-phase flow and by neglecting the gravity head and wall shear,

$$\frac{1}{\rho}\frac{\partial P}{\partial x} + V\frac{\partial V}{\partial x} = 0 \tag{5-302}$$

For a pipe noded as in Figure 5-12, integration of Equation 5-302 with the assumptions of steady state and of constant density from point j to point j + 1 yields a Bernoulli-type equation for the pressure change from point j to point j + 1 as follows:

$$\Delta P_{j\to(j+1)} = -\left(P_{j+1} - P_j\right) = \frac{\rho}{2}\left(V_{j+1}{}^2 - V_j{}^2\right) \tag{5-303}$$

The pressure drop given by Equation 5-303 typically is referred to as the reversible pressure drop. The term reversible is used because the pressure loss associated with a contraction can be regained by a pressure rise at an expansion of the same magnitude. If no area change occurs between j and j + 1, the velocity of the flow does not change, and Equation 5-303 predicts $\Delta P_{j\to(j+1)} = 0$ as expected. If a smooth area change occurs between sections j and j + 1, then the irreversible losses may be small, and Equation 5-303 yields an approximation to the pressure drop from point j to j + 1. If the area change between sections j and j + 1 is abrupt, however, the irreversible losses cannot be ignored, and it is standard practice to add a form-loss factor to Equation 5-303 to account for the additional irrecoverable pressure loss caused by the area change in question. This yields a general equation for the pressure drop between sections j and j + 1 when an abrupt area change is present, such that:

$$\Delta P_{j\to(j+1)} = -\left(P_{j+1} - P_j\right) = \frac{\rho}{2}\left(V_{j+1}{}^2 - V_j{}^2\right) + K\cdot\frac{\rho V_s^2}{2} \tag{5-304}$$

where V_s is the velocity at the cross section where the area change occurs. Once the loss coefficient K for the specific area change in question has been determined, either theoretically or experimentally, the pressure drop at the abrupt area change can be calculated using Equation 5-304.

Abrupt Expansion

To determine the loss coefficient for an abrupt expansion, consider the expansion of Figure 5-13. If the pipes run full and the flow is assumed steady, two simplifying assumptions may be made that allow the pressure change across the expansion to be calculated. First, assume that the pressure and velocity at section j are uniform across the cross section. This assumption is valid for the high Reynolds-number flow found in most practical applications. Second, assume that the pressure and velocity at section j + 1 are also uniform. This assumption is valid if section j + 1 is sufficiently downstream of the expansion where the mixing caused by the turbulence has had a chance to even out the velocity profile again. A control-volume analysis using steady flow equations may now be made on the fluid contained between sections j and j + 1.

Application of the momentum equation for steady, incompressible flow neglecting wall friction to the fluid between sections j and j + 1 yields the following force balance:

$$-\left(P_{j+1}-P_j\right)A_{j+1}=\rho A_{j+1}V_{j+1}\left(V_{j+1}-V_j\right) \tag{5-305}$$

Application of the Bernoulli equation for an incompressible fluid yields:

$$\frac{P_j}{\rho g}+\frac{V_j^2}{2g}-H_L=\frac{P_{j+1}}{\rho g}+\frac{V_{j+1}^2}{2g} \tag{5-306}$$

where H_L is the total head loss across the expansion. Substitution Equation 5-305 into Equation 5-306 yields:

$$H_L=\frac{\left(V_j-V_{j+1}\right)^2}{2g} \tag{5-307}$$

From continuity, $A_{j+1}V_{j+1} = A_jV_j$ so that we may rewrite Equation 5-307 as:

$$H_L=\frac{V_j^2}{2g}\left(1-\frac{A_j}{A_{j+1}}\right)^2 \tag{5-308}$$

Comparison of this result with Equation 5-301 shows that the loss coefficient K for an abrupt expansion at the j + 1/2 interface is:

$$K=\left(1-\frac{A_j}{A_{j+1}}\right)^2 \tag{5-309}$$

when the mean velocity V of Equation 5-304 is taken as V_j. Substitution of the result for K into Equation 5-304 yields:

$$\Delta P_{j\rightarrow(j+1)} = -\left(P_{j+1} - P_j\right) = \rho V_{j+1}\left(V_{j+1} - V_j\right) \tag{5-310}$$

which is exactly the result expressed in Equation 5-305.

Abrupt Contraction

Consider the abrupt contraction of Figure 5-14. Although an abrupt contraction is geometrically the reverse of an abrupt expansion, it is not possible to solve exactly for the loss coefficient for an abrupt contraction using a control volume analysis on the fluid between sections j and j + 1 as was done for the abrupt expansion of Figure 5-13. This is because the pressure at section j just upstream of the contraction varies in an unknown way as a result of the curvature of the streamlines and the acceleration of the fluid. Thus, application of the steady-flow momentum equation to the fluid at section j is not valid. Without the relationship between pressure and velocity provided by the momentum equation (as in Equation 5-305 for the case of the abrupt expansion), it is not possible to solve explicitly for the total head loss across the contraction. Loss coefficients have been determined experimentally for circular coaxial pipes and fairly high Reynolds numbers, and Massey (Massey, 1968., pp. 219) recommends the use of Table 5-5a when determining values for K.

Once K has been determined using Table 5-5a, the pressure drop across the abrupt contraction may be calculated as follows. The flow at section j has a velocity V_j, while the flow upon reaching section j + 1 has a velocity V_{j+1} that is higher than V_j because of the abrupt cross-section change. Using Equation 5-304 to calculate the change in pressure from points j to j + 1 caused by the abrupt area change yields:

$$\Delta P_{j\rightarrow(j+1)} = -\left(P_{j+1} - P_j\right) = \frac{\rho}{2}\left(V_{j+1}{}^2 - V_j{}^2\right) + K \cdot \frac{\rho V_{j+1}^2}{2} \tag{5-311}$$

where K is taken from Table 5-5a.

Thin Plate Orifice

As in the case of the abrupt contraction, it is not possible to determine theoretically the loss coefficient across a thin-plate orifice, and experimental data must be used. For a sharp-edged thin plate orifice in a straight conduit (Figure 5-15), Idel'Chik (Idel'Chik, 1960, pp. 139) suggests that the following expression be used for the loss coefficient K in the presence of high Reynolds numbers ($\geq 10^5$):

$$K = \left(1 + 0.707\sqrt{1 - \frac{A_{j+1/2}}{A_j}} - \frac{A_{j+1/2}}{A_j}\right)^2 \tag{5-312}$$

This curve fit also agrees well with the data plotted in White (White, 1979, pp. 384) for the irrecoverable head loss across a thin-plate orifice.

Once the loss coefficient K for a sharp-edged, thin plate orifice has been determined using Equation 5-312, the pressure drop across the orifice may be calculated as follows. The flow at section j has a velocity V_j, while the flow upon reaching section j + 1/2 has a velocity $V_{j+1/2}$, which is higher than V_j because of the abrupt cross-section change. Using Equation 5-304 to calculate the change in pressure from points j to j + 1/2 caused by the abrupt area change yields:

$$\Delta P_{j\rightarrow(j+1/2)} = -\left(P_{j+1/2} - P_j\right) = \frac{\rho}{2}\left(V_{j+1/2}{}^2 - V_j{}^2\right) + K \cdot \frac{\rho V_{j+1/2}^2}{2} \tag{5-313}$$

where K is calculated using Equation 5-312. Another abrupt area change occurs between points j+1/2 and j+1. The flow at section j+1/2 has a velocity $V_{j+1/2}$, while the flow at section V_{j+1} has a velocity V_{j+1}, which is less than $V_{j+1/2}$ because of the expansion in cross section. Because the irreversible losses caused by the presence of the orifice have already been accounted for in the pressure drop between j and j+1/2 and should not be accounted for twice, the pressure change between j+1/2 and j+1 is simply:

$$\Delta P_{(j+1/2)\rightarrow(j+1)} = -\left(P_{j+1} - P_{j+1/2}\right) = \frac{\rho}{2}\left(V_{j+1}{}^2 - V_{j+1/2}{}^2\right) \tag{5-314}$$

Adding Equations 5-313 and 5-314 (noticing that $V_j = V_{j+1}$) shows that the total pressure drop from points j to j + 1 for the orifice of Figure 5-15 is:

$$\Delta P_{j\rightarrow(j+1)} = -\left(P_{j+1} - P_j\right) = \frac{\rho}{2} K V_{j+1/2}^2 \tag{5-315}$$

where K is calculated according to Equation 5-312.

Model as Coded

The WCOBRA/TRAC-TF2 backward difference approach to determine the $V\nabla V$ term in the WCOBRA/TRAC-TF2 momentum equation is known to be numerically stable. For smooth area changes, however, this backward or upwind difference scheme is not accurate and does not conserve momentum. For abrupt area changes, it can be shown that the upwind difference scheme for $V\nabla V$ will result in pressure changes that include both reversible and irreversible effects. Upwind differencing is accurate for abrupt expansions and overestimates the pressure change for an abrupt contraction.

It has been shown that the accuracy of a central difference representation of $V\nabla V$ is quite accurate for smooth area changes and for the reversible portion of an abrupt area change. Central differencing is, in general, unconditionally unstable, however, based on linear stability analyses.

An approach to improve momentum conservation is therefore to determine factors based on geometry that change the upwind differencing of the $V\nabla V$ so that its accuracy is consistent with central differencing.

A central difference for $V\nabla V$ for 1D flow yields:

[ ]a,c (5-316)

In WCOBRA/TRAC-TF2, velocities are calculated at cell edges; therefore cell-center velocities must be estimated from cell-edge velocities. Equation 5-316 can be written in terms of the cell edge velocities by applying the following equations based on constant volumetric flow from cell center to the cell edge:

[ ]a,c (5-317)

(5-318)

and

[ ]a,c (5-319)

If Equations 5-317 and 5-318 are substituted into the summed portion of Equation 5-316, and Equations 5-317 and 5-319 are substituted into the difference portion of Equation 5-316, an upwind difference form that is as accurate as central differencing is obtained for $V\nabla V$.

[ ]a,c (5-320)

These equations assume that [ ]^{a,c}, but similar sets of equations can be derived for [ ]^{a,c}. In the WCOBRA/TRAC-TF2 code, Equation 5-320 is the approximation used in 1D momentum convection terms to improve the conservation of momentum. If the cell edge flow areas and cell center flow areas are all equal, the WCOBRA/TRAC-TF2 representation for $V\nabla V$ is then reduced to:

[ ]a,c (5-321)

If constant volumetric flow from cell edge j-1/2 to cell edge j+1/2 is assumed, Equation 5-320 in the form of the Bernoulli equation is equivalent to:

[ ]a,c (5-322)

Substitute the constant volumetric flow relations Equations 5-317 and 5-319 into the momentum convection term of Equation 5-322 to obtain the Bernoulli equation:

[ ]a,c (5-323)

It is seen from the above derivation of the momentum convection term and the assumptions made that the equation of motion for single-phase liquid (a near incompressible fluid) to a very good approximation satisfies the conservative form of the momentum equation (and thus the Bernoulli equation). Convected momentum flux between momentum cells should be nearly conserved. Reversible form losses caused by flow area and elevation changes should be evaluated correctly. For a compressible single-phase vapor, the change in its microscopic density because of fluid pressure and temperature variation over a mesh-cell distance generally is small. Approximating constant density within a fluid cell should cause only a small error in conserving convected vapor momentum flux between momentum cells. A spatial variation in the fluid void fraction across a mesh cell can result in a momentum-flux conservation error because of the constant volumetric-flow assumption. Therefore, for rapidly changing void fractions or densities within a short distance, WCOBRA/TRAC-TF2 [ ]a,c.

With flow area ratios in the momentum convection term, WCOBRA/TRAC-TF2 [

]a,c

[

]a,c

[ ]a,c (5-324)

where [

]^{a,c}

[ ] a,c (5-325)

Table 5-5b compares the original data and the K value predicted using Equation 5-325. Inspection of Table 5-5b shows that Equation 5-325 very closely predicts the standard loss coefficients measured experimentally.

The bracketed factor in Equation 5-325 is the K factor to be applied to [

]^{a,c}

The pressure losses predicted by WCOBRA/TRAC-TF2 at a sudden contraction, expansion and the combination of a sudden contraction and expansion are compared with the test data (Massey, 1963; King and Brater, 1963 and Archer, 1913) in Table 5-6, Table 5-7 and Table 5-8, respectively.

For the case of a thin plate orifice, the loss coefficient recommended by Idel'Chik is [

]^{a,c}

[

]^{a,c}

Scaling Considerations

There are no scale dependent parameters in the WCOBRA/TRAC-TF2 form loss methodology. The geometry should be accurately represented by the code, and the unrecoverable loss should be accounted for when [ ]^{a,c}.

Conclusions

Modeling the momentum-convection term with area ratios conserves momentum flux convection between momentum cells and provides an accurate evaluation of reversible Bernoulli flow losses. [

]^{a,c}

[

]^{a,c}

5.10 FORM LOSS AT THE JUNCTION BETWEEN A 1D COMPONENT AND 3D VESSEL COMPONENT

The pressure change calculated at a vessel/one- dimensional component junction requires special consideration so that the correct form losses are [ ]^{a,c}.

Figure 5-16 illustrates the momentum cell used at the junction between the cold leg and the downcomer of a PWR, where the 1D face [ ]^{a,c}. Equation 5-326 shows the momentum gradient term for the 1D components in the numerical differencing form, which is consistent with Equation 5-320.

[ ]^{a,c} (5-326)

When the 1D component has a constant flow area flow and flow is from the vessel into the 1D component, this equation reduces to:

[ ]^{a,c} (5-327)

where V_{BD} is the boundary velocity. Therefore, the pressure change from the 1D component momentum equation is predicted as:

[ ]^{a,c} (5-328)

The velocity at point J in Figure 5-16 is assumed to be equal to [

]^{a,c}.

Consequently, Equation 5-328 will predict a reversible pressure change of:

[ ]^{a,c} (5-329)

or:

[ ]^{a,c} (5-330)

Another important vessel/pipe junction is the broken cold leg nozzle. It can be visualized as shown in Figure 5-17. Fluid in the annular downcomer converges on the nozzle, where it must then make a turn into the nozzle. Applying the Bernoulli equation from point zero to point two in Figure 5-17, it is obtained that:

$$P_0 - P_2 = \frac{1}{2}\rho_2 V_2^2 - \frac{1}{2}\rho_0 V_o^2 \quad (5\text{-}331)$$

Typically, V_o is small and the contribution of the second term on the right hand side of Equation 5-331 is negligible and the pressure drop become can be approximated by:

$$P_0 - P_2 = \frac{1}{2}\rho_2 V_2^2 \quad (5\text{-}332)$$

which is the recoverable loss for the nozzle and [ ]^{a,c}.

For a typical PWR geometry, the irrecoverable loss through the nozzle has been calculated to be K = [ ]^{a,c} from the UPTF data (Section 19). The equation for irrecoverable loss is:

$$P_0 - P_2 = K\frac{\rho V_2^2}{2} \quad (5\text{-}333)$$

Combining the recoverable losses from Equation 5-332 and irrecoverable loss from Equation 5-333, the total pressure change for a typical PWR geometry is:

$$\left[\qquad\qquad\right]^{a,c} \quad (5\text{-}334)$$

Therefore, the loss coefficient of [ ]^{a,c} is applied at the broken cold leg/vessel junction in the one-dimensional component.

When a gap is specified for the 1D connection to the vessel, or when the connection is at the top or bottom of the vessel cell (vertical 1D component connection), the velocity facing the 1D component, V_{BD}, is set equal to [ ]^{a,c}. Applying Equation 5-326 for flow from the 1D component into the vessel and for flow out of the vessel, it is obtained that:

$$\left[\qquad\qquad\right]^{a,c} \quad (5\text{-}335)$$

where V_{BD} is the boundary velocity, and is set to [ ]^{a,c}.

For the hot leg connection, the outlet nozzle is modeled as part of the vessel (Figure 5-18), with a 1D pipe component connected horizontally for the hot leg.

Scaling Considerations and Conclusions

There are no scale dependent parameters in the WCOBRA/TRAC-TF2 form loss methodology at 1D/3D junction. The unrecoverable loss should be accounted for when [ ]^{a,c}.

The 1D/3D junction and recommended irrecoverable losses coefficient was calibrated against data from UPTF experiments (Section 19). No scale dependent bias has been observed in the calculated results.

5.11 TEE COMPONENT MOMENTUM CONVECTION

Model Basis

To demonstrate how the TEE momentum source is implemented in the code, the conservative form of the liquid momentum equation for a positive flow is written as:

$$\mathrm{vol}_j \frac{\partial\left[\left(1-\alpha_j\right)\rho_{\ell_j} V_{\ell_{j+1/2}}\right]}{\partial t} + A_{j+1/2}\left(1-\alpha_j\right)\rho_{\ell_j} V_{\ell_{j+1/2}} V_{\ell_{j+1/2}} - A_{j-1/2}\left(1-\alpha_{j-1}\right)\rho_{\ell_{j-1}} V_{\ell_{j-1/2}} V_{\ell_{j-1/2}} = \text{R.H.S.} \tag{5-336}$$

where R.H.S. stands for the terms on the right-hand side of the equation. After using the chain rule to expand the time-derivative term and substituting in the finite-difference liquid mass equation, the momentum equation can be written as:

$$\frac{\partial V_{\ell_{j+1/2}}}{\partial t} + \frac{A_{j-1/2}\left(1-\alpha_{j-1}\right)\rho_{\ell_{j-1}}}{\mathrm{vol}_j\left(1-\alpha_j\right)\rho_{\ell_j}} V_{\ell_{j-1/2}}\left(V_{\ell_{j+1/2}} - V_{\ell_{j-1/2}}\right) = \text{R.H.S.} \tag{5-337}$$

This form of the momentum equation requires major changes to the way that the code passes boundary information between components, therefore it is not used directly. Applying the finite-difference mass equation again, and eliminating $A_{j-1/2}\left(1-\alpha_{j-1}\right)\rho_{\ell_{j-1}} V_{\ell_{j-1/2}}$, it is obtained that:

$$\frac{\partial V_{\ell_{j+1/2}}}{\partial t} + \frac{A_{j+1/2}}{\mathrm{vol}_j} V_{\ell_{j+1/2}}\left(V_{\ell_{j+1/2}} - V_{\ell_{j-1/2}}\right) + \frac{V_{\ell_{j+1/2}} - V_{\ell_{j-1/2}}}{\left(1-\alpha_j\right)\rho_{\ell_j}} \frac{\partial\left[\left(1-\alpha_j\right)\rho_{\ell_j}\right]}{\partial t} = \text{R.H.S.} \tag{5-338}$$

If a TEE junction is present at a 1D cell, the following term is added to the left side of Equation 5-336:

$$-A_T\left(1-\alpha_T\right)\rho_{l_T} V_T V_T \cos\theta \tag{5-339}$$

where the subscript T indicates the first cell in the side leg of the TEE or the interface between the jth cell of the primary (through input, this cell is labeled JCELL) and the first cell in the side leg, depending on the type of variable, and θ is the angle of incidence of the TEE side leg from the direction of lower-numbered cells in the primary tube. After this modified momentum equation is converted to a form similar to Equation 5-338, a correction to the left side of the difference equation for liquid motion is obtained in the form:

$$-\frac{A_T\left(1-\alpha_T\right)\rho_{\ell_T}}{\mathrm{vol}_j\left(1-\alpha_j\right)\rho_{\ell_j}} V_T\left(V_{j-1/2} + V_T\cos\theta\right) \tag{5-340}$$

As far as time levels are concerned, this term is evaluated in a linearized implicit manner that is consistent with the rest of the 1D momentum-flux term. In the standard two-step notation, it is:

$$-\frac{A_T(1-\alpha_T)\rho_{\ell_T}}{vol_j(1-\alpha_j)\rho_{\ell_j}}\left[\tilde{V}_T^{n+1}\left(2\tilde{V}_T^n\cos\theta+\tilde{V}_{j-1/2}^n\right)\right.$$

$$\left.+\tilde{V}_T^n\tilde{V}_{j-1/2}^{n+1}-\tilde{V}_T^n\left(\tilde{V}_{j-1/2}^n+\tilde{V}_T^n\cos\theta\right)\right] \qquad (5\text{-}341)$$

The vapor equation uses a similar term.

Model as Coded

Subroutine ETEE generates the quantities necessary for the source term given by Equation 5-341, and subroutines FEMOM and TF1DS1 add this source term to the momentum equations.

The velocities $V_{l_{j+1/2}}$ and $V_{l_{j-1/2}}$ are calculated as they are for all momentum cells in the 1D components. That is, velocities are calculated at cell edges in the code, therefore cell-center velocities must be estimated from cell-edge velocities and the momentum gradient is upwind differenced.

It has been shown in Section 5.9 that the accuracy of a central difference representation of $V\nabla V$ is quite accurate for smooth area changes and for the reversible portion of an abrupt area change, as shown in Equations 5-316 through 5-320.

When the pipe is of a constant flow area, Equation 5-320 becomes:

[ ]^{a,c} (5-342)

Equation 5-342 is the form in which Equation 5-338 is written.

It is worth noting that [

]^{a,c}

[ ]^{a,c} (5-343)

Scaling Considerations

The equations and methods used to calculate the tee momentum terms are independent of scale except that [

]^{a,c}.

Conclusions

To accurately evaluate the momentum convection at the internal junction between the main and branch pipes of the TEE component, [

]^{a,c}

[a,c

]

[ ] a,c

[

]a,c

[

a,c

]

a,c

5.12 CRITICAL FLOW MODEL

In the event of a hypothetical LOCA in a PWR, the rate of depressurization of the primary loop is dominated by the rate of fluid discharge at the break. During the blowdown phase of the Large and Intermediate Break LOCA, and much of transient for the Small Break LOCA, the discharge will be choked (critical flow).

There are two options available in WCOBRA/TRAC-TF2. The first option is to choose the critical flow packages in TRAC-P [ ]^{a,c}. The second option is to choose the Homogeneous Relaxation Model for the subcooled and most portions of the two-phase region. The following sections give descriptions to both options.

5.12.1 PF1 Critical Flow Model Option (ICFLOW=2)

Model Basis

The TRAC-P [ ]^{a,c} two-phase, two-component, choked-flow model was developed from first principles using the characteristic analysis approach (or the method of characteristics, MOC). The TRAC-P [ ]^{a,c} subcooled choked-flow model (Abuaf-Jones-Wu or AJW model) is a modified form of the Burnell model and was developed by (Abuaf et al., 1983).

In general, with the 5 or 6 equation codes such as TRAC-PD2 (Liles, 1981) and TRAC-PF1 (Liles, 1988), choking calculations can be done simply by using a sufficiently fine mesh for components with smooth area changes. However, the TRAC-P [ ]^{a,c} quasi-steady choked-flow model saves computational time because it allows a much coarser mesh. For components with abrupt area changes, a one-dimensional fine mesh can cause erroneous natural-choking results. For all such cases, a separate choking model is almost a necessity. Thus, a choking model not only improves computational efficiency but also accounts for effects such as sharp area changes and frictional pressure losses.

5.12.1.1 Sub-model Selection Based on Void Fraction

This critical flow model option contains three basic submodels which are used depending on the void fraction as follows:

[

]^{a,c}

Figure 5-19 shows the selection of sub-models for this choke flow model option.

The interpolation region is necessary to avoid the discontinuity between the critical flow rates calculated by the subcooled and two-phase sub-models. In this region the liquid and vapor velocities are linearly interpolated with void fraction. A similar interpolation region at $\alpha = 0.999$ is unnecessary because the critical flow rates calculated by the two-phase model naturally approach those of single-phase vapor.

5.12.1.1.1 Void Fraction Estimate

The precise nature of the void fraction used to determine which model is used is dependent on the length-to-diameter ratio as determined from the geometry of the adjacent donor cell as:

$$L/D = \frac{\Delta X}{2}\left(\frac{\pi}{\Delta V/\Delta X}\right)^{\frac{1}{2}} \tag{5-344}$$

where ΔV and ΔX are the adjacent cell volume and length.

The models used for determining the void fraction for both $L/D < 1.5$ and $L/D \geq 1.5$ assume that the two-phases are in equilibrium at the choking plane (which is taken to be at the cell edge). For both types of model stagnation conditions are also calculated at the cell center, but in different ways.

For $L/D < 1.5$ the stagnation conditions are calculated directly from the cell center conditions as supplied to the critical flow model from the calling routine. Thus, stagnation conditions are calculated as follows:

$$H_{o_c} = x_c\left(H_{v_c} + \frac{1}{2}U_{v_c}^2\right) + (1-x_c)\left(H_{\ell_c} + \frac{1}{2}U_{\ell_c}^2\right) \tag{5-345}$$

or:

$$H_{o_c} = H_{m_c} + x_c\frac{1}{2}U_{v_c}^2 + (1-x_c)\frac{1}{2}U_{\ell_c}^2 \tag{5-346}$$

and

$$S_{o_c} = x_c S_{v_c} + (1-x_c)S_{\ell_c} \tag{5-347}$$

where x is the quality, and the subscript "c" is the cell center.

For $L/D \geq 1.5$ the thermodynamic condition at the cell center is converted to an equivalent equilibrium condition assuming constant enthalpy, i.e.,:

$$\alpha_{eq} = \frac{x_{eq}\rho_{\ell_c}^{sat}}{\rho_{v_c}^{sat} + x_{eq}\left(\rho_{\ell_c}^{sat} - \rho_{v_c}^{sat}\right)} \tag{5-348}$$

where:

$$x_{eq} = \frac{H_{m_c} - H_{\ell_c}^{sat}}{H_{v_c}^{sat} - H_{\ell_c}^{sat}} \tag{5-349}$$

and the saturated conditions correspond to the cell center pressure P_c. The stagnation enthalpy and entropy are determined as in Equations 5-346 and 5-347, except that x_{eq} is used and the thermodynamic quantities are taken at saturation.

For $L/D < 1.5$, α_c is used to determine which model is used (subcooled or two-phase), while for $L/D \geq 1.5$, α_{eq} is used.

5.12.1.2 Subcooled (AJW) Model

The subcooled critical velocity (a_{sc}), is taken as the maximum of a homogeneous equilibrium value a_{HE} and a velocity determined from the application of Bernoulli's equation:

$$a_{sc} = \text{maximum}\{a_{HE}, a_{Be}\} \tag{5-350}$$

where:

$$a_{HE} = F_e / \rho_{m_e} \tag{5-351}$$

and

$$a_{Be} = \left(U_{\ell_c}^2 + \frac{(P_c - P_{nuc})}{\rho_{\ell_e}} \right)^{\frac{1}{2}} \tag{5-352}$$

where P_{nuc} is the nucleation pressure.

The mass flux (F_e) is the maximum mass flux at the cell edge consistent with assuming an isentropic expansion from the cell center stagnation conditions to an equilibrium state at the cell edge. The degree of freedom with which the mass flux is maximized is the pressure at the cell edge.

Thus:

$$F_e = \rho_{m_e}^{sat} \left(2 \left(H_{o_c} - H_{m_e}^{sat} \right) \right)^{1/2} \tag{5-353}$$

is maximized where $H_{m_e}^{sat}$ and $\rho_{m_e}^{sat}$ are defined in terms of the edge quality (x_e) and the saturation values of the individual phase quantities, i.e.,

$$H_{m_e}^{sat} = x_e H_{v_e}^{sat} + (1 - x_e) H_{\ell_e}^{sat} \tag{5-354}$$

and

$$\frac{1}{\rho_{m_e}^{sat}} = \frac{x_e}{\rho_{v_e}^{sat}} + \frac{1-x_e}{\rho_{\ell_e}^{sat}} \tag{5-355}$$

and the cell edge quality is determined assuming the isentropic expansion:

$$x_e = \frac{s_{0_c} - s_{\ell_e}^{sat}}{s_{v_e}^{sat} - s_{\ell}^{sat}} \tag{5-356}$$

The value of critical velocity so obtained is equal to the homogeneous equilibrium value for cell center conditions which are at equilibrium, but can significantly deviate from the homogeneous equilibrium value when non-equilibrium effects are evident.

For the alternative critical velocity (a_{Be}), the driving force is the pressure gradient between the cell center and the nucleation pressure at the cell edge. Because of nucleation delay effects, the nucleation pressure (P_{nuc}) can be considerably lower than the local saturation pressure (P_{sat}). The delay in nucleation is modeled using a correlation developed by Alamgir and Lienhard (1981), and Jones (1980).

$$P_{nuc} = P_{sat} - \max\left\{ 0.0, 0.258\sigma^{1.5}\left(\frac{T_{\ell_c}}{T_{crit}}\right)^{13.76} \frac{(1+13.25\Sigma^{0.8})^{0.5}}{(k_B T_{crit})^{1/2}(1-\rho_v/\rho_\ell)} \right.$$
$$\left. - 27\,(0.072)^2 \rho_{\ell_e}\left(\frac{A_e}{A_c}\right)^2 \frac{U_{\ell_e}^2}{2} \right\} \tag{5-357}$$

The rate of depressurization Σ is determined from the pressure gradient between the cell center and the cell edge:

$$\Sigma = \frac{|U_{\ell_e}|(P_c - P_e)}{1.01325\times 10^{11}\Delta X/2} \tag{5-358}$$

The first term in Equation 5-357 represents the static depressurization effect and is based on classical nucleation theory (Alamgir and Lienhard, 1981). The second term accounts for turbulent fluctuations in the flowing liquid (Jones, 1980).

5.12.1.3 Two-phase Model (Method of Characteristics, MOC Model)

The WCOBRA/TRAC-TF2 two-phase choking model is an extension of one developed by Ransom and Trapp (Ransom, 1980) that incorporates an additional inert gas component. Thermal equilibrium is assumed to exist between the phases. The two-fluid flow field under thermal equilibrium is described by the inert gas continuity equation, the overall continuity equation, two phasic momentum equations, and

the mixture energy equation. Since the non-differential source terms do not enter into the characteristic analysis, the equations are:

$$\frac{\partial \rho_m}{\partial t} + \frac{\partial (\rho_m U_m)}{\partial x} = 0 \tag{5-359}$$

$$\begin{aligned} &\alpha\rho_g\left[\frac{\partial U_g}{\partial t} + U_g\frac{\partial U_g}{\partial x}\right] + \alpha\frac{\partial P}{\partial x} \\ &+ C_{VM}\alpha(1-\alpha)\rho_m\left[\frac{\partial U_g}{\partial t} + U_\ell\frac{\partial U_g}{\partial x} - \frac{\partial U_\ell}{\partial t} - U_g\frac{\partial U_\ell}{\partial x}\right] = 0 \end{aligned} \tag{5-360}$$

$$\begin{aligned} &(1-\alpha)\rho_\ell\left[\frac{\partial U_\ell}{\partial t} + U_\ell\frac{\partial U_\ell}{\partial x}\right] + (1-\alpha)\frac{\partial P}{\partial x} \\ &+ C_{VM}\alpha(1-\alpha)\rho_m\left[\frac{\partial U_\ell}{\partial t} + U_g\frac{\partial U_\ell}{\partial x} - \frac{\partial U_g}{\partial x} - U_\ell\frac{\partial U_g}{\partial x}\right] = 0 \end{aligned} \tag{5-361}$$

$$\frac{\partial (\rho_m s_m)}{\partial t} + \frac{\partial \left[\alpha\rho_g U_g s_g + (1-\alpha)\rho_\ell U_\ell s_\ell\right]}{\partial x} = 0 \tag{5-362}$$

$$\frac{\partial (\alpha\rho_a)}{\partial t} + \frac{\partial (\alpha\rho_a U_g)}{\partial x} = 0 \tag{5-363}$$

where C_{VM} is the virtual mass coefficient; s is the entropy; and subscripts a, g, ℓ, and m refer to the non-condensable gas, steam/gas mixture, liquid, and total mixture, respectively. The last terms in Equations 5-360 and 5-361 represent interphasic force terms caused by relative acceleration. These terms are discussed in detail in (Ransom and Trapp, 1980). Following Ransom and Trapp's formulation, the energy equation is written in the form of the mixture-specific entropy that is conserved for adiabatic flow (with the irreversibilities associated with interphasic mass transfer and relative phase acceleration neglected). No basic difficulty in the analysis is experienced, however, if the mixture energy equation is written in terms of the internal energy or enthalpy.

In the thermal-equilibrium case, ρ_v, ρ_ℓ, s_g, s_ℓ, and ρa are known functions of p_a and p_v. If we assume that Dalton's law of partial pressures applies, Equations 5-359 through 5-363 can be written in terms of the five unknowns p_v, α, V_g, V_ℓ, and p_a. The matrix representation of these equations is:

$$A(\bar{U})\frac{\partial \bar{U}}{\partial t} + B(\bar{U})\frac{\partial \bar{U}}{\partial x} = 0 \tag{5-364}$$

where $\bar{U}$ consists of p_v, α, V_g, V_ℓ, and p_a, and the complete matrices for the system are given in Figure 5-20 and Figure 5-21.

The characteristic roots, λi, of the above system of equations are defined as the roots of the fifth-order polynomial,

$$\text{determinant}\left(\underline{\underline{A}}\lambda - \underline{\underline{B}}\right) = 0 \tag{5-365}$$

Choking occurs when the signal propagating with the largest velocity relative to the fluid is stationary; that is, the maximum value of the real part of a characteristic root, $\lambda_{i,re,max}$, is zero. WCOBRA/TRAC-TF2 obtains the characteristic roots of Equation 5-365 numerically. This method advantageously maintains generality and facilitates computations under different assumptions.

5.12.1.4 Single-Phase Vapor Model

The single-phase vapor choked-flow model is based on isentropic expansion of an ideal gas (White, 1979). A throat pressure, p_e, is calculated from the stagnation pressure, p_o, such that:

$$p_e = p_o \left(\frac{2}{\gamma + 1}\right)^{\gamma/\gamma - 1} \tag{5-366}$$

where γ is the specific heat ratio. A downstream throat temperature, T_e, is calculated from the stagnation temperature, T_o, using the ideal gas relation:

$$T_e = T_o \left(\frac{2}{\gamma + 1}\right) \tag{5-367}$$

When T_e is greater than the saturation temperature at p_e, the fluid flow at the throat is predicted to be superheated by the ideal gas relations. The continuity equation, in conjunction with the ideal gas relations, yields a fluid choking velocity,

$$V_{ge} = \sqrt{\frac{2}{\gamma + 1} RT_o} \tag{5-368}$$

where R is the gas constant.

If T_e is less than or equal to the saturation temperature at p_e, then the fluid flow at the throat is not predicted to be superheated by the ideal gas relations, and the choking velocity is calculated using iterations to maximize mass flux along the isentrope that extends from the superheated conditions upstream of the throat to the two-phase conditions at the throat. This method assumes that no delay in condensation occurs as the steam expands to the saturated two-phase state at the throat.

5.12.2 Homogeneous Relaxation Model Option (ICFLOW=3)

Model Basis

In WCOBRA/TRAC-TF2 a more seamless critical flow model was developed which eliminated the ad-hoc interpolation region between the subcooled and two-phase region. This critical flow model option contains three basic sub-models which are used depending on the upstream condition as follows:

[

]^{a,c}

In comparison with the TRAC-P [ ]^{a,c} choke model, this option uses Homogeneous Non-equilibrium Relaxation model for the subcooled and much of the two-phase upstream conditions. The MOC method is only briefly used as the transition to the single phase vapor model. The choice of specific models is shown graphically in Figure 5-22.

In this section, the Homogeneous Non-equilibrium Relaxation model is discussed for this option, the other two sub-models are discussed in the Section 5.12.1.

5.12.2.1 Homogeneous Non-equilibrium Relaxation Model (HRM)

5.12.2.1.1 Conservation Equations

HRM critical flow models are based on the following assumptions:

- Steady State
- Homogeneous model (equal velocity)
- Non-equilibrium (thermal non-equilibrium)

The HRM suggested by Downar-Zapolski (1996) was modified to include the non-condensable mass conservation equation with an additional assumption of constant flow area (Ohkawa, 2007b), and is shown next.

Mass conservation equation:

$$\frac{d}{dz}(\rho_m u) = 0 \tag{5-369}$$

Momentum conservation equation:

$$\frac{d}{dz}(\rho_m uu) = -\frac{dP}{dz} - \left(\frac{dP}{dz}\right)_{FR} + \rho_m g \tag{5-370}$$

where $(dP/dz)_{FR}$ term includes the entrance pressure loss and the frictional pressure loss.

Entrance Loss:

$$\left(\frac{dP}{dz}\right)_{ENT} = \left\{1 + K_e - \left(\frac{A_2}{A_1}\right)^2\right\} \times \frac{\rho_m \cdot u^2}{2} \tag{5-371}$$

where, A_2 / A_1 is the area ratio shown in Figure 5-23. The smaller area represents the break path where the choking takes place.

The explicit form of Colebrook-White (White, 1979) was used for the single phase friction factor.

$$\left(\frac{dP}{dZ}\right)_{FR}^{1\varphi} = \frac{f}{D_h} \times \frac{G_\ell^2}{2\rho_\ell} \tag{5-372}$$

$$\begin{aligned} f &= \text{Max}\left(0.01, \frac{64}{Re}\right) \quad \text{for } Re \le 500 \\ f &= \text{Max}\left(\frac{64}{Re}, fc\right) \quad \text{for } Re > 500 \end{aligned} \tag{5-373}$$

$$fc = \frac{1}{\left\{-2 \times \log\left[\frac{\varepsilon/D}{3.7} + \frac{2.51}{Re} \times \left(1.14 - 2 \times \log\left(\frac{\varepsilon}{D} + \frac{21.25}{Re^{0.9}}\right)\right)\right]\right\}^2} \tag{5-374}$$

The relative roughness of 3.0×10^{-5} is used.

Levy's two-phase friction multiplier (Levy, 1960) was used, and is expressed as,

$$\left(\frac{dP}{dZ}\right)_{FR}^{2\phi} = \frac{f}{D_h} \cdot \frac{G_m^2}{2\rho_\ell} \cdot \phi_{LO}^2 \tag{5-375}$$

$$\phi_{LO}^2 = \left(\frac{1-x}{1-\alpha}\right)^{1.75} \tag{5-376}$$

Energy conservation equation:

$$\frac{d}{dz}\left(\rho_m \cdot (h_m + u^2/2) \cdot u\right) = 0 \tag{5-377}$$

Vapor mass conservation equation:

$$\frac{d}{dz}(\alpha_g \rho_g u) = \Gamma_g \tag{5-378}$$

where ρ_g is the vapor phase density, Γ_g is the vapor generation rate. When the liquid is subcooled, there is no phase transition, and Γ_g is specified by Equations 5-379 and 380. The liquid phase becomes superheated as the pressure decreases along the flow channel. The de-superheating occurs due to flashing. The HRM explicitly specifies the vapor generation rate with relaxation, as,

$$\Gamma_g = 0 \quad \text{for} \quad T_\ell < T_{sat} \tag{5-379}$$

$$\frac{\Gamma_g}{\rho_m} = \frac{x_e - x}{\Theta} = (1-x)\frac{h_\ell - h_{fv}}{h_{gv} - h_{fv}} \cdot \frac{1}{\Theta} \quad \text{for } T_\ell \geq T_{sat} \tag{5-380}$$

where for $P \geq 10$ Bar:

$$\Theta = \Theta_0 \cdot \alpha^{-0.54} \cdot \phi^{-1.76} \tag{5-381}$$

$$\phi = \frac{P_{sat}(T_\ell) - P}{P_c - P_{sat}(T_\ell)} \tag{5-382}$$

$$\Theta_0 = 3.84 \times 10^{-7} \text{ sec} \tag{5-383}$$

and where for $P < 10$ Bar:

$$\Theta = \Theta_0 \cdot \alpha^{-0.257} \cdot \psi^{-2.24} \tag{5-384}$$

$$\psi = \frac{P_{sat}(T_\ell) - P}{P_{sat}(T_\ell)} \tag{5-385}$$

$$\Theta_0 = 6.51 \times 10^{-4} \text{ sec} \tag{5-386}$$

where, h is the specific enthalpy, P is the pressure, T is the temperature, u is the mixture velocity, ρ is the fluid density, x is the quality, and subscripts "ℓ", "G", "v", "g", "m", and "fv" signify liquid, combined gas phase, steam vapor, saturated steam, mixture, and saturated liquid at steam partial pressure $\left(= h_\ell\left(P_v, T_{sat}\left(P_v\right)\right)\right)$, respectively. Here the equilibrium quality in the presence of non-condensable, x_e is defined as,

$$x_e = \frac{h - h_{fv}}{h_{gv} - h_{fv}} \tag{5-387}$$

This definition assumes that at equilibrium, both phases are "Thermally" in equilibrium. The relaxation time correlation is taken directly from the original model (Downar-Zapolski, 1996), even though it is recognized that the relaxation time for evaporation process $\left(T_{sat}\left(P_v\right) < T_\ell < T_{sat}\left(P\right)\right)$, would be different from that for the flashing process in which case, $T_\ell > T_{sat}\left(P\right)$.

The last equation is the non-condensable gas mass conservation equation:

$$\frac{d}{dz}(\alpha_g \rho_a u) = 0 \tag{5-388}$$

where ρ_a is the non-condensable gas density.

This model lacks an explicit flashing delay model such as found in Amos and Schrock (1984) and Lee and Schrock (1990). However, the relaxation parameter as a function of void fraction and pressure effectively acts to delay the nucleation and flashing. [

]^{a,c}

5.12.2.1.2 Numerical Methods

Assumptions for Developing the Working Model

The following primary variables were selected; the mixture velocity (u), the total pressure (P), the void fraction (α), the liquid temperature (T_ℓ), the non-condensable partial pressure (P_a).

It is assumed that the steam and the non-condensable gas are in thermal equilibrium and the combined gas phase follows Dalton's partial pressure law, $P=P_v+P_a$. It is further assumed that the non-condensable gas can be treated as an ideal gas. This assumption implies that the steam and the non-condensable gas are in thermal equilibrium at $T_{sat}(P_v)$.

Numerical Model

Equations 5-369, 5-370, 5-377, 5-378, 5-388 were expanded using the following relationships,

$$\rho_m = \alpha\rho_G + (1-\alpha)\rho_\ell$$

$$\rho_G = \rho_v(P_v, T_{sat}(P_v)) + \rho_a(P_a, T_{sat}(P_v)) = \rho_g + \rho_a$$

$$\rho_m h_m = \alpha\rho_g h_g + \alpha\rho_a h_a + (1-\alpha)\rho_\ell h_\ell$$

$$h_a = e_a + \frac{P_a}{\rho_a}$$

The steam in the combined gas phase is saturated at the partial pressure of vapor, P_v. The temperature of vapor is then at its saturation at the partial pressure, and is thermally equilibrium with the non-condensable. The non-condensable gas is assumed to follow ideal gas law.

With above assumption a working mathematical model for the numerical treatment was derived in a matrix form as,

$$\begin{bmatrix} A_{11} & A_{12} & A_{13} & A_{14} & A_{15} \\ A_{21} & A_{22} & A_{23} & A_{24} & A_{25} \\ A_{31} & A_{32} & A_{33} & A_{34} & A_{35} \\ A_{41} & A_{42} & A_{43} & A_{44} & A_{45} \\ A_{51} & A_{52} & A_{53} & A_{54} & A_{55} \end{bmatrix} \begin{bmatrix} \frac{dU}{dZ} \\ \frac{dP}{dZ} \\ \frac{dx}{dZ} \\ \frac{dT_\ell}{dZ} \\ \frac{dP_a}{dZ} \end{bmatrix} = \begin{bmatrix} 0 \\ -\left(\frac{dP}{dZ}\right)_{fr} + \rho_m g\cos\theta \\ 0 \\ 0 \text{or} (1-x) \times \frac{h_\ell - h_{fv}}{h_{gv} - h_{fv}} \times \frac{1}{\Theta} \\ 0 \end{bmatrix} \quad (5\text{-}389)$$

A_{1j} are derived by expanding the mixture mass equation, Equation 5-369,

$$\frac{d\rho_m}{dZ} + \frac{\rho_m}{u}\frac{du}{dZ} = 0 \quad (5\text{-}390)$$

Expanding $\frac{d\rho m}{dZ}$, and noting that $T_S = T_{sat}(P_V)$,

$$\frac{d\rho_m}{dZ} = \left\{\alpha\left(\frac{d\rho_g}{dP_v} + \frac{\partial\rho_a}{\partial T}\frac{dT_s}{dP_v}\right) + (1-\alpha)\frac{\partial\rho_\ell}{\partial P}\right\}\frac{dP}{dZ} + \left\{-(\rho_\ell - \rho_G)\right\}\frac{d\alpha}{dZ} + \left\{(1-\alpha)\frac{\partial\rho_\ell}{\partial T_\ell}\right\}\frac{dT_\ell}{dZ} + \left\{-\alpha\left(\frac{d\rho_g}{dP_v} + \frac{\partial\rho_a}{\partial T}\frac{dT_s}{dP_v}\right) + \alpha\frac{\partial\rho_a}{\partial P_a}\right\}\frac{dP_a}{dZ} \quad (5\text{-}391)$$

From Equations 5-389 and 5-391, coefficients A_{11} through A_{15} are obtained as,

$$A_{11} = \frac{\rho_m}{u} \tag{5-392}$$

$$A_{12} = \alpha\left(\frac{d\rho_g}{dP_v} + \frac{\partial\rho_a}{\partial T}\frac{dT_s}{dP_v}\right) + (1-\alpha)\frac{\partial\rho_\ell}{\partial P} \tag{5-393}$$

$$A_{13} = -(\rho_\ell - \rho_G) \tag{5-394}$$

$$A_{14} = (1-\alpha)\frac{\partial\rho_\ell}{\partial T_\ell} \tag{5-395}$$

$$A_{15} = -\alpha\left(\frac{d\rho_g}{dP_v} + \frac{\partial\rho_a}{\partial T}\frac{dT_s}{dP_v}\right) + \alpha\frac{\partial\rho_a}{\partial P_a} \tag{5-396}$$

A_{2j} through A_{5j} were derived in a similar fashion.

The governing equations shown in Equations 5-369, 5-370, 5-377, 5-378 and 5-388 were [

]^{a,c}

The choking is assumed to occur at the exit, and the criteria for choking is [

]^{a,c} The sensitivity of dP/dZ criteria was investigated by Ohkawa (2007a) and - 10^9 Pa/m was found to be adequate. When G_0 is lower than the critical mass flux, G_c, the pressure gradient at the exit does not reach the criterion. When G_0 is higher than G_c, a singular point is reached before the exit. For the entire validation data set examined, at least [

]^{a,c}

5.12.3 Model as Coded

Subroutine CHOKE is the top of critical flow package and selects sub-models based on the selected options and upstream fluid conditions. CHOKE and SOUND contain the coding for the critical flow models. The necessary input to CHOKE includes the following:

AREA	Cell-edge area
ARATIO	Ratio of cell-edge to donor cell flow areas
DADX	(Cell-edge area – cell area)/(0.5 x cell length)
DXC	Donor cell length
FAC	Donor cell flow area
ALPC	Donor cell void fraction
PC	Donor cell pressure

PAC	Donor cell partial pressure of air
TLC	Donor cell liquid temperature
RHOLC	Donor cell liquid density
RHOVC	Donor cell steam/gas-mixture density
SIGMA	Donor cell surface tension
VL	Momentum-solution liquid velocity
VV	Momentum-solution steam/gas-mixture velocity
VLO	Old-time liquid velocity
VVO	Old-time steam/gas-mixture velocity
VLC	Donor cell cell-center liquid velocity
VVC	Donor cell cell-center steam/gas-mixture velocity
ICFLOW	Critical Flow Model Option Flag

The output variables are:

OUTPUT:	
ICHOKE	Choking indicator: ICHOKE = 0, unchoked flow ICHOKE = 1, subcooled choked flow ICHOKE = 2, two-phase choked flow ICHOKE = 3, single-phase vapor choked flow
VL	Time Averaged Liquid Choke Velocity
VV	Time Averaged Vapor Choke Velocity
DFLDP	Derivative of VL with respect to Pressure
DFVDP	Derivative of VV with respect to Pressure

5.12.3.1 Initial Calculations

Upon entry to subroutine CHOKE, several preliminary calculations are performed to prepare for either a subcooled-liquid choking calculation; a two-phase, two-component choking calculation; or a single-phase vapor choking calculation.

The two choked-flow multipliers are set to the user-input values as specified in the INOPTS NAMELIST data or are defaulted to 1.0 if no user-input values are specified. The cell length-to-hydraulic-diameter ratio, L/D, is checked to determine how subroutine SOUND will calculate the stagnation properties given the cell-center conditions.

[

]^{a,c}

[

]a,c

[ ]a,c (5-397)

(5-398)

and

[ ]a,c (5-399)

where α_c is the cell-center void fraction, ρ_{gc} and $\rho_{\ell c}$ are the cell-center phasic densities, and V_g and V_ℓ are the momentum-solution phasic velocities. If a negative slip is calculated, the slip is reset to 1.0, and the calculational sequence proceeds. This should never occur, but in the event that countercurrent flow is sent to CHOKE, a slip of 1.0 will allow CHOKE to run without failing. (Choked flow will not occur in this case anyway.)

5.12.3.2 Determination of Choking Velocities Using the Appropriate Model for ICFLOW=2

At this point, subroutine CHOKE branches to the appropriate choked-flow model based on the void fraction (either actual or equilibrium as determined by the L/D check described above).

[

]a,c

[

]^{a,c}

5.12.3.2.1 Subcooled Liquid

[ ]^{a,c} a subcooled-liquid calculation is performed to determine the choking velocities.

First, subroutine SOUND is called to determine the maximum mass flux and the corresponding cell-edge conditions. From this maximum mass flux, the value of the homogeneous equilibrium sound speed to be used in conjunction with the donor cell conditions to give the correct mass flow is then calculated, such that:

$$\left[\quad\right]^{a,c} \tag{5-400}$$

where G_{max} is the critical mass flux returned by SOUND and ρ_{mc} is the (donor cell) cell-center mixture density calculated in Equation 5-397.

[

]^{a,c}

$$\left[\quad\right]^{a,c} \tag{5-401}$$

where p_{sat} is the saturation pressure corresponding to T_ℓ, the donor cell liquid temperature; σ is the surface tension; $\rho_{\ell e}$ and ρ_{ge} are cell-edge densities; A_e and A_c are cell-edge and cell-center flow areas; and V_ℓ is the momentum-solution liquid velocity. [

]^{a,c}

$$\left[\quad\right]^{a,c} \tag{5-402}$$

where V_ℓ is again the momentum-solution liquid velocity, p_e is the cell-edge (choke-plane or throat) pressure returned by subroutine SOUND, p_c is the cell-center pressure, and Δx is the cell length.

The code then evaluates [ ]^{a,c}:

[ ]^{a,c} (5-403)

where $V_{\ell c}$ is the cell-center liquid velocity calculated from Equation 5-434 to be described later in this section, $\rho_{\ell e}$ is the cell-edge liquid density as evaluated in subroutine SOUND, p_c is the cell-center pressure, and p_{nuc} is the cell-edge nucleation pressure, Equation 5-401.

The liquid choking velocity is taken as the [

]^{a,c}

[ ]^{a,c} (5-404)

If a sound-speed multiplier was specified through the user-input INOPTS NAMELIST data, this is applied to the liquid choking velocity to give a final predicted value of:

[ ]^{a,c} (5-405)

If the liquid velocity as determined in the momentum solution is less than this maximum choking velocity, the flow is flagged as being unchoked and the calculation is ended. If, however, the liquid velocity determined in the momentum solution is greater than or equal to this maximum choking velocity, then the liquid velocity is reset to be equal to the choking velocity. In addition, a predicted steam/gas-mixture velocity is calculated according to:

[ ]^{a,c} (5-406)

where S is the slip ratio as determined in Equation 5-399. If the predicted steam/gas mixture choking velocity, V_{ge}^{p} , has changed directions from the momentum-solution steam/gas-mixture velocity, V_g , the steam/gas-mixture choking velocity is reset to zero.

5.12.3.2.2 Two-phase, Two-Component Fluid

[ ]^{a,c} a two-phase, two-component choking calculation is done to determine the choking velocities.

Equation 5-365 is extremely difficult to solve analytically. Thus, WCOBRA/TRAC-TF2 obtains the characteristic roots of Equation 5-365 numerically. This method advantageously maintains generality and facilitates computations under different assumptions.

The solution of Equation 5-365 requires that p_a, p_v, α, ρ_a, ρ_v, ρ_ℓ, s_a, s_v, and s_ℓ and their derivatives be specified at the cell edge, where the choking criterion is applied. However, these quantities are known only at the cell center. Direct use of the cell-center quantities yields erroneous results caused by the presence of steep gradients near the choking plane. Therefore, an estimate of the thermodynamic state at the cell edge is necessary. To obtain this estimate, subroutine SOUND is called. In addition to determining the thermodynamic state at the cell edge, SOUND also calculates the homogeneous equilibrium sound speed which is used as a first estimate for the largest characteristic root. (When the non-homogeneous effects are not dominant, the desired root is close to the homogeneous equilibrium sound speed.)

Because equilibrium is assumed to occur at the cell edge, subroutine THERMO is called to determine saturation properties at the cell edge corresponding to the cell-edge pressure, P_e, estimated in the call to SOUND. The cell-edge void fraction may then be calculated, such that:

$$\left[\quad\right]^{a,c} \tag{5-407}$$

where ρ_{me} is the cell-edge mixture density calculated by subroutine SOUND, and $\rho_{\ell e}$ and ρ_{ge} are the saturated liquid and steam/gas-mixture densities for a cell-edge pressure of p_e.

In addition, the entropies and the quantities, $\rho^*_{\ell e}$, ρ^*_{ge}, $s^*_{\ell e}$, and s^*_{ge} necessary for evaluating the elements of matrix B (as shown in Figure 5-21) are defined at the cell-edge, such that:

$$s_{\ell e} = c_{v\ell} \ln\left(\frac{T_e}{273.15}\right) \tag{5-408}$$

$$s_{ve} = c_{v\ell} \ln\left(\frac{T_e}{273.15}\right) + \left(\frac{1}{\rho_{ve}} - \frac{1}{\rho_{\ell e}}\right)\frac{dT}{dp_v} \tag{5-409}$$

$$s_{ae} c_{pa} \ln\left(\frac{T_e}{273.15}\right) - R_a \ln\left(\frac{\max\left\{p_{ae},\ 1.0\times10^{-5}\right\}}{1.0\times10^{5}}\right) \tag{5-410}$$

$$s_{ge} = s_{ae}\left(\frac{\rho_{ae}}{\rho_{ge}}\right) + s_{ve}\left(1 - \frac{\rho_{ae}}{\rho_{ge}}\right) \tag{5-411}$$

and

$$\rho^{*}_{\ell e} = \left(\frac{\partial \rho_{\ell e}}{\partial p}\right)_T + \left(\frac{\partial \rho_{\ell e}}{\partial T}\right)_p \frac{dT}{dp_v} \tag{5-412}$$

$$\rho^{*}_{ve} = \left(\frac{\partial \rho_{ve}}{\partial p_v}\right)_T + \left(\frac{\partial \rho_{ve}}{\partial T}\right)_{pv} \frac{dT}{dp_v} \tag{5-413}$$

$$\begin{aligned} s^{*}_{ve} = {} & \frac{1}{T_e}\left[\left(\frac{\partial e_{ve}}{\partial p_v}\right)_T + \left(\frac{\partial e_{ve}}{\partial T}\right)_{p_v} \frac{dT}{dp_v}\right] \\ & - \frac{p_{ve}}{\rho^2_{ve} T_e}\left[\left(\frac{\partial \rho_{ve}}{\partial p_v}\right)_T + \left(\frac{\partial \rho_{ve}}{\partial T}\right)_{p_v} \frac{dT}{dp_v}\right] \end{aligned} \tag{5-414}$$

and

$$\begin{aligned} s^{*}_{\ell e} = {} & \frac{1}{T_e}\left[\left(\frac{\partial e_{\ell e}}{\partial p}\right)_T + \left(\frac{\partial e_{\ell e}}{\partial T}\right)_p \frac{dT}{dp_v}\right] \\ & - \frac{p_e}{\rho^2_{\ell e} T}\left[\left(\frac{\partial \rho_{\ell e}}{\partial p}\right)_T + \left(\frac{\partial \rho_{\ell e}}{\partial T}\right)_p \frac{dT}{dp_v}\right] \end{aligned} \tag{5-415}$$

where T_e is the cell-edge saturation temperature corresponding to the cell-edge partial pressure of steam, p_{ve}; $c_{v\ell}$ is the liquid constant-volume specific heat (defined in subroutine SETEOS); ρ_{ae}, ρ_{ve}, ρ_{ge}, and $\rho_{\ell e}$ are the cell-edge saturation densities corresponding to the cell-edge pressure, p_e; c_{pa} and R_a are the non-condensable-gas constant-pressure specific heat and the gas constant (both defined in subroutine SETEOS); and p_{ae} is the cell-edge partial pressure of the non-condensable gas as estimated by SOUND.

Next, CHOKE tries to determine the mass flux such that none of the characteristic roots of the governing system of partial differential equations given by Equations 5-359 through 5-363 has a positive real part and that the maximum root is zero. The solution of Equation 5-365 [

]^{a,c}:

$$\left[\quad\right]^{a,c} \tag{5-416}$$

[ ]^{a,c}

To set up the elements of matrix B, CHOKE calculates first-guess approximations of the steam/gas-mixture and liquid cell-edge velocities from the homogeneous equilibrium sound speed, a_{HE}, and the cell-center momentum-solution slip value computed in Equation 5-399, such that:

[ ]a,c (5-417)

and

[ ]a,c (5-418)

where a_{HE} is the homogeneous equilibrium sound speed by returned subroutine SOUND, [

]a,c

The predicted values of the choking velocities to be used in conjunction with the donor cell conditions to give the correct mass-flow rate are now calculated, such that:

[ ]a,c (5-419)

(5-420)

and

[ ]a,c (5-421)

where α_e is the cell-edge void fraction calculated in Equation 5-407; ρ_{ge} and $\rho_{\ell e}$ are the cell-edge saturation densities corresponding to the cell-edge pressure, p_e; ρ_{gc}, $\rho_{\ell c}$, and ρ_{mc} are the cell-center steam/gas-mixture, liquid, and total mixture densities; [

]^{a,c}

If the mixture velocity as determined in the momentum solution is less than this predicted mixture velocity, the flow is flagged as being unchoked and the calculation is ended. If, however, the mixture velocity determined in the momentum solution is greater than (or equal to) the predicted mixture choking velocity, then the steam/gas mixture, liquid, and total mixture velocities are reset to the predicted choking values.

5.12.3.2.3 Interpolation Region Between Subcooled and Two-Phase Models

[ ]^{a,c}, an interpolation between the subcooled-liquid and the two-phase, two-component choking calculation is performed to determine the predicted choking velocities.

Initially, liquid and steam/gas-mixture choking velocities are calculated using the two-phase, two-component model. In addition, liquid and steam/gas-mixture choking velocities are calculated using the subcooled-liquid choking model. These velocities are combined to produce the predicted liquid and steam/gas-mixture choking velocities using a linear interpolation in alpha, such that,

[ ] a,c (5-422)

and

[ ] a,c (5-423)

where $V_{\ell,sc}$ and $V_{g,sc}$ are the liquid and steam/gas-mixture choking velocities calculated using the subcooled-liquid model; $V_{\ell,tp}$ and $V_{g,tp}$ are the liquid and steam/gas-mixture choking velocities calculated using the two-phase, two-component choking model; α_c is the cell-center void fraction (either actual or equilibrium, depending on the value of L/D); and [

]^{a,c}.

5.12.3.2.4 Single-phase Vapor

[ ]^{a,c}, single-phase vapor model is used to determine the choking velocities. Subroutine SOUND is first called to determine cell-edge conditions and the maximum mass flux. From this maximum mass flux, the value of the homogeneous equilibrium sound speed to be used in conjunction with donor cell conditions to give correct mass flow is then calculated, such that:

[ ]a,c (5-424)

where G_{max} is the critical mass flux returned by SOUND and ρ_{me} is the (donor cell) cell-center mixture density calculated in Equation 5-397. If a sound-speed multiplier was specified through the user-input INOPTS NAMELIST data, this is applied to the steam/gas-mixture sound speed to give a predicted steam/gas-mixture choking velocity of:

[ ]a,c (5-425)

If the momentum-solution steam/gas-mixture velocity, V_g, is less than this predicted steam/gas-mixture choking velocity, the flow is flagged as being unchoked and the calculation is ended. If, however, the steam/gas-mixture velocity as determined in the momentum solution is greater than or equal to the predicted choking velocity, then the steam/gas-mixture velocity is reset to be equal to the predicted steam/gas-mixture choking velocity. In addition, a predicted liquid velocity is calculated according to:

[ ]a,c (5-426)

where S is the slip ratio as determined in Equation 5-399. If the predicted liquid choking velocity at the cell edge, $V_{\ell e}^{p}$, has changed directions from the momentum-solution liquid velocity, V_ℓ, it is reset to zero.

5.12.3.3 New-Time Choking Velocities

Finally, new-time phasic choking velocities are computed by [ ]a,c:

[ ]a,c (5-427)

and

[ ]a,c (5-428)

where, $V_{\ell e}^{p}$ and V_{ge}^{p} are the predicted liquid and steam/gas-mixture choking velocities just calculated, and V_ℓ^n and V_g^n are the old-time liquid and steam/gas-mixture velocities (either momentum solution or choking). [

]a,c

This concludes the first pass through the choking model calculation. A second pass is necessary to evaluate the velocity derivatives. This is described in the next section.

5.12.3.4 Second-Pass Velocity and Velocity Derivatives

To calculate the derivatives of the liquid and steam/gas-mixture choking velocities with respect to pressure, a second pass through subroutine CHOKE is made [

]^{a,c}

[ ]^{a,c} (5-429)

and

[ ]^{a,c} (5-430)

where $V^{p}_{\ell,2nd}$ and $V^{p}_{g,2nd}$ are the second-pass predicted liquid and steam/gas-mixture choking velocities, and V^{n}_{ℓ} and V^{n}_{g} are the old-time liquid and steam/gas-mixture velocities (either momentum-solution or choked).

Once the actual and second-pass new-time liquid and steam/gas-mixture choking velocities have been determined, the derivatives with respect to pressure are calculated as follows:

[ ]^{a,c} (5-431)

and

[ ]^{a,c} (5-432)

where V^{n+1}_{ℓ} and V^{n+1}_{g} are the actual new-time choking velocities, and $V^{n+1}_{\ell,2nd}$ and $V^{n+1}_{g,2nd}$ are the second-pass, [

]^{a,c}

With the determination of the new-time choking velocities and their derivatives with respect to pressure, the choking calculation performed in subroutines CHOKE and SOUND is now complete. At this point, the logic returns to the calling subroutine.

5.12.3.5 Cell Center Momentum Solution Velocities

The velocities obtained from the momentum solution are cell-edge values. However, to evaluate stagnation conditions (in subroutine SOUND), it is necessary to know the phasic velocities at cell center. This transition between cell edge and cell center is accomplished in subroutine VOLV by averaging the mass flux between cell edges, such that:

[ ]a,c (5-433)

and

[ ]a,c (5-434)

where V_{gc} and $V_{\ell c}$ are the transformed cell-center velocities, ρ_g and ρ_l are the liquid and steam/gas-mixture densities, α is the void fraction, V_ℓ and V_g are the liquid and steam/gas-mixture velocities, and A is the cross-sectional flow area. The subscripts e- and e+ refer to upstream cell-edge and downstream cell-edge quantities, while the subscript c refers to cell-center quantities for the particular cell in question. It is assumed that $\rho\alpha$ at the upstream face is equal to the upstream cell product value, whereas $\rho\alpha$ at the downstream face is taken to be equal to the current cell value, because densities and void fractions are normally associated with cell-center rather than cell-edge positions.

5.12.3.6 New-Time Choking Velocities

New-time phasic choking velocities are computed by [ ]a,c:

[ ]a,c (5-435)

and

[ ]a,c (5-436)

where $V_{\ell e}^p$ and V_{ge}^p are the predicted liquid and steam/gas-mixture choking velocities, and V_ℓ^n and V_g^n are the old-time liquid and steam/gas-mixture velocities (either momentum solution or choking). [ ]a,c

[

]a,c

5.12.4 Model as Coded (ICFLOW=3 Option)

ICFLOW=3 option replaces the subcooled model and much of MOC model with the Homogeneous Non-equilibrium Relaxation Model (HRM). The sub-model is selected as follows,

[

]a,c

Only the computational steps associated with HRM are described here since other sub-models were already described in detail. [

]a,c

Scaling Considerations

The critical flow model options available in WCOBRA/TRAC-TF2 have inherent scale dependence. The assumption of one-dimensional flow model which by its nature assumes no dependence of scale, and use of simplification and correlations imply that the model performance with regard to the scale will have to be demonstrated. For example, the constant which controls the flashing used in HRM was originally developed from small scale experiment. It is likely that the model would show some scale dependence.

Since the break sizes in the postulated LOCA may vary from less than 0.5 in^2 to a full primary pipe flow area (~0.7m Dia.), it is important to characterize any trend in prediction that may exist relative to global parameters such as pressure, subcooling as well as scale. In Volume 3 of WCAP-12945-P-A, the TRAC-PF1 critical flow model (ICFLOW=2) as implemented in WCOBRA/TRAC has been compared to the Marviken (1982) critical flow data as well as the LOFT data. At these larger ends of break spectrum,

no scale effect has been observed in these comparisons for the TRAC-PF1 critical flow model. The HRM (ICFLOW=3) was assessed in Section 12 of this document for much wider range of break area and upstream conditions with satisfactory results. The assessment results show no significant scale dependence.

Conclusions

The critical flow model options in the WCOBRA/TRAC-TF2 code have been assessed for their intended purposes, namely ICFLOW=2 for LBLOCA, and ICFLOW=3 for the FULL SPECTRUM LOCA methodology with satisfactory performance. The assessment result for ICFLOW=3 option is documented in Section 12 of this document which concluded that there is no significant trend relative to Pressure, Quality, and scale. The bias and uncertainty present in the critical flow model is accounted for in the PWR calculations by ranging the break flow in addition to the break area ranging.

5.13 TEE COMPONENT OFFTAKE MODEL

The WCOBRA/TRAC-TF2 TEE-component offtake model is a modified model from the TRAC-P [ ]^{a,c} offtake model. It specifically handles the case when a small break is made in a large pipe containing horizontal stratified flow. One example of a transient that is particularly well suited for use with the offtake model is the LOCA, in which a small break occurs in one of the large diameter horizontal pipes of the reactor inlet or outlet legs. During this transient, horizontal stratified flow may occur, and the flow quality discharged at the break will depend on whether the break is above or below the liquid level. To accurately follow the progression of the transient, it is essential that the offtake flow be predicted correctly.

The TRAC-P [ ]^{a,c} TEE-component offtake model predicts the offtake flow quality that exits the break based on conditions in the main pipe in a manner similar to that developed for use in the RELAP5/MOD2 code. When the entrance plane to the break is submerged, the offtake flow consists mostly of liquid with possibly an entrained gas component. When the entrance plane is above the liquid level, the offtake flow is mostly gas with possibly an entrained liquid component.

The model is implemented as an option that the user may turn on using the INOPTS namelist data flag IOFFTK. When IOFFTK = 1 (default = 0), the user is required to insert an additional line of input for each TEE component within the input deck specifying the value of the variable IENTRN. This new Card Number 15 requires IENTRN = 1 to implement the offtake model for a particular TEE. Similarly, no offtake model is implemented for any TEE for which IENTRN = 0. To use the model for its intended purpose, the following input guidelines are suggested.

1. The side tube of the TEE is required to be either top, bottom, or centrally located off the main tube.

2. The main-tube-junction cell must be horizontal.

3. The side tube diameter of the TEE must be smaller than the main tube diameter.

4. The side tube of the TEE must be oriented 90° to the main tube.

If these four conditions are not met by the input deck TEE geometry, the problem currently terminates in the initialization stage with a fatal error concerning inappropriate offtake geometry (or in the case of item #3 the problem executes with a warning and without application of the offtake model).

Model Basis

Several studies have been performed to investigate the discharge characteristics of a small break located on a horizontal pipe containing stratified flow. In these studies, the offtake was either top, bottom, or centrally oriented from the main tube as shown in Figure 5-25. The following discussion briefly describes each of these three offtake geometries and the [

]^{a,c}.

In each of the three offtake geometries, a critical height at which gas or liquid entrainment begins, h_b, may be calculated using major-phase conditions at the entrance plane such that:

$$h_b = \frac{C_l W_k^{0.4}}{(g\rho_k \Delta\rho)^{0.2}} \tag{5-437}$$

where C_l = a constant determined from data, W_k = major-phase mass-flow rate, g = gravitational constant, ρ_k = major-phase density, and $\Delta\rho = \rho_\ell - \rho_g$ = phasic density difference. For an upward offtake or for a side-oriented offtake with a liquid level below the offtake center, the major phase comprises the gas component. For a downward offtake or for a side-oriented offtake with a liquid level above the offtake center, the liquid component constitutes the major phase. The values of the constant C_l [

]^{a,c} are summarized in Table 5-9. This formulation for h_b can be derived theoretically for each of the three offtake geometries by considering the force exerted on the liquid particles by the accelerating gas flow for liquid entrainment in upward or side-oriented offtakes and by considering surface instability effects for gas entrainment in downward offtakes (Smoglie, 1984, Harleman, Morgan and Purple, 1959 and Lubin and Springer, 1967).

An actual characteristic height, h, measured as the distance from the offtake entrance plane to the liquid level, may be determined for each of the three offtake geometries as shown in Figure 5-26. The non-dimensional height ratio, R, then may be represented as:

$$R = \frac{h}{h_b} \tag{5-438}$$

where h = actual characteristic height and h_b = critical height as defined by Equation 5-437.

[

]^{a,c}

For an upward offtake,

[ ]a,c (5-439)

[

]a,c

[ ]a,c (5-440)

For a side-oriented offtake,

[ ]a,c (5-441)

[ ]a,c

For a downward offtake,

[ ]a,c (5-442)

[ ]a,c

Model as Coded

The coding for the TEE-component offtake model is contained in subroutine OFFTKE. Upon entry into subroutine OFFTKE, several initial calculations take place. [

]a,c

[ ]a,c (5-443)

[ ]a,c

Next, several tests are performed to determine whether to continue the calculation. Subroutine OFFTKE is designed to handle only the case of two-phase, co-current flow out of the main tube break. If these conditions are not met, the offtake calculation ends and the logic returns to the calling subroutine. This is also true if horizontal stratified flow does not exist in the main-tube-junction cell (as indicated by the horizontal flow weighting factor, W_{st}, defined by equation 4-117) or if the average diameter of the offtake is greater than or equal to the main-tube-junction cell average diameter.

If co-current, horizontal stratified flow out of the main-tube-junction cell does exist, subroutine OFFTKE continues with its initial calculations. [

]^{a,c}

$$[\quad]^{a,c} \tag{5-444}$$

[

]^{a,c} After the initial calculations have been performed, the logic splits to handle each of the three possible geometries: upward offtake, side-oriented, or downward offtake. The TEE-component offtake model in subroutine OFFTKE calculates the void fraction that exits out the main tube junction cell based on the offtake geometry and the liquid level conditions in the junction cell of the main tube.

Upward Offtake

For the case of the upward offtake, the major-flow component is the gas phase. The actual characteristic height for the upward offtake as shown in Figure 5-26 is approximated as:

$$[\quad]^{a,c} \tag{5-445}$$

[

]^{a,c}

The major-phase mass-flow rate at the offtake entrance plane is calculated as:

$$[\quad]^{a,c} \tag{5-446}$$

[

]^{a,c}

The critical entrainment height then may be calculated such that:

$$[\quad]^{a,c} \tag{5-447}$$

[

]^{a,c}

[

]a,c

[ ]a,c (5-448)

The offtake flow quality at the entrance plane is then:

[ ]a,c (5-449)

Side-Oriented Offtake

For the case of the side-oriented offtake, the major-flow component may be either the gas phase or the liquid phase. When the liquid level in the main tube is below the offtake center, the gas phase is the major-flow component and liquid entrainment may occur. However, if the liquid level in the main tube is above the offtake center, the liquid phase becomes the major-flow component and gas entrainment may be possible. The following description details both cases of the side-oriented offtake.

For the case of the side-oriented offtake with a gas major-flow component and possible liquid entrainment, the actual characteristic height (as shown in Figure 5-26) is approximated as:

[ ]a,c (5-450)

The major-phase mass-flow rate at the offtake entrance plane is calculated as:

[ ]a,c (5-451)

[ ]a,c

[ ]a,c (5-452)

[

]a,c

The offtake flow quality at the entrance plane is then:

[ ]a,c (5-453)

where:

[ ]a,c (5-454)

[ ]a,c

For the case of the side-oriented offtake with a liquid major-flow component and possible gas entrainment, the actual characteristic height is calculated the same way as in Equation 5-450. The major-phase mass-flow rate at the offtake entrance plane is calculated as:

[ ]a,c (5-455)

[ ]a,c

[ ]a,c (5-456)

[

]a,c

The offtake flow quality at the entrance plane is then:

[ ]a,c (5-457)

[

]a,c

[ ]a,c (5-458)

[ ]a,c

Downward Offtake

For the case of the downward offtake, the major-flow component is the liquid phase. The actual characteristic height for the downward offtake as shown in Figure 5-26 is approximated as:

[ ]a,c (5-459)

The critical entrainment height then may be calculated [

]a,c

[ ]a,c (5-460)

The offtake flow quality at the entrance plane is then:

[ ]a,c (5-461)

[

]a,c

[ ]a,c (5-462)

[ ]a,c

For each of the three possible offtake geometries, the solution procedure within subroutine OFFTKE follows the same logic. Once the offtake flow quality at the entrance plane is determined based on Equations 5-449, or 5-453, or 5-457 or 5-461, a first prediction of the offtake void fraction is calculated as:

[ ]a,c (5-463)

[

]a,c

[ ]^{a,c}

Then an additional adjustment is performed on $\alpha_m^{n+1,1}$ to obtain the offtake void fraction prediction.

The adjustment is a [

]^{a,c}

[a,c] (5-464)

[ ]^{a,c}

Finally, the offtake void fraction prediction [

]^{a,c}

[a,c] (5-465)

[

]^{a,c}

[a,c] (5-466)

Scaling Considerations

The offtake model is most applicable when the transient being modeled includes a small break in a large pipe containing horizontal stratified flow. [

]^{a,c}

Conclusions

The WCOBRA/TRAC-TF2 TEE-component offtake model predicts the flow discharged from a small break in a large pipe containing horizontal stratified flow. The current model is able to accommodate three different offtake geometries: upward offtake, side-oriented offtake, and downward offtake. Using subroutine OFFTKE, WCOBRA/TRAC-TF2 calculates a prediction for the offtake void fraction from flow correlations for the particular offtake geometry being modeled. This first prediction of the offtake void fraction is then [

]^{a,c} The technique used to implement the offtake model into the two-step numerics scheme is demonstrated to work effectively in Section 12, Volume 2.

5.14 LIQUID LEVEL CALCULATION

In order to calculate a stable mixture level in the core (Figure 5-27), the liquid drain donoring scheme used in TRAC-BF1 (Borkowski and Wade, 1992) and Section 3.4.8.3 of the RELAP5 Theory Manual (INEL, 1995) is included in WCOBRA/TRAC-TF2.

The criteria for the presence of the mixture level in Node J are:

1. $\alpha_{J+1} \geq$ AL_LIMITU and $\alpha_{J-1} <$ AL_LIMITL (Note that (a) this is not the commonly used slug-to-annular transition or the elevation of a large void fraction jump, (b) AL_LIMITU and AL_LIMITL are defaulted to [ ]^{a,c} based on the boil-off transient observation that the liquid drain rate decreases noticeably when the void fraction exceeds [ ]^{a,c})
2. $V_{vj} < U_{crit}$: Drop lifting vapor velocity (Note that this is the same criterion as the vapor fraction sharpener for the Single Phase Vapor transition, which will most likely preclude the reflood mixture front due to the presence of entrainment at the quench front.)

$$U_{crit} = \left(\frac{4}{3} \frac{We_d}{C_{D_d}} \frac{g_c \sigma \Delta\rho}{\rho_v^2} \right)^{\frac{1}{4}} \tag{5-467}$$

where:

We_d = $\frac{\rho_v U_{crit}^2 D_d}{\sigma}$,

C_{D_d} = droplet drag coefficient (-),

D_d = droplet diameter (ft),

g_c = gravitational constant (ft/s^2),

$\Delta\rho$ = $\rho_\ell - \rho_v$ (lbm/ft^3),

ρ_ℓ = liquid density (lbm/ft^3),

ρ_v = vapor density (lbm/ft^3),

σ = surface tension (lbm/s^2),

U_{crit} = critical velocity (ft/s)

When the mixture level is detected, mass and energy convections are modified to accurately compute the contribution to the nodal mass and energy equations for the J-1, J, and J+1 cell by modifying the donored vapor and liquid fraction at cell faces j and j-1 as shown in Table 5-10.

The mixture level, MX_LEVEL, is defined for a channel as follows:

$$MX\_LEVEL = \sum_{J=2}^{N} L_{F,J} DX_J \tag{5-468}$$

where:

$L_{F,J}$ = fractional level, $L_{F,IJ} = \begin{cases} \frac{\alpha_{J+1}-\alpha_J}{\alpha_{J+1}-\alpha_{J-1}} \\ 0 \text{ if above the mixture'} \\ 1 \text{ if below the mixture} \end{cases}$

α = void fraction,

J = node number,

N = highest node number in the channel,

DX = node length

The momentum solutions (phasic momenta) are not modified. The phasic velocities, V_k, are derived from the phasic momentum divided by $(\alpha_k \rho_k A)_{ave}$ as usual. If the liquid phase is "draining," the donor cell (for the void fraction and enthalpies) is selected as shown in Table 5-10 to be consistent with the phasic velocity in draining configuration.

Modification of donor void fraction as described in Table 5-10 is not performed when:

a. A channel is in the "REFLOOD heat transfer process," that is, if the cell, the cell below, or the cell above is in "Top Deluge" or if the cell below is in "HOT WALL";
b. The fractional level is within 0.005 of the node boundary. That is, if MX_LEVEL(node) > 0.995 or if MX_LEVEL(node) < 0.005.

5.15 COUNTER-CURRENT FLOW LIMITATION MODEL

Model Description

The WCOBRA/TRAC-TF2 code contains the capability to enforce three types of CCFL limit lines in the 1D Loop component cell faces and the vertical flow path in the Vessel component via the Northwestern CCFL model (Hsieh et al, 1980), which with proper input, offers an ability to form the Wallis type correlation (Wallis, 1969) or the Kutateladze type correlation (Kutateladze, 1951) in addition to the perforated plate CCFL correlation. The Northwestern CCFL limit line is expressed as:

$$\sqrt{|H_f^*|} + m \cdot \sqrt{H_g^*} = C \tag{5-469}$$

where:

$$H_g^* = j_g \left[\frac{\rho_g}{gw(\rho_f - \rho_g)}\right]^{1/2}, H_f^* = j_f \left[\frac{\rho_f}{gw(\rho_f - \rho_g)}\right]^{1/2} \tag{5-470}$$

and:

$$w = d_h^{(1-\beta)} \cdot L^{\beta}$$

β is an input parameter

When β is 0, the Northwestern correlation becomes equivalent to the Wallis type correlation,

$$\sqrt{|j_f^*|} + m \cdot \sqrt{j_g^*} = C \tag{5-471}$$

where:

$$j_g^* = j_g \left[\frac{\rho_g}{gd_h(\rho_f - \rho_g)}\right]^{1/2} \quad \text{and} \quad j_f^* = j_f \left[\frac{\rho_f}{gd_h(\rho_f - \rho_g)}\right]^{1/2} \tag{5-472}$$

When β is 1, the Northwestern correlation becomes equivalent to the Kutateladze type correlation,

$$\sqrt{|K_f^*|} + m \cdot \sqrt{K_g^*} = C \tag{5-473}$$

where:

$$K_g^* = j_g \left[\frac{\rho_g^{\,2}}{g\sigma(\rho_f - \rho_g)}\right]^{1/4} \quad \text{and} \quad K_f^* = j_f \left[\frac{\rho_f^{\,2}}{g\sigma(\rho_f - \rho_g)}\right]^{1/4} \tag{5-474}$$

The perforated plate CCFL correlation is enforced when β is defined as:

$$\beta = \tanh(r \cdot k \cdot d_h) \tag{5-475}$$

where:

d_h = the hole diameter,

$$L = \left[\frac{\sigma}{g(\rho_f - \rho_g)}\right]^{1/2}$$

$r = A_h/A_T$ (hole area divided by total plate area)

and a wave number defined by:

$k = \frac{2\pi}{t_p}$ in which t_p is the thickness of the plate.

Bankoff (1981) defined the constant, C for a perforated plate as[2],

$$C = \begin{cases} 1.07 + 4.33 \times 10^{-3} L^*, \text{for } L^* \leq 200 \\ 1.94, \text{for } L^* > 200 \end{cases} \quad (5\text{-}476)$$

Where,

$$L^* = n\pi d_h \left[\frac{g(\rho_f - \rho_g)}{\sigma}\right]^{1/2} \quad (5\text{-}477)$$

and n is the number of holes in the perforated plate.

Scaling Considerations

The basis of the models ranges from subscale to full scale relative to the PWR application. The value of constants in the correlation, m, and C reflect particular geometry, scale and pressure where the correlation is to be applied.

5.16 REFERENCES

1. Abuaf, N., Jones, O. C. Jr., and Wu, B. J. C., 1983, "Critical Flashing Flows in Nozzles with Subcooled Inlet Conditions," *Journal of Heat Transfer*, 105, 2, 379, pp. 65-74.

2. Adams, J. E. and Clare, A. J., 1983, "A Preliminary Study of Droplet Breakup at PWR Spacer Grids," Central Electric Generating Board, PWR/HTWS/P Pg. 130.

3. Adams, J. E. and Clare, A. E., 1984, "Droplet Breakup and Entrainment at PWR Spacer Grids," International Workshop on Fundamental Aspects of Post-Dryout Heat Transfer, Salt Lake City.

4. Alamgir, M. and Lienhard, J. H., 1981, "Correlation of Pressure Undershoot During Hot-Water Depressurization," *Transactions of the ASME, Journal of Heat Transfer*, Vol. 103, pp. 52-55.

5. Amos, C. N. and Schrock, V. E., 1984, "Two-Phase Critical Flow in Slits," *Nuclear Science and Engineering*, 88, pp. 261-274.

[2] Bankoff (1981) actually states that C = 2 above $L^* = 200$; however, the as-coded (default) value is 1.94 to remove the discontinuity at $L^* = 200$.

6. Andreychek, T. S., Chow, S. K., and Hochreiter, L. E., 1988, "APWR LOCA Test Program Final WDR Guide Test and Analysis Report," WCAP-11928.

7. Archer, W. H., 1913, "Experimental Determination of Loss of Head Due to Sudden Enlargement in Circular Pipes," *Trans. ASCE.* Vol. 76, Pg. 999.

8. Ardron, K. H. and Bryce, W. M., 1990, "Assessment of horizontal stratification entrainment model in RELAP5/MOD2 by comparison with separate effects experiments," *Nuclear Engineering and Design*, 122, pp. 263-271.

9. Bankoff, S. G., et al., 1981, "Countercurrent Flow of Air/Water and Steam/Water Through a Horizontal Perforated Plate," *Int. J. Heat Mass Transfer*, 24 (8), 1381-1395.

10. Bestion, D., 1990, "The physical closure laws in the CATHARE code," *Nuclear Engineering and Design*, 124, pp. 229-245.

11. Bird, R. B., Stewart, W. E., and Lightfoot, E. N., 1960, Transport Phenomena, John Wiley and Sons.

12. Borkowski, J. A. and Wade, N. L., 1992, "TRAC-BF1/MOD1: An Advanced Best-Estimate Computer Program for BWR Accident Analysis," NUREG/CR-4356, Volume I, R4.

13. Chen, C. Y., 1955, "Filtration of Aerosols by Fibrous Media," Chem. Rev., Vol. 55, pg. 595.

14. Churchill, S. W., 1977, "Friction-Factor Equation Spans All Fluid-Flow Regimes," Chemical Engineering, Nov. 7, pp. 91-92.

15. Cicchitti, A., Lombardi, C., Silvestri, M., Soldaini, G. and R. Zavatarelli, 1960, "Two-Phase Cooling Experiments: Pressure Drop, Heat Transfer and Burnout Measurements," Energia Nucleare 7, pp. 407-425.

16. Coddington, P. and Macian, R., 2002, "A study of the performance of void fraction correlations used in the context of drift-flux two-phase flow models," *Nuclear Engineering and Design*, 215, pp. 199-216.

17. Collier, J. G. et al., 1972, "Two-Phase Pressure Drop and Void Fractions in Tubes," AERE-R-6454, HTFS Design Report 15 (HTFS-DR-15).

18. Collier, J. G., 1972, Convective Boiling and Condensation, McGraw-Hill Book Company, New York.

19. Cousins, L. B., et al., 1965, "Liquid Mass Transfer in Annular Two-Phase Flow," Paper C4 presented at the Symposium on Two-Phase Flow Volume 2, Exeter, England, pp. 401-430.

20. Crane, C. O., 1969, "Flow of Fluids Through Valves, Fittings, and Pipe," Technical Paper No. 410 published by Crane Co.

21. Dallman, J. C. and Kirchner, W. L., 1980, Los Alamos Scientific Laboratory, "De-Entrainment Phenomena on Vertical Tubes in Droplet Cross Flow," USNRC Report, NUREG/CR-1421.

22. Davies, C. N., 1952, "The Separation of Airborne Dust and Particles," *Proc. Inst. Mech. Engrs.* (London), Vol. 1B, No. 5, pg. 185.

23. Downar-Zapolski, P., Bilicki, Z., Bolle, L. and Franco, J., 1996, "The Non-equilibrium Relaxation Model for One-dimensional Flashing Liquid Flow," *International Journal of Multiphase Flow*, Vol. 22, No. 3, pp. 473-486.

24. Dukler, A. E., Wicks, M. and Cleveland, K. T., 1964, "Frictional Pressure Drops in Two-Phase Flow," *AIChE Journal* 10, 44.

25. Dukler, A. E., and Smith, L., 1979, "Two-Phase Interactions in Countercurrent Flow Studies of the Flooding Mechanism," NUREG/CR-0617.

26. Grace, J. R., Wairegi, T. and Brophy, J., 1978, "Break-Up of Drops and Bubbles in Stagnant Media," *Can. J. Chem. Eng.*, Vol. 56, pp. 3-8.

27. Harleman, D. R. L., Morgan, R. L., and Purple, R. A., 1959, "Selective Withdrawal from a Vertically Stratified Fluid," International Association for Hydraulic Research, 8th Congress, Montreal, Canada, August 24-29.

28. Henstock, W. H. and Hanratty, T. J., 1976, "The Interfacial Drag and the Height of the Wall Layer in Annular Flows," *AIChE Journal*, Vol. 22, No. 6, pp. 990-1000.

29. Hochreiter, L. E., et al., 1976, "G-2, 17x17 Refill Heat Transfer Tests and Analysis," WCAP-8793.

30. Hsieh, C., et al., 1980, "Countercurrent Air/Water and Steam/Water Flow above a Perforated Plate," NUREG/CR-1808.

31. Idel'Chik, I. E., 1960, "Handbook of Hydraulic Resistance," AEC-tv-6630.

32. INEL, 1995, "RELAP5/MOD3 Code Manual Volume I: Code Structure, System Models, and Solution Methods," NUREG/CR-5535, Volume I.

33. Ishii, M., 1975, Thermo-Field Dynamic Theory of Two-Phase Flow, Eyrolles.

34. Ishii, M., 1977, "One-Dimensional Drift-Flux Model and Constitutive Equations for Relative Motion Between Phases in Various Two-Phase Flow Regimes," Argonne National Laboratory report ANL-77-47.

35. Ishii, M. and Chawla, T. C., 1979, "Local Drag Laws in Dispersed Two-Phase Flow,"Argonne National Laboratory report ANL-79-105, NUREG/CR-1230.

36. Ishii, M. and Grolmes, M. A., 1975, "Inception Criteria for Droplet Entrainment in Two-Phase Concurrent Film Flow," *AIChE Journal*, Vol. 21, No. 2, pg. 308.

37. Ishii, M. and Mishima, K., 1984, "Two-Fluid Model and Hydrodynamic Constitutive Relations," *Nucl. Eng. and Design*, Vol. 82, pp.107–126.

38. Jones, O. C., 1980, "Flashing Inception in Flowing Liquids," *Transactions of the ASME, Journal of Heat Transfer*, Vol. 102 pp. 439-444.

39. Kataoka, I., and Ishii, M., 1982, "Mechanism and Correlation of Droplet Entrainment and Deposition in Annular Two-Phase Flow," Argonne National Laboratory report ANL-82-44, NUREG/CR 2885.

40. Kataoka, I., and Ishii, M., 1983, "Mechanistic Modeling and Correlations for Pool Entrainment Phenomenon," Argonne National Laboratory report ANL-83-37, NUREG/CR-3304.

41. Kataoka, I., and Ishii, M., 1987, "Drift flux model for large diameter pipe and new correlation for pool void fraction," *Int. J. Heat Mass Transfer*, Vol. 30, No. 9, pp. 1927-1939.

42. Kataoka, I., Ishii, M.,and Mishima, K., 1983, "Generation and Size Distribution of Droplet in Annular Two-Phase Flow," *Transactions of the ASME, Journal of Fluids Engineering*, Vol. 105, pp. 230-238.

43. King, H. W. and Brater, E. F., 1963, Handbook of Hydraulics, McGraw Hill Book Company, Inc., New York, pp. 6-21.

44. Kitscha J. and Kocamustafaogullari G., 1989, "Breakup Criteria for Fluid Particles," *Int. J. Multiphase Flow*, Vol. 15, No. 4, pp. 573-588

45. Kutateladze, S. S., 1951, *Izv. Akad. Nauk SSSR, Otd. Tekhn. Nauk* 8, 529.

46. Lee, N., et al., 1981, "PWR FLECHT SEASET Unblocked Bundle, Forced and Gravity Reflood Task Data Evaluation and Analysis Report," NUREG/CR-2256.

47. Lee, S. L., et al., 1982, "Re-entrainment of Droplets from Grid Spacers in Mist Flow Portion of a LOCA Reflood of a PWR, NRC/ANS Topical Meeting on Basic Thermal Hydraulic Mechanisms in LWR Analysis," NUREG/CR-0043.

48. Lee, S. L., 1984a, "Measurement of Grid Spacer's Enhanced Droplet Cooling Under Reflood Condition in a PWR by LDA," Department of Mechanical Engineering, SUNY at Stony Brook.

49. Lee, S. L., et al., 1984b, "A Study of Droplet Hydrodynamics Across a Grid Spacer," NUREG/CR-4034.

50. Lee, S. Y. and Schrock, V. E., 1990, "Critical Two-Phase Flow in Pipes for Subcooled Stagnation States with a Cavity Flooding Incipient Flashing Model," *Transaction of the ASME, J. of Heat Transfer*, Vol. 112, pp. 1032-1040.

51. Levy, S., 1960, "Steam Slip-Theoretical Prediction From Momentum Model," *Journal of Heat Transfer*, 82, pp. 113-124.

52. Lime, J. F., 2001, "Memorandum on Interfacial Drag from M. Ishii to R. Nelson, July 28, 1987," Los Alamos National Laboratory document LA-RA-01-1591.

53. Liles, D. R., et al., 1981, "TRAC-PD2, An Advanced Best-Estimate Computer Program for Pressurized Water Reactor Loss-of-Coolant Accident Analysis," NUREG/CR-2054.

54. Liles, D. R., et al., 1988, "TRAC-PF1/MOD1 Correlations and Models," NUREG/CR-5069.

55. Lovell, T. W., 1977, "The Effect of Scale on Two-Phase Counter-Current Flow Flooding in Vertical Tubes," Masters Thesis, Thayer School of Engineering, Dartmouth College.

56. Lubin, B. T. and Springer G. S., 1967, "The formation of a dip on the surface of a liquid draining from a tank," *J. Fluid Mech.*, Vol. 29, Part 2, 385-390.

57. Marviken Project, 1982, "The Marviken Full-Scale Critical-Flow Tests," EPRI-NP 2370.

58. Massey, B. S., 1968, Mechanics of Fluids, Van Nostrand Co., New York.

59. Nikuradse, J., 1933, "Strömungegesetze in Rauhen Rohren," VDI-Forschungshelf, 361, 1933 or NACA-TM-1292.

60. Ohkawa, K., 2007a, "Assessment of Homogeneous Non-equilibrium Relaxation Critical Flow Model," 15th *International Conference on Nuclear Engineering*, ICONE15-10708, Nagoya, Japan, April 22-26.

61. Ohkawa, K., 2007b, "Development of Homogeneous Non-equilibrium Relaxation Critical Flow Model with Non-condensable Gas," Paper-151, *The 12th International Topical Meeting on Nuclear Reactor Thermal-Hydraulics (NURETH-12)*, Pittsburgh, Pennsylvania, USA, September 30 – October 4.

62. Okubo, T. and Sugimoto, J., 1984, "Overview of JAERI's 17x17 Type Small Scale Reflood Experiments," JAERI.

63. Ohnuki, A., Adachi, H., and Murao, Y., 1988, "Scale Effects on Countercurrent Gas-liquid Flow in a Horizontal Tube Connected to an Inclined Riser," *Nuclear Engineering and Design* 107, pp. 283-294.

64. Owens, W. L., 1981, "Two-Phase Pressure Gradient," *International Heat Transfer Conference*, Boulder, Colorado.